Genesis and origin of terrestrial materials within the carbonate deposits of the Western-Istrian Anticline

Perković, Ivor

University of Zagreb

Faculty of Mining, Geology and Petroleum Engineering

Ivor Perković

GENESIS AND ORIGIN OF TERRESTRIAL MATERIALS WITHIN THE CARBONATE DEPOSITS OF THE WESTERN-ISTRIAN ANTICLINE

DOCTORAL DISSERTATION

Zagreb, 2024

University of Zagreb

Faculty of Mining, Geology and Petroleum Engineering

Ivor Perković

GENESIS AND ORIGIN OF TERRESTRIAL MATERIALS WITHIN THE CARBONATE DEPOSITS OF THE WESTERN-ISTRIAN ANTICLINE

DOCTORAL DISSERTATION

Supervisor:
Prof. Goran Durn, PhD

Zagreb, 2024.

Sveučilište u Zagrebu

Rudarsko-geološko-naftni fakultet

Ivor Perković

POSTANAK I PODRIJETLO KOPNENIH MATERIJALA U SLIJEDU KARBONATNIH NASLAGA ZAPADNOISTARSKE ANTIKLINALE

DOKTORSKI RAD

Mentor:
Dr.sc. Goran Durn, redoviti profesor

Zagreb, 2024.

Information about the mentor:
Prof. Goran Durn, PhD
University of Zagreb
Faculty of Mining, Geology and Petroleum Engineering
Department of mineralogy, petrology and mineral resources

Zahvaljujem se mentoru dr. sc. Goranu Durnu na Vašem vodstvu, podršci, neprocjenjivim savjetima, brizi o mom napretku i na svome znanju koje ste mi prenijeli, kako znanstvenom kako ljudskom. Hvala Vam što ste uvijek bili tu, motivirali me te mi pomogli savladati sve izazove koji su se našli na ovom putu. Pod Vašim vodstvom nijedan problem nije bio prevelik, a to je zbog toga što sam uvijek imao Vašu podršku i pomoć, kad god je to bilo potrebno. Osim toga, na ovome putu niste dijelili sa mnom samo izazove i prepreke, već i mnoge lijepe trenutke i ugodne razgovore koje su me izgradili kao znanstvenika i kao osobu, a kojih ću se rado sjećati i na kojima sam Vam zahvalan.

Zahvaljujem se dr. sc. Igoru Vlahoviću, za svu pomoć i podršku koju ste mi pružili tijekom doktorata, a pogotovo na detaljnim i korisnim komentarima prilikom pisanja znanstvenih radova koji su obogatili i unaprijedili moj znanstveni izričaj. Iznimno sam Vam zahvalan što ste uvijek bili dostupni i spremni za bilo kakvu diskusiju, pomoć ili pružanje korisnog savjeta, pogotovo u području sedimentologije. Hvala Vam i na svim ugodnim razgovorima i šalama koje uvijek uljepšaju dan na fakultetu, ali i koje posebno obogate i učine zabavnijim dan na terenu. Posebno Vam hvala na svoj pomoći u finalizaciji mog doktorskog rada, koja je bila ključna za njegov uspješan završetak, te Vam se zahvaljujem što ste prihvatili biti predstojnik povjerenstva.

I would like to thank DSc Andrea Mindszenty, for sharing your beautiful and vast knowledge with me, which was crucial for my scientific development, as it helped me to grasp most complex mechanisms and topics in the study of palaeosols. I am also thankful for all substantial and warm discussions with you that I always enjoyed, and for all the good memories from the field trips and from my time in Budapest. I am also extremely thankful for all your help during the finalization of this thesis, and that you accepted to be a part of the committee for the evaluation of this thesis, which is an honour and a privilege.

Zahvaljujem se dr. sc. Blanki Cvetko Tešović, na svoj pomoći, podršci i korisnim diskusijama bez kojih ovaj doktorat ne bi bio isti. Zahvalan sam Vam i na pomoći i društvu na našim terenskim istraživanjima, gdje Vaš entuzijazam i pozitivna energija uvijek obogate dan na terenu te ga učine posebnim. Hvala Vam što ste prihvatili biti član povjerenstva te što ste mi pomogli u finalizaciji doktorata, a pogotovo sam Vam zahvalan na brizi i ugodnim razgovorima koji su mi pomogli prebroditi teška razdoblja, što ću zauvijek pamtiti i cijeniti.

Zahvaljujem dr. sc. Maji Martinuš, na korisnim savjetima i diskusijama, te pomoći i podršci u izradi ovog doktorskog rada, koja su omogućila podizanje ovog istraživanja na jednu višu razinu. Hvala ti za odlično društvo na našim terenskim istraživanjima, gdje ih je tvoj entuzijazam i kritički pogled uvijek uljepšao i unaprijedio.

Zahvaljujem Darku Matešiću na pomoći i podršci u izradi doktorata, a pogotovo na svoj pomoći u terenskim istraživanjima bez koje puno toga ne bi bilo ostvareno. Hvala ti također i na svim diskusijama i razgovorima kako ljudskim kako znanstvenim, koji me uvijek zaintrigiraju i razvesele.

Zahvaljujem svojim cimerima dr. sc. Šimi Biliću i dr. sc. Tomislavu Brenku, na svoj pomoći u znanstvenome radu, te dijeljenju kako dobrih kako teških trenutaka kada ste mi uvijek pružili potrebnu podršku. Hvala vam pogotovo na raznoraznim diskusijama i raspravama koje uvijek

uljepšaju dan te ga učine zanimljivijim i zabavnijim. Posebno hvala Šimi, na posebnim tipovima diskusija.

Zahvaljujem dr. sc. Duji Smirčiću, na svoj podršci i pomoći, ali pogotovo na svim druženjima, razgovorima i svirkama, koje su pomogli prebroditi dosadna ili teška razdoblja, ali i uljepšati ona dobra. Hvala ti na svim korisnim savjetima, kako ljudskim, kako znanstvenim, kako ribolovnim ili glazbenim.

Zahvaljujem se dr. sc. Michaeli Hruškovoj Hasan, što je pomogla usmjeriti te omogućiti sve analize i analitičke metode koje su bile brojne. Hvala Vam na Vašem entuzijazmu i interesu u moj laboratorijski rad, uz koji nikad nije bio problem probati nešto novo ili savladati razne izazove u laboratorijskom radu.

Zahvaljujem se našim tehničarima, Branki Prši i Vinku Baranašiću na odrađenom velikome dijelu laboratorijskog posla, te na svoj pomoći prilikom mog rada u laboratoriju. Posebno se zahvaljujem Vinku, što si bio entuzijastičan suputnik na mom putovanju kroz svijet XRD-a, te se veselim našem daljnjem zajedničkom radu i usavršavanju.

Zahvaljujem se Boženi Vlainić, što je uvijek sa smiješkom i uz topli razgovor pomagala s papirologijom kroz sve ove godine.

Zahvaljujem se dr. sc. Andrei Čobić, dr. sc. Darku Tibljašu i dr. sc. Sabini Strmić Palinkaš uz koje je započeo moj znanstveni put, što ste me uveli u svijet znanosti i usadili mi ljubav prema mineralogiji i znanstvenome radu. Hvala vam na svim razgovorima, diskusijama i druženjima koje su me izgradile kao znanstvenika ali i osobu.

Zahvaljujem se dr. sc. Sreči Davoru Škapinu na izvrsnim SEM fotografijama i EDS analizama koje su bile ključne u određenim segmentima ovog doktorata.

Zahvaljujem se Željki Kurelec i Andrei Gmajnički iz Ureda za poslijediplomski na pomoći s obrascima i razumijevanju mojih obaveza na doktorskome studiju.

Zahvaljujem se svim mojim dragim kolegama bez kojih ovaj put ne bi bio isti. Hvala vam na svim savjetima, diskusijama i podršci koju ste mi pružili.

Posebno se zahvaljujem prijateljima i obitelji na njihovoj stalnoj podršci i na svemu što ste učinili za mene, te na svim sretnim i teškim trenutcima koje smo zajedno podijelili.

Hvala ti Domenika…

ABSTRACT

The Western Istrian Anticline represents a major structure of the Istrian peninsula, which comprises four depositional megasequences separated by four regionally important unconformities. This research focuses on the terrestrial materials from the 1st Unconformity and 3rd Unconformity primarily characterised by bauxites and palaeosols. The 1st Unconformity was studied at two localities: the Rovinj-1 bauxite deposit and the Zlatni rt palaeosol, which were found to be derived from polygenetic parent material. The most important find in the Rovinj-1 deposit was the climate aridification during the end of bauxite deposition and subsequent deposition of its cover. Glauconite was found in the upper parts of the cover deposits, and it was also found in the Zlatni rt palaeosol, where it was studied in detail as a rare example of glauconite formation during the palaeosol flooding. The 3rd Unconformity was studied at the Minjera locality, where analysed material was found to be primarily derived from aeolian sources. Their study revealed differences in palaeotopography during formation of individual bauxite deposits, shown also in the mineralogical and geochemical differences. The pyritisation in these deposits was determined to be a multi-phase process, since four stages of pyritisation were observed. This work also aimed to determine the differences and similarities in the behaviour of trace elements and REEs between oxidising and reducing conditions in palaeosols and bauxites. It was determined that iron oxides were found to be a primary source of their enrichment under oxidising conditions while the immobility of certain elements, their scavenging by pyrite and release upon the dissolution of iron oxides were the primary drivers of enrichment and depletion of different elements under reducing conditions.

PROŠIRENI SAŽETAK

Uvod

Zapadnoistarska antiklinala kao SZ dio Jadranske karbonatne platforme predstavlja nedeformirani dio Jadranske mikroploče. Njezine se naslage sastoje od četiriju megasekvencija, međusobno odijeljenim četirima diskordancijama, u sklopu kojih su taložene kopnene naslage. 1. megasekvencija predstavlja karbonatne naslage taložene između bata i starijeg kimeridža koje se primarno sastoje od mikritnih, peloidalnih te bioklastičnih do ooidnih vapnenaca. Nakon njihova taloženja započinje nastanak boksita, paleotala i breča 1. diskordancije tijekom starijeg kimeridža do mlađeg titona. Porastom morske razine u mlađem titonu započinje 2. megasekvencija taloženjem Kirmenjak vapnenaca, nakon kojih slijedi taloženje izmjene ranodijagenetskih i kasnodijagenetskih dolomita i debelog slijeda pretežito plitkomorskih vapnenaca. Na prijelazu iz starijeg u mlađi apt došlo je do regresije i početka 2. diskordancije u sklopu koje su taložena močvarna paleotla i breče. Oscilirajućom transgresijom u mlađem albu završila je 2. diskordancija te započelo taloženje 3. megasekvencije u sklopu koje je taložen debeli slijed vapnenaca i dolomita. Taloženje tih naslaga završava u različito vrijeme, od mlađeg cenomana do mlađeg santona okopnjavanjem uzrokovanim početkom kolizije Jadranske mikroploče s Euroazijskom pločom. U sklopu te 3. diskordancije talože se primarno boksiti uz različite tipove paleotala i špiljskih sedimenata. U paleocenu je došlo do transgresije kojom je započelo lokalno taloženje slatkovodnih do bočatih kozinskih naslaga, nakon kojih u eocenu slijedi taloženje marinskih foraminiferskih vapnenaca, prijelaznih naslaga, globigerinskih lapora te fliša. Konačna kolizija s Euroazijskom pločom uzrokovala je izdizanje cijelog područja Istre čime je započela 4. diskordancija koja obuhvaća kopnene materijale taložene sve do danas, a primarno je predstavljena crvenično tlima te pedosedimentnim kompleksima crvenica i lesa. Karbonatne i siliciklastične naslage četiriju megasekvencija detaljno su istražene te predstavljaju dobro utemeljen stratigrafski okvir koji olakšava i omogućava detaljno izučavanje kopnenih materijala taloženih tijekom trajanja četiriju navedenih diskordancija, odnosno tijekom prekida taloženja. Kopneni materijali koji su predmet istraživanja ove doktorske disertacije slabije su istraženi u odnosu na okolne marinske karbonatne i siliciklastične naslage. Za kopnene materijale u području Zapadnoistarske antiklinale bitno više relevantnih znanstvenih podataka postoji za one vezane za 2. i 4. diskordanciju dok su naslage 1. i 3. diskordancije znatno manje istražene te su stoga bile i glavni predmet istraživanja ovog doktorskog rada. Naslage 1. i 3. diskordancije predstavljene su primarno boksitima a dijelom i različitim tipovima paleotala. Boksiti i paleotla kao i njihova neposredna podina i krovina izrazito su važan i vrijedan izvor informacija o paleoklimatskim i paleookolišnim uvjetima koji su egzistirali tijekom istraživanih diskordancija. Tako boksiti jasno ukazuju na uvjete tropske i vlažne klime te na dugotrajnost kopnenih faza tijekom kojih su formirani. Analiza mineralnog i geokemijskog sastava boksita i paleotala može pružiti dodatni uvid u kemijske i fizičke promjene prilikom njihove geneze, posebno analizom minerala glina te sastava i ponašanja elemenata u tragovima i elemenata rijetkih zemalja (REE). Također, tijekom transgresije je došlo do piritizacije boksita i taloženja krovinskih naslaga koje su specifične za individualna ležišta, tako da analiza

piritiziranih boksita i njihove neposredne krovine pruža uvid u inicijalnu fazu transgresije. Upravo takvi slijedovi naslaga koje tijekom svog postanka bilježe promjene okoliša, pa tako i prevladavanje oksidativnih i reduktivnih uvjeta, predstavljaju izvrstan materijal za proučavanje i analizu razlika i sličnosti ponašanja elemenata u tragovima i elemenata rijetkih zemalja u specifičnim okolišima. Obzirom da su paleotla vezana za 2. diskordanciju nastala u reduktivnim okolišima, a crvenična tla vezana za 4. diskordanciju u oksidativnim uvjetima, saznanja vezana za tu problematiku dobivena istraživanjem boksita 1. i 3. diskordancije, upotpunjena su rezultatima dobivenim istraživanjem kopnenih materijala 2. i 4. diskordancije. Nadalje, na temelju sastava teške frakcije utvrđena je poligenetska provenijencija ishodišnih materijala iz kojih su nastali boksiti i paleotla 1. i 3. diskordancije. Posljednji cilj ove disertacije ispunjen je djelomice, budući da se zbog ograničenosti dobivenih rezultata bez dodatnih kompleksnih istraživanja nije mogla provesti detaljnija paleogeografska rekonstrukcija kretanja područja Zapadnoistarske antiklinale i geotektonskih promjena u njezinom okruženju. S druge strane, tijekom istraživanja za potrebe doktorskog rada ostvareni su i izvorno neplanirani rezultati i utvrđene nove znanstvene spoznaje od kojih osobito treba istaknuti pronalazak glaukonita u potopljenome paleotlu na lokaciji Zlatni rt, aridifikaciju klime utvrđenu u ležištu boksita Rovinj-1 i epigenetske promjene istražene u nalazištima boksita Minjera.

Ciljevi i hipoteze

Glavni ciljevi ovog rada bili su: (1) rekonstruirati paleoklimu i okoliš u kojima su nastajali kopneni materijali 1. i 3. diskordancije na temelju mineraloških, geokemijskih i mikropedoloških podataka, (2) utvrditi provenijenciju ishodišnog materijala iz kojeg su nastali boksiti 1. i 3. diskordancije na temelju geokemijskih podataka i podataka iz teške mineralne frakcije, (3) rekonstruirati razvoj Zapadnoistarske antiklinale na temelju evolucije provenijencije ishodišnih materijala sve četiri diskordancije i (4) utvrditi razlike i sličnosti u ponašanju lantanida i elemenata u tragovima između reduktivnih i oksidativnih uvjeta u materijalima sve četiri diskordancije. Ovi ciljevi su bazirani na sljedećim hipotezama: (1) mineralogija, kemizam i mikropedološke značajke odražavaju paleoklimu i paleookoliš u kojem nastaju boksiti i paleotla, (2) provenijencija boksita i paleotala može se utvrditi na temelju njihovog kemizma i sastava teške frakcije, (3) kretanje Zapadnoistarske antiklinale i geotektonske promjene u njezinom okruženju mogu se utvrditi na temelju evolucije provenijencije materijala iz svih diskordancija te (4) lantanidi i elementi u tragovima se u paleotlima i boksitima različito ponašaju u reduktivnim i oksidativnim uvjetima.

Znanstveni doprinos

Tijekom izrade disertacije objavljena su četiri znanstvena rada (tri u časopisima u Q1 i jedan u Q3 prema prema bazi WoS odnosno tri u Q1 i jedan u Q2 prema bazi Scopus) a jedan rad je predan na recenziju u časopis Ore Geology Reviews (Q2 prema bazi WoS odnosno Q1 prema bazi Scopus). Na svih pet radova pristupnik je glavni autor (tri puta prvi autor i dva puta dopisni autor). Za doktorski rad su od do sada objavljena četiri rada odabrana tri. Utvrđeno je kako mineralogija, kemizam i mikropedološke značajke odražavaju paleoklimu i paleookoliš u kojem nastaju boksiti

i paleotla (1. i 3. diskordancija) te je utvrđeno kako se provenijencija boksita i paleotala može utvrditi temeljem sastava teške i lake mineralne frakcije (1. i 3. diskordancija). Osim toga sustavno je istraženo, opisano i detaljno znanstveno obrazloženo ponašanje lakih, srednjih i teških lantanida te indikativnih elemenata u tragovima u reduktivnim i oksidativnim uvjetima u tlima, paleotlima i boksitima (sve četiri diskordancije). Kao najvažniji znanstveni doprinos treba istaknuti: (1) pronalazak glaukonita u potopljenome paleotlu na lokaciji Zlatni rt i interpretaciju njegove geneze, (2) utvrđivanje aridifikacije klime koja se odražava u gornjem dijelu ležišta boksita Rovinj-1 i njegovoj neposrednoj krovini, (3) razumijevanje ponašanja elemenata rijetkih zemalja (REE) u oksidativnim i reduktivnim uvjetima u boksitima i paleotlima, što je posebno važno za REE koji su jedna od kritičnih sirovina izuzetno važnih za današnje društvo i tehnologiju, a za koje boksiti predstavljaju potencijalnu mineralnu sirovinu te (4) prepoznavanje i interpretaciju epigenetskih promjena u boksitima Minjere.

Metode i postupci

Prikazano istraživanje se temelji na mineraloškim i geokemijskim podacima koji su prikupljeni širokim rasponom analitičkih metoda. Za mineraloško analizu korištena je rendgenska difrakcija na prahu uzorcima (XRPD), infracrvena spektroskopija s Fourierovom transformacijom (FTIR) i analiza teške i lake mineralne frakcije. Geokemijski podaci prikupljeni su korištenjem rendgenske fluorescencije (XRF), masene spektrometrije s induktivno spregnutom plazmom (ICP-MS) i analize stabilnih izotopa sumpora u željeznim sulfidima, zajedno s pretražnom elektronskom mikroskopijom s energijski disperzivnom rendgenskom spektroskopijom (SEM-EDS). Valja istaknuti uporabu Rietveldovog utočnjavanja, koja je korištena u svrhu prikupljanja semikvantitativnog mineraloškog sastava iz difraktograma dobivenih XRPD-om. Izdvojena je i frakcija manja od <2 μm iz dijela uzoraka, koja je snimljena XRPD-om nakon izrade orijentiranih preparata te nakon odabranih tretmana s ciljem identifikacije individualnih minerala glina, prema smjernicama koje su dali Brindley & Brown (1980), Moore & Reynolds (1997) i Srodon (2007). Iz dijela uzoraka izrađeni su petrografski preparati, koji su intepretirani na klasični petrografski način, ali i korištenjem mikropedološkog pristupa. Prikupljeni su i podaci o specijaciji željeza, koji su iskorišteni za diskriminaciju promjena u redukcijskom potencijalu vodene okoline, uz koje su analizirani i stabilni izotopi sumpora u svrhu određivanja utjecaja aktivnosti mikroorganizama te izvora sumpora. Osim toga, korištenjem geokemijskih podataka prikupljenih ICP-MS-om i XRF-om, izvršena je i multivarijantna statistička analiza, pri čemu je obavljena korelacijska analiza putem korelacijskih matrica i analiza glavnih komponenti (PCA).

Rezultati i zaključci

U sklopu ovog doktorskog rada analizirani su boksiti nastali u sklopu 1. i 3. diskordancije u svrhu determinacije njihove geneze, provenijencije te promjena u paleoklimi i paleookolišu tijekom i nakon njihovog postanka. U svrhu utvrđivanja sličnosti i razlika u ponašanju elemenata rijetkih zemalja te elemenata u tragovima između reducirajućih i oksidativnih uvjeta u paleotlima uz prethodno navedene boksite i paleotla analizirana su i paleotla vezana za 2. diskordanciju i

crvenična tla vezana za 4. diskordanciju. U sklopu prve diskordancije analizirana su dva lokaliteta, ležište boksita Rovinj-1 i paleotlo s lokaliteta na Zlatnome rtu, za koje je utvrđeno kako su nastali iz poligenetskog ishodišnog materijala, koji se sastojao od eolskog materijala, vulkanskog materijala i netopivog ostatka podinskih karbonatnih stijena. To je primarno utvrđeno iz teške mineralne frakcije iz ležišta Rovinj-1, gdje su utvrđeni amfiboli, euhedralni cirkoni, klinozoisit, grant i epidot. Ležište Rovinj-1 pokazuje uniformni mineraloški i kemijski sastav kroz cijeli analizirani profil, što ukazuje na formaciju kroz *in situ* procese, no pojava klastičnog boksita u njegovom gornjem dijelu sugerira preradu i djelomično parautohtono podrijetlo. Prisutnost klastičnih litologija u površinskom dijelu posljedica je redukcije vegetacijskog pokrova, koji inače štiti boksite od vodene erozije tijekom bujičnih događaja. Sama redukcija vegetacijskog pokrova je posljedica aridifikacije klime, na što upućuje porast udjela željezovih oksida te pojava impregnacije željezovim oksidima u gornjem dijelu ležišta. Promatrani trend aridifikacije u boksitu nastavlja se u njegovoj krovini, koja se sastoji od ciklične izmjene vapnenaca s laporima/glinama i *black-pebble* brečama. U krovini je ovaj klimatski trend vidljiv prema postupnom padu udjela kaolinita i porastu ilita te miješanoslojnog ilit-smektita, a poklapa se s klimatskim trendovima u mlađem titonu na području sjeverozapadne Europe. Krovina boksita predstavlja tzv. *blue hole* sekvenciju, koja karakteristično započinje slatkovodnom fazom, zatim taloženjem vapnenaca u uvjetima fluktuirajućeg saliniteta, a završava taloženjem tipičnih marinskih vapnenaca. Prisutnost oogonija charophyta i miliolidnih foraminifera ukazuje na uvjete varijabilnog saliniteta u krovini ležišta, koji u konačnici prelaze u potpuno marinske vapnence Kirmenjak formacije, što odgovara klasičnoj *blue hole* sekvenciji. Prisutnost glaukonita u gornjem dijelu pokrovne sekvence i prijelaz iz euksiničnih u oksične do ekvivokalne redoks uvjete sugerira sve veći utjecaj mora. Glaukonit je također pronađen unutar paleotla na lokalitetu Zlatni rt, što predstavlja rijetko zabilježeni primjer nastanka glaukonita u potopljenom paleotlu. Samo paleotlo je nastalo u močvarnim uvjetima te je derivirano iz prethodno navedenih ishodišnih materijala kao i erozijom deriviranog lokalnog feralitičnog materijala, na što ukazuju prisutnost pedogenog kaolinita i blizina ležišta Rovinj-1. Sam glaukonit je nastao na dva načina – direktnim ulaskom željeza, kalija i magnezija u strukture ilita i mješanoslojnog ilit-smektita te mikrobijalnim otapanjem prisutnih minerala glina gdje je iz otopljenog silicija i aluminija u magnezijem, kalijem i željezom bogatom okolišu direktno precipitirao glaukonit. Glaukonit je prisutan u dva oblika – kao dvovalentnim ili trovalentnim željezom bogat glaukonit, koji su prisutni u žilicama zajedno s piritom, što ukazuje na fluktuirajući redoks potencijal okoline tijekom njegovog formiranja. To je povezano s oscilacijama morske razine kako je napredovala transgresija. Ovo paleotlo je prekriveno transgresivnim *black pebble* brečama, koje su zabilježene i u krovini ležišta Rovinj-1. Kraj transgresije karakterizira taloženje vapnenaca Kirmenjak formacije na oba lokaliteta, te precipitacija pirtnih kora u paleotlu.

S ciljem utvrđivanja provenijencije te promjena u paleookolišu treće diskordancije analizirana su boksitna ležišta Minjere, no iz dobivenih podataka nije bilo moguće izraditi detaljniju paleoklimatsku rekonstrukciju, osim što je zaključeno da su ovi boksiti taloženi u tropskoj i vlažnoj klimi. Materijal iz kojeg su nastali boksiti Minjere primarno je deriviran iz eolski donešenog materijala na što upućuje prisutnost amfibola i staurolita, ali i uz potencijalni doprinos netopivog

ostatka podinskih vapnenaca. Morfologija individualnih boksita Minjere i njihov raspored upućuju na razlike u paleotopografiji prigodom njihovog taloženja, budući da su boksiti ležišta Minjere na sjevernoj obali rijeke Mirne (ležište D-1) taloženi na topografski višem položaju u odnosu na boksite koji se nalaze južno od rijeke Mirne (ležište D-15). Na to upućuje prisutnost dubljih i većih kanjonskih boksitnih tijela na sjevernoj strani, te prisutnost plićih ponikvastih i manjih kanjonskih boksitnih tijela uz veću debljinu Kozinskih naslaga na južnoj strani. Ova razlika u paleotopografiji odražena je i u geokemijskom i mineraloškom sastavu dvaju analiziranih boksitnih tijela, ležišta D-1 na sjevernoj te ležišta D-15 na južnoj strani. Ležište D-1 je veće kanjonsko ležište, debljine preko 20 m, primarno boehmitnog sastava, dok je ležište D-15 primarno kaolinitnog sastava uz veću količinu topljivijih elemenata poput Ba, Sr, Cs, Rb, Ca, Mg i Zn. Viša paleotopografska pozicija D-1 ukazuje na njegovu veću udaljenost od vodnog lica, te shodno tome veći intenzitet izluživanja, što je rezultiralo jačim ispiranjem silicija i ostalih topljivijih elemenata te prelaskom kaolinita u boehmit, za razliku od ležišta D-15.

Najveći doprinos istraživanja ovih ležišta je u rekonstrukciji njihove piritizacije, koja je njihovo glavno obilježje, te je utvrđeno kako se ona odvijala u četiri faze. U prvoj fazi precipitirani su framboidalni pirit te mikronski anhedralni pirit, koji su zamijenili željezne okside u matriksu, boksitnim klastima te u lamelama ooida, nakon čega je u drugoj fazi preko ove dvije morfologije pirita kristalizirao koloformni pirit. Prisutnost ovih morfologija u prve dvije faze ukazuje na otopine prezasićene u odnosu na pirit, što se promijenilo u trećoj fazi kad su otopine postale podzasićene, na što upućuje nastanak euhedralnog pirita, koji je primarno prisutan kao obrasline pirita nastalih tijekom prve dvije faze. Posljednja faza karakterizirana je nastankom piritnih žila koje presijecaju ranije nastale piritne morfologije i strukturne elemente. Prikazana evolucija faza piritizacije potvrđena je i vrijednostima stabilnih izotopa sumpora, budući da je raspon dobivenih vrijednosti $\delta^{34}S$ od -40.86 do 2.32 ‰. Negativne vrijednosti ukazuju na otvoreni sustav s neograničenim izvorom sulfata, što je uzrokovalo intenzivnu mikrobijalnu redukciju sulfata iz prezasićenih otopina u odnosu na pirit, dok više vrijednosti ukazuju na tranziciju prema zatvorenom sustavu s ograničenim izvorom sulfata i smanjenjem mikrobijalne redukcije sulfata i smanjenjem zasićenosti otopina. Organska tvar potrebna za mikrobnu redukciju sulfata potječe iz močvarnog okoliša koji je uspostavljen na boksitima u početnim fazama transgresije, što je vidljivo iz više slojeva ugljena zabilježenih u početnom dijelu krovine. Transgresija je započela u paleocenu, gdje se početno taloženje odvijalo u jezerskim uvjetima koji su postupno prelazili u bočate i na kraju u potpuno marinske uvjete, na što ukazuje taloženje Foraminiferskih vapnenaca preko Kozinskih naslaga. Ovakva taložna sekvencija u krovini boksita Minjere još je jedan primjer *blue hole* sekvencije nakon faze boksitizacije, slično kao i u slučaju boksitnog ležišta Rovinj-1.

Osim detaljne rekonstrukcije nastanka 1. i 3. diskordancije, jedan od ciljeva istraživanja bilo je i utvrđivanje sličnosti i razlika u ponašanju elemenata rijetkih zemalja te elemenata u tragovima između reducirajućih i oksidirajućih uvjeta u paleotlima i boksitima, temeljem podataka prikupljenih iz sve četiri diskordancije. Otkrivene su jasne razlike u njihovom ponašanju između oksidirajućih i reducirajućih uvjeta kao i neke sličnosti između njih. Te su razlike prvenstveno

uzrokovane promjenama u mobilnosti elemenata pri različitom redoks potencijalu te precipitaciji redoks-specifičnih faza koje obogaćuju pojedine elemente. Kao referentni materijali za proučavanje oksidirajućih uvjete odabrana su crvenična tla, crveni boksiti ležišta Rovinj-1 i crveni boksiti iz Minjere. U crvenicama elementi u tragovima su pod utjecajem feromanganskih oksida i organske tvari. Organska tvar (oksidabilna frakcija) zadržava elemente poput Pb, Sb i V, dok feromanganski oksidi (reducibilna frakcija) dovode do obogaćenja u Co, Mn i Pb. U crvenim boksitima iz ležišta Rovinj-1 elementi poput Sr, U, Mo, P, S, W, Cd i V povezani su sa željezovim oksidima te su obogaćeni radi njihovog povećanog sadržaja. Crveni boksit iz Minjere pokazuje obogaćenje u Pb, Sb i V u usporedbi s njihovim piritiziranim ekvivalentima. Usprkos tome što su referentni materijal za reducirajuće uvjete kredna paleotla su bila izložena subrecentnoj oksidaciji koja je dovela do nastanka sekundarnih željezovih oksida i jarosita, koji su obogaćeni Co, Sb, V te posebice Cu, Mo, Ni, Pb i Zn. Osim određenih elemenata u tragovima, željezovi oksidi pokazuju afinitet prema lakim i srednjim elementima rijetkih zemalja, što dovodi do njihovog obogaćenja u crvenicama i crvenim boksitima. Cerij pokazuje pozitivne anomalije u crvenicama, što je posljedica njegove oksidacije iz Ce^{3+} u Ce^{4+} koji je imobilan. Gornji dio boksita ležišta Rovinj-1 pokazuje obogaćenje lakih i srednjih elemenata rijetkih zemalja uz negativnu Ce anomaliju, što je posljedica zadržavanja Ce u površinskim slojevima boksita koji je erodiran. Osim toga, utvrđeno je i obogaćenje Ce pri dnu ležišta, što je vjerojatno posljedica ili nastanka fluorokarbonatnih lantanidnih minerala u blizini karbonatne podine, ili taloženja i geneze boksita u dvije faze, gdje donji dio ležišta predstavlja nekadašnji gornji dio boksita prve faze.

Kao referentni materijali za proučavanje reducirajućih uvjeta odabrana su kredna paleotla i piritizirani boksiti iz ležišta Rovinj-1 i ležišta Minjera. Kredna paleotla pokazuju obogaćenje u Cd, Sb, V, U i Mo, što ukazuje na reducirajuće uvjete. Uz pirit (oksidabilna frakcija) su vezani Cu, Mo, Ni, Pb, Sb i Zn, ali su udjeli ovih elemenata u odnosu na druge faze u piritu puno manji, što je moguće posljedica subrecentne oksidacije i oslobađanja ovih elemenata iz njegove kristalne rešetke. U ležištu Rovinj-1 inicijalno je poplavljivanje uzrokovalo postanak euksiničnih uvjeta, koji su doveli do obogaćenja halkofilnih elemenata poput As, Co, Cu, Mo, Ni, Sb, V, Tl i Zn kroz formiranje pirita. Nastavkom transgresije u promjenjivim redoks uvjetima nastavili su se akumulirati redoks-osjetljivi elementi poput U, V i Mo uz prestanak akumulacije većine halkofilnih elemenata. Kao i u slučaju ležišta Rovinj-1, na boksitima Minjere formiran je močvarni okoliš u inicijalnoj fazi transgresije, u kojem je došlo do piritizacije i obogaćenja halkofilnih elemenata poput As, Cd, Cu, Co, Hg, Ni, Mo, Sb, Se, U i Tl i otapanja željezovih oksida, što je dovelo do mobilizacije i osiromašenja u Pb, Sb i V. Na mobilnost kompleksa elemenata rijetkih zemalja ne utječu značajno reducirajući uvjeti, ali radi njihove povezanosti s željezovim oksidima otapanje željezovih oksida u reducirajućim uvjetima dovodi do remobilizacije i uklanjanja srednjih elemenata rijetkih zemalja. Ovaj proces utvrđen je u gotovo svim analiziranim materijalima iz 1., 2. i 3. diskordancije. Osim mobilizacije srednjih elemenata rijetkih zemalja utvrđeno je i obogaćenje teških elemenata rijetkih zemalja, koje nije izravno povezano s redoks uvjetima, ali je posljedica interakcije analiziranih materijala s bočatim do marinskim otopinama, zbog toga što takve otopine dovode do pojačane adsorpcije teških elemenata rijetkih zemalja na minerale glina.

Iz prikupljenih rezultata utvrđeno je kako postoje i razlike i sličnosti u ponašanju elemenata u tragovima i elemenata rijetkih zemalja u oksidirajućim i reducirajućim uvjetima. U oksidirajućim uvjetima elementi poput Co, Pb, Sb i V su obogaćeni, što je primarno posljedica njihovog afiniteta prema željezovim i manganskim oksidima koji nastaju u oksidirajućim uvjetima. U reducirajućim uvjetima obogaćeni su halkofilni i redoks-osjetljivi elementi poput As, Cd, Co, Cu, Mo, Ni, Pb, Sb, U te Zn, što je posljedica ili njihove imobilnosti u reducirajućim uvjetima ili afiniteta prema piritu. Neki elementi kao što su Co, Pb, Sb, U i Mo pokazuju obogaćenje i u reducirajućim i u oksidirajućim uvjetima. Elementi rijetkih zemalja pokazuju obogaćenje laganih i srednjih elemenata rijetkih zemalja u oksidirajućim uvjetima radi njihovog afiniteta prema željezovim oksidima, dok su osiromašeni u reducirajućim uvjetima u kojima se željezovi oksidi otapaju uz gotovo uvijek prisutno obogaćenje teškim elementima rijetkih zemalja.

Geotektonska rekonstrukcija zapadnoistarske antiklinale temeljena na promjeni provenijencije ishodišnog materijala ostvarena je samo djelomice, jer je iz boksita 1. i 3. diskordancije dobiven vrlo mali broj zrna teških i lakih minerala, iz kojih je bilo moguće napraviti samo okvirnu rekonstrukciju tipa njihovog matičnog materijala, ali ne i određivanje jasnog izvora. Osim toga, oprez prigodom provenijencijske rekonstrukcije ishodišnog materijala je neophodan i zbog toga što su boksiti produkt dugotrajnog i kontinuiranog kemijskog trošenja, što često modificira originalni geokemijski potpis ishodišnog materijala.

Tijekom istraživanja za potrebe ovog doktorskog rada dobiveni su i značajni neplanirani novi podaci čime su dobivena nova znanja o istraživanom području. To uključuje pronalazak glaukonita u potopljenom paleotlu na lokaciji Zlatni rt, aridifikaciju klime u ležištu boksita Rovinj-1, razlike u ponašanju elemenata u tragovima i elemenata rijetkih zemalja u oksidirajućim i reducirajućim uvjetima, kao i epigenetske promjene u nalazištima boksita Minjera i njihovu polifaznu piritizaciju.

KEYWORDS

Western Istrian Anticline

Karst bauxites

Palaeosols

Pyritisation of karst bauxites

Rare Earth Elements

Trace elements

KLJUČNE RIJEČI

Zapadnoistarska antiklinala

Krški boksiti

Paleotla

Piritizacija krških boksita

Elementi rijetkih zemalja

Elementi u tragovima

TABLE OF CONTENTS

LIST OF FIGURES:

1. INTRODUCTION

1.1. Geology of the Western Istrian Anticline

The Istrian peninsula (Fig. 1) represents the NW part of the ancient Adriatic Carbonate Platform (Vlahović et al., 2005), recognised as the undeformed, stable part of the Adria Microplate (Schmid et al., 2008, 2020). The Adriatic Carbonate Platform is one of the largest carbonate platforms of Mesozoic age in the Perimediterranean region, whose deposits comprise a substantial part of the entire carbonate suaccession of the Croatian Karst Dinarides, ranging in age from the Middle Permian (or even Upper Carboniferous) to the Eocene (Vlahović et al., 2005). The Istrian part of the Platform does not record the full succession of the Adriatic Carbonate Platform, although it is composed of a succession of carbonate deposits more than 2000 m thick, ranging from Middle Jurassic (Bathonian) to Eocene age, overlain by Palaeogene Kozina deposits, Foraminifera limestones, Transitional beds, Globigerina marls, and Flysch deposits (Vlahović et al., 2023 and references therein). According to Velić et al. (1995) this succession can be divided into four megasequences separated by long-lasting unconformities(Tišljar et al., 1998).

The 1st large-scale Megasequence (M1, Fig. 1) is composed of limestones of early Bathonian to early Kimmeridgian age, which comprise micritic, peloidal and bioclastic to oolitic limestones. The beginning of the emergence in the early Kimmeridgian marks the end of M1, which started by the karstification of Oxfordian to lower Kimmeridgian Muča and Lim units and locally their reworking into the regressive Rovinj breccias (Velić & Tišljar, 1988). Their deposition was followed by the deposition of source material and formation of bauxites (Šinkovec, 1974; Velić & Tišljar, 1988) and palaeosols (Velić & Tišljar, 1988; Vlahović et al., 2003; Perković et al., 2024). The end of the subaerial exposure phase starts with the deposition of the Kirmenjak unit, comprised of mudstones alternating with black-pebble breccias (Tišljar, 1986), followed by cyclic alternation of late and early diagenetic dolomites and thick succession of predominantly shallow-marine limestones (Tišljar & Velić, 1991). Rapid regression of the Adriatic Carbonate Platform was recorded in the early/late Aptian causing beginning of the 2nd Unconformity represented by emergence breccias, black-pebble breccias, and palaeosols, mainly deposited in palaeokarst pits representing waterlogged marsh soils (Ottner et al., 1999; Hrenović et al., 2014). The duration of the emergence phase was variable, from 11–19 Ma depending on varying intensity of synsedimentary tectonics modifying the eustatic signal. This resulted in variable lowering of relative sea-level, erosion and karstification, during the late Aptian and early Albian (Velić et al., 1989; Tišljar et al., 1995; Matičec et al., 1996). The 3rd large-scale Megasequence (M3, Fig. 1) comprises carbonates of upper Albian to upper Cenomanian/upper Santonian age, whose deposition was initiated with a gradual and oscillating transgression which comprises three to six short emergences, represented mainly by coarse brecciated zones, infilled with greenish-grey and greenish-yellow clays, followed with the reestablishment of the more or less continuous shallow-marine carbonate deposition (Tišljar et al., 1995). The majority of this megasequence is composed of limestones with sporadic occurrences of dolomites (Tišljar et al., 1998). Late Cretaceous

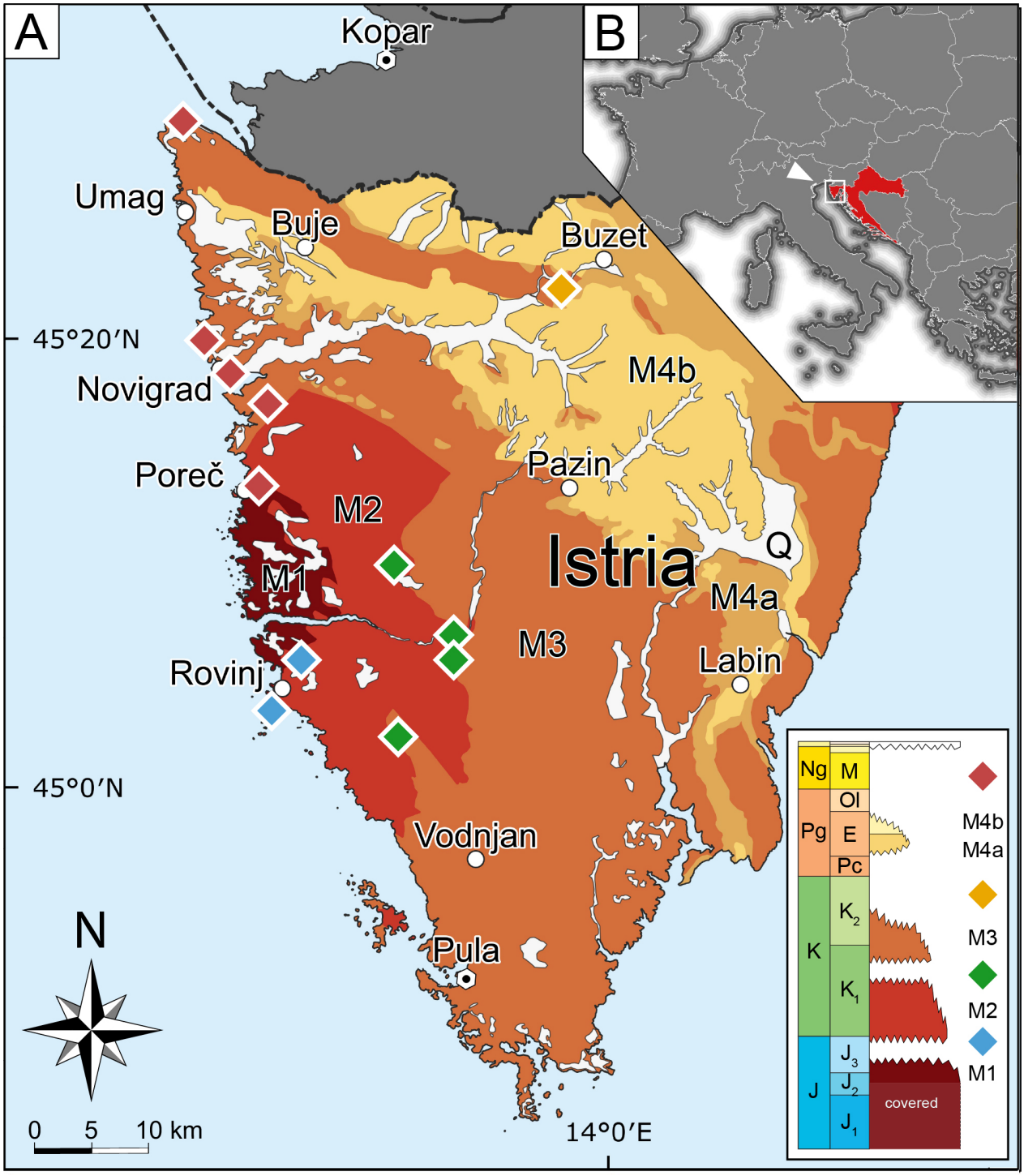

Figure 1. Geological map of Istrian peninsula and its position in Europe. (A) Geological map of Istria, modified after Velić et al. (1995) with the schematic geological column. Legend: M1 – 1st Megasequence (lower Bathonian–lower Kimmeridgian); M2 – 2nd Megasequence (upper Tithonian–lower/upper Aptian); M3 – 3rd Megasequence (lower/upper Albian–upper Santonian); M4a – Carbonate deposits of the 4th Megasequence (lower–middle Eocene); M4b – Clastic deposits of the 4th Megasequence (middle–upper Eocene); Q – Quaternary deposits. (B) Map of central, western and southern Europe with the indicated location of Istrian peninsula.

movement of the Adriatic Carbonate Platform towards Eurasia gradually disrupted the carbonate deposition, and was also marked with the onset of collisional processes and the development of the Western Istrian Anticline (Matičec, 1994), as a result of which an another long-lasting emergence ensued, recorded as the 3rd regional unconformity. During this subaerial exposure phase, more than 10,000 known bauxite occurrences and small bauxite deposits have developed, which indicate the widespread and intense bauxitisation. Besides the bauxitisation, other materials such as calcretes formed (Brlek & Glumac, 2014) together with cave sediments and breccias through extensive karstification of the emerged areas (Otoničar, 2007). The 3rd unconformity records the apparent stratigraphic gap estimated between 28 My (in southern Istria and Mt. Učka klippe) to 40 My (in northern Istria), and is locally recorded to be more than 74 My in the area of the Western Istrian Anticline, as in places erosional remnants of Eocene Foraminiferal limestones transgressively overlie different levels of karstified Lower Cretaceous limestones (the oldest being Valanginian in age; Matičec et al., 1996). The beginning of the deposition of the 4th Megasequence (Palaeocene–upper Eocene, M4a and M4b, Fig. 1) marks the end of the 3rd unconformity. It started with the deposition of freshwater to brackish lagoonal Kozina beds, which transgressively pass into the marine units of the Foraminifera limestones (M4a), Transitional beds, and Globigerina marls, topped by flysch deposits (M4b; Matičec et al., 1996; Vlahović et al., 2005). Further collision with Eurasia (Schmid et al., 2008, 2020) triggered another emergence phase, i.e. the 4th unconformity, that proceeds up to today and is accompanied with various deposits and soils/palaeosols among which terra rossa, loess–palaeosol sequences and pedo-sedimentary complexes predominate. Terra rossae are polygenetic relict soils, with parent material mainly derived from insoluble carbonate residue, aeolian dust, flysch deposits, and sporadically bauxite material (Durn et al., 2007), filling depressions and cracks in karstified terrain. During the Pleistocene loess deposition occurred over some parts of the Istrian peninsula, which commonly overlies or is incorporated in terra rossa also producing loess–palaeosol sequences. Erosional and depositional processes operating on the karst terrains, induced by climatic changes, tectonics, and/or deforestation, might be responsible for both the patchy distribution of terra rossa and the thick pedo-sedimentary complexes in uvala- and dolina-type karst depressions in Istria (Durn et al., 2007).

1.2. Previous studies

Carbonate deposits in the succession of the Western Istrian Anticline have been studied in detail and are well-described (Tišljar & Velić, 1987, 1991; Velić & Tišljar, 1988; Velić et al., 1989, 1995; Tišljar et al., 1995, 1998; Vlahović et al., 2023), and as such they provide a very good stratigraphic framework within which the terrestrial materials related to the aforementioned unconformities can be studied in detail. Only the materials from the 2nd unconformity (Ottner et al., 1999; Hrenović et al., 2014) and the 4th unconformity (Durn et al., 1999, 2007; Durn, 2003) have been studied in detail, while the bauxites and materials from the 1st and 3rd unconformity, which are the main subject of this dissertation, have only been studied partially (Šinkovec, 1974; Šinkovec et al., 1994; Peh & Kovačević Galović, 2014). Several papers from the last decade discuss the subject of bauxites from the 3rd unconformity (Galović et al., 2012; Peh & Kovačević Galović, 2014; Peh &

Galović, 2016), but only one of those papers explicitly studied those bauxites (Peh & Kovačević Galović, 2014). Consequently, this research will significantly contribute to the current knowledge regarding the evolution of the 1st and 3rd unconformity, with the use of multiple new methods and the collection of new samples.

1.3. Karst bauxites

As karst bauxites represent the main materials which characterise the 1st and 3rd unconformity, their understanding is essential for this work. Karst bauxites are one of the two types of bauxite, recognized according to their respective bedrock: lateritic bauxites, which form on aluminosilicate-bearing rock through its weathering, and karst bauxites, which form on carbonate bedrock from the weathering and accumulation of aluminosilicate materials from external sources and insoluble carbonate residue during its karstification (Bardossy, 1982; Combes & Bardossy, 1995). The process of bauxitisation is as the result of chemical weathering in a humid tropical to subtropical climate (Bardossy, 1982; D'Argenio & Mindszenty, 1992, 1995; Combes & Bardossy, 1995; Mindszenty et al., 1995; Mindszenty, 2016) for extensive periods of time, usually longer than 100 Ka (Bardossy, 1982; Birkeland, 1985). Since their formation requires prolonged periods of subaerial exposure, their formation has also been largely linked to periods of tectonic instability (D'Argenio & Mindszenty, 1995; Mindszenty et al., 1995). The periods of widespread bauxite formation are also linked to the global periods of elevated humidity, temperature and volcanism (D'Argenio & Mindszenty, 1992; Mindszenty, 2016). As such, bauxites have been extensively used in palaeoclimatic and geotectonic reconstruction in numerous studies (Mongelli, 1997; Mameli et al., 2007; Mongelli et al., 2015; Ellahi et al., 2017; Chanvry et al., 2020; Brlek et al., 2021; Yang et al., 2022; Zhou et al., 2023). Concerning all these aspects unique to karst bauxites, their presence in the succession of the Western Istrian Anticline is of a great importance. Besides their use as a palaeoclimatic indicator, the study of their microstructure and mineralogy allows the additional insight into the palaeoenvironmental changes during and after their formation. One of the possible changes in the palaeoenvironment recorded in bauxites is the incipience of transgression, which can be recorded in bauxite as the appearance of pyrite or siderite and various redoximorphic forms or through resilicification. Therefore, a careful interpretation of these features together with their cover enables the reconstruction of the transgression that follows their formation.

1.4. Rare earth elements in bauxites

Rare earth elements (REEs) are a critical raw material for today's technologically oriented society (Mongeli et al., 2021) and are an indispensable raw material for the transition towards renewable energy (Golroudbary et al., 2022) . This, coupled with the fact that REEs are also very good proxies for the environment in which the bauxites formed, led to the increasing number of recent research focused on the behaviour of REEs in bauxites (Mongelli et al., 2014, 2017; Cao et al., 2017; Yuste et al., 2017; Abedini et al., 2018, 2019a, b; Chen et al., 2018; Reinhardt et al., 2018; Yang et al., 2019; Khosravi et al., 2021; Tomašić et al., 2021; Villanova-de-Benavent et al., 2023). Variations in REE concentrations throughout the bauxite profile provide an insight into the physicochemical

changes during bauxitisation, which can be extrapolated to the behaviour of other trace elements as well, leading to a more detailed palaeoenvironmental reconstruction of bauxite formation (Maksimović & Pantó, 1991; Maksimović et al., 1991; Mongelli, 1997; Zarasvandi et al., 2012; Abedini & Calagari, 2014; Mongelli et al., 2014, 2017; Abedini et al., 2018, 2019a; Reinhardt et al., 2018; Yang et al., 2019; Khosravi et al., 2021; Tomašić et al., 2021; Villanova-de-Benavent et al., 2023). Bauxites from the 1st and 3rd unconformity are too poor in REEs to be considered a viable ore for their exploitation, but they are nevertheless enriched enough to be used for the study of their behaviour in bauxites and similar materials. Also, as it was already mentioned, the studied bauxites comprise both those formed in oxidative and reducing palaeoenvironments, where REE analysis and comparison between these two bauxite types can provide a more complete understanding of lanthanide behaviour in bauxites and similar materials and their response to changes in redox conditions in the environment. As such, this research will also include REE data from the 2nd unconformity (Cretaceous palaeosols – reducing conditions) and 4th unconformity (terra rossa soils – oxidising conditions) which will be compared to phreatic and vadose bauxites from the 1st and 3rd unconformity to allow a more reinforced study of REE behaviour between soil materials formed in differing redox conditions.

1.5. Methodology

The mineralogical and geochemical data form the foundation of this research where X-ray powder diffraction (XRPD), Fourier transform infrared spectroscopy (FTIR), together with heavy and light mineral fraction analysis were used as methods for mineralogical data collection; X-ray fluorescence (XRF), inductively coupled plasma mass spectrometry (ICP-MS), stable sulphur isotope analysis of iron sulphides as methods for geochemical data collection, together with scanning electron microscopy coupled with energy dispersive x-ray spectroscopy (SEM-EDS) as an additional method for collection of both mineralogical and geochemical data. In addition, petrographic thin sections were prepared from the selected samples, which in addition to the classical petrographic methods were also analysed with a micropedological approach in order to gain additional insight into the conditions which were present inside and outside the bauxites and palaeosols during their formation, as certain pedological processes such as clay illuviation or iron remobilisation can be assessed much better with such approach. The guidelines described in Stoops (2021) were used as the basis for the micropedological interpretation of the samples.

Since it is almost impossible to qualitatively describe and identify minerals through the examination of petrographic thin sections due to the cryptocrystalline character of the minerals present in the bauxite and highly clayey palaeosols, XRPD was used as the main method for the mineralogical analyses. In addition to the determination of the bulk mineralogical composition of the samples, special attention has been paid to the determination of clay mineralogy, considering their importance in the interpretation of the environment in which the bauxite was formed. The basis for their determination was the XRPD analysis of the <2 μm fraction, separated from selected samples of bauxite and accompanying materials, which was recorded after several treatments, in

order to distinguish different clay minerals that produce a similar or same diffraction image during X-ray diffraction of the untreated sample. The samples were recorded after: a) air drying, b) ethylene glycol solvation after magnesium or potassium saturation, d) heating at 300°C after magnesium or potassium saturation, e) heating at 550°C after magnesium or potassium saturation, and f) DMSO treatment after potassium saturation.

Clay mineralogy was interpreted from the obtained diffractograms according to the guidelines found in Brindley & Brown (1980), Moore & Reynolds (1997) and Środoń 2006). In addition to determining the qualitative mineralogical composition and clay mineralogy, the quantitative mineralogical composition of the samples was determined using the Rietveld refinement, which is based on the crystallochemical data of the minerals present and the instrumental settings of the goniometer. The samples on which the quantitative mineralogical composition was determined had to be prepared in a precisely defined way in order to avoid the shortcomings of this method, where the preferred orientation of the crystallites and the uneven distribution of crystallite sizes in the sample may represent the main and usual causes of errors. The samples have been wet ground using propylene glycol in a micronizing mill for 15 minutes, after which they were dried and loaded for XRPD analysis. This type of grinding was necessary in order to obtain a sample with a homogeneous distribution of particles that do not exceed the size of 10 μm (O'Connor & Chang, 1986), which is an important prerequisite for proper quantification using the Rietveld method. After drying and sieving, the samples prepared in this way were side loaded with the application of rough glass on the surface of the sample (Kleeberg et al., 2008), in order to disturb the preferred orientation of the crystallites on the surface, which allows for more accurate quantification.

In addition to the mentioned X-ray diffraction approach for the analysis of clay minerals, Fourier transform infrared spectrometry (FTIR) was used as another important method for their identification. FTIR enables obtaining data on the vibrations of bonds in the structure of minerals, which ultimately enables a more accurate determination of the mineralogy of clay and other minerals present while obtaining additional data on their structure.

Some of the very important minerals essential for the provenance determination of the parent material cannot be determined with certainty by any of the abovementioned methods, due to the small grain sizes (<200 μm) and low concentration of these minerals in the bauxite samples. Some of these minerals are zircons, titanium oxides, apatite, quartz, kyanite, staurolite, tourmalines and garnets, which share a high specific gravity (>2.89 g/cm^3) based on which they can be separated using the sodium polytungstate solution concentrated from a larger amount of bauxite sample. From the obtained concentrated heavy mineral fraction, thin sections were made, from which it was possible to determine the proportion of individual minerals and establish the provenance of the parent material. In addition to the analysis of the heavy mineral fraction, SEM-EDS analysis of selected bauxite samples provided valuable data on the micromorphology and chemistry of clay minerals and other minerals.

Additionally, a part of this research was focused on the description and analysis of trace elements and lanthanides behaviour, where in addition to geochemical data obtained by SEM-EDS, it was necessary to obtain the geochemical composition of bulk samples. By analysing bulk samples with inductively coupled plasma mass spectrometry (ICP-MS), it was possible to obtain very precise concentrations of trace elements and lanthanides, regardless of their low concentrations in bauxite samples. In addition to trace elements and lanthanides, major element concentrations were also determined, but by using X-ray fluorescence (XRF) on bulk samples, due to low precision and the impossibility of ICP-MS to measure elements with high concentrations in the sample.

Very important data for bauxites altered in the reducing conditions are the values of stable sulphur isotopes, which cannot be obtained by ICP-MS analysis of the bulk sample but require special preparation of the sample. The values of stable sulphur isotopes provided essential information about the aqueous environment in which the bauxite was pyritised and reflected the marine influence and microbial activity in the aqueous medium within which the pyritisation took place. From selected grey bauxite samples, the sulphur isotopes were obtained through the measurement of silver sulphide with a mass spectrometer, which was precipitated from the iron sulphides present in the samples using the chromous chloride distillation method (Canfield et al., 1986). The sulphur isotope acquisition was coupled with the collection of iron speciation data, which is used for an additional insight into the redox changes in the environment during the sediment deposition and is commonly used for the discrimination of different water-column redox states, from fully oxic, equivocal, through anoxic-ferruginous, to anoxic-euxinic states (Poulton & Canfield, 2011; Poulton, 2021). This was achieved through the acquisition of iron abundances in different iron-binding phases, which can then be used to obtain the amount of highly reactive iron (Fe_{hr}), whose concentration relative to the total iron pool and iron-sulphide related pool (Fe_{py}) was used to reconstruct the redox conditions, together with the amount of total iron (Fe_{tot}). Fe_{hr} comprises carbonate associated iron (Fe_{carb}), pyrite (Fe_{py}), ferric oxides (Fe_{ox}) and magnetite (Fe_{mag}). This was all done following the standard chemical protocol, described by Poulton & Canfield (2005), where each iron associated phase such as carbonates, iron oxides and magnetite was separately dissolved, after which the iron content in the produced solution was measured using atomic absorption spectroscopy (AAS). The Fe_{hr}/Fe_{tot} ratio was used to discriminate between oxic, equivocal and anoxic depositional conditions, where the values higher than 0.38 indicate deposition under anoxic conditions, values between 0.22 and 0.38 indicate deposition under equivocal conditions, while the values lower than 0.22 indicate deposition under oxic conditions (Poulton & Canfeld, 2011). The anoxic conditions can be further evaluated using the Fe_{py}/Fe_{hr} ratio, which allows the discrimination between ferruginous and euxinic conditions, where values lower than 0.6 indicate deposition under ferruginous conditions, and those higher than 0.8 deposition under euxinic conditions (Poulton, 2021).

Multivariate statistical analysis was also performed on geochemical data obtained with ICP-MS and XRF, in order to obtain additional insight into the relationship between different individual elements and their association with different mineral phases. Since the geochemical data represent

a compositional dataset, i.e. variables sum to a constant value, the dataset was pretreated using the central log-transformation, using the compositions package in R, to remove the constant sum constraint of the data. Two statistical techniques were employed, principal component analysis (PCA) and the construction of correlation matrices. PCA was done using the stats package in R, while correlation matrices were constructed from the obtained Pearsons ρ values and were sorted using hierarchical clustering based on Ward's method, which was all performed using the corrplot package in R (Wei & Simko, 2017). The used cutoff p-value was 0.05, below which the individual elemental correlations were considered statistically insignificant.

1.6. Objectives and hypotheses of the research

Main objectives of this research were: (1) the reconstruction of paleoclimate and palaeoenvironment in which the materials from the 1st and 3rd Unconformities were forming, based on the mineralogical, geochemical and micropedological data, (2) to determine the provenance of the parent materials from which the bauxites of the 1st and 3rd Unconformities were formed, based on the geochemical data and data from the heavy mineral fraction, (3) to reconstruct the evolution of the Western Istrian Anticline, based on the changes in provenance of the parent material of all four unconformities and (4) to determine the similarities and differences in the lanthanide and trace element behaviour between the reducing and oxidising environments in the materials of all four unconformities.

These objectives were based on following hypotheses: (1) mineralogy, chemistry and micropedological features reflect the palaeoclimate and palaeoenvironment in which bauxites and palaeosols form, (2) The provenance of bauxites and palaeosols can be determined based on the chemical data and data from the heavy mineral fraction, (3) the changes in the parent material provenance of all four unconformities can be used as a basis for the reconstruction of the evolution of the movement and geotectonic changes in its vicinity, and (4) lanthanides behave differently in oxidising and reducing pedoenvironments in bauxites and palaeosols.

1.7. Scientific contribution

The primary new scientific contribution of this study is the determination of the parent material from which the bauxites of the 1st and 3rd Unconformities were formed, together with their palaeoclimatic and palaeoenvironmental reconstruction. This was obtained through the collection of new samples and employment of a wide array of instrumental methods and approaches, as there are very few publications in which these bauxites were the primary research subject. Additional new scientific contributions is the description of REE and trace element behavior between the oxidising and reducing pedoenvironment, which is especially important for REEs which are one of the critical raw materials important for the today's society, especially since bauxites are one of their potential sources.

Paper 1

Durn, G., Perković, I., Stummeyer, J., Ottner, F. & Mileusnić, M. (2021): Differences in the behaviour of trace and rare-earth elements in oxidizing and reducing soil environments: Case study of Terra Rossa soils and Cretaceous palaeosols from the Istrian peninsula, Croatia. Chemosphere, 283, 131286.

Chemosphere 283 (2021) 131286

Contents lists available at ScienceDirect

Chemosphere

journal homepage: www.elsevier.com/locate/chemosphere

Differences in the behaviour of trace and rare-earth elements in oxidizing and reducing soil environments: Case study of Terra Rossa soils and Cretaceous palaeosols from the Istrian peninsula, Croatia

Goran Durn [a], Ivor Perković [a,*], Jens Stummeyer [b], Franz Ottner [c], Marta Mileusnić [a]

[a] University of Zagreb, Faculty of Mining, Geology and Petroleum Engineering, Pierottijeva 6, 10 000, Zagreb, Croatia
[b] Bundesanstalt für Geowissenschaften und Rohstoffe Hannover, Germany
[c] Institute of Applied Geology, University of Natural Resources and Life Sciences, Vienna, Austria

ARTICLE INFO

Handling Editor: Lena Q. Ma

Keywords:
Redox conditions in karst soils
REE/Trace elements characteristics
Terra rossa
Wetland palaeosols
Istrian peninsula

ABSTRACT

This study compares the differences between the distribution of trace elements and rare-earth elements (REEs) formed under reducing and oxidizing soil conditions during pedogenesis on carbonate bedrock. Terra rossa (TR) soils, representing pedogenesis under oxic conditions, and Cretaceous palaeosols (CP), representing pedogenesis under reducing conditions, were sampled on the Istrian peninsula. They were studied by ICP-MS, ICP-OES, XRF, XRD, sequential extraction and statistical analyses. The differences in trace-element behaviour between the TR and CP stem from different redox conditions, but the most remarkable difference was observed in the behaviour of the REEs. Statistical analyses revealed that in TR soils all the REEs showed a very positive correlation, while in CPs the light REEs and heavy REEs showed an internal, very positive correlation. TR soils have almost twice as much REEs as CPs. This difference is pedogenetic, as both materials have a very similar amount of REEs in the residual fraction. While TR soils have the same amount of REEs in fractions other than the residual fraction, CPs have almost no REEs in these fractions. Different REE patterns obtained from sequential extraction, such as a middle-REE enrichment and a positive Ce anomaly in TR soils and light-REE depletion, heavy-REE enrichment, positive Ce and Eu anomalies in CPs, contributed to an understanding of the redox and pedogenetic processes. This study successfully emphasized the influence of different redox conditions on the behaviour of trace and rare-earth elements during pedogenesis on a carbonate bedrock and the ability of the REEs to track pedogenetic processes.

1. Introduction

Redox conditions are some of the most important factors affecting the behaviour of rare-earth elements (REEs) and other trace elements in soils. They can directly increase, or otherwise influence, the mobility of dissolved elemental species or initiate the dissolution or precipitation of the corresponding mineral phases and materials, resulting in different and recognizable trace-element signatures in soils. Two common soil constituents, organic matter and Fe–Mn oxides, are particularly sensitive to redox variations and can be present in soils in sufficient quantities to affect the trace-element and REE concentrations in soils. Many studies have recognized their importance as redox-sensitive materials in soils, being either major or minor subjects of these studies, which were mostly conducted on wetland soils (Dia et al., 2000; Grybos et al., 2007, 2009, 2009; Davranche et al., 2011, 2019, 2019; Guénet et al., 2018; Catrouillet et al., 2020) or other soil materials (Cao et al., 2001; Laveuf et al., 2008, 2012). Only a few studies were focused on trace elements and in particular the REEs as a proxy for redox conditions during pedogenesis on karst terrains (e.g., Laveuf et al., 2008, 2012). Most of the studies that analysed such soils used REEs as a proxy for paleo-conditions or paleoclimate (Feng, 2010; Feng et al., 2012; Han et al., 2017; Chang et al., 2019; Liankai et al., 2020; Zhou et al., 2020) without using it as a proxy for the soil-redox history. Some of the studies only looked at cerium (Feng, 2010; Feng et al., 2012; Chang et al., 2019; Liankai et al., 2020), and only two studies, to the best of our knowledge, used all the REEs to interpret the redox processes in karst soils (Laveuf et al., 2008, 2012). Also, as far as we know, the study by Laveuf et al. (2012), is the only one to directly compare two soil materials formed in

* Corresponding author.
E-mail address: ivor.perkovic@rgn.hr (I. Perković).

https://doi.org/10.1016/j.chemosphere.2021.131286
Received 1 April 2021; Received in revised form 15 June 2021; Accepted 17 June 2021
Available online 19 June 2021

opposite redox environments based on their trace-element signatures, focusing on the REEs. We believe that a similar study would add to the current body of knowledge.

Based on a review of previous studies, for this study we selected two soil materials formed in contrasting redox environments on a carbonate bedrock, with a similar approach in mind but with the addition of statistical analyses for the different REEs. This study is expected to improve our understanding of the relationship between redox conditions and trace elements, particularly the REEs, during karst pedogenesis. REEs are also extensively used as tracers of other pedogenetic processes (Laveuf et al., 2008, 2012, 2012; Feng, 2010; Cheng et al., 2012; Feng et al., 2012; Mihajlović et al., 2014; Han et al., 2017; Chang et al., 2019; Liankai et al., 2020). This study is expected to contribute by using REEs as the tracers of various pedological and depositional processes as an additional tool. Other redox-sensitive elements such as U, Mo, V, Fe and Mn are also useful proxies for past redox conditions (Wanty and Goldhaber, 1992; Gambrell, 1994; Palumbo et al., 2001; Duncan and Shaw, 2003; Pédrot et al., 2008; Shaheen et al., 2016; Smedley and Kinniburgh, 2017; Fuller et al., 2020; Rinklebe et al., 2016) and will be analysed along with the REEs.

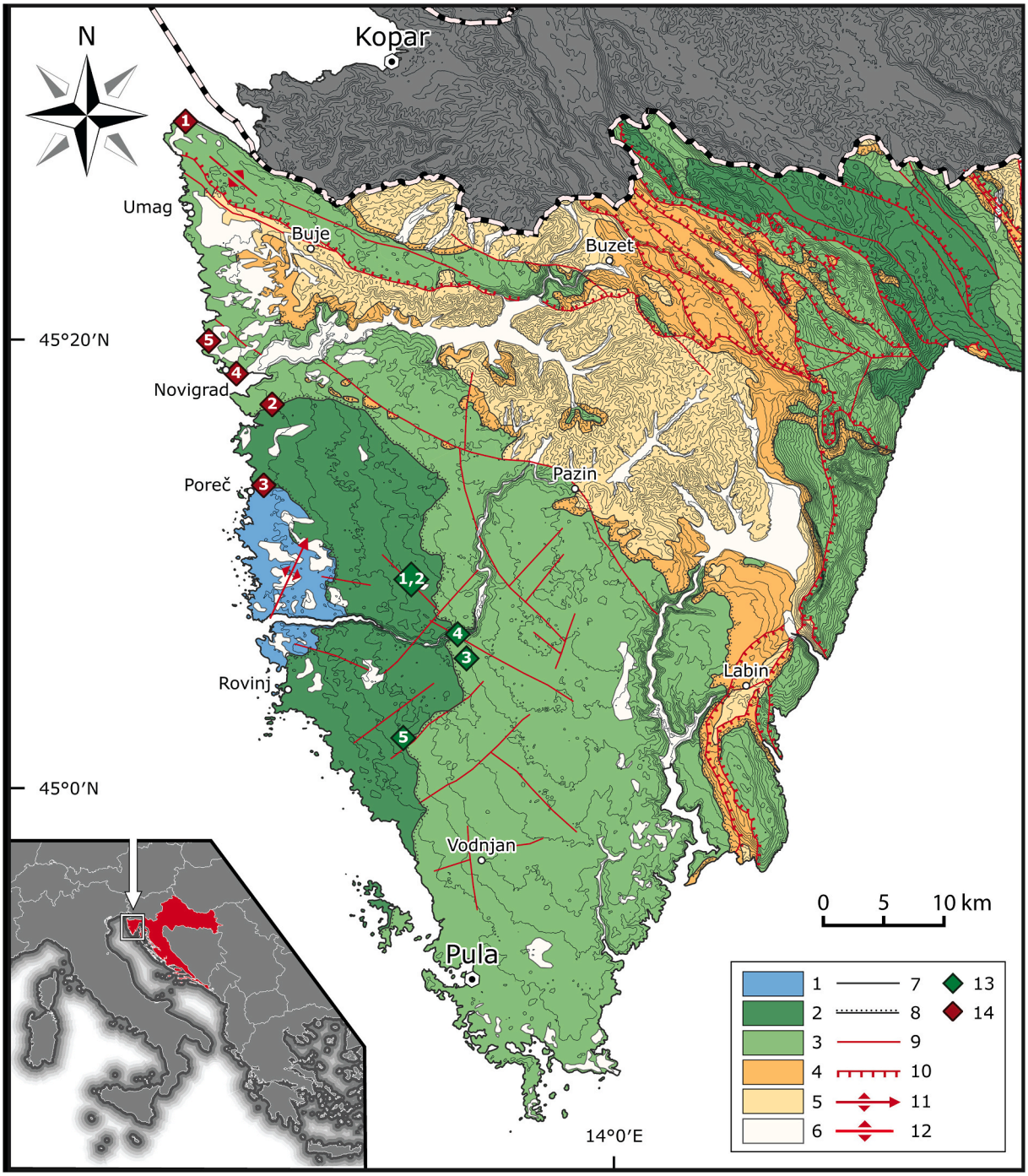

Fig. 1. Geological map of Istrian peninsula, outlining the large-scale megasequences and major faults, modified after: Velić et al. (1995) and Basic geological map of Croatia, 1:300,000; 1 - Jurassic, 2 - Lower Cretaceous, 3 - Upper Cretaceous, 4 - Lower Eocene, 5 - Middle to Upper Eocene, 6 - Quaternary, 7 - normal geological boundary, 8 - erosional geological boundary, 9 - normal fault, 10 - reverse fault,11 - Western Istrian anticline, 12 – Savudrija-Buzet anticline, 13 – sampling sites of Cretaceous palaeosols, 14 – sampling sites of terra rossa.

Some of the selected materials for this study are the terra rossa (TR) soils. On the Istrian peninsula, these are extensively studied (Durn et al., 1999, 2001, 2007, 2013, 2019, 2001, 2013; Ivanić et al., 2020) polygenetic relict soils with a high content of crystalline iron oxides, consisting mainly of hematite and sporadically of goethite. These soils were selected as a representative soil material for the oxic conditions in this study. Cretaceous palaeosols (CPs) were selected as representative soil materials formed under reducing conditions because they developed in a karst wetland more than 110 million years ago and show typical hydromorphic features. Very few studies (Ottner et al., 1999; Durn et al., 2006; Hrenović et al., 2014) have been carried out on CPs, compared to TR soils. Therefore, the trace-element patterns should confirm the known facts, while also adding new insights into the pedogenetic processes in TR soils, while shedding new light on the pedogenetic processes and genesis of the CPs. Both materials developed on a carbonate bedrock with a very low insoluble residue (<1%). We postulate that their contribution during bedrock weathering had a negligible effect on the observed trace-element signatures. This is important because our study should also demonstrate that parent materials can develop significantly different trace-element signatures simply by pedogenesis on a karst terrain.

Overall, this study should contribute significantly to a better understanding of the behaviour of trace and rare-earth elements during the karst pedogenesis under different redox conditions and provide some additional insights into the use of these elements as tracers for depositional and pedogenetic processes.

2. Study area and sampling

A knowledge of the basic geological framework and the evolution of the Istrian peninsula (Fig. 1) is necessary for a complete understanding of the important processes that led to the formation of TR soils and the CPs.

The Istrian Peninsula represents the NW part of the Adriatic carbonate platform (Vlahović et al., 2005), recognized as its stable part during the neotectonic deformation, known as the stable Adria (Schmid et al., 2008, 2020). This part of the platform consists of a succession of carbonate deposits more than 2000 m thick, ranging from the Middle Jurassic (Bathonian) to Paleogene (Eocene). According to Velić et al. (1995), this succession can be divided into four mega-sequences separated by long-lasting emersions (Tišljar et al., 1998). The first (Early Bathonian - Early Kimmeridgian), second (Late Tithonian - Early/late Aptian) and third (Late Albian - Late Santonian) mega-sequences consist exclusively of carbonate rocks, whereas the succession of the fourth (Eocene) mega-sequence begins with the deposition of foraminiferal limestones and ends with flysch deposition (Matičec et al., 1996; Tišljar et al., 1998; Tišljar and Velić, 1987; Velić et al., 1989, 1995; Vlahović et al., 2005).

Carbonate deposition in the second mega-sequence ended in the Late-to-Early Aptian with the onset of a rapid regression that ultimately led to regional emersion and the formation of the palaeosols analysed in this study. The duration of the emersion phase was variable, from 11 to 19 Ma, and was caused by the varying intensity of the synsedimentary tectonics that modified the eustatic signal. This resulted in variable lowering of the relative sea level, erosion and karst formation (Velić et al., 1989; Tišljar et al., 1995; Matičec et al., 1996), which led to the formation of emersion breccias, black-pebble breccias and CPs that originally formed as water-saturated soils in paleokarst pits (Ottner et al., 1999; Hrenović et al., 2014). Based on their previous research (Durn et al., 2006) the authors of this study suggest that the CPs probably formed from insoluble carbonate residues and volcanic material transported and deposited in water bodies (e.g., coastal wetlands) located in karstic depressions on an emergent carbonate terrain of low elevation and relief. The CPs are truncated soils and, as far as we know, are represented only by B and/or C horizons. CPs show clear evidence of subaerial exposure (Durn et al., 1999). Their colour, weak soil structure, presence of root remains, nodular pedofeatures, burrows, and channels, now mainly filled with pyrite framboids, indicate that they have been pedogenetically modified (Durn et al., 2006). Most of these features suggest hydromorphic processes and overall formation in a reductive pedo-environment, making CPs a suitable representative of soil material formed under reducing conditions for this study.

TR soils were formed during the final emergence of the Istrian peninsula, triggered by the collision of the Adriatic microplate with Eurasia (Schmid et al., 2008, 2020). This was also accompanied by different sediments and soils/palaeosols, among which TR, loess-palaeosol sequences and pedo-sedimentary complexes predominate. TR soils from the Istrian Peninsula are polygenetic relict soils whose parent material is derived mainly from an insoluble carbonate residue, aeolian dust, flysch sediments, and sporadically from tephra and bauxite material (Durn et al., 2007), filling depressions and cracks in the karstified terrain. The typical soil profile of TR consists of a thin A horizon and a thick B horizon, which can be subdivided into several sub-horizons in terms of different colours and soil textures. One of the main features of TR is the red colour of the B horizon, which is a result of rubification, the preferential formation of hematite over goethite (Boero and Schwertmann, 1989). This reflects the minimal water retention and the continuity of the oxic conditions, making TR a suitable representative of the soil material formed in an oxic pedo-environment.

TR soils mark the subaerial unconformity of the fourth large-scale mega-sequence. Wetland soils are associated with the subaerial unconformity of the second large-scale mega-sequence and are considered CPs. The sampling sites represent typical TR and CP sites and were selected based on our previous studies, which showed that the insoluble residue of carbonate bedrock is lower than 1% (Tab. S8). TR samples were collected from B horizons, while CP were sampled from the upper part of the truncated palaeosol profiles.

3. Methodology

Five TR (Fig. 2) samples (2.5 YR to 10R in Munsell Hue) and five CP (Fig. 2.) samples (5BG to 10BG in Munsell Hue) overlying limestones were collected from nine sites in Istria and subsequently air-dried.

Five TR samples (2.5 YR to 10R in Munsell Hue) were collected from the B horizon at five localities: Savudrija, Vabriga, Poreč, Novigrad and Mareda (corresponding to the localities 1, 2, 3, 4 and 5 in Fig. 1). The sampling locations represent typical TR sites on the Istrian peninsula with well-developed profiles and were selected based on our previous studies and experience. Four sampling sites, i.e., Savudrija, Vabriga, Novigrad and Mareda, are located on Late Cretaceous (Cenomanian) limestones (Fig. 1), whereas the sampling site near Poreč is located on Late Jurassic (Late Kimmeridgian) limestones (Fig. 1). Both the Late Jurassic and Late Cretaceous limestones have a very small amount of insoluble residue (0.48–0.86 wt%; Tab. S8), whose contribution during the bedrock weathering could not mask and influence the trace-element fingerprint of the pedological processes. This is important as it allows a reliable comparison of the pedogenetic processes between all the sampling sites with respect to their different bedrocks.

Five Cretaceous palaeosol (5BG to 10BG in Munsell Hue) samples were collected from the upper part of the truncated palaeosol profiles at four localities: Tri jezerca Quarry, Kanfanar Quarry, Lim Channel and Bale Quarry (corresponding to the localities 1, 2, 3, 4 and 5 in Fig. 1), with two samples taken at Tri jezerca Quarry and one sample taken at the other sampling sites. These are almost all the sites where CPs are found on the Istrian peninsula, and they are exclusively associated with quarries and road cuts where they are exposed in rock succession. The CPs at all the sampling sites formed on Early Cretaceous (Early/Late Aptian) limestones with a very small amount of insoluble residue (0.32–0.46%, Tab. S8). The exposed palaeosol outcrop was heavily oxidized at all four sites and was thoroughly removed to sample the unaltered material.

A collected portion of each disturbed soil/palaeosol sample was

Fig. 2. Exposed outcrop of Cretaceous limestones in the Kanfanar quarry with visible Cretaceous palaeosol horizon (a) and terra rossa soil (b) overlying the outcrop. Cretaceous palaeosol horizon is partly masked with the blocks of architectural stone.

gently crushed and sieved through a 2-mm mesh for subsequent mineralogical and chemical analyses. The mineral compositions of the bulk sample and the < 2-μm fraction were determined by X-ray powder diffraction (XRD) using a Philips diffractometer (graphite monochromator, Cu–K_α radiation, proportional counter). The XRD patterns of the bulk sample and the non-oriented < 2-μm fraction were recorded after air drying. The XRD patterns of the oriented < 2-μm fraction were recorded after the following treatments: (a) Mg saturation, (b) K saturation, (c) Mg saturation and ethylene glycol solvation, (d) Mg saturation and glycerol solvation, (e) K saturation and DMSO solvation, and (f) heating for 2 h at 550 °C. The clay minerals were identified using the methods of Brown (1961), Brindley and Brown (1980), and Moore and Reynolds (1997). Semi-quantitative XRD analyses were used to determine the contents of quartz, plagioclase, K-feldspar, pyrite and gypsum by measuring the relative intensities of the characteristic diffraction lines of each mineral. Estimates of the iron oxide content were based on the amount of iron that can be extracted with Na-dithionite citrate bicarbonate. Semi-quantitative estimates of the clay minerals in the 2-μm fraction were based on the relative intensities of the characteristic X-ray peaks using the method of Johns et al. (1954). The estimated amounts of minerals were represented by plus signs (+), but no quantitative value was assigned to each +.

The amount of insoluble residue from the carbonate bedrock was obtained by dissolving carbonate minerals. Samples were carefully crushed, passed through a 4-mm sieve, and then treated with a 1-M NaOAc solution buffered at pH 5 with HOAc (Jackson, 1979; Tessier et al., 1979). The soil/palaeosol pH in H_2O was determined in suspensions with a volume ratio of 1:5. The organic carbon content was determined using a LECO C744 carbon analyser and is expressed as a weight percentage. In the determination of the organic carbon, the samples were pre-treated with 18% hot hydrochloric acid to remove any carbonates that were present. The contents of the major and trace elements (including REEs) in the bulk samples (fraction < 2 mm) were determined by XRF and ICP-MS, respectively. X-ray fluorescence was performed using Phillips PW 1400 and PW 1480 instruments. The analytical precision was better than 2% for the major elements and better than 5% for the trace elements. International standards were used to calibrate the sample analyses. Synthetic standards were used for the elements or concentration ranges not covered by international standards. ICP-MS was performed using a SCIEX model 250 instrument. The analytical precision was better than 5%. However, a determination of the total concentration in the soils does not provide information about the mobility of metals. Availability depends critically on the chemical form in which a metal is bound. Methods for determining the various forms of metals in soils include sequential extraction, in which a series of individual reagents are used to extract operationally defined phases from the soil in a defined sequence. In all the methods, the extracting agents are used in order of increasing reactivity so that the sequentially extracted fractions correspond to the trace elements associated with fractions of lower mobility. Although there are several sequential extraction procedures used to evaluate the changes in metal fractionation and mobility during the oxidation or reduction of soils, the procedure proposed by Tessier et al. (1979) is the most widely used. In this study the sequential extraction scheme described in detail in Tessier et al. (1979) was used. The sequential extraction was carried out to obtain the following four fractions: exchangeable (I), bound to carbonates or acid soluble (II), bound to ferromanganese oxides or reducible (III), and bound to organic matter and sulphides or oxidizable (IV). The residual fraction (V) was calculated as the difference between the total content of a given element and the sum of the first four fractions (I to IV). After leaching the samples, As, Ba, Cd, Co, Cr, Cu, Fe, Mn, Mo, Ni, Pb, Sb, V, and Zn were determined using ICP-OES. Subsequently, REEs from the leaching solutions were analysed at trace levels (after dilution) using ICP-MS. The reproducibility of the analysis was checked by replicate

analyses of the samples TR1 and CP5, and was satisfactory. Some elements are at concentrations below the instrument's detection limit (0.002 mg/kg), but this is only a problem for the exchangeable fraction and in some cases for the acid-soluble fraction, when it may affect the HREE, Pr or Eu concentrations in some samples. The mean values for these elements are then averaged from other valid measurements in CP or TR. This is mainly a problem when calculating Ce or Eu anomalies and is also addressed in Table 2 as NA (not applicable) values. The REE values were normalized to upper-continental-crust values using those from Taylor and McLennan (1985). In this study, LREE refers to the light rare-earth elements and includes the REEs from La to Gd, while HREE refers to the heavy rare-earth elements and includes the REEs from Tb to Lu. MREE is used only occasionally and refers to the middle rare-earth elements and includes Sm, Eu and Gd.

The $(Yb/La)_{ucc}$ and $(LREE/HREE)_{ucc}$ ratios were calculated from values normalized to the upper continental crust, which can be found in Taylor and McLennan (1985).

Raw Eu and Ce anomalies were calculated using the following equations according to Lawrence et al. (2006):

$$Ce^* = \frac{Ce_N}{Pr_N{}^*\left(\frac{Pr_N}{Nd_N}\right)} \quad Eu^* = \frac{Eu_N}{\sqrt[3]{Sm_N^2 * Tb_N}}$$

Statistical analyses were performed using the REE values obtained using ICP-MS, which were pre-treated and standardized to produce z-values according to Davis (1986).

$$Z - value = \frac{observed\ value - \ mean\ value}{standard\ deviation}$$

The raw data was pre-treated in Excel, while statistical analyses and data representations were made with R. Spearman's rank-order correlation coefficient was used as a means of quantifying the correlation. A p-value of less than 0.05 was considered to be statistically significant. Correlation matrices were constructed from the obtained Spearman's ρ values and were sorted using hierarchical clustering based on Ward's method, which was all done using the corrplot package in R (Wei and Simko, 2017).

4. Results

The raw data used for the graphical representations in Figs. 3–8 can be found in the appendix in Tables S1, S2, S3, S4 and S5.

4.1. Bulk and clay mineralogy

Phyllosilicates make up a large proportion of the CPs, followed by pyrite in minor amounts. Only one sample contained gypsum. The clay mineral phases detected are ordered and irregularly oriented illite/smectite mixed layer minerals and illitic material. Chlorite was found in only two samples (Table 1). TR soils consist of quartz, plagioclase, K-feldspar, micaceous clay minerals (illitic material and mica), kaolinites (both poorly and well-crystallized kaolinite), chlorite, vermiculite, mixed-layer clay minerals, hematite and goethite (Table 1). The presence of low-charge vermiculite or high-charge smectite is sporadic and of local importance. The dominant clay minerals in the clay fraction are kaolinite and illitic material.

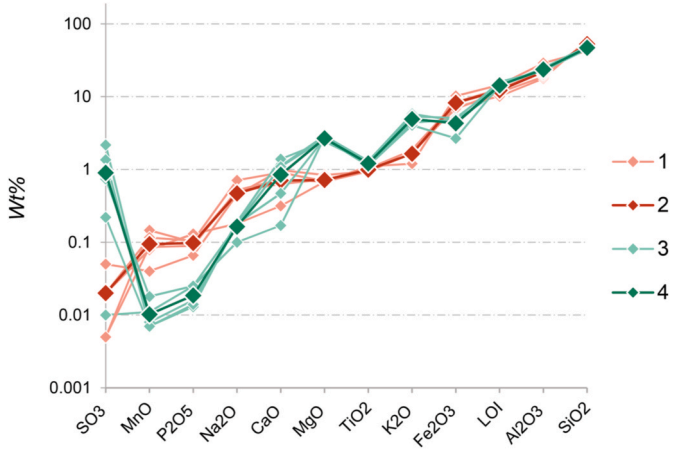

Fig. 3. Major oxide composition in the < 2 mm fraction of analysed soils/palaeosols, 1 – Terra rossa samples, 2 – Terra rossa mean value, 3 - Cretaceous palaeosol samples, 4 – Cretaceous palaeosol mean value.

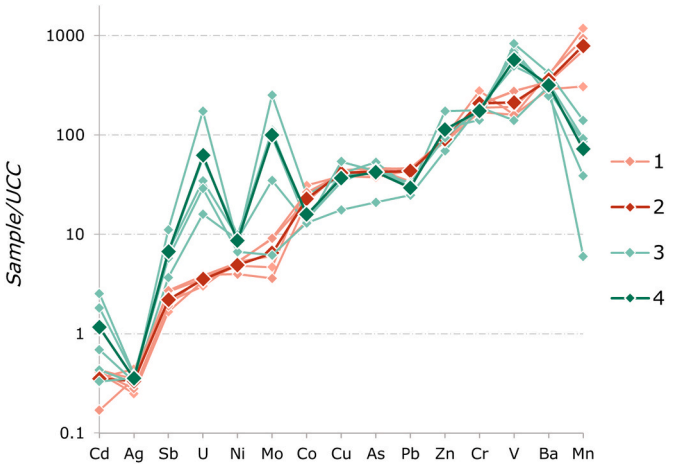

Fig. 4. Distribution trace elements in terra rossa soil and Cretaceous palaeosol samples, 1 – Terra rossa samples, 2 – Terra rossa mean value, 3 - Cretaceous palaeosol samples, 4 – Cretaceous palaeosol mean value.

4.2. Major, trace and REE geochemistry

Compared to TR, CPs are enriched in K_2O, MgO, SO_3, U, Mo Sb, V and Cd, while TR soils are enriched in TOC, MnO, Na_2O, P_2O_5 and Fe_2O_3 compared to CP (Figs. 3 and 4 and Table S6).

The Sr/Ba values (Table 2) in CP range from 0.14 to 0.68 and in TR from 0.04 to 0.09. The total content of REEs in CP ranges from 93.64 to 126.33 mg/kg (Table 2), while in TR it ranges from 199.89 to 312.77 mg/kg (Table 2). The $(LREE/HREE)_{ucc}$ ratios in TR range from 1.06 to 1.14 (Table 2), indicating a slight LREE enrichment relative to the HREEs. In CP, they range from 0.66 to 0.98, indicating an enrichment of the HREEs relative to the LREEs (Table 2).

4.3. Sequential extraction

There are significant differences in the concentrations of trace elements between the TR soils and CPs for each sequential extraction step (Fig. 5). Cd, Ni, Co and Zn are considered the most mobile in CPs (<50% of the total content in the residual fraction), while Mn, Sb, Co and Pb are considered most mobile in TR soils (<50% of the total content in the residual fraction, Fig. 5). The most immobile elements (>80% in the residual fraction) in CPs are Sb, As, V, Ba and Cr, and in TR soils they are Cu, V, Zn, Cr, Ni, As and Mo (Fig. 5).

In CPs more than 90% of the REEs are in the residual fraction, which is only 55% of the total inventory of REEs in the TR soils (Fig. 6). In CPs, the predominant sink besides the residual fraction is the oxidizable fraction, while the reducible, acid-soluble and exchangeable fractions in CPs hardly contribute to the total inventory of REEs (Fig. 6). In TR soils, the reducible and oxidizable fractions compete as sinks for the REEs (Fig. 6), while the acid-soluble and exchangeable fractions hardly contribute to the total inventory of REEs.

In the data from the REEs, obtained by sequential extraction, several characteristic processes and patterns can be described, most of which

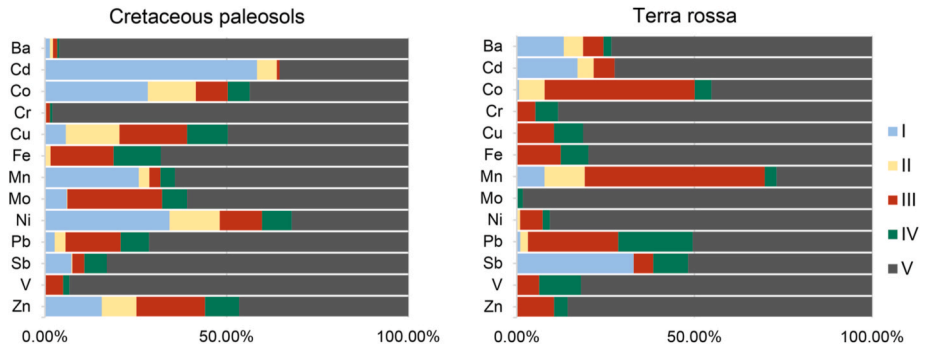

Fig. 5. Location of analysed elements in sequential fractions of terra rossa soils and Cretaceous palaeosols (mean values of 5 samples for both materials). I - exchangeable fraction, II – acid-soluble fraction, III – reducible fraction, IV – oxidizable fraction, V – residual fraction.

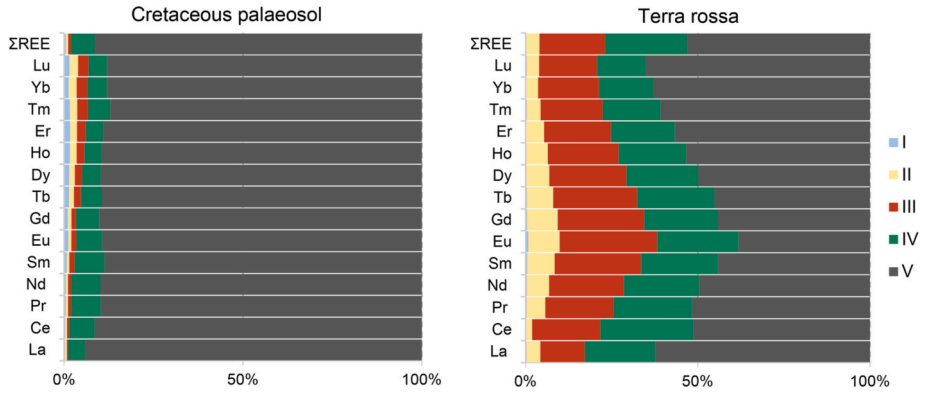

Fig. 6. Amount of specific REE in each sequential extraction step within terra rossa and Cretaceous palaeosols (mean values of 5 samples for both materials). I - exchangeable fraction, II – acid-soluble fraction, III – reducible fraction, IV – oxidizable fraction, V – residual fraction.

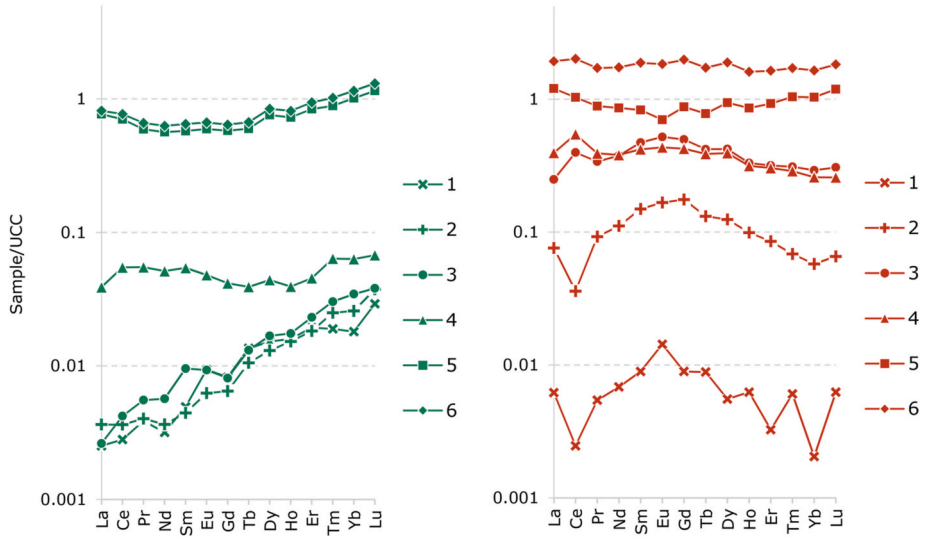

Fig. 7. Mean REE concentrations in each sequential extraction step for CP (left) and TR (right). In the exchangeable fraction within TR a jagged effect appears as a result of incomplete data for Thulium and Lutetium; 1 –exchangeable fraction, 2 – acid-soluble fraction, 3 – reducible fraction, 4 – oxidizable fraction, 5 – residual fraction, 6 – total amount of REE.

can be seen in the diagram of Fig. 7. The residual fraction from both the TR soils and CPs is depleted in the MREEs and LREEs in the CPs, but enriched in the HREEs in the CPs and in the LREEs in the TR soils. The residual fraction also shows a slightly positive Eu anomaly in most CP samples and a negative one in the TR soil (Table 3). There is also a detectable, slightly positive Ce anomaly in the residual fraction in three CP samples (Fig. 8, Table 3).

In the TR soil, the oxidizable, reducible and acid-soluble fractions show an enrichment in MREEs, with the oxidizable and reducible fractions showing a pronounced anomaly and the residual fraction showing a slightly positive Ce anomaly (Fig. 8, Table 3), while the acid-soluble fraction shows a negative one (Fig. 7, Table 3). In the exchangeable fraction of the TR soil there is very little REE, but it shows MREE enrichment and a negative Ce anomaly (Fig. 7, Table 3). In CPs, the

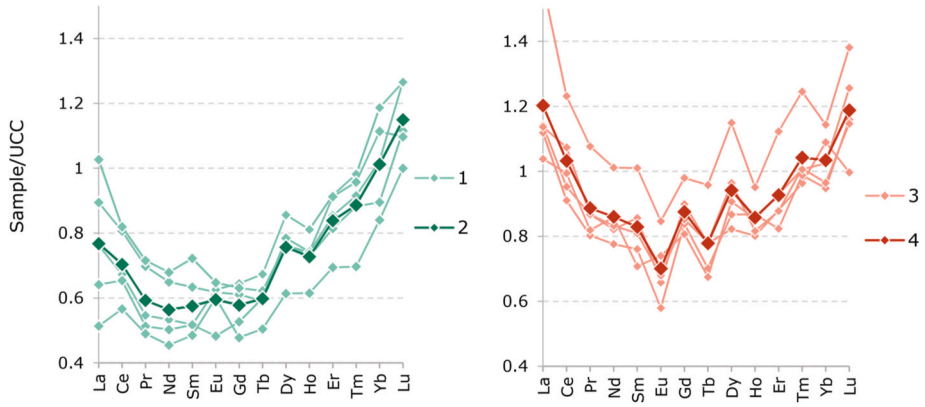

Fig. 8. REE values in the residual fraction for both CP and TR; 1 – Cretaceous palaeosol samples, 2 – Cretaceous palaeosol mean value, 3 – Terra rossa samples, 4 – Terra rossa mean value.

Table 1
Semi-quantitative mineral composition of the < 2 mm fraction of the investigated soil/palaeosol samples based on the analysis of <2 mm and <2 μm fraction.

Sample	Q	Pl	Kf	HG	Py	G	M + Ill*	MLIS	Kl	V	C	LcV	MC
TR 1	29	1	1	5			++		+++	+	+	+	+
TR 2	31	1	1	6			++		+++	+	+		+
TR 3	25	1	1	7			++		+++	+	+		+
TR 4	23	2	1	6			++		+++	+	+		+
TR 5	16	1	1	7			++		+++	+	+		+
CP1					1	2	+++	+					
CP2					1		++	++			+		
CP3					2		++	++					
CP4					2		+++	+			+		
CP5							++	+					

TR: Terra rossa, CP: Cretaceous palaeosol, Q: Quartz, Pl: Plagioclase, Kf: K-feldspar, HG: Hematite + Goethite, Py: Pyrite, G: Gypsum, M + III*: Mica + Illitic material (in Cretaceous palaeosol mica is not present), MLIS: Mixed-layer illite-smectite, Kl: Kaolinite, V: Vermiculite, C: Chlorite, LcV: Low-charge vermiculite, MC: Mixed-layer clay mineral (other than MLIS), Q, Pl, Kf, HG, Py and G in wt. %, +: relative abundance of clay minerals within horizons based on X-ray diffraction (no quantitative value is assigned to +).

Table 2
Total amount of REE together with LREE/HREE and Sr/Ba ratio values; ΣREE is in ppm while LREE/HREE was normalized with its upper continental crust ratios.

	TR1	TR2	TR3	TR4	TR5	CP1	CP2	CP3	CP4	CP5
Sr/Ba	0.04	0.05	0.09	0.06	0.06	0.35	0.29	0.68	0.14	0.23
ΣREE	199.89	297.29	312.77	280.93	305.07	107.14	93.64	98.26	125.15	126.33
(LREE/HREE)ucc	1.11	1.13	1.11	1.06	1.12	0.66	0.75	0.67	0.90	0.98

Table 3
Numerical values of Ce and Eu anomalies throughout sequential extraction steps in TR and CP samples; NA – anomalies which could not be calculated because of unmeasurable concentrations of elements used in the calculation, I – exchangeable fraction, II – acid-soluble fraction, III – reducible fraction, IV – oxidizable fraction, V – residual fraction.

		CP1	CP2	CP3	CP4	CP5	TR1	TR2	TR3	TR4	TR5
I	Eu*	1.43	1.16	NA	1.27	NA	NA	1.49	1.74	NA	1.87
I	Ce*	0.79	0.83	1.37	0.86	NA	0.80	0.62	0.81	0.30	0.21
II	Eu*	1.19	0.65	1.07	0.93	NA	1.16	1.14	1.10	1.26	1.19
II	Ce*	0.76	1.07	0.80	0.69	0.89	0.37	0.61	0.78	0.18	0.21
III	Eu*	0.96	0.94	0.93	0.71	0.78	1.08	1.11	1.14	1.19	1.16
III	Ce*	0.82	0.79	0.68	0.72	0.93	1.98	1.43	1.23	1.11	1.27
IV	Eu*	0.93	1.06	0.91	1.01	0.98	1.03	1.02	1.09	1.05	1.09
IV	Ce*	0.86	0.96	0.93	0.87	1.05	1.92	1.55	1.22	1.17	1.30
V	Eu*	1.11	1.22	0.89	1.00	0.94	1.06	0.85	0.85	0.78	0.79
V	Ce*	1.20	1.07	1.25	1.08	1.09	1.27	1.19	1.07	1.10	1.04

oxidizable fraction has very little REEs, but it shows a pronounced LREE and a slight HREE enrichment (Fig. 7). Reducible, exchangeable, and acid-soluble fractions within the CPs have very low REE contents, consisting almost exclusively of HREEs (Fig. 7).

4.4. Multivariate statistical analysis

Looking at the correlation matrices (Fig. 9), the difference in correlation that the REEs exhibit between TR and CP is very striking. In the TR soil all the REEs are very positively correlated, while in the CPs they are divided into two internally, very positively correlated groups, i.e., LREEs

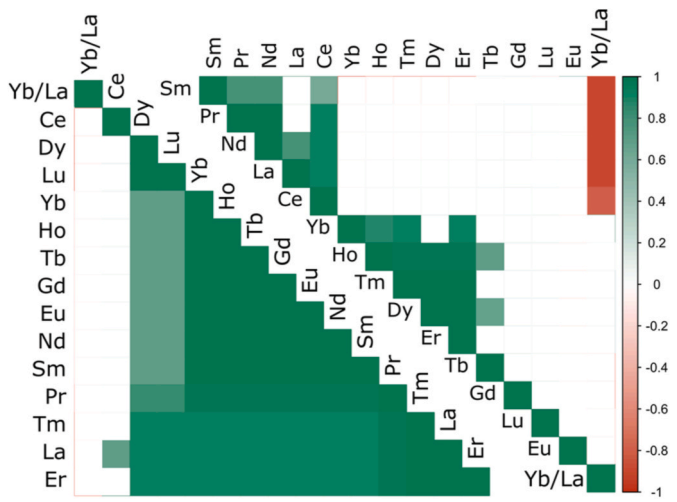

Fig. 9. Correlation matrices constructed from relationships between REE values in CP (right upper corner) and TR (left lower corner); blank cells represent statistically insignificant values.

and HREEs, which are not correlated with each other. The MREEs in the CPs do not show any significant correlation and are not correlated with the other REEs (Fig. 9). In CPs, most of the LREEs are negatively correlated with the $(Yb/La)_{ucc}$ ratio, while in the TR soil there is no significant correlation between the REEs and the $(Yb/La)_{ucc}$ ratio (Fig. 9).

Parameters of the statistically analysed REE data are in Table S7.

5. Discussion

5.1. Differences in the major elements and the mineralogy between the terra rossa soils and the Cretaceous palaeosols

For both the TR soils and CPs the chemical data obtained agree well with the mineral data. The high K_2O content (Fig. 3) in the CPs compared to the TR soils is a clear indication that illitic material is the dominant phase. Smectites from illite/smectite mixed-layer clay minerals from CPs at the Tri Jezerca quarry are aluminium-rich montmorillonites without any iron substitution in the octahedral position (Ottner et al., 1999), to which the obtained MgO values from this study (Fig. 3) correspond well. Higher SO_3 values (Fig. 3) in the CPs reflect the formation of gypsum and pyrite. Surface (sub)recent pyrite oxidation leads to supergene gypsum formation. Jarosite was not detected in our study, but is probably present in small amounts, below the detection limit for XRD analysis (<1%), as previously found at one of the investigated localities from this study (Hrenović et al., 2014).

Higher Na_2O values are found in TR soils (Fig. 3) compared to the CPs, to reflect the presence of plagioclase, which was not detected in the CPs. Higher Fe_2O_3 values (Fig. 3) in the TR soils result from the formation of hematite and goethite, mineral phases specific to the oxidizing, well-drained, and neutral pedo-environment in which TR soil is formed (Boero and Schwertmann, 1989; Durn et al., 2007). A high MnO content is also associated with the formation in an oxic pedo-environment, where manganese oxides and iron oxides together often form nodules or concretions.

Metals present in the operationally defined fractions of treated TR soils and CPs (Fig. 5) are not necessarily bound to the same phases (minerals or organic matter) within each fraction and can be assigned to different compounds accordingly. The residual phase is related to silicate minerals in both the TR soils and CPs, but the reducible and oxidizable fractions differ. The oxidizable fraction in the CP consists of pyrite (very low TOC content in CPs, Table S6). Metals present in the oxidizable fraction of the TR soil are bound to organic material (no sulphides and higher TOC content in TR soils, Fig. 3 and Table S6). Almost no manganese in the reducible fraction (Fig. 5) in the CPs indicates that it is probably composed of jarosite and iron oxides, whereas in the TR soil it is composed of ferromanganese oxides.

5.2. Behaviour of trace elements enriched in Cretaceous palaeosols

The enrichment within CPs compared to the TR soils in Cd, Sb, V, and especially in U and Mo (Fig. 4) is mainly related to the reducing conditions prevailing in the CPs during their formation. U, Mo and V are reduced to their immobile forms in the presence of a strong reducing agent, such as H_2S, and anaerobic microbial activity. This relates the accumulation of these elements to the anoxic conditions that prevail during the formation of CPs.

Most of the molybdenum is found in the residual fraction, where it is most probably associated with its insoluble species and clays (Fig. 5). Surprisingly, much more molybdenum is present in the reducible fraction than in the oxidizable fraction (Fig. 5), as pyrite is known to incorporate molybdenum under euxinic conditions (Tossell, 2005; Neubert et al., 2008; Frascoli and Hudson-Edwards, 2018). This is probably a consequence of a sub-recent CP exhumation, when molybdate was released from the oxidized pyrite and adsorbed onto newly formed iron oxides or jarosite in an acidic environment, as reported by Frascoli and Hudson-Edwards (2018). Molybdenum in TR soils, unlike CPs, is located almost exclusively within the residual fraction, with only a small amount of molybdenum bound to the organic material from the oxidizable fraction (Fig. 5).

In CPs almost all the vanadium is in the residual fraction (Fig. 5), probably as hydroxides and within clays, as some studies reported similar results (Wanty and Goldhaber, 1992; Peacor et al., 2000; Reijonen et al., 2016). In addition to the residual fraction, vanadium is also present in a small amount in the reducible fraction (Fig. 5). This is probably a result of its oxidation to more mobile forms (V^{5+}, V^{4+}), which were subsequently adsorbed onto newly formed iron oxides and jarosite (Wei et al., 2018), like molybdenum. Vanadium is present in lower concentrations in TR soils compared to CPs. In TR soils, it is associated with iron oxides and is also abundant in the oxidizable fraction (Fig. 5). Here, it is associated with organic matter, which usually acts as an adsorbent for vanadium (Reijonen et al., 2016; Shaheen et al., 2016).

Cadmium enrichment is associated with the exchangeable fraction (Fig. 5.). This is surprising because cadmium is normally associated with pyrite, which is abundant in CPs. Cadmium is immobilized under reducing conditions but can be remobilized under oxic and acidic conditions (Gambrell, 1994; Tabelin et al., 2018). It is, therefore, possible that in the sub-recent exhumation of CPs, the increased cadmium mobility is related to the onset of oxic conditions, and the lowered pH (Tab. S6) caused by the pyrite dissolution.

Antimony is also significantly enriched in CPs compared to TR soils. The exact enrichment mechanism remains unclear, but is probably related to the reducing conditions or the enrichment in clays.

5.3. Behaviour of trace elements enriched in terra rossa soil

Compared to CPs, TR soils are not significantly enriched in any trace elements except Mn, which is simply related to the presence of ferromanganese oxides in TR soils, but there are visible differences in the trace-element distribution when comparing the sequential extraction of both materials (Fig. 5). Iron and manganese oxides (the reducible fraction) are a significant sink for Co and Pb in TR soils, which are commonly enriched in ferromanganese oxides in soils (Crowther et al., 1983; Dawson et al., 1985; Latrille et al., 2001; Palumbo et al., 2001; Liu et al., 2002). Some amount of lead is also found in the oxidizable fraction, which is expected since soil's organic matter is known to accumulate lead (Fujikawa and Fukui, 2001; Reimann et al., 2015). In TR soils, only Sb, Cd, Ba and Mn are in the exchangeable fraction, while all the other elements are bound in reducible, oxidizable and residual

fractions. This contrasts with CPs, where Cd, Co, Cu, Mn, Mo, Ni, Sb and Zn are bound in the exchangeable fraction, and in larger amounts. This is probably a consequence of the different mineralogical composition, since the main clay phase in TR is kaolinite, which has a much lower adsorption capacity than illitic material and illite-smectite, dominant clay phases in CPs (Table 1).

5.4. REE behaviour in Cretaceous palaeosols

In CPs, LREE and HREE are very positively correlated within each group (Fig. 9), with no correlation between them. This means that each group (LREEs and HREEs) behaves as a distinct group of elements within the CPs, with different processes influencing their behaviour. The Eu in CPs does not correlate in any way with the LREE or HREEs (Fig. 9). This, coupled with minor but observable, positive Eu anomalies (Fig. 9, Table 3), most probably reflects a reduction to Eu^{2+}, which more readily replaces Ca^{2+} or Sr^{2+} in the mineral (Honty et al., 2008; Migdisov et al., 2016). There are two other interesting and important, statistically obtained findings. The first is the insignificant correlation between individual HREEs and $(Yb/La)_{ucc}$, implying that variations in individual HREE concentrations do not affect the differences in $(Yb/La)_{ucc}$ values. The second is the strong negative correlation between the LREEs and $(Yb/La)_{ucc}$ (Fig. 9), implying that variations in individual LREE concentrations negatively affect the variations in $(Yb/La)_{ucc}$ within the CPs. Overall, these two results suggest that only LREE behaviour had a significant effect on $(Yb/La)_{ucc}$, and since the values of this ratio show HREE enrichment, it is reasonable to assume that LREE removal is a likely cause of the observed high values of $(Yb/La)_{ucc}$.

In sequential extraction, exchangeable, acid soluble and reducible fractions show HREE enrichment, but this is of little significance as the REE values obtained in these fractions are very low and close to the detection limit for most HREEs. Regardless, this could be the result of a sub-recent transition to a very low pH during pyrite oxidation (Fig. S6), which is below the point of zero charge for most soil compounds. This would limit the availability and adsorption of LREEs, which have a lower ionic potential than HREEs, to newly formed iron oxides and jarosite along with the rest of the colloidal soil fraction. As expected, the residual fraction reflects the pattern of REEs obtained for the total values of the REEs, but with a more pronounced LREE depletion, HREE enrichment (Fig. 7.) and a slightly positive Ce anomaly (Fig. 8., Table 2.). Fulvic and humic acids are usually formed from the organic matter in a marshy environment and preferentially bind LREEs as opposed to HREEs (Dia et al., 2000; Cao et al., 2001; Moermond et al., 2001; Aide and Aide, 2012). Organic matter is remobilized in a reducing environment (Shiller, 2002; Pédrot et al., 2008; Davranche et al., 2011), which can lead to the depletion of LREEs. In view of the geographical location and the circumstances under which the CPs were formed, it can be assumed that groundwater might be connected to the sea. This is recorded in CPs by the high Sr/Ba ratios, which are higher than 0.2 in three samples, indicating a brackish environment, and higher than 0.5 in one sample (Table 2.), indicating a marine environment (Wei and Algeo, 2020). This is important because in seawater, HREEs are more abundant than LREEs (Coppin et al., 2002; Censi et al., 2010; Deng et al., 2017) and increased ionic strengths in marine and brackish environments result in a lower adsorption of LREEs to clay minerals in contrast to HREEs, as shown by several experimental studies (Coppin et al., 2002; Davranche et al., 2011; Cheng et al., 2012; Hao et al., 2019). This could influence, to some extent, the REE concentrations in clay minerals during their formation, with a greater incorporation of HREEs in the clay interlayer spaces during their authigenesis, as observed in the residual fraction of CPs. Another commonly observed process in soils is the dissolution of ferromanganese oxides in a reducing pedo-environment (Cao et al., 2001; Neaman et al., 2004; Grybos et al., 2007; Laveuf et al., 2008; Davranche et al., 2011). The precipitation of Fe–Mn oxides in the oxic and their subsequent dissolution in a re-established reducing environment (Davranche et al., 2011) during groundwater fluctuations could lead to LREE depletion. The earlier occurrence of such a process is recorded in slightly positive Ce anomalies in the residual fraction. Manganese oxides drive and host cerianite precipitation (Braun et al., 1998; Bau, 1999; Dia et al., 2000), which in turn remains in the soils where manganese oxides were dissolved (Laveuf et al., 2012), leading to the development of a positive Ce anomaly in the residual fraction. Two of the previously mentioned processes most probably led to the formation of the observed REE patterns, as they both fractionate REEs through LREE depletion. These are the dissolution of ferromanganese oxides and REE fractionation within clays in high-ionic-strength environments (brackish and marine environments). We can tentatively propose that such processes led to the development of the observed REE patterns within CPs, along with a contribution from other processes that could not be confirmed by this study. REE behaviour in CPs will be revisited and supported by additional samples and analyses, as this is part of an ongoing study.

5.5. REE behaviour in terra rossa soils

Multivariate statistical analyses show a very positive correlation between all the REEs in TR soils (Fig. 9). This can be used to describe their behaviour as a coherent group of elements in such a pedo-environment, except for Ce, which was confirmed in the rest of the data.

In TR soils the sequential extraction data, the reducible and oxidizable fractions account for almost 50% of the total content of REEs (Fig. 7.). Within TR soils, the acid-soluble, reducible, and oxidizable fractions show a MREE enrichment (Fig. 7.). A LREE-to-MREE enrichment is typical for ferromanganese oxides (Tang and Johannesson, 2003; Quinn et al., 2006; Laveuf et al., 2008; Jiang et al., 2011; Zhou et al., 2020), but also for organic matter in neutral-to-alkaline pH (Davranche et al., 2011; Aide and Aide, 2012). This range includes the pH of terra rossa soils (Table S6), which are also characterized by the abundance of ferromanganese oxides (Boero and Schwertmann, 1989; Durn et al., 1999; Ivanić et al., 2020). A positive Ce anomaly is a common feature of oxic pedo-environments, associated with manganese oxides. Mn^{4+} acts as an electron acceptor for Ce^{3+} and oxidizes it to Ce^{4+} (Braun et al., 1998; Coelho and Vidal-Torrado, 2000; Ohta and Kawabe, 2001; Pédrot et al., 2008), when it is either adsorbed on ferromanganese oxides (Koppi et al., 1996; Coelho and Vidal-Torrado, 2000; Neaman et al., 2004) or it precipitates to residual cerianite (Braun et al., 1998; Bau, 1999; Dia et al., 2000). Therefore, it can be concluded that Ce is most probably present as residual cerianite in the residual fraction, while in the reducible fraction it is most probably directly bound in ferromanganese oxides. A positive Ce anomaly was also observed in the oxidizable fraction. One study (Pourret et al., 2008) suggested that in a neutral-to-alkaline environment, the complexation of Ce^{3+} with carbonates induces its oxidation to Ce^{4+}, whereupon it readily binds to humic acid. This removes it from organic-rich waters, resulting in a positive cerium anomaly in the precipitate coupled to a negative one in solution. It is important to note that this can only take place effectively in alkaline-to-neutral environments, where carbonate species are mobile and abundant (Pourret et al., 2008). In TR soils, ferromanganese oxides are probably responsible for most of the oxidation of Ce^{3+} to Ce^{4+}, with oxidation during carbonate complexation playing a minor role. This can nevertheless apply to the terra rossa soils from this study, as they exhibit conditions similar to those described by Pourret et al. (2008) and show negative Ce anomalies in the exchangeable and acid-soluble fractions. The exchangeable and acid-soluble fractions were probably an available source for the development of a positive Ce anomaly in the oxidizable fraction, as well as in the reducible fraction. This most probably occurs during water percolation, when such processes could take place. The observed negative Eu anomaly in the residual fraction probably originates from the parent material, which is a mixture of aeolian dust, flysch, insoluble limestone residue and volcanic dust (Durn et al., 2007).

5.6. Comparison of REE behaviour between Cretaceous palaeosols and terra rossa soils

In addition to the differences described above that are evident in the statistical, numerical, and sequential extraction data, one of the most important and significant differences between the REEs in TR soils and CPs can be inferred from the total amount of REEs in each extraction step alone. In TR soils, almost 50% of the total amount of REEs is in the acid soluble, reducible and oxidizable fraction, while almost the entire amount of REEs is in the residual fraction within the CPs (Fig. 6). The residual fraction has a similar amount of REEs for both TR soils and CPs. This, together with the fact that TR soil has almost half the total amount of REEs in fractions other than the residual fraction and that TR soil has twice as much REEs as CP, suggests that the observed difference in the total amount of REEs is principally pedogenetic.

6. Conclusion

This study showed that the materials formed on a carbonate bedrock exposed to different soil environments (oxic and reducing) developed corresponding differences in their trace-element signatures that were almost exclusively pedogenetic. Cd, Sb, V and especially U and Mo are enriched in CP, a result of pedogenesis in the reducing conditions, while TR is enriched in Mn, a result of the pedogenesis in oxic conditions. The most notable difference between TR soils and CPs observed in this study was the behaviour of the REEs.

TR soils have almost twice as much REEs as CPs, which can be attributed exclusively to the pedogenetic processes, since both materials have a similar amount of REEs in the residual fraction and TR soils have almost the same amount of REE bound in acid-soluble, reducible and oxidizable fractions as CPs in the residual fraction. This difference also proves the influence of the redox conditions during pedogenesis on the behaviour of the REEs. The accumulated REEs were released in a reducing environment from solubilized organic matter and ferromanganese oxides, leaving only the REEs accumulated and bound in clays, while in the oxic environment of TR soils, ferromanganese oxides and organic matter accumulated REEs. A detailed study of the REE patterns in CPs, coupled with statistical analyses, allowed such an interpretation, as the observed, slightly positive Ce anomalies in the residual fraction and the LREE depletion indicate the dissolution of ferromanganese oxides. In CPs, the statistical analyses showed the difference in fractionation between the LREEs and HREEs, which might be related to the pedogenetic and depositional processes. In TR soils it confirmed the anomalous behaviour of Ce, while the other REEs showed a positive correlation between them.

Overall, REEs were successfully used to trace the pedogenetic history of both Cretaceous palaeosols and terra rossa soils. Particularly noteworthy was the use of statistical analyses and sequential extraction, which allowed a detailed comparison between the TR soils and CPs based on trace-element behaviour. Since there are virtually no studies that directly compare two soil materials formed in opposite redox environments, especially on karst soils, this study contributes significantly to the current knowledge on this topic.

Credit author statement

Goran Durn: Conceptualization, Methodology, Validation, Investigation, Writing – review & editing, Supervision, Project administration, Funding acquisition. Ivor Perković; : Investigation, Methodology, Validation, Writing – original draft, Visualization. Jens Stummeyer: Investigation, Methodology. Franz Ottner: Investigation, Methodology. Marta Mileusnić; : Investigation, Methodology.

Declaration of competing interest

The authors declare that they have no known competing financial interests or personal relationships that could have appeared to influence the work reported in this paper.

Acknowledgements

We would like to thank our three anonymous reviewers on helpful suggestions and comments which improved our manuscript substantially. We would also like to thank Tamara Troskot- Čorbić for determination of the total carbon and the TOC content. This work has been supported in part by the Croatian Science Foundation (project no. IP-2019-04-8054).

Appendix A. Supplementary data

Supplementary data to this article can be found online at https://doi.org/10.1016/j.chemosphere.2021.131286.

References

Aide, M.T., Aide, C., 2012. Rare earth elements: their importance in understanding soil genesis. ISRN Soil Sci. 1–11 https://doi.org/10.5402/2012/783876.

Bau, M., 1999. Scavenging of dissolved yttrium and rare earths by precipitating iron oxyhydroxide: experimental evidence for Ce oxidation, Y-Ho fractionation, and lanthanide tetrad effect. Geochem. Cosmochim. Acta 63. https://doi.org/10.1016/S0016-7037(99)00014-9.

Boero, V., Schwertmann, U., 1989. Iron oxide mineralogy of terra rossa and its genetic implications. Geoderma 44. https://doi.org/10.1016/0016-7061(89)90039-6.

Braun, J.J., Viers, J., Dupré, B., Polve, M., Ndam, J., Muller, J.P., 1998. Solid/liquid REE fractionation in the lateritic system of Goyoum, East Cameroon: the implication for the present dynamics of the soil covers of the humid tropical regions. Geochem. Cosmochim. Acta 62. https://doi.org/10.1016/S0016-7037(97)00344-X.

Brindley, G.W., Brown, G., 1980. Crystal Structures of Clay Minerals and Their X-Ray Identification, Crystal Structures of Clay Minerals and Their X-Ray Identification. https://doi.org/10.1180/mono-5.

Brown, G., 1961. The X-Ray Identification and Crystal Structures of Clay Minerals, second ed. Mineralogical society (Great Britain), Clay minerals group, London.

Cao, X., Chen, Y., Wang, X., Deng, X., 2001. Effects of redox potential and pH value on the release of rare earth elements from soil. Chemosphere 44, 655–661. https://doi.org/10.1016/S0045-6535(00)00492-6.

Catrouillet, C., Guenet, H., Pierson-Wickmann, A.C., Dia, A., Lecoz, M.B., Deville, S., Lenne, Q., Suko, Y., Davranche, M., 2020. Rare earth elements as tracers of active colloidal organic matter composition. Environ. Chem. 17 https://doi.org/10.1071/EN19159.

Censi, P., Zuddas, P., Randazzo, L.A., Saiano, F., Mazzola, S., Aricò, P., Cuttitta, A., Punturo, R., 2010. Influence of dissolved organic matter on rare earth elements and yttrium distributions in coastal waters. Chem. Ecol. 26, 123–135. https://doi.org/10.1080/02757541003627720.

Chang, C., Song, C., Beckford, H.O., Wang, S., Ji, H., 2019. Behaviors of REEs during pedogenetic processes in the karst areas of Southwest China. J. Asian Earth Sci. 185 https://doi.org/10.1016/j.jseaes.2019.104023.

Cheng, H., Hao, F., Ouyang, W., Liu, S., Chunye, L., Wenjing, Y., 2012. Vertical distribution of rare earth elements in a wetland soil core from the Sanjiang Plain in China. J. Rare Earths 30, 731–738. https://doi.org/10.1016/S1002-0721(12)60120-3.

Coelho, M.R., Vidal-Torrado, P., 2000. Cerium (Ce) in some nodular ferricretes developed in soils of the adamantina formation. Sci. Agric. 57 https://doi.org/10.1590/S0103-90162000000200021.

Coppin, F., Berger, G., Bauer, A., Castet, S., Loubet, M., 2002. Sorption of lanthanides on smectite and kaolinite. Chem. Geol. 182, 57–68. https://doi.org/10.1016/S0009-2541(01)00283-2.

Crowther, D.L., Dillard, J.G., Murray, J.W., 1983. The mechanisms of Co(II) oxidation on synthetic birnessite. Geochem. Cosmochim. Acta 47. https://doi.org/10.1016/0016-7037(83)90298-3.

Davis, J.C., 1986. Statistics and Data Analysis in Geology. Wiley & Sons inc, New York.

Davranche, M., Gruau, G., Dia, A., Coz-bouhnik, M. Le, Pédrot, M., Pourret, O., 2019. Rare earth elements in wetlands. In: Rinklebe, J., Knox, A.S., M P (Eds.), Trace Elements in Waterlogged Soils and Sediments. Taylor & Francis Group/CRC Press, pp. 135–162.

Davranche, M., Grybos, M., Gruau, G., Pédrot, M., Dia, A., Marsac, R., 2011. Rare earth element patterns: a tool for identifying trace metal sources during wetland soil reduction. Chem. Geol. 284 https://doi.org/10.1016/j.chemgeo.2011.02.014.

Dawson, B.S.W., Fergusson, J.E., Campbell, A.S., Cutler, E.J.B., 1985. Distribution of elements in some Fe-Mn nodules and an iron-pan in some gley soils of New Zealand. Geoderma 35. https://doi.org/10.1016/0016-7061(85)90026-6.
Deng, Y., Ren, J., Guo, Q., Cao, J., Wang, H., Liu, C., 2017. Rare earth element geochemistry characteristics of seawater and porewater from deep sea in western Pacific. Sci. Rep. 7, 1–13. https://doi.org/10.1038/s41598-017-16379-1.
Dia, A., Gruau, G., Olivié-Lauquet, G., Riou, C., Molénat, J., Curmi, P., 2000. The distribution of rare earth elements in groundwaters: assessing the role of source-rock composition, redox changes and colloidal particles. Geochem. Cosmochim. Acta 64. https://doi.org/10.1016/S0016-7037(00)00494-4.
Duncan, T., Shaw, T.J., 2003. The mobility of Rare Earth Elements and Redox Sensitive Elements in the groundwater/seawater mixing zone of a shallow coastal aquifer. Aquat. Geochem. 9, 233–255. https://doi.org/10.1023/B:AQUA.0000022956.20338.26.
Durn, G., Aljinović, D., Crnjaković, M., Lugović, B., 2007. Heavy and light mineral fractions indicate polygenesis of extensive terra rossa soils in Istria, Croatia. In: Mange, M., Wright, D. (Eds.), Heavy Minerals in Use. Developments in Sedimentology. Elsevier, pp. 701–737. https://doi.org/10.1016/S0070-4571(07)58028-3.
Durn, G., Hrenović, J., Sekovanić, L., 2013. Terra rossa as the substrate for biological phosphate removal from wastewater. Clay Miner. 48, 725–738. https://doi.org/10.1180/claymin.2013.048.5.05.
Durn, G., Mindszenty, A., Tišljar, J., Mileusnić, M., 2006. Clay mineralogy of bauxites and palaeosols in Istria formed during regional subaerial exposures of the Adriatic Carbonate Platform. In: Vlahović, I., Tibljaš, D., Durn, G. (Eds.), 3rd Mid-European Clay Conference: Field Trip Guidebook. University of Zagreb, Faculty of Science and Faculty of Mining, Geology and Petroleum Engineering, Zagreb, Croatia, pp. 3–30.
Durn, G., Ottner, F., Slovenec, D., 1999. Mineralogical and geochemical indicators of the polygenetic nature of terra rossa in Istria, Croatia. Geoderma 91, 125–150. https://doi.org/10.1016/S0016-7061(98)00130-X.
Durn, G., Škapin, S.D., Vidović, N., Rennert, T., Ottner, F., Ružičić, S., Cukrov, N., Sondi, I., 2019. Impact of iron oxides and soil organic matter on the surface physicochemical properties and aggregation of Terra Rossa and Calcocambisol subsoil horizons from Istria (Croatia). Catena 183. https://doi.org/10.1016/j.catena.2019.104184.
Durn, G., Slovenec, D., Čović, M., 2001. Distribution of Iron and manganese in terra rossa from Istria and its genetic implications. Geol. Croat. 54, 27–36. https://doi.org/10.4154/GC.2001.03.
Feng, J.L., 2010. Behaviour of rare earth elements and yttrium in ferromanganese concretions, gibbsite spots, and the surrounding terra rossa over dolomite during chemical weathering. Chem. Geol. 271, 112–132. https://doi.org/10.1016/j.chemgeo.2010.01.003.
Feng, J.L., Lin, Y.C., Gao, S.P., Zhang, J.I.F., 2012. Enrichment of trace elements in ferromanganese concretions from terra rossa and their potential desorption. Geochem. J. 46, 151–161. https://doi.org/10.2343/geochemj.1.0156.
Frascoli, F., Hudson-Edwards, K.A., 2018. Geochemistry, mineralogy and microbiology of molybdenum in mining-affected environments. Minerals. https://doi.org/10.3390/min8020042.
Fujikawa, Y., Fukui, M., 2001. Vertical distribution of trace metals in natural soil horizons from Japan. Part 2: effects of organic components in soil. Water Air Soil Pollut. 131 https://doi.org/10.1023/A:1011927802703.
Fuller, A.J., Leary, P., Gray, N.D., Davies, H.S., Mosselmans, J.F.W., Cox, F., Robinson, C. H., Pittman, J.K., McCann, C.M., Muir, M., Graham, M.C., Utsunomiya, S., Bower, W. R., Morris, K., Shaw, S., Bots, P., Livens, F.R., Law, G.T.W., 2020. Organic complexation of U(VI) in reducing soils at a natural analogue site: implications for uranium transport. Chemosphere 254, 126859. https://doi.org/10.1016/j.chemosphere.2020.126859.
Gambrell, R.P., 1994. Trace and toxic metals in wetlands-A review. J. Environ. Qual. 23 https://doi.org/10.2134/jeq1994.00472425002300050005x.
Grybos, M., Davranche, M., Gruau, G., Petitjean, P., 2007. Is trace metal release in wetland soils controlled by organic matter mobility or Fe-oxyhydroxides reduction? J. Colloid Interface Sci. 314 https://doi.org/10.1016/j.jcis.2007.04.062.
Grybos, M., Davranche, M., Gruau, G., Petitjean, P., Pédrot, M., 2009. Increasing pH drives organic matter solubilization from wetland soils under reducing conditions. Geoderma 154. https://doi.org/10.1016/j.geoderma.2009.09.001.
Guénet, H., Demangeat, E., Davranche, M., Vantelon, D., Pierson-Wickmann, A.C., Jardé, E., Bouhnik-Le Coz, M., Lotfi, E., Dia, A., Jestin, J., 2018. Experimental evidence of REE size fraction redistribution during redox variation in wetland soil. Sci. Total Environ. 631–632. https://doi.org/10.1016/j.scitotenv.2018.03.005.
Han, G., Li, F., Tang, Y., 2017. Organic matter impact on distribution of rare earth elements in soil under different land uses. Clean 45. https://doi.org/10.1002/clen.201600235.
Hao, W., Flynn, S.L., Kashiwabara, T., Alam, M.S., Bandara, S., Swaren, L., Robbins, L.J., Alessi, D.S., Konhauser, K.O., 2019. The impact of ionic strength on the proton reactivity of clay minerals. Chem. Geol. 529 https://doi.org/10.1016/j.chemgeo.2019.119294.
Honty, M., Clauer, N., Šucha, V., 2008. Rare-earth elemental systematics of mixed-layered illite-smectite from sedimentary and hydrothermal environments of the Western Carpathians (Slovakia). Chem. Geol. 249, 167–190. https://doi.org/10.1016/j.chemgeo.2007.12.009.
Hrenović, J., Durn, G., Goić-Barišoć, I., Kovačić, A., 2014. Occurrence of an environmental Acinetobacter baumannii strain similar to a clinical isolate in paleosol from Croatia. Appl. Environ. Microbiol. 80 https://doi.org/10.1128/AEM.00312-14.
Ivanić, M., Durn, G., Škapin, S.D., Sondi, I., 2020. Size-related mineralogical and surface physicochemical properties of the mineral particles from the recent sediments of the Eastern Adriatic Sea. Chemosphere 249. https://doi.org/10.1016/j.chemosphere.2020.126531.
Jackson, M.L., 1979. Soil Chemical Analysis - Advanced Course. Soil Science Department, University of Wisconsin, Madison.
Jiang, X.J., Lin, X.H., Yao, D., Guo, W.D., 2011. Enrichment mechanisms of rare earth elements in marine hydrogenic ferromanganese crusts. Sci. China Earth Sci. 54 https://doi.org/10.1007/s11430-010-4070-4.
Johns, W.D., Grim, R.E., Bradley, W.F., 1954. Quantitative estimations of clay minerals by diffraction methods. J. Sediment. Petrol. 24, 242–251. https://doi.org/10.1306/d42697b5-2b26-11d7-8648000102c1865d.
Koppi, A.J., Edis, R., Field, D.J., Geering, H.R., Klessa, D.A., Cockayne, D.J.H., 1996. Rare earth element trends and cerium-uranium-manganese associations in weathered rock from Koongarra, Northern Territory, Australia. Geochem. Cosmochim. Acta 60. https://doi.org/10.1016/0016-7037(96)00047-6.
Latrille, C., Elsass, F., Van Oort, F., Denaix, L., 2001. Physical speciation of trace metals in fe-Mn concretions from a rendzic lithosol developed on Sinemurian limestones (France). Geoderma 100. https://doi.org/10.1016/S0016-7061(00)00083-5.
Laveuf, C., Cornu, S., Guilherme, L.R.G., Guerin, A., Juillot, F., 2012. The impact of redox conditions on the rare earth element signature of redoximorphic features in a soil sequence developed from limestone. Geoderma 170, 25–38. https://doi.org/10.1016/j.geoderma.2011.10.014.
Laveuf, C., Cornu, S., Juillot, F., 2008. Rare earth elements as tracers of pedogenetic processes. Compt. Rendus Geosci. 340, 523–532. https://doi.org/10.1016/j.crte.2008.07.001.
Lawrence, M.G., Greig, A., Collerson, K.D., Kamber, B.S., 2006. Rare earth element and yttrium variability in South East Queensland waterways. Aquat. Geochem. 12 https://doi.org/10.1007/s10498-005-4471-8.
Liankai, Z., Hongbing, J., Shijie, W., Gang, L., Xiuming, L., Xiao, W., QuocDinh, N., DaiTrung, N., 2020. Geochemical implications of rare earth elements in terra rossa in tropical karst area: a case study in northern Vietnam. Appl. Sci. 10 https://doi.org/10.3390/app10030858 (Switzerland).
Liu, F., Colombo, C., Adamo, P., He, J.Z., Violante, A., 2002. Trace elements in manganese-iron nodules from a Chinese alfisol. Soil Sci. Soc. Am. J. 66 https://doi.org/10.2136/sssaj2002.6610.
Matičec, D., Vlahović, I., Velić, I., Tišljar, J., 1996. Eocene limestones overlying Lower Cretaceous deposits of western Istria (Croatia): did some parts of present Istria form land during the Cretaceous? Geol. Croat. 49 https://doi.org/10.4154/GC.1994.46.
Migdisov, A., Williams-Jones, A.E., Brugger, J., Caporuscio, F.A., 2016. Hydrothermal transport, deposition, and fractionation of the REE: experimental data and thermodynamic calculations. Chem. Geol. 439, 13–42. https://doi.org/10.1016/j.chemgeo.2016.06.005.
Mihajlović, J., Giani, L., Stärk, H.J., Rinklebe, J., 2014. Concentrations and geochemical fractions of rare earth elements in two different marsh soil profiles at the North Sea, Germany. J. Soils Sediments 14, 1417–1433. https://doi.org/10.1007/s11368-014-0895-3.
Moermond, C.T.A., Tijink, J., Van Wezel, A.P., Koelmans, A.A., 2001. Distribution, speciation, and bioavailability of lanthanides in the Rhine-Meuse estuary, The Netherlands. Environ. Toxicol. Chem. 20 https://doi.org/10.1002/etc.5620200909.
Moore, D.M., Reynolds, R.C.j., 1997. X-Ray Diffraction and the Identification and Analysis of Clay Minerals, second ed. Oxford University Press.
Neaman, A., Mouélé, F., Trolard, F., Bourrié, G., 2004. Improved methods for selective dissolution of Mn oxides: applications for studying trace element associations. Appl. Geochem. 19 https://doi.org/10.1016/j.apgeochem.2003.12.002.
Neubert, N., Nägler, T.F., Böttcher, M.E., 2008. Sulfidity controls molybdenum isotope fractionation into euxinic sediments: evidence from the modern Black Sea. Geology 36. https://doi.org/10.1130/G24959A.1.
Ohta, A., Kawabe, I., 2001. REE(III) adsorption onto Mn dioxide (δ-Mn02) and Fe oxyhydroxide: Ce(III) oxidation by δ-MnO2. Geochem. Cosmochim. Acta 65, 695–703. https://doi.org/10.1016/S0016-7037(00)00578-0.
Ottner, F., Durn, G., Schwaighopfer, B., Tišljar, J., 1999. Clay minerals in paleosols of cretaceous age in Istria, Croatia. Chin. Sci. Bull. 44, 145–151. https://doi.org/10.1360/sb1999-44-S1-145.
Palumbo, B., Bellanca, A., Neri, R., Roe, M.J., 2001. Trace metal partitioning in Fe-Mn nodules from Sicilian soils. Italy. Chem. Geol. 173 https://doi.org/10.1016/S0009-2541(00)00284-9.
Peacor, D.R., Coveney, R.M., Zhao, G., 2000. Authigenic illite and organic matter: the principal hosts of vanadium in the Mecca Quarry Shale at Velpen, Indiana. Clay Clay Miner. 48 https://doi.org/10.1346/CCMN.2000.0480301.
Pédrot, M., Dia, A., Davranche, M., Bouhnik-Le Coz, M., Henin, O., Gruau, G., 2008. Insights into colloid-mediated trace element release at the soil/water interface. J. Colloid Interface Sci. 325 https://doi.org/10.1016/j.jcis.2008.05.019.
Pourret, O., Davranche, M., Gruau, G., Dia, A., 2008. New insights into cerium anomalies inorganic-rich alkaline waters. Chem. Geol. 251 (1–4), 120–127. https://doi.org/10.1016/j.chemgeo.2008.03.002.
Quinn, K.A., Byrne, R.H., Schijf, J., 2006. Sorption of yttrium and rare earth elements by amorphous ferric hydroxide: influence of pH and ionic strength. In: Marine Chemistry. https://doi.org/10.1016/j.marchem.2005.05.011.
Reijonen, I., Metzler, M., Hartikainen, H., 2016. Impact of soil pH and organic matter on the chemical bioavailability of vanadium species: the underlying basis for risk assessment. Environ. Pollut. 210 https://doi.org/10.1016/j.envpol.2015.12.046.
Reimann, C., Fabian, K., Schilling, J., Roberts, D., Englmaier, P., 2015. A strong enrichment of potentially toxic elements (PTEs) in Nord-Trøndelag (central Norway) forest soil. Sci. Total Environ. 536 https://doi.org/10.1016/j.scitotenv.2015.07.032.
Rinklebe, J., Shaheen, S.M., Frohne, T., 2016. Amendment of biochar reduces the release of toxic elements under dynamic redox conditions in a contaminated floodplain soil. Chemosphere 142. https://doi.org/10.1016/j.chemosphere.2015.03.067.

Schmid, S.M., Bernoulli, D., Fügenschuh, B., Matenco, L., Schefer, S., Schuster, R., Tischler, M., Ustaszewski, K., 2008. The Alpine-Carpathian-Dinaridic orogenic system: correlation and evolution of tectonic units. Swiss J. Geosci. 101, 139–183. https://doi.org/10.1007/s00015-008-1247-3.

Schmid, S.M., Fügenschuh, B., Kounov, A., Maţenco, L., Nievergelt, P., Oberhänsli, R., Pleuger, J., Schefer, S., Schuster, R., Tomljenović, B., Ustaszewski, K., van Hinsbergen, D.J.J., 2020. Tectonic units of the Alpine collision zone between Eastern Alps and western Turkey. Gondwana Res. 78, 308–374. https://doi.org/10.1016/j.gr.2019.07.005.

Shaheen, S.M., Rinklebe, J., Frohne, T., White, J.R., DeLaune, R.D., 2016. Redox effects on release kinetics of arsenic, cadmium, cobalt, and vanadium in Wax Lake Deltaic freshwater marsh soils. Chemosphere 150. https://doi.org/10.1016/j.chemosphere.2015.12.043.

Shiller, A.M., 2002. Seasonality of dissolved rare earth elements in the lower Mississippi River. Geochem. Geophys. Geosyst. 3 https://doi.org/10.1029/2002gc000372.

Smedley, P.L., Kinniburgh, D.G., 2017. Molybdenum in natural waters: a review of occurrence, distributions and controls. Appl. Geochem. 84, 387–432. https://doi.org/10.1016/j.apgeochem.2017.05.008.

Tabelin, C.B., Igarashi, T., Villacorte-Tabelin, M., Park, I., Opiso, E.M., Ito, M., Hiroyoshi, N., 2018. Arsenic, selenium, boron, lead, cadmium, copper, and zinc in naturally contaminated rocks: a review of their sources, modes of enrichment, mechanisms of release, and mitigation strategies. Science of the Total Environment. https://doi.org/10.1016/j.scitotenv.2018.07.103.

Tang, J., Johannesson, K.H., 2003. Speciation of rare earth elements in natural terrestrial waters: assessing the role of dissolved organic matter from the modeling approach. Geochem. Cosmochim. Acta 67, 2321–2339. https://doi.org/10.1016/S0016-7037(02)01413-8.

Taylor, S.R., McLennan, S.M., 1985. The continental crust: its composition and evolution. An examination of the geochemical record preserved in sedimentary rocks. Continent. Crust: Composit. Evol. Exam. Geochem. Record Preserv. Sediment. Rocks.

Tessier, A., Campbell, P.G.C., Bisson, M., 1979. Sequential extraction procedure for the speciation of particulate trace metals. Anal. Chem. 51, 844–851. https://doi.org/10.1021/ac50043a017.

Tišljar, J., Velić, I., 1987. The Kimmeridgian tidal-bar calcarenite facies of western Istria (Western Croatia, Jugoslavia). Facies 17. https://doi.org/10.1007/BF02536792.

Tišljar, J., Vlahović, I., Matičec, D., Velić, I., 1995. Platformni facijesi od gornjeg titona do gornjega alba u zapadnoj Istri i prijelaz u tempestitne, klinoformne i rudistne biolititne facijese donjega cenomana u južnoj Istri, ekskurzija B (Platform facies from the Upper Tithonian to Upper Albian in western. In: Vlahović, I., Velić, I. (Eds.), 1st Croatian Geological Congress, Excursion Guide-Book, pp. 67–110. Zagreb, Croatia.

Tišljar, J., Vlahović, I., Velić, I., Matičec, D., Robson, J., 1998. Carbonate facies evolution from the late albian to middle cenomanian in southern istria (Croatia): influence of synsedimentary tectonics and extensive organic carbonate production. Facies 137–152. https://doi.org/10.1007/bf02537361.

Tossell, J.A., 2005. Calculating the partitioning of the isotopes of Mo between oxidic and sulfidic species in aqueous solution. Geochem. Cosmochim. Acta 69. https://doi.org/10.1016/j.gca.2005.01.016.

Velić, I., Matičec, D., Tišljar, J., Vlahović, I., 1995. Opći prikaz geološke građe Istre (A review of the geology of Istria). Lst Croatian Geol. Congress, Excurs. Guidebk. 5–30.

Velić, I., Tišljar, J., Sokač, B., 1989. The variability of thicknesses of the Barremian, Aptian and Albian carbonates as a consequence of changing depositional environments and emersion in Western Istria (Croatia, Yugoslavia). Mem. Soc. Geol. It. 40 (1987), 209–218, 40 (1987). pp. 209–218.

Vlahović, I., Tišljar, J., Velić, I., Matičec, D., 2005. Evolution of the adriatic carbonate platform: palaeogeography, main events and depositional dynamics. Palaeogeogr. Palaeoclimatol. Palaeoecol. 220, 333–360. https://doi.org/10.1016/j.palaeo.2005.01.011.

Wanty, R.B., Goldhaber, M.B., 1992. Thermodynamics and kinetics of reactions involving vanadium in natural systems: accumulation of vanadium in sedimentary rocks. Geochem. Cosmochim. Acta 56, 1471–1483. https://doi.org/10.1016/0016-7037(92)90217-7.

Wei, D., Liu, T., Zhang, Y., Cai, Z., He, J., Xu, C., 2018. Vanadium bioleaching behavior by Acidithiobacillus ferrooxidans from a vanadium-bearing shale. Minerals 8, 1–12. https://doi.org/10.3390/min8010024.

Wei, T., Simko, V., 2017. R Package "Corrplot": Visualization of a Correlation Matrix.

Wei, W., Algeo, T.J., 2020. Elemental proxies for paleosalinity analysis of ancient shales and mudrocks. Geochem. Cosmochim. Acta 287, 341–366. https://doi.org/10.1016/j.gca.2019.06.034.

Zhou, W., Han, G., Liu, M., Song, C., Li, X., 2020. Geochemical distribution characteristics of rare earth elements in different soil profiles in Mun River Basin, Northeast Thailand. Sustainability 12. https://doi.org/10.3390/su12020457.

Paper 2*

***Perković, I.**, Cvetko Tešović, B., Martinuš, M., Škapin, S. D., Vlahović, I., Matešić, D. & Durn, G.(2024): Glauconitisation of an Upper Jurassic palaeosol: Case study of the Zlatni Rt, Istria, Croatia. Catena, 238, 107841.*

*This article was published in Catena, 238, Perković, I., Cvetko Tešović, B., Martinuš, M., Škapin, S. D., Vlahović, I., Matešić, D. & Durn, G., Glauconitisation of an Upper Jurassic palaeosol: Case study of the Zlatni Rt, Istria, Croatia, 107841, Copyright Elsevier (2024).

Catena 238 (2024) 107841

Contents lists available at ScienceDirect

Catena

journal homepage: www.elsevier.com/locate/catena

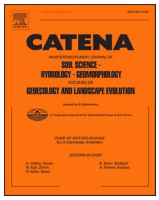

Glauconitisation of an Upper Jurassic palaeosol: Case study of the Zlatni Rt, Istria, Croatia

Ivor Perković [a], Blanka Cvetko Tešović [b], Maja Martinuš [b], Srečo D. Škapin [c], Igor Vlahović [a], Darko Matešić [a], Goran Durn [a,*]

[a] University of Zagreb, Faculty of Mining, Geology and Petroleum Engineering, Pierottijeva 6, HR-10000 Zagreb, Croatia
[b] University of Zagreb, Faculty of Science, Department of Geology, Horvatovac 102a, HR-10000 Zagreb, Croatia
[c] Jožef Stefan Institute, Advanced Materials Department, Jamova cesta 39, SI-1000 Ljubljana, Slovenia

ARTICLE INFO

Keywords:
Glauconite
Bacterial clay authigenesis
Oscillating transgression
Upper Jurassic
Istria

ABSTRACT

Glauconite formation is generally perceived as a process occurring in deep-marine environments, but in the last few decades its formation in shallow-marine environments is progressively more recognised and utilized for palaeoenvironmental reconstructions. One such example is the lower Kimmeridgian to upper Tithonian Zlatni Rt palaeosol, which is especially unique since the glauconite occurrence is hosted within the palaeosol material. Micromorphological, mineralogical, and chemical characterisation of the palaeosol was followed by the detailed analysis and description of glauconite using SEM-EDS, XRPD and FTIR. In addition, lithofacies and micropalaeontological analyses have been carried out on the carbonate succession under- and overlying the palaeosol in order to better understand the stratigraphic framework. The palaeosol formed in hydromorphic conditions, in contact with brackish to marine porewater, and is composed of mixed-layer illite–smectite, illite, kaolinite, vermiculite, pyrite, marcasite and titanium oxides. The glauconite was formed after the formation of the palaeosol, predominantly through fixation of potassium and iron into illite and mixed–layer illite–smectite, while part of the glauconite formed authigenically, with evidence for microbial influence. The glauconite is present in a more oxidised and more reduced form, which alternate together with pyrite in veins, indicating fluctuations in the redox potential. This can be connected to the variations in the supply of organic matter and sea-level oscillations during the initial stages of the transgression. Glauconite formation was locally followed by the formation of transgressive breccias and a complete drowning of the area. During this phase lagoonal Kirmenjak limestone was deposited throughout the area, while in the palaeosol coarse pyrite crystals precipitated. Presented study documents a unique glauconite occurrence and proposes that it can be successfully used for the detailed palaeoenvironmental reconstruction of the initial flooding of subaerially exposed terrains.

1. Introduction

The Istrian peninsula, located in the northwestern part of the Adriatic Sea, is built up of the thick succession of Middle Jurassic to Eocene deposits divided into four depositional megasequences (Velić et al., 1995). The first two megasequences are separated by the Upper Jurassic unconformity of significant stratigraphic hiatus (Oxfordian/early Kimmeridgian to late Tithonian; Fig. 1), marked by the formation of bauxites (Šinkovec, 1974; Durn et al., 2003), palaeosols and regression breccias (Velić and Tišljar, 1988), which illustrate the variability of the subaerially exposed carbonate terrain. This study focuses on one of such palaeosols, cropping out at the Zlatni Rt cape near Rovinj, which is very well preserved and specific due to the presence of glauconite with a complex mode of formation. The most accepted theory of glauconite formation is through the potassium uptake by authigenic iron-rich smectites, which precipitate in semi-confined micromilleus of faecal pellets and carbonate bioclasts (Odin and Matter, 1981; Meunier and El Albani, 2007; Baldermann et al., 2015; Banerjee et al., 2016, 2020), although several other theories have been proposed in the past. The glauconitisation takes place at temperatures below 15 °C and low sedimentation rates in environments such as the shelf (Odin and Matter, 1981; Baioumy and Boulis, 2012; Bansal et al., 2018; López-Quirós et al.,

* Corresponding author.
E-mail addresses: ivor.perkovic@rgn.unizg.hr (I. Perković), bcvetko@geol.pmf.unizg.hr (B. Cvetko Tešović), maja.martinus@geol.pmf.unizg.hr (M. Martinuš), sreco.skapin@ijs.si (S.D. Škapin), igor.vlahovic@rgn.unizg.hr (I. Vlahović), darko.matesic@rgn.unizg.hr (D. Matešić), goran.durn@rgn.unizg.hr (G. Durn).

https://doi.org/10.1016/j.catena.2024.107841
Received 27 September 2023; Received in revised form 17 January 2024; Accepted 19 January 2024

2020; Baldermann et al., 2022; Giresse, 2022) or deep-marine environments (Giresse and Wiewióra, 2001; Baldermann et al., 2013), but glauconite can be formed in other environments as well. In the last two decades, glauconite formation in shallow-marine environments such as lagoonal to estuarine environments (El Albani et al., 2005; Huggett and Cuadros, 2005; Banerjee et al., 2012; Huggett et al., 2017), as well as in lacustrine to pedogenic environments (Huggett and Cuadros, 2010) has been more and more recognised, challenging the mainly accepted view on the environment in which glauconite forms. One of additional examples is the Zlatni Rt palaeosol, which represents one of the few cases where glauconite formed from or within a palaeosol in newly established shallow-marine environment. The Zlatni Rt palaeosol has not been studied in the past, because the focus was on its underlying and overlying deposits (Vlahović et al., 2003). As such, this study will also aim to reconstruct the development of the Zlatni Rt palaeosol and the concurrent evolution of its environment based on a detailed micropedological, mineralogical and geochemical dataset. To provide a stratigraphic framework and to better understand the evolution of the environments that preceded and followed the formation of the Zlatni Rt palaeosol, lithofacial and micropalaeontological analyses have been

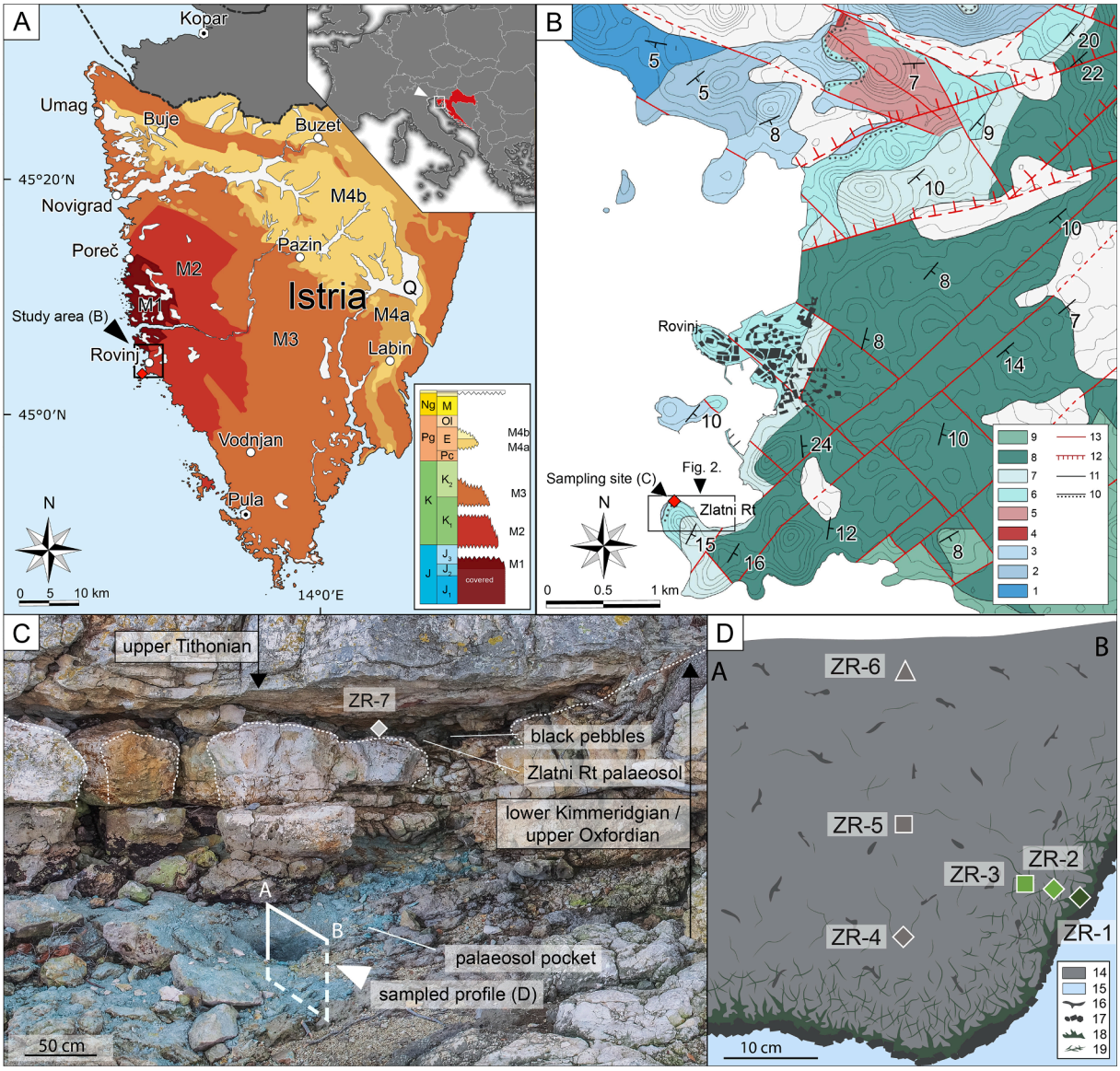

Fig. 1. Location of study area and illustration of the Zlatni Rt-1 outcrop. (A) Map showing large-scale units separated by regional unconformities in Istria, modified after Velić et al. (1995) together with the inset showing location of Istria; Legend: M1 – 1st Megasequence (lower Bathonian–lower Kimmeridgian); M2 – 2nd Megasequence (upper Tithonian–lower/upper Aptian); M3 – 3rd Megasequence (lower/upper Albian–upper Santonian); M4a – Carbonate deposits of the 4th Megasequence (Lower–Middle Eocene); M4b – Clastic deposits of the 4th Megasequence (Middle–Upper Eocene); Q – Quaternary deposits. (B) Geology of the studied area modified after Matičec et al. (2015) and the data provided by the GEO-5 company: Legend: 1 – Monsena unit (lower Bathonian–Callovian; 2 – Lim unit (Oxfordian–Kimmeridgian); 3 – Muča unit (Oxfordian–Kimmeridgian); 4 – Bauxite (uncovered); 5 – Bauxite (covered); 6 – Kirmenjak unit (upper Tithonian); 7 – Zlatni Rt unit (upper Tithonian); 8 – Rovinj unit (lower Berriasian); 9 – Materada unit (upper Berriasian–lower Valanginian); 10 – Unconformity; 11 – Normal geological boundary; 12 – Reverse faults; 13 – Normal faults. (C) Photograph of the studied palaeosol outcrop Zlatni Rt-1, where the palaeosol can be seen as a horizon embedding the black pebbles and infilling the karstified features in the bedrock, in which a large palaeosol pocket has been accumulated. On this photograph the location of the ZR-7 sample has been indicated, together with the main sampling profile (A–B; presented on Fig. 1D) located within the palaeosol pocket. (D) Illustration of the sampled profile (A–B) in the palaeosol pocket, with indicated sampling sites of samples ZR-1 to ZR-6. Legend: 14 – palaeosol; 15 – lower Kimmeridgian bedrock; 16 – reworked pyrite rhizoconcretions; 17 – diagenetic pyrite crusts developed on the bedrock; 18 – glauconite rich zone; 19 – glauconite vein rich transitional zone.

carried out on samples collected from the carbonate rocks of the Zlatni Rt profile.

The detailed study of the Zlatni Rt palaeosol together with its underlying and overlying deposits should significantly improve the present understanding of the subaerially exposed carbonate landscape and its subsequent drowning on this part of the Adriatic Carbonate Platform (AdCP), while at the same time providing new data about the palaeosol itself which was not yet studied. This study also aims to provide valuable new knowledge on the formation of glauconite in shallow-marine environments elsewhere, based on the detailed mineralogical and geochemical characterisation of this unique instance of glauconite formation.

2. Geological setting

Istria is the largest Croatian peninsula, located in its northwesternmost part, built of carbonate and clastic deposits ranging in age from Middle Jurassic to Eocene (Fig. 1A). Relatively small NE part of Istria (Ćićarija Mt. and topmost part of the Učka Mt.) represent a part of the Dinaridic mountain belt, while western, central and southern parts of Istria are tectonically much less disturbed and considered a relatively undeformed part of the Adria Microplate (Schmid et al., 2008). Western, central and southern Istria is composed of the gentle Western Istrian Anticline built of lower Bathonian to Lower Eocene carbonates and northeast and east of it, by the Pazin Flysch Basin filled with Middle to Upper Eocene turbidite deposits (Velić et al., 1995; Vlahović et al., 2023, and references therein). Mesozoic carbonates in Istria were formed on the NW part of the intra-Tethyan Adriatic Carbonate Platform developed on the Adria Microplate basement (Vlahović et al., 2005 and references therein). The entire succession of Istrian deposits is divided into four depositional megasequences, separated by long-lasting regional unconformities (Velić et al., 1995a).

The evolution of the studied Upper Jurassic succession comprising the Zlatni Rt palaeosol should be discussed within the geological framework of the late Oxfordian–Kimmeridgian–late Tithonian events recorded along the NE part of the Adria Microplate. These events indicate the first compressional event after a very long period of extensional tectonics ending in the Early Jurassic and a Middle Jurassic period without any significant tectonic activity (Vlahović et al., 2005 and references therein). These events are a consequence of the extensive gentle folds formed as the far field expression of the transition from intra-oceanic to continental obduction of ophiolites, which occurred along the NE Adria Microplate active margin (Picotti and Cobianchi, 2019 and references therein). As a result, for a few million years during the middle part of the Late Jurassic very different environments were established on the previously more or less uniform shallow-marine area of the AdCP (Vlahović et al., 2001) – some areas remained shallow-marine, while others were either temporarily drowned in the form of elongated troughs influenced by the open sea (see Vitzthum et al., 2022 and references therein) or temporarily subaerially exposed (Vlahović et al., 2003).

The best example of a very distinct Upper Jurassic unconformity showing a long-lasting stratigraphic hiatus is exposed in the NW part of the AdCP, within the Western Istrian Anticline, at Zlatni Rt locality south of Rovinj (Fig. 1A, B). The Zlatni Rt palaeosol was formed during the early Kimmeridgian to late Tithonian terrestrial phase, which separates the first, lower Bathonian to lower Kimmeridgian M1 Megasequence and second, upper Tithonian to lower/upper Aptian M2 Megasequence. More precisely, it is situated between the Oxfordian to lower Kimmeridgian Muča and Lim units of the M1 (Fig. 1B), and upper Tithonian Kirmenjak unit of the M2. The Muča unit comprises three lithofacies types, all indicating the high-energy environments (Velić and Tišljar, 1988, and references therein). These are the peloidal and skeletal wackestones, ooidal grainstones and ooidal and bioclastic grainstones to rudstones. The Muča unit appears as lenses within the Lim unit composed of peloidal packstones deposited in a lagoonal environment (Velić and Tišljar, 1988, and references therein). Locally overlying Rovinj breccias (Velić and Tišljar, 1988) have formed during the regression that preceded the subaerial exposure and are composed of clasts of these two units. The long-lasting phase of subaerial exposure that followed is locally marked with bauxites (Šinkovec, 1974; Velić and Tišljar, 1988) showing an erosional contact with the Lim and Muča units or the Rovinj breccias (Velić and Tišljar, 1988). Besides the formation of bauxites, the phase of subaerial exposure is also recorded in the form of unconformity between the lower Kimmerdigian Lim and Muča units and the upper Tithonian Kirmenjak unit (Vlahović et al., 2003), in places marked by the well-developed palaeosols, such as the Zlatni Rt palaeosol (Velić and Tišljar, 1988; Vlahović et al., 2003) discussed in the present study. The end of the subaerial exposure phase is marked by the oscillating transgression, best recorded on top of the Rovinj bauxite (Šinkovec, 1974; Velić and Tišljar, 1988), after which the typical Kirmenjak unit was deposited, composed of the cyclical alternation of mudstones, mudstones with indications of subaerial exposure and lenses or intercalations of black pebble breccias (Tišljar, 1986; Velić and Tišljar, 1988).

3. Material and methods

3.1. Study area and sampling sites

Study sites are located on the Zlatni Rt Cape south of the city of Rovinj in the western Istria (Fig. 1A, B). The same palaeosol with its underlying and overlying deposits was studied at three outcrops enabling better insight in the lateral variability of the depositional environments on the local scale. From E to W the succession was studied at Zlatni Rt-1, Zlatni Rt-2 and Zlatni Rt-3 profiles (Fig. 2). The Zlatni Rt-1 section is the most complete and therefore used as a reference section, since the palaeosol material is best preserved on this outcrop.

3.2. Methods

3.2.1. Sedimentological and micropalaeontological analyses

Lithology and sedimentology of the three Zlatni Rt sections were studied and described in the field at cm-scale. A total of 37 samples were collected and prepared for thin section analyses (Fig. 2). Sedimentological and micropalaeontological analyses are based on thin-sections study following Flügel (2004), while benthic foraminifera and dasyclad algae were determined based on the observation of diagnostic characteristics provided by Velić (2007, and references therein).

3.2.2. Micromorphological and petrographical analyses of palaeosol samples

The main portion of this study is based on detailed analyses of seven palaeosol samples. One sample was collected from the glauconite-rich zone (ZR-1; Fig. 1D), together with two samples (ZR-2 and ZR-3; Fig. 1D) from the transitional zone between the glauconite and the palaeosol pocket (5G 2.5/2, 5G 4/2 and 5G 5/2 in Munsell hue respectively). Sample ZR-2 represents the section of the transitional zone which is enriched in glauconite and is close to the glauconite-rich zone, while the sample ZR-3 represents the section of the transitional zone in which the glauconite is scarcer and which is more distal from the glauconite-rich zone. Three samples (ZR-4, ZR-5 and ZR-6; Fig. 1D) were selected from the palaeosol pocket (5GY 6/1 in Munsell hue), from its upper, middle and lower portion. Only one sample (ZR-7; Fig. 1C) was collected from the main unconformity horizon (5GY 6/1 in Munsell hue), since it was particularly difficult to obtain a sufficient amount of material as it was washed out during its exposure on the outcrop. This sample was weathered on the outcrop, making most of the obtained data of diminished quality compared to the other samples, but it was analysed nonetheless to obtain some clue about the composition of this section of the palaeosol. Certain portions from samples ZR-1, ZR-2, ZR-3 and ZR-5 were suitable for preparation of thin sections, while samples

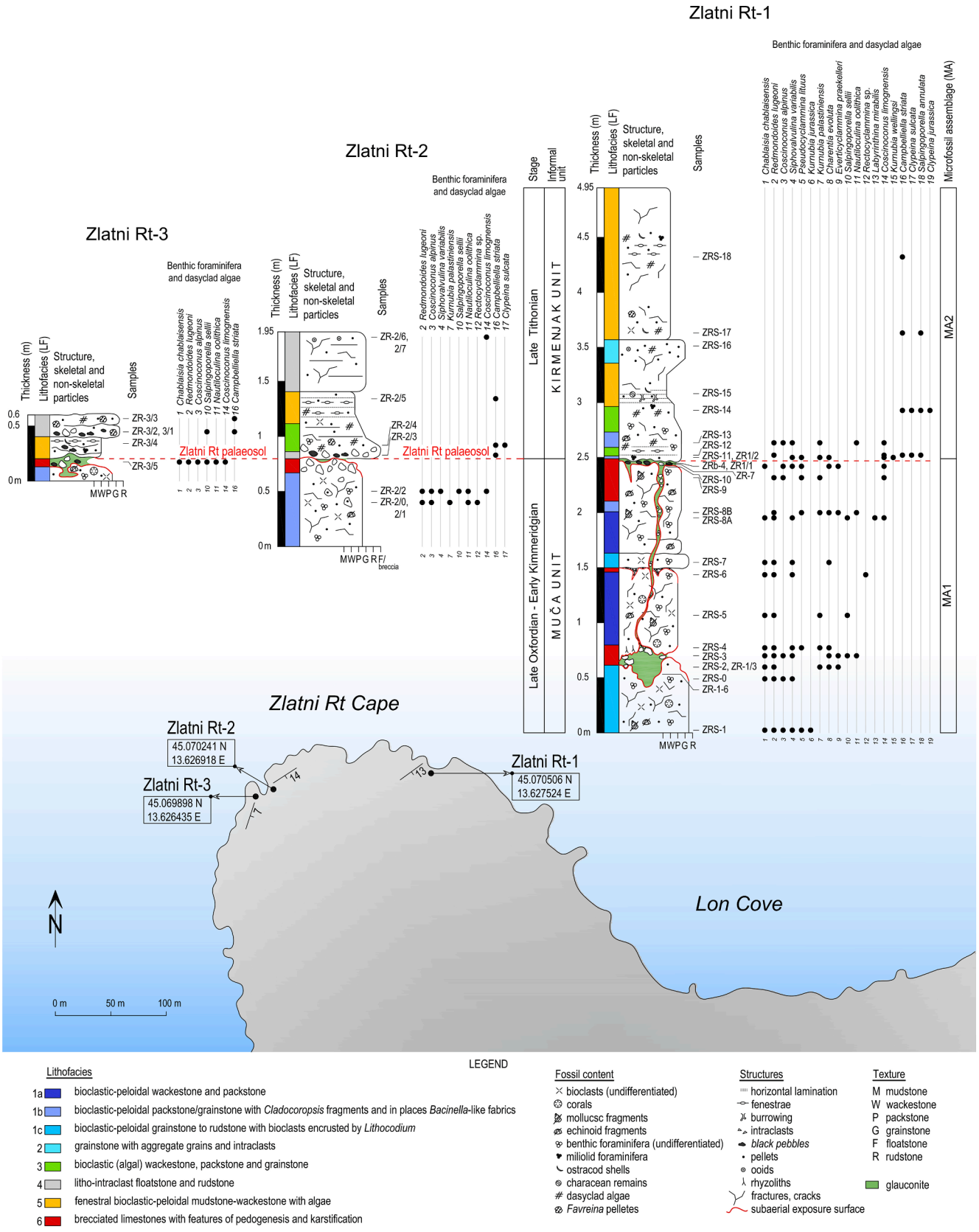

Fig. 2. Illustration of three Zlatni Rt sections showing their geographic position, structures, textures, microfossil content and lithofacies.

ZR-4, ZR-6 and ZR-7 were unsuitable, as they would easily fracture or dissipate during the grinding stage. These four samples were cut in centimetre-thick slabs which were adhered to the glass slides. After the epoxy has cured, samples were ground using a ceramic saw without the water coolant, since the clay would disaggregate upon contact with water. After the grinding stage, they were polished until the thickness of 30 μm was reached, using the 500 grit corundum abrasive powder, followed with the polishing with the 1000 grit corundum abrasive powder, while using mineral oil as a solvent during both polishing stages. Micromorphological and petrographical analyses were performed according to guidelines outlined in Stoops (2021), using the OPTIKA B-1000 series polarizing microscope equipped with the OPTIKA C-P6 FL camera and OPTIKA PROVIEW software.

3.2.3. X-ray powder diffraction (XRPD)

For the XRPD analysis, a portion of each bulk sample was gently crushed and sieved through a 0.5 mm sieve, after which 2 mL of sieved material was separated and ground with 7 mL of isopropyl alcohol using the McCrone mill, with the grinding time of 15 min. The slurry was collected on watch glass and left to air-dry. The dried samples were gently disaggregated using the agate pestle and mortar, and side loaded using a roughened glass slide. This was done to produce a randomly oriented sample with uniform grain size. The randomly oriented sample is mandatory for proper polytype determination of phyllosilicates while the random orientation and uniform grain size is required for proper Rietveld refinement. The Rietveld refinement was performed in Profex v. 5.0.1 software (Doebelin and Kleeberg, 2015), using the default structural files already present in the software and structural files from the crystallography open database (Graulis et al., 2009). Polytype determination is a useful tool in the area of clay mineralogy, as the formation of different polytypes of the same phyllosilicate is linked to different environments, which makes the identification of different polytypes an useful tool for deciphering the formational and depositional history of the studied material. All seven bulk samples were analysed using X-ray powder diffraction on Malvern Panalytical Empyrean diffractometer using 0.5° divergent and anti-scatter slits, 0.03 and 0.04 rad soller slits, Cu–Kα radiation, 45 kV, 40 mA and a PIXcel 3D detector. The measurement time per step was 78.8 s with the step size of 0.0130°2θ. The XRD patterns from the bulk samples were used for the quantitative assessment of bulk mineralogy of the palaeosol samples and polytype determination of present clay minerals, which was done according to the data from Moore and Reynolds (1997). For the detailed insight into the mineralogy of clay minerals, the clay fraction was separated from ZR-2, ZR-3 and ZR-5 samples. XRD patterns from the clay fraction were recorded on both non-oriented and oriented samples in the same conditions as the bulk samples. For the preparation of oriented samples, the suspension of clay fraction was pipetted onto glass slides which were left to air-dry. XRD patterns from the oriented samples were measured after air drying (AD), saturation with ethylene glycol (EG), dimethyl sulphoxide (DMSO) as well as after heating to 350 and 600 °C. The clay minerals were identified using the guidelines from Moore and Reynolds (1997) and Środoń (2006).

3.2.4. Fourier transform infrared spectroscopy (FTIR)

For the additional analysis of clay minerals, the infrared spectra of extracted clay fractions and ground bulk samples were recorded on the Bruker alpha II FTIR spectrometer. The samples were prepared as pressed KBr pellets with 1–3 mg of sample mixed with 200 mg of KBr. Samples were recorded in transmission mode, with FTIR spectra recorded between 400 and 4000 cm^{-1} which were later analysed in the OPUS Version 8.7 software. The absorption bands were classified and assigned to a specific mineral phase and vibrational mode where possible, using the data from Slonimskaya et al. (1986), Andersen and Brečević (1991), Madejova et al. (2001) and Zviagina et al. (2020).

3.2.5. Scanning electron microscopy with energy dispersive spectrometry (SEM-EDS)

Samples ZR-2, ZR-3 and ZR-4 were selected for the SEM-EDS analysis. Samples were cut into 1 cm^3 cubes, and polished with 800, 1000 and 2000 grit corundum abrasive powders while using mineral oil as a lubricant. Detailed microstructural analysis was carried out using a field emission scanning electron microscope FE-SEM Ultra plus (Carl Zeiss, Germany) equipped with an energy dispersive spectrometer (EDS, Inca 400, Oxford Instruments), which was used to obtain the elemental composition of selected spots on clay minerals. The EDS analysis was performed employing accelerating voltage of 18 kV and working distance of 6.0 mm. For quantitative elemental analysis an acquisition time of 60 s per spectra was applied. Prior to SEM-EDS examinations, the samples were coated with a thin carbon layer providing an electrically conductive surface. SEM-EDS data was primarily used for the analysis of clay minerals and their compositions. The EDS data was subsequently transformed into structural formulas on the basis of $O_{10}(OH)_2$ (per half formula unit), which can be found in Supplementary tables 1, 2 and 3. Al was assigned to the tetrahedral position where needed together with Ti and Si, while Fe, Mg and rest of Al were assigned to the octahedral position, with K and Na assigned to the interlayer space. The obtained EDS data from the used instrument does not provide the amount of ferric and ferrous iron, but only that of total iron, which complicates the calculation of structural formulas. To calculate the structural formulas, it was assumed that the ratio between ferrous and ferric iron was 1:1, as to provide the least error, since glauconite contains iron in both valence states.

3.2.6. X-ray fluorescence (XRF)

All seven samples were analysed using Hitachi X-MET8000 handheld XRF. Five consecutive measurements with the duration of 40 s each were performed and averaged. This was used for the determination of major oxides and trace elements. As the detection limit and accuracy of this instrument is not ideal for most trace elements, two samples (ZR-1 and ZR-5) were selected and sent for additional geochemical measurements to the commercial ACME Analytical Laboratory, Canada, where rare earth elements and certain refractory elements were measured using ICP mass spectrometry following the lithium metaborate/tetraborate fusion and nitric acid digestion. REEs were normalized using the values of Post-Archean Australian Shale (PAAS) according to the values from Taylor and McLennan (1985).

4. Results

4.1. Lithostratigraphy and biostratigraphy

4.1.1. Description of outcrops

The three studied sections are exposed along the northern coast of the Zlatni Rt cape (Fig. 2). They correlate well and each section is divided on two parts by a palaeosol (named the Zlatni Rt palaeosol in this paper) marking regional unconformity. Lower parts of the sections belong to the Muča unit and upper parts to the Kirmenjak unit (Fig. 2).

The Zlatni Rt-1 section is five metres thick with three subaerial exposure surfaces in its lower part. The first surface is present at 0.6 m of the section, the second, very weakly expressed at 1.5 m, and the third marked as the Zlatni Rt palaeosol at 2.5 m of the section (Fig. 2). The lowest subaerial exposure surface present at 0.6 m is marked by irregular relief with brecciated material and grey clay filling the depressions and cavities. Here, a 0.5 m deep lenticular karstic cavity filled with palaeosol material (referred to as palaeosol pocket in the paper) and glauconite is present. Glauconite is found together with several millimetre-thick pyrite crusts which envelop the bedrock and carbonate clasts within the palaeosol pocket (Fig. 1D). Here it forms a centimetre-thick glauconite-rich zone, which gradually transitions through the network of glauconite veinlets (transitional zone) into the grey clay of the palaeosol pocket which is mostly devoid of glauconite (Fig. 1D) and

contains numerous slickensides. This palaeosol pocket with glauconite is the most interesting part of the Zlatni Rt-1 section and represents the focus of the detailed mineralogical and geochemical analyses for this study. The main subaerial exposure surface – the Zlatni Rt palaeosol at 2.5 m of the section – is characterised by irregular relief with 5–30 cm thick horizon of bedrock fragments and abundant black pebbles embedded within the palaeosol material (Fig. 1C). The part of the section between the Zlatni Rt palaeosol and the lowest subaerial exposure surface with palaeosol pocket is intersected by vertical to subvertical fractures with relics of lithoclasts and black pebbles, i.e., dissolution channels (Fig. 1C). Similar palaeosol material (grey clay with glauconite) present in the palaeosol pocket is also found both in the dissolution channels and the Zlatni Rt palaeosol, together with weathered glauconite and pyrite crusts on their sides. It is important to note that such dissolution channels are not present in the Kirmenjak unit immediately overlying the Zlatni Rt palaeosol. The same Zlatni Rt palaeosol horizon is found on the nearby Zlatni Rt-2 and Zlatni Rt-3 outcrops, which together with the biostratigraphic data confirmed it as the regional unconformity (Fig. 2).

The Zlatni Rt-2 and Zlatni Rt-3 sections are 2 and 0.5 m thick, respectively. On both outcrops the Zlatni Rt palaeosol is very weathered, making it unsuitable for the detailed geochemical and mineralogical study. Consequently, only sedimentological and micropalaeontological studies were carried out on these two sections to document the lateral

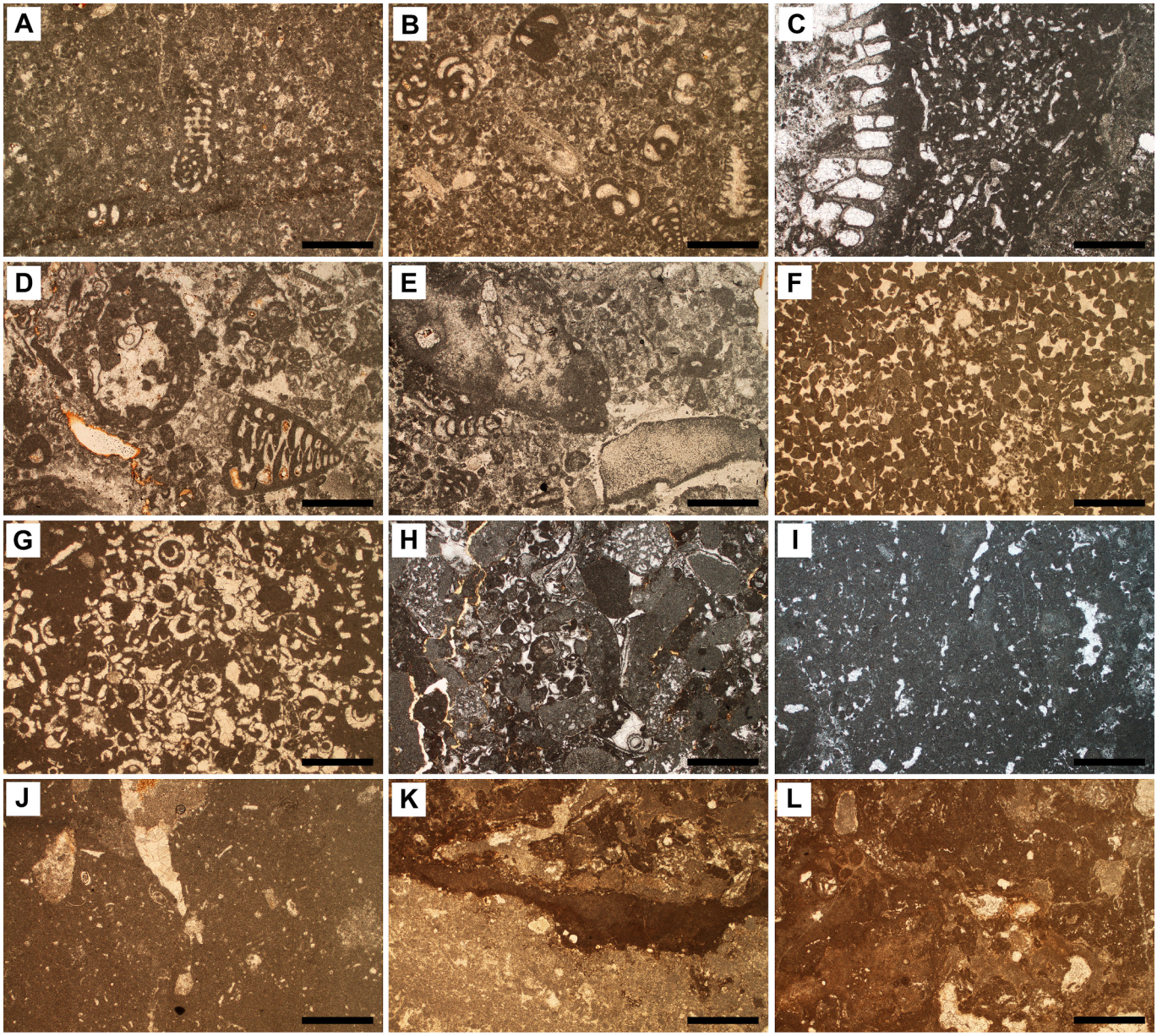

Fig. 3. Lithofacies (LF) of the Zlatni Rt sections. **(A)** LF1a: Bioclastic-peloidal wackestone–packstone with *Labyrinthina mirabilis* (sample ZRS-8a). **(B)** LF1b: Bioclastic-peloidal packstone–grainstone with *Charentia evoluta*, *Siphovavulina variabilis*, *Redmondoides lugeoni* and *Coscinoconus limognensis* (sample ZRS-8b). **(C)** LF1b: Bioclastic-peloidal packstone–grainstone with coral fragment encrusted by *Lithocodium–Bacinella*-like fabrics (sample ZR-3/5). **(D)** LF1c: Bioclastic-peloidal grainstone–rudstone with unidentified agglutinated foraminifera and *Redmondoides lugeoni* (sample ZRS-2). **(E)** LF1c: Bioclastic-peloidal grainstone–rudstone with micritized fragments of *Cladocoropsis* encrusted by *Troglotella incrustans* (sample ZRS-0). **(F)** LF2: Grainstone with aggregate grains, peloids and small intraclasts (sample ZRS-16). **(G)** LF3: Bioclastic (algal) wackestone–packstone with *Campbelliella striata* and *Salpingoporella annulata* (sample ZRS-14). **(H)** LF4: Litho-intraclastic floatstone–rudstone with *Campbelliella striata* (sample ZR2/3). **(I)** LF5: Fenestral bioclastic-peloidal wackestone (sample ZR3/4). **(J)** LF5: Fenestral bioclastic-peloidal mudstone–wackestone with ostracods and miliolids (sample ZRS-18). **(K)** LF6: Subaerially exposed packstone–grainstone with brownish soil crust (calcrete) (sample ZRS-4). **(L)** LF6: Calcrete with rhizoconcretions, clotted fabrics with peloid accumulations and alveolar-septal fabrics (sample ZRS-4). All scale bars = 1 mm.

variability of the unconformity in the studied area (Fig. 2). On both outcrops the karstification is not that deep as on the main outcrop, ranging from 30 to 50 cm into underlying rocks, with a 10–20 cm thick layer of bedrock fragments and black pebbles intermixed with a palaeosol representing the unconformity.

4.1.2. Lithostratigraphy

Observation of macro- and microscopic lithological features and fossil assemblages enabled recognition of six lithofacies (LF1–LF6) in Zlatni Rt sections (Fig. 2; Supplementary Table 1). The lower parts of the sections (the Muča unit) comprise bioclastic-peloidal limestones with abundant bioclasts and various microencrusters (LF1; Fig. 3A–E). Benthic foraminifera are very diverse and constitute a major part of LF1, whereas different bioclasts (fragments of echinoderms, *Cladocoropsis*, bivalves, gastropods and corals) are often micritized and encrusted by *Lithocodium* and *Bacinella*-like fabrics. Three LF1 subtypes are discerned based on the textural type reflecting the water energy (Fig. 2, 3A–E). The inferred depositional environments were part of the moderate- to high-energy shallow carbonate platform interior. Limestones with features of pedogenesis and karstification are common in the Muča unit, comprising LF6 and indicating prolonged terrestrial conditions (Fig. 3K, L).

The upper parts of all sections belonging to the Kirmenjak unit significantly differ from the Muča unit: fenestral bioclastic-peloidal mudstone–wackestone prevails (LF5; Fig. 3I, J) with the occurrence of the litho-intraclastic floatstone and rudstone (LF4; Fig. 3H) and bioclastic limestones with dasyclad algae (LF3; Fig. 3G). Aggregate grains grainstone is in places present within this unit (LF2; Fig. 3F). Important component of all lithofacies of the Kirmenjak unit is the occurrence of dasyclad algae, which are in places abundant (Figs. 2, 3G). Described lithofacies association indicates deposition mostly in low to moderate water energy restricted shallow subtidal environments (LF3) or very shallow subtidal and intertidal with influence of brackish/fresh-water environments (LF5). In this unit, occasionally moderate- to high-energy conditions were established (LF2, LF4).

4.1.3. Biostratigraphy

Biostratigraphy of Upper Jurassic carbonate deposits of the AdCP has been the focus of numerous scientific studies, but the first official zonation based exclusively on Mesozoic benthic foraminifera that can be used platform-wide was established by Velić (2007 and reference therein). Late Jurassic biozonation is based on microfossils, mostly benthic foraminifera and calcareous algae. The investigated Zlatni Rt carbonate sequence is characterised by microfossil assemblages with rich benthic foraminifera and, to a lesser extent, calcareous algae (Figs. 2, 3). Within the studied sections two microfossil assemblages can be recognised.

Microfossil assemblage 1 (MA1) corresponds to the LF1 (Fig. 3A–E) in deposits beneath the studied Zlatni Rt palaeosol horizon. Among the foraminifera in the Upper Jurassic carbonates of the AdCP, species of the genus *Kurnubia* are the most important index taxa (Velić, 2007). Besides *Kurnubia jurassica*, *K. palastiniensis* and *K. wellingsi*, in the MA1 other biostratigraphically significant taxa are also present (Supplementary Table 1). The highly diversified foraminifera association of MA1 indicates Late Jurassic age – Oxfordian and early Kimmeridgian, confirming that they belong to the informal Muča unit. From a biostratigraphic point of view MA1, as an assemblage characteristic for Jurassic carbonate deposits of Istria, best corresponds to the *Coscinoconus alpinus and Chablaisia chablaisensis* abundance zone (Velić and Tišljar, 1988; Vlahović et al., 2003), but also corresponds to the biozonation data for the entire AdCP by Velić (2007, see p. 28). Chronostratigraphically it would correspond to the middle part of the *Salpingoporella selli* assemblage zone after Velić and Tišljar (1988).

Microfossil assemblage 2 (MA2) corresponds to the LF2–LF5 (Fig. 3F–J) from the upper parts of sections with the first microfossil assemblage of the overlying M2 Megasequence (Fig. 1A) which is characterised by extremely rare benthic foraminifera (mostly small miliolids). Calcareous algae are more frequent to locally abundant, especially in LF3 (Fig. 3G), represented by *Campbelliella striata*, *Clypeina jurassica*, *C. sulcata* and *Salpingoporella annulata. Favreina* cf. *salevensis* cross-sections are also identified. Assemblage MA2 assigns the Kirmenjak unit to the *Campbelliella striata* taxon range zone, chronostratigraphically corresponding to the late Tithonian.

4.2. Micromorphology, mineralogy and geochemistry of the Zlatni Rt palaeosol and the palaeosol pocket

4.2.1. Micromorphology

To properly understand the paragenetic relationship between present mineral phases and glauconite, a detailed micromorphological characterisation of palaeosol samples was performed. The palaeosol is composed of 1–5 mm peds (i.e. aggregates of soil particles), separated with planes, fractures, striated/illuviated clay or glauconite veinlets. The b-fabric is mostly cross-striated to random striated (Fig. 4A, B), with sporadic granostriation around pedoclasts (Fig. 4A) and porostriation around ped boundaries (Fig. 4A). Pedofeatures are abundant, mostly comprising pedoclasts (Fig. 4A), reworked clay coatings (Fig. 4A, C), pyrite root replacements (Fig. 4A), clay pisoids (Fig. 4D) and pyrite crystals (Fig. 4A, B, D–F). The groundmass is predominantly cryptocrystalline, which hinders the mineralogical determination of present minerals, except for the glauconitic mineral which can be distinguished based on its colour and birefringence in some instances (Fig. 4A–F). The observed occurrences of glauconite are restricted to the contact zone between the carbonate bedrock and clay as well as in the transitional zone, where it appears in two types which differ in morphology and colour. The first type is dark to bluish-green which appears very dense and fine-grained (Fig. 4F), compared to the second type which is completely translucent, light green to yellowish-green and coarser-grained (Fig. 4F).The colour of these two types of glauconite indicates that the first type contains more total iron due to its stronger hue and more ferrous iron due to its bluish-green hue, and that the second type contains less total iron and more ferric iron than the dark-green type, due to its lighter green to yellowish-green hue. It should be clarified that based on the methods available to us, the exact proportions of both ferrous and ferric iron in these two types of glauconite can only be assumed based on their optical appearance. Both glauconites primarily appear in a network of veinlets, surrounded locally with a dissolution halo (Fig. 4A–E). They display both sharp (Fig. 4B, C, E) and gradual contact with the groundmass (Fig. 4F). First type of glauconite can be gradually replaced with the second type, which is locally also gradually replaced with the first type of glauconite. In the ZR-1 sample, both types of glauconite completely replace certain parts of the groundmass (Fig. 4F). Both glauconite types display a paragenetic relationship with iron sulphides, which in places appear as veinlets and crystal clusters within the glauconitised areas (Fig. 4C). Besides the iron sulphides related to glauconite, several different types of pyrite were distinguished, based on their morphology and relationship with other microstructural features. Pyrite in the Zlatni Rt palaeosol can appear as interstitial 10–50 μm large euhedral crystals with biogenic features (Fig. 4A) and as large euhedral crystals which overprint previously formed micromorphological features and glauconite (Fig. 4B, D, E). The large euhedral crystals correspond to the macroscopically observed pyrite encrusting the carbonate bedrock and grains.

4.2.2. Mineralogy

XRPD analysis of bulk samples has shown that the Zlatni Rt palaeosol shows a range of composition, differing mostly in clay mineralogy. Palaeosol samples ZR-4, ZR-5 and ZR-6 are primarily composed of $1M_d$ illite, $2M_1$ illite, mixed-layer illite-smectite and secondarily from well- and poorly-crystallised kaolinite, pyrite, marcasite, anatase and rutile (Table 1). Palaeosol sample ZR-7 consists of illite, calcite and minor amounts of halite, gypsum and glauconite (Table 1, Supplementary Fig. 1). Due to the very small amount of ZR-7 sample, the clay fraction

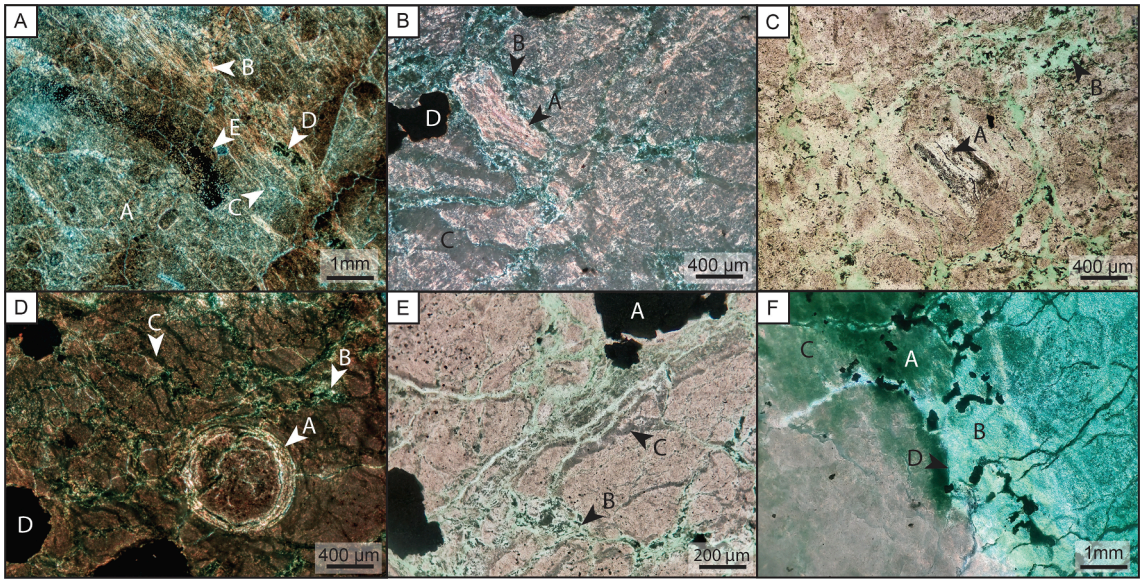

Fig. 4. Photomicrographs of the Zlatni Rt palaeosol. **(A)** Visible granostriation around pedoclasts, random striation, cross-striation and porostriation of the b-fabric (A and B) coupled with glauconite veinlets (C) visible throughout the photomicrograph, as well as the glauconite (D) and pyrite (E) root replacements in the centre of the photomicrograph; sample ZR-5 (XPL). **(B)** Reworked clay coating (A) enveloped with a network of glauconite veinlets (B), surrounded with a dissolution halo (C) in the lower left of the photomicrograph. Cross- and random striation of the b-fabric is also visible, together with large pyrite crystals (D); sample ZR-2 (XPL). **(C)** Reworked clay coating (A) and a network of glauconite and pyrite veins (B); sample ZR-2 (PPL). **(D)** Clay pisoid (A), a network of glauconite veins (B) with a visible dissolution halo (C), and large pyrite crystals (D); sample ZR-3 (XPL). **(E)** Large pyrite crystals (A) together with glauconite and pyrite veins (B) surrounded with a dissolution halo (C); sample ZR-2 (PPL). **(F)** Completely glauconitized groundmass composed of two types of glauconite (reduced – A and oxidised – B), showing a gradual replacement of the groundmass (C), while displaying both sharp (D) and gradual contacts (E) between them; sample ZR-1 (PPL).

Table 1
Quantitative mineral composition of bulk samples obtained with the Rietveld refinement method.

	Gl	Ill		Ill-sm	Kln		Py	Mrc	Rt	Ant	Hal	Clc	Gy
	($1M_{tv}$)	($1M_d$)	($2M_1$)		(P)	(C)							
ZR-1	38.4 %	48.1 %	6.4 %				5.3 %	1.2 %		0.6 %			
ZR-2	40.9 %	55.3 %	2.3 %				1.4 %			0.1 %			
ZR-3	17.7 %	44.4 %	13.5 %		16.2 %*		5.9 %	1.5 %		0.8 %			
ZR-4		23.3 %	15.8 %	24.7 %	26.9 %	5.4 %	1.7 %	1.0 %	0.1 %	1.1 %			
ZR-5		23.9 %	14.8 %	30.9 %	22.2 %	5.9 %	1.3 %	0.2 %	0.1 %	0.9 %			
ZR-6		20.5 %	18.1 %	31.0 %	18.9 %	7.8 %	1.5 %	0.5 %	0.6 %	1.1 %			
ZR-7	6.1 %		24.2 %	28.1 %	2.2 %*				0.2 %	0.7 %	0.6 %	36.8 %	1.1 %

Legend: Gl – glauconite, Ill – illite, Ill-sm – mixed-layer illite–smectite, Kln (P) – poorly-crystallised kaolinite, Kln (C) – well-crystallised kaolinite, Py – pyrite, Mrc – marcasite, Rt – rutile, Ant – anatase, Hal – halite, Clc – calcite, Gy – gypsum, * – total amount of kaolinite in the sample.

was not extracted, and carbonates were not removed. The samples ZR-1, ZR-2 and ZR-3 display major differences in mineralogy when compared to the other palaeosol samples, as they are primarily composed of $1M_d$ illite and glauconite ($1M_{tv}$ polytype), with minor amounts of $2M_1$ illite, pyrite, marcasite and anatase (Supplementary Fig. 1 and Table 2). The ZR-3 sample also contains a significant amount of kaolinite.

Clay fraction was extracted from the ZR-3 and ZR-5 palaeosol samples (Fig. 5B, 5C) and the glauconite-rich ZR-1 sample (Fig. 5A). The composition of the clay fraction from the ZR-3 sample is the same as the one from the ZR-5 sample (Fig. 5C), as they both contain illite, mixed-layer illite-smectite, well and poorly crystalline kaolinite as well as minor amounts of dioctahedral vermiculite (Fig. 5B, 5C). Despite the fact that the mixed-layer illite-smectite was not detected in the bulk sample from the ZR-3 sample, it was detected in its clay fraction, which is probably due to a very low amount of clay fraction (<2 µm) in the ZR-3 sample (Supplementary Fig. 1) in which the majority of mixed-layer illite–smectite was located. The ZR-1 contains some glauconite and contains more illite at the expense of mixed-layer illite–smectite (Fig. 5C) compared to the clay fractions from the ZR-3 and ZR-5 samples, while also containing well- and poorly-crystalline kaolinite, as well as dioctahedral vermiculite. Presence of illite in the clay fraction from all three clay fraction samples prevented a proper characterisation of mixed-layer illite-smectite, but the ~ 11 Å position of the broad illite (001)/smectite(001) peak (Fig. 5B, C) indicates that it contains more illitic than smectitic layers, while the presence of the peak in the 5.3° to 8.7°2θ indicates that it is ordered to some degree, which is expected for mixed-layer illite–smectites with higher amount of illitic layers (Środoń, 1980). Mixed-layer illite–smectite in the ZR-1 sample has more illite layers, which is apparent from the higher 2θ° position of the illite(001)/smectite(001) peak (Fig. 5A) compared to the mixed-layer illite-smectite in ZR-3 and ZR-5 samples.

4.2.3. FTIR

FTIR measurements support and corroborate the results obtained by XRPD measurements, while also provide additional information about the structural and chemical properties of clay minerals. Presence of illite was indicated with 3647, 1029, 1017, 835, 800, 754, 696, 536, 470 and 426 cm^{-1} bands in the absorption spectra (Table 2; Supplementary Fig. 2A; cf. Slonimskaya et al., 1986; Zviagina et al., 2020). Despite sharing some absorption bands with illite, glauconite was easily distinguished from illite, based on 3647, 3528, 1116, 1083, 815, 627, 571, 516, 489, 456 and 433 cm^{-1} absorption bands (Table 2; Supplementary

Table 2
Detected bands in bulk and clay fraction samples, with their band and mineral phase assignment.

ZR-1	ZR-2	ZR-2 < 2 μm	ZR-3	ZR-3 < 2 μm	ZR-4	ZR-5	ZR-5 < 2 μm	ZR-6	ZR-7	Assigned band	Assigned mineral
		3697	3698	3698	3696	3698	3697	3698	3700	ν AlOHAl	Kaolinite
	3646			3647	3647	3646	3647	3646		ν AlOHAl	Illite
3624	3627	3621	3622	3627	3621	3621	3621	3621	3618	ν AlOHAl	Illite, Kaolinite
3607	3606	3611	3605	3600			3601		3608	ν AlOHMg	Illite, Glauconite
				3589						ν MgOHMg	Glauconite
3562	3560	3566	3562	3567	3568	3567	3567	3566	3565	ν (Mg,Al)OHFe^{3+}	Glauconite
				3545	3544					ν MgOHFe^{2+}	Glauconite
3528	3529	3525	3530	3528	3526		3527			ν Fe^{2+}OHFe^{3+}	Glauconite
				3506						ν Fe^{2+}OHFe^{3+}	Glauconite
3442	3441	3441	3447	3445		3444	3448		3432	ν H_2O	
3411	3428				3413			3423		ν H_2O	
3387										ν H_2O	
1634	1636	1634	1638	1637	1636	1638	1637	1634	1628	δ H_2O	
1439	1418							1432	1428	ν_3 CO_3	
1115		1113	1113	1113	1113	1113	1113	1112		ν SiO_{apical}	Illite, Glauconite
1086	1081				1087				1086	ν SiO_{apical}	Glauconite
		1027	1029	1032	1029	1033	1030	1031	1021	ν SiO	Illite
					1017					ν SiO	Illite
1009		1009	1007	1008	1005	1009	1008	1010		ν SiO	Illite, Glauconite
					938	937		937	936	δ AlOHAl	Kaolinite
915	914	912	913	913	913	912	912	913	913	δ AlOHAl	
	879								875	ν_2 CO_3	Calcite
834		836	835	834	833	835	835	833	832	δ AlOHMg	
819	817									δ Fe^{3+}OHFe^{3+}	Glauconite
		795	796	795	797	793	794	793	798	δ Al-O-Al	Illite
759	760	754	755	753	753	753	753	754	753	δ Al-O-Si, Si-O	Illite
	712								712	ν_4 CO_3	Calcite
		696	697	696	695	693	693	695	692	δ Si-O out of plane	Illite
674	676	668		668	670	669	668	668		δ Si-O, Fe-O	Glauconite
630					634			631		δ AL-O, Si-O	
563	565	570	567				572	564	569	δ AL-O	Kaolinite
				534	533	535	533	533		δ_3 Si-O-Si	Illite
	523	525	529						521	δ_3 Si-O-Si	Illite (Fe)
517	518									δ_3 Si-O-Si	Glauconite
	488									δ_3 Si-O-Fe	Glauconite
469	466	471	469	470	472	471	471	472	470	δ_2 Si-O-Si	Illite
451	457									δ_2 Si-O-Si	Glauconite
434	435	431	431						431	δ_1 Si-O	Glauconite
				427	427	426	426	427		δ_1 Si-O	Illite

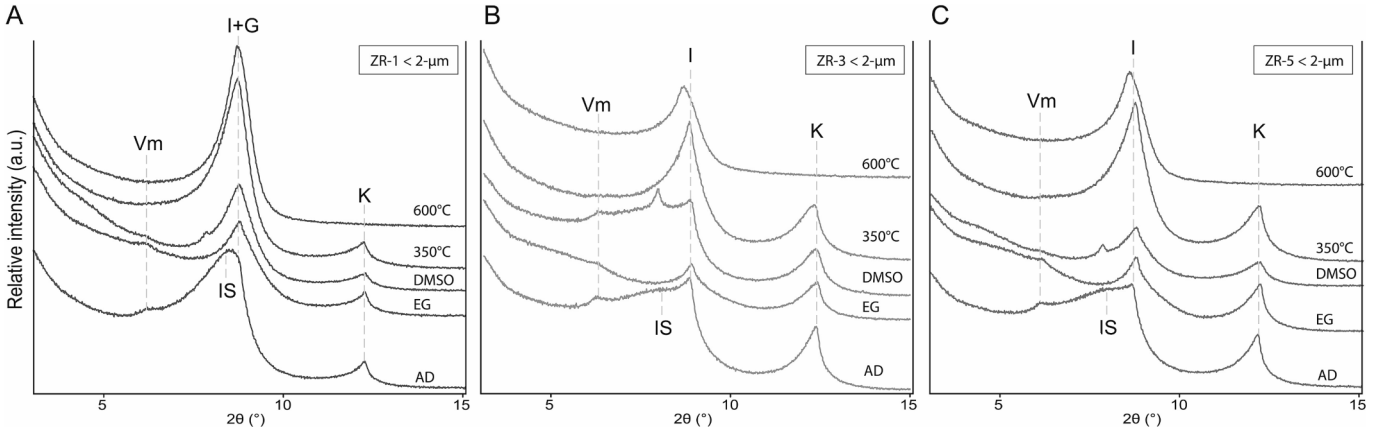

Fig. 5. X-ray diffractograms of bulk samples and clay fractions. **(A)** X-ray diffractogram of the clay fraction extracted from sample ZR-1. **(B)** X-ray diffractogram of the clay fraction extracted from sample ZR-3. **(C)** X-ray diffractogram of the clay fraction extracted from sample ZR-5; abbreviations of mineral phases: G – glauconite, I – illite, IS – mixed-layer illite–smectite, K – kaolinite, Vm – dioctahedral vermiculite; Abbreviations of different treatements: AD: air drying, EG: saturation with ethylene glycol, DMSO: dimethyl sulphoxide; 350°C, 600°C: heating temperatures.

Fig. 2A; cf. Zviagina et al., 2020), which are also broader than the ones produced by illite, indicating a more disordered structure (Slonimskaya et al., 1986). Kaolinite was detected in most samples based on 3698, 3623 and 936 cm^{-1} bands, since the others were not visible due to the overlap with illite absorption band. Calcite is abundant in ZR-2 and ZR-7 samples, with visible 1795, 875 and 712 cm^{-1} bands (Tables 2; Supplementary Fig. 2A, cf. Andersen and Brečević, 1991) which are very weak in ZR-2 sample, suggesting its low amount. Glauconite-related bands indicate the presence of ferric and ferrous iron as well as magnesium and aluminium in its structure. Iron and magnesium are not present in the spectra produced from illite-rich samples, indicating that illites contain mostly aluminium. A shift in δ_1 and δ_3 Si-O-Si bands

produced by illites in the ZR-3 sample was observed, which is characteristic for illites with increased iron content in their structure (Table 2; Supplementary Fig. 2A; cf. Zviagina et al., 2020). Absorption spectra from clay fractions of samples ZR-2, ZR-3 and ZR-5 (Table 2; Supplementary Fig. 2B) did not show any significant differences from those produced from the bulk samples from which they were extracted (Table 2; Supplementary Fig. 2A), except for the clay fraction from sample ZR-2, which displays the same shift in δ_1 and δ_3 Si-O-Si bands as the sample ZR-3. $2M_1$ and $1M_d$ polytypes, together with mixed layer illite–smectite and kaolinites with different degrees of crystallinity, which were identified in the XRPD data, were impossible to distinguish in the IR spectra, although the shape of the 3647 cm^{-1} band, which shows a superposition of broader and sharper bands at this frequency (Supplementary Figure 2), indicates the presence of illites and/or mixed layer illite–smectite with different degrees of structural ordering. While this was the main drawback of FTIR compared to XRPD in our study, it allowed an additional insight into the structure of major clay phases. The main contribution was the additional confirmation of glauconite, as it confirmed the disordered structure (broad peaks) and the presence of both ferrous and ferric iron in its structure, both indicative for glauconite. FTIR analysis also allowed the identification of iron in the structure of illite from samples ZR-2, ZR-3 and ZR-7, while also confirming the dioctahedral nature of illite in all samples (very weak Mg-related absorption bands, which are associated with glauconite, and strong Al-related absorption bands).

4.2.4. SEM-EDS

SEM analysis was mainly used for morphological characterisation of glauconite, although other mineral phases were characterised as well. Different glauconite morphologies were observed. Glauconite primarily occurs as platelets with "caterpillar" morphology (Fig. 6A), but also occurs as replacement of cylindrical structures, which are interpreted as rootlets (Fig. 6B). In certain clay sections, the clay has a speckled appearance, with interchanging darker and brighter areas (Fig. 6C) which is interpreted as the replacement of iron-poor clay minerals (darker areas) with glauconite (brighter areas). Flaky morphologies of other clay minerals were observed, with such morphologies best visible around pedoclasts (Fig. 6D) and pyrite crystals, which likely represent illite and mixed-layer illite-smectite. Pyrite appears in several different morphologies, coinciding with the observations obtained from thin section analysis. The pyrite appears as smaller cubes and rarely octahedral crystals which are between 5 and 10 μm in size (Fig. 6E), but it also appears as crystals larger than 100 μm which are exclusively present as octahedrons or cuboctahedrons (Fig. 6F). Smaller crystals mainly appear dispersed throughout the samples, but they are usually also observed in groups which form cylindrical shapes (Fig. 6E), corresponding to pyritised roots observed in thin sections and hand specimens. Despite its presence being confirmed by XRPD, marcasite was not identified through SEM, as observed iron sulphides showed only habits from the cubic system. Besides pyrite, few occurrences of zinc sulphide were detected, but only in the sample ZR-1, based on the EDS-spectra.

Besides being used for identification of different phases, EDS data were primarily collected for chemical characterisation of glauconite and illite and calculation of their formulas. After the formula calculation, EDS data were plotted on the $M^+/4Si$ vs. $Fe/\sum oct$ diagram for classification, with outlines of clay compositional fields taken from Meunier and El Albani (2007) and Baldermann et al. (2017; Fig. 7). Out of 142 analysed spots, most belong to illite and mixed-layer illite-smectite, while only 25 belong to glauconite. Illite and mixed-layer illite-smectite do not fall in any of the fields calculated by Meunier and El Albani (2007), but they fall in the field which represents the series between Al-smectite and muscovite, presented in Baldermann et al. (2017). On this plot it is visible that the analysed clay minerals form a continuous series from mixed-layer illite-smectite to illite and finally to glauconite. Two trends are visible in the plotted data, one which is related to illitisation processes and the second one which is related to the glauconitisation processes. Based on the EDS data, glauconite appears to be aluminium-rich, but it does not fall in the field of ferrian illite/aluminium-rich glauconite. The formulas calculated from the EDS data can be found in the supplementary data (Supplementary Tables 2–4).

4.2.5. Geochemistry

Obtained major oxide values correspond well to the mineralogical composition of samples determined with XRPD and FTIR. Samples ZR-1 and ZR-2, which contain glauconite, display higher values of Fe_2O_3, MgO and K_2O, together with lower Al_2O_3 values and TiO_2 values (Fig. 8A). The high SO_3 values in ZR-1, ZR-4, ZR-5 and ZR-6 samples correspond to the presence of iron sulphides, while the high CaO value in the ZR-7 sample reflects the abundance of calcite (Fig. 8A). Trace elements highlight the geochemical differences between the glauconite-rich zone (ZR-1), transitional zone (ZR-2 and ZR-3), palaeosol pocket (ZR-4, ZR-5 and ZR-6) and the palaeosol horizon (ZR-7). The glauconite-rich zone displays an enrichment in chalcophile elements (Zn, As and Mo) which also has an unusually large amount of V, which was not

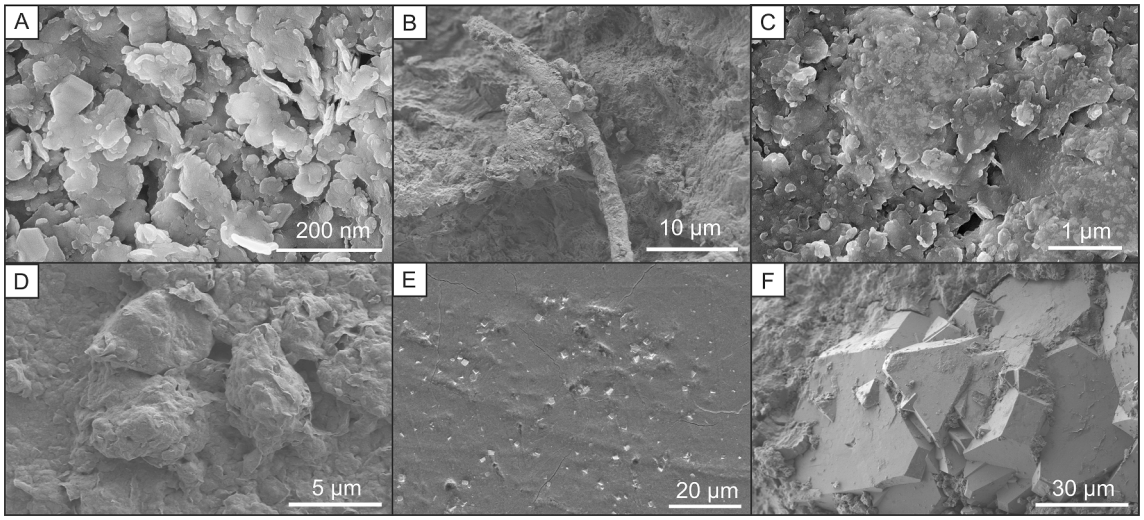

Fig. 6. SEM photomicrographs of the samples ZR-1, ZR-3 and ZR-5. **(A)** Caterpillar structure of glauconite; sample ZR-1. **(B)** Glauconitised rootlet; sample ZR-3. **(C)** Glauconitised clay minerals; sample ZR-3. **(D)** Flaky morphology of clay minerals, possibly illite and illite–smectite; sample ZR-5. **(E)** Group of pyrite cubes; sample ZR-3. **(F)** Cuboctahedral morphology of large pyrite crystals; sample ZR-3.

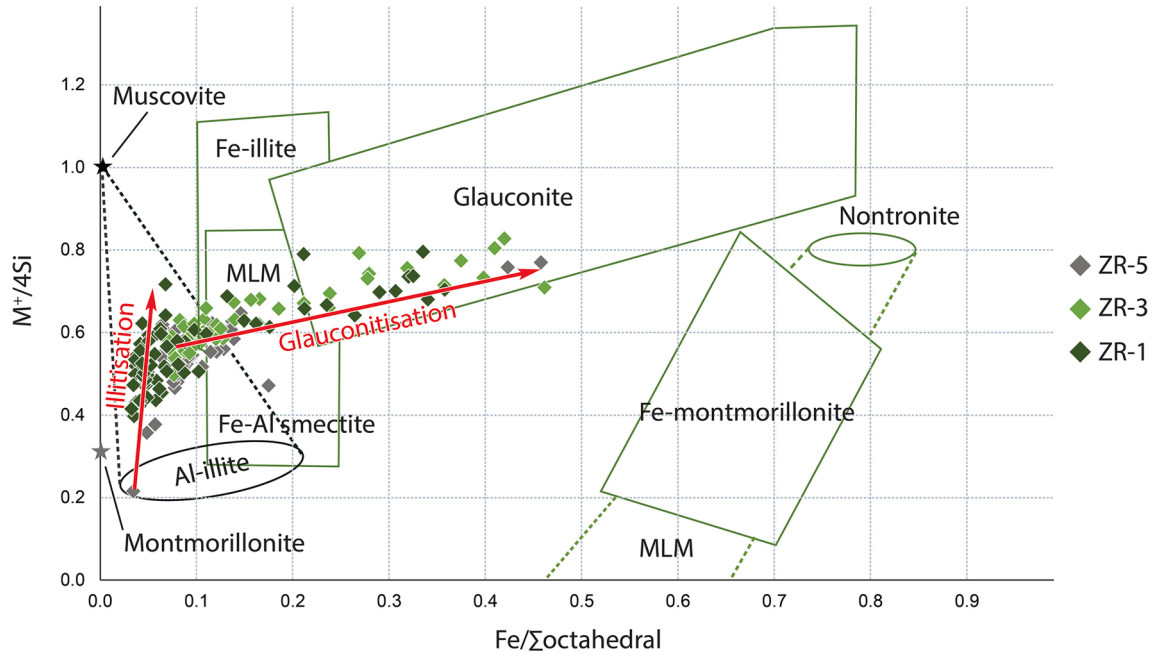

Fig. 7. $M^{+}/4Si$ vs. Fe/∑octahedral plot on which the EDS points measured in samples ZR-1, ZR-3 and ZR-5 have been plotted. Areas marked by green lines represent data from Meunier and El Albani (2007), while the areas marked by black full and dotted lines and stars represent data from Baldermann et al. (2017); MLM – mixed-layer mineral.

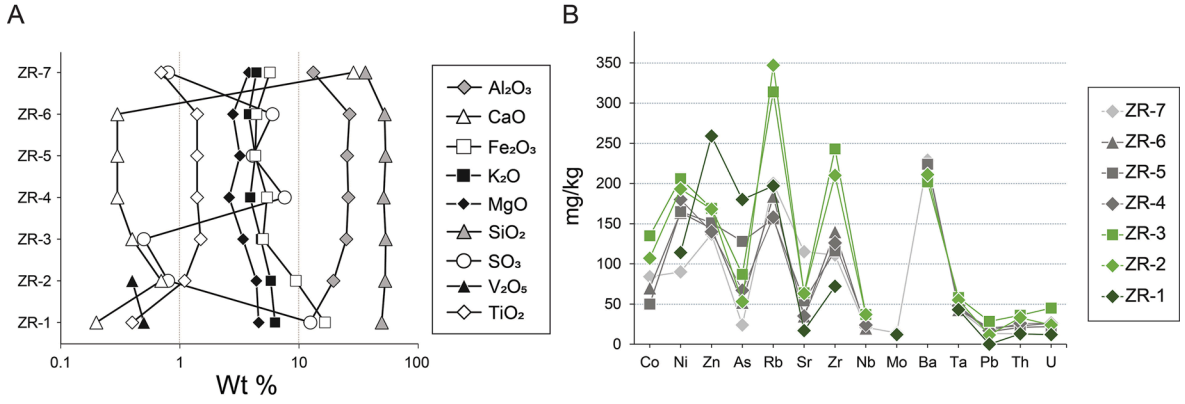

Fig. 8. Plots constructed from XRF data. **(A)** Plot showing values of major oxides. **(B)** Plot showing the values of trace elements.

detected in other samples (Fig. 8A). It also has the lowest values of Sr, Zr, Th and U compared to the other samples. The transitional zone, especially its distal part (sample ZR-3) displays an enrichment in siderophile (Co and Ni), high field strength (Zr, Nb, Ta and Th) and large ion lithophile elements (Rb, Sr and Ba) when compared to the samples from the glauconite-rich zone and the palaeosol pocket (Fig. 8B). Sample ZR-3 also displays an enrichment in Pb and U, which is not present in the ZR-2 sample (Fig. 8B). The samples (ZR-3, ZR-4 and ZR-5) from the palaeosol pocket do not display any significant enrichments or depletions when compared to other samples (Fig. 8B). The sample ZR-7 from the palaeosol horizon has very low trace element values, but is enriched in Sr and Ba, while also having a detectable amount of Mo, similarly to the ZR-1 sample (Fig. 8B).

To determine if the samples were under the marine influence during their formation, Sr/Ba values were calculated according to Wei and Algeo (2020). The Sr/Ba ratio values were highest in the sample ZR-7, displaying the value of 0.5, while the ratio in the samples ZR-2, ZR-3 and ZR-5 have the values between 0.24 and 0.32 (Table 3). This altogether indicates their formation in marine to brackish environment, according to Wei and Algeo (2020).

Table 3
Calculated Sr/Ba ratios.

	ZR-1	ZR-2	ZR-3	ZR-4	ZR-5	ZR-6	ZR-7
Sr/Ba	–	0.30	0.32	–	0.24	–	0.50

Rare earth elements (REE) were analysed only in two samples, in one from the transitional zone (ZR-2) and in one from the palaeosol pocket (ZR-5). Both samples display the same distribution of REEs, showing the depletion in light and middle REEs, coupled with an enrichment in HREEs (Fig. 9). The ZR-5 sample also shows a slight negative Ce anomaly (Fig. 9).

5. Discussion

5.1. Evolution of depositional environments

Upper Oxfordian–lower Kimmeridgian limestones of the Muča unit, abundant in various bioclasts, especially benthic foraminifera (LF1), are

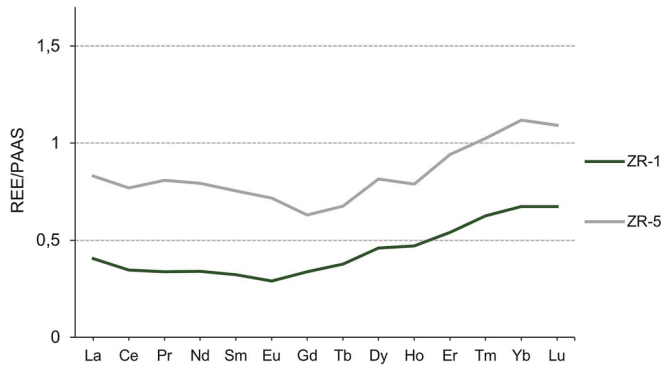

Fig. 9. Spider diagram showing the REE values in the sample ZR-1 and ZR-5 normalised to the Post-Archean Australian Shale, according to values from Taylor and MacLennan (1985).

interpreted as shallow marine deposits that formed in lagoonal environments of an ancient AdCP. Microencrusters such as *Bacinella irregularis*, *Lithocodium aggregatum* and *Thaumatoporella parvovesiculifera*, which commonly encrust coral and molluscs fragments, also indicate shallow lagoon with oligotrophic conditions, low sediment accumulation rate, normal salinity and clear and oxygenated marine waters (e.g., Leinfelder et al., 1993; Schmid and Leinfelder, 1996). The *Bacinella–Lithocodium* association is a characteristic constituent of Upper Jurassic platform carbonates in western Tethys (e.g., Leinfelder et al., 1993; Dupraz and Strasser, 1999; Vedrine et al., 2007), including the AdCP.

Karstified shallow marine carbonates with overprinted pedogenic features (LF6) appear in several levels within the Muča unit and point to the cessation of carbonate production and prolonged terrestrial conditions (Fig. 2). The terrestrial phase marked by subaerial exposure surface at 0.6 m of the Zlatni Rt-1 section likely started under semi-arid climate (as indicated by calcretes; cf. Esteban and Klappa, 1983; Alonso-Zarza, 2003) and probably changed towards warm humid climate conditions (as indicated by palaeokarstification; cf. Ford and Williams, 2007). The irregular relief, brecciation, bedrock lithoclasts, black pebbles and grey clay with glauconite within the Zlatni Rt palaeosol at 2.5 m indicates its formation under warm humid climate conditions. These two prominent subaerial exposure surfaces share some similar characteristics. Results of mineralogical and geochemical analyses have shown that the palaeosol material (grey palaeosol with glauconite) deposited in the palaeosol pocket is composed of the same material as the Zlatni Rt palaeosol, indicating that this material was probably redeposited downwards, filling the palaeosol pocket. Such interpretation is corroborated by the presence of numerous vertical to subvertical fractures between the two subaerial exposure surfaces, in places filled with lithoclasts, black pebbles and palaeosol material, which are interpreted as dissolution channels connecting the two surfaces (Fig. 1C, Fig. 2).

The terrestrial phase recorded by the Zlatni Rt palaeosol lasted during the late Kimmeridgian and early Tithonian, as constrained by biostratigraphy (Fig. 2). However, due to the unknown thickness of the karstified Muča unit, the exact beginning of this terrestrial phase cannot be determined. It may be assumed that subaerial exposure surfaces within the Muča unit are the result of either sea-level changes during the uplift of that part of the AdCP or the variations in the rate of the uplift itself. This uplift, which in the end caused a long-lasting terrestrial phase during which the Zlatni Rt palaeosol and Rovinj bauxite (Šinkovec, 1974) were formed, was probably triggered in response to the overburden pressure generated by the oceanic crust during the obduction of the Vardar Ocean ophiolites in the Late Jurassic (Schmid et al., 2008, 2020; Picotti and Cobianchi, 2019; van Hinsbergen et al., 2020), which generated a flexural forebulge in the front of the obduction zone. Karstification of the uplifted carbonate terrain produced laterally variable geomorphology, including much deeper karstic landforms which hosted bauxitisation in the Rovinj-1 bauxite deposit (Šinkovec, 1974) located less than 5 km NNE from the Zlatni Rt (Fig. 1B), and smaller karstic landforms such as those on the studied outcrops.

Flooding of the previously exposed land occurred during the late Tithonian, producing a mixture of lithoclasts, black pebbles and palaeosol material, which is preserved in all three studied sections in shallow palaeokarstic depressions and dissolution channels (Fig. 2). These deposits are interpreted as transgressive breccia, whose mixture of different lithoclasts and abundant black pebbles indicates reworking of terrestrial deposits formed in supratidal brackish to freshwater marshes (Tišljar, 1986). Their dark colour suggests the presence of organic matter (mostly plant material; Flügel, 2004 and references therein) and pyrite. Interchange of fenestral micritic (LF5) and bioclastic limestones (LF3) with in places present litho-intraclastic floatstone and rudstone (LF4) and aggregate grain grainstone (LF2) in the Kirmenjak unit points to establishment of predominantly low to moderate water energy lagoonal environments, interrupted with periods of moderate to high energy conditions. The low diversity fossil association composed of small benthic foraminifera, dasyclad algae and *Favreina*-pellets, indicates restricted lagoonal conditions (cf. Flügel, 2004).

5.2. Formation of the Zlatni Rt palaeosol

The original source of the parent material from which the Zlatni Rt palaeosol has formed is hard to properly discern as it was most likely modified during and after its burial, but several aspects of the original material can be deduced from observed pedofeatures and outcrop observations. The morphology of the karstified bedrock surface is mostly characterised by a relatively low relief, but in the section where the palaeosol pocket is located the bedrock is heavily karstified, including several vertical shafts reaching c. 1 m below the unconformity into a pocket filled with the palaeosol material (Figs. 1C, 2). This indicates that after the subaerial exposure phase was initiated, the bedrock had to be exposed to karstification processes for a sufficiently long period of time enough to create such palaeorelief before the introduction of the source material for the palaeosol, indicating that the source material was not brought and accumulated immediately after the onset of the subaerial exposure phase. The composition of the palaeosol pocket indicates the seasonal interchange of phreatic and vadose conditions, as the material is hydromorphically altered and contains iron sulphides and pyritised roots (Figs. 4A, B, D–F, Fig. 6F, Table 1), pointing towards its formation in waterlogged conditions, while vertic features such as reworked clay coatings, granostriation, cross-striation, random striation (Fig. 4A–C) and slickensides indicate its formation in seasonally vadose conditions during the formation of the palaeosol, as these features formed as a result of repeated wetting and drying in clay-rich soils.

The high Sr/Ba ratio (Table 3), an enrichment in HREE and a negative cerium anomaly (Fig. 9) indicate that the palaeosol formed in contact with brackish to marine waters. Sr/Ba ratio ranges between 0.24 and 0.5 (Table 3), which indicates the formation in brackish to marine environment (Wei and Algeo, 2020), while the enrichment in HREE and a slight negative Ce anomaly are likely inherited from the seawater, which usually displays such REE signature (Alibo and Nozaki, 1999; Censi et al., 2007; Deng et al., 2017). Increased ionic strength in the marine environment also impairs the adsorption of light REEs onto clay minerals, while the adsorption of heavy REEs is not significantly affected (Coppin et al., 2002; Davranche et al., 2011; Hao et al., 2019; Durn et al., 2021), which can in turn lead to elevated heavy REE concentrations. Similar patterns were observed in the Cretaceous palaeosols from the succession of the Western Istrian Anticline, where the enrichment in heavy REEs was a result of similar processes (Durn et al., 2021). Brackish to marine influence coupled with seasonal wetting and drying might also explain the abundance of illite and ordered mixed-layer illite-smectite within the palaeosol. Several works have shown that upon repeated wetting and drying of smectite or mixed-layer illite–smectite in the presence of potassium, illitic layers form from smectitic layers through

partial layer collapse (Eberl et al., 1986; Huggett and Cuadros, 2005, 2010), which can also be a consequence of reduction from ferric to ferrous iron within the smectite structure, leading to the increase in the layer charge (Huggett and Cuadros, 2010). Such processes also produce structures disordered along the c axis (Andreoli et al., 1989) and could account for the formation of disordered $1M_d$ illite and ordered mixed-layer illite-smectite which likely represents an intermediate phase from which $1M_d$ illite finally formed. Alternative scenario which could produce $1M_d$ illite and ordered mixed layer illite–smectite from initial smectitic phases is the exposure to high temperatures during the burial diagenesis, but that seems highly unlikely in our case. Namely, the Zlatni Rt palaeosol is located close to the axis of the Western Istrian Anticline, and that part of the structure was uplifted already during the Early Cretaceous due to the active synsedimentary tectonic deformation, and was probably only partially covered by Palaeogene deposits (see discussion in Matičec et al., 1996), therefore overlying succession was very thin, probably less than 1000 m. In addition, geothermal gradients in the area of the former AdCP are lower than average, mostly 10–30 °C/1000 m (Jelić et al., 2005), so maximal temperatures reached during the burial were probably within 30–45 °C range, which are well below the temperatures needed for the illitisation of smectite during burial diagenesis (Pytte and Reynolds, 1989; Huggett, 2004).

A major portion of parent material from which the Zlatni Rt palaeosol and contemporaneous bauxites formed was likely derived from a volcanic source, as several levels of bentonites/tuffs of Kimmeridgian–Tithonian age are documented in the nearby Gorski Kotar area (Šćavničar and Nikler, 1976; Vlahović et al., 1994; Velić et al., 2002) and of early Kimmeridgian age in the Trento Plateau, NE Italy (Pellenard et al., 2013; Picotti and Cobianchi, 2017), which were derived from the volcanic centres formed during obduction of the Vardar Ocean (Picotti and Cobianchi, 2017). The vicinity and age of these materials suggest that volcaniclastics were also deposited on the Istrian part of the AdCP, which is also supported by the abundance of zircon and apatite grains in the contemporaneous Rovinj-1 bauxite body (Šinkovec, 1974). The volcanic input also accounts for the source of smectite, which commonly forms during the alteration of volcanic ash, as it is a prerequisite phase from which ordered mixed layer illite–smectite and $1M_d$ illite could have formed through repeated wetting and drying.

Additional contribution of the insoluble limestone residue of Kimmeridgian limestones which was accumulating during the karstification of the emerged carbonate terrain should not be excluded, as the limestones of the Muča unit contain a relatively high content of insoluble residue (2.19 %; Durn et al., 1999). The insoluble residue of analysed limestones from the Muča unit is mainly composed of illite, indicating that it is one of the sources from which the main portion of detrital $2M_1$ illite could have been derived. One of the other clay minerals detected in the Zlatni Rt palaeosol was kaolinite, in both well and poorly crystallized form. Well crystallized kaolinite is less common than the poorly crystallized kaolinite (Table 1) and is probably inherited, whereas the poorly crystallized kaolinite is of pedogenic origin. The formation of kaolinite in surface environments is restricted to pedogenesis in tropical soils (Wilson, 1999), which when coupled with the presence of pedogenic kaolinite points towards ferralitic soils as one of the sources of the parent material from which the Zlatni Rt palaeosol has formed. The presence of the bauxite body of the same age (Šinkovec, 1974; Fig. 1B) nearby the Zlatni Rt palaeosol further confirms the formation of ferralitic soils in the vicinity, as bauxitisation must have been accompanied with the formation of tropical soils, surrounding the karstic depressions in which bauxites were forming. As such, the ferralitic soils surrounding the karstic depression were a more likely source of the ferralitic material, since the bauxitisation was restricted to palaeodepressions which were serving as sediment traps. This, as well as palaeotopographic position of the studied outcrop above the palaeodepressions filled by bauxitic material, also explains the absence of bauxitic minerals in the Zlatni Rt palaeosol, and accounts for the detrital input of dioctahedral vermiculite which can form in tropical soils (Wilson, 1999; Durn, 2003; Mareschal et al., 2011; Han et al., 2014), which was detected in the palaeosol pocket. Some of the ferralitic material could have been derived from bauxite pockets in the vicinity, as pisoids with similar structure as those from the Rovinj bauxite body (Šinkovec, 1974) were observed in the Zlatni Rt palaeosol (Fig. 4D). This altogether indicates that the material from the surrounding ferralitic material in the well-developed palaeorelief during the subaerial exposure phase contributed to the material from which the Zlatni Rt palaeosol had formed, which was also an important source of iron during the glauconitisation process.

5.3. Glauconite formation

The green material present in the studied palaeosol was studied in detail by FTIR, XRPD and SEM-EDS. Presence of 1.517 Å peak (Supplementary Fig. 1), characteristic iron containing stretching and bending bands and their broad character (Table 2; Supplementary Fig. 2A, B), coupled with its composition (Fig. 7), confirm that this phase is indeed glauconite. Geochemical data (Fig. 8A) also correlates well with FTIR, XRPD and SEM-EDS data, as the samples enriched in glauconite display an enrichment in iron, potassium and magnesium which is also visible in EDS data (Fig. 7). Glauconite was detected in samples ZR-1, ZR-2, ZR-3 and ZR-7, but it is most abundant in samples ZR-1 and ZR-2. These two samples also display an enrichment in vanadium (Fig. 8A) while the sample ZR-1 is also enriched in chalcophile elements (Fig. 8B). Vanadium is commonly enriched in clays in a reducing environment (Wanty and Goldhaber, 1992; Peacor et al., 2000; Shaheen et al., 2019), while the enrichment in chalcophile elements is related to the abundance of iron sulphides and presence of zinc sulphide in ZR-1 sample, which are absent in sample ZR-2. The presence of glauconite in sample ZR-7 indicates that its formation was not restricted to the palaeosol pocket but occurred throughout the palaeosol.

It is generally accepted that the formation of glauconite is preceded by the neoformation of iron-rich smectite in faecal pellets and bioclasts, which is then converted to glauconite by potassium and iron fixation from marine pore waters (Odin and Matter, 1981; Meunier and El Albani, 2007; Baldermann et al., 2015, Banerjee et al., 2016, 2020). One of other theories on the origin of glauconite, the layer lattice theory (Burst, 1958; Hower, 1961), explains the glauconitisation process by fixation of iron and potassium into the pre-existing mineral phases. In the case of Zlatni Rt palaeosol it seems that processes similar to those proposed by both aforementioned theories led to the formation of glauconite. Based on EDS data (Fig. 7), together with textural evidence from thin sections and SEM photomicrographs (Figs. 4, 7), it appears that glauconite formed gradually from present clay phases and authigenically, through recrystallisation and re-precipitation of dissolved clay phases, followed by potassium and iron fixation. Gradual replacement of present mineral phases with glauconite is evident from a continuous series between mixed-layer illite-smectite, illite and glauconite (Fig. 7) and from SEM photomicrographs, on which a replacement of individual crystals can be seen (Fig. 6C), most likely that of illite and mixed-layer illite-smectite with glauconite. This can be seen on a larger scale in thin sections (Fig. 4F), where a gradual replacement of the groundmass by glauconite is visible. Glauconite formation is accompanied by a dissolution mechanism that is prevalent in the transition zone between the glauconite-rich zone and the palaeosol pocket, where many glauconite-filled fractures are surrounded by a dissolution halo (Fig. 4C, E). This is evident from the deficit of kaolinite and mixed-layer illite-smectite in the glauconite-rich zone and the transition zone (Fig. 4A, B; Table 2), which were likely more affected by the dissolution processes. This is especially true for kaolinite which is known to be unstable in saline fluids (Huggett and Cuadros, 2005, 2010) and during high activity of Fe ions, which is then accompanied by the formation of glauconite (Pugliese Andrade et al., 2014). The caterpillar structures were first described by Odin and Matter (1981) as being characteristic for nascent glauconites and were observed in glauconites from this study as well (Fig. 6A). Newer studies on glauconites with similar structures also

suggest connection of these structures with microbial activity (Zanin et al., 2004; Eder et al., 2007; Sánchez-Navas et al., 2008; López-Quirós et al., 2019), where precursor iron-rich smectite might precipitate from microbial gels enriched in Al, Si, K and Fe which are released and retained upon them during the microbially facilitated dissolution of surrounding phases (Sánchez-Navas et al., 2008). Lowering of the pH caused by microbial activity can facilitate the dissolution of present mineral phases (Baldermann et al., 2013; López-Quirós et al., 2019), which likely led to the dissolution of smectite if present and smectite layers in mixed-layer illite-smectite, as smectites are unstable in low pH (Bauer et al., 2001; Amram and Ganor, 2005). This dissolution process, which is especially apparent in the transitional zone (Fig. 4C, E), is likely responsible for the enrichment in high field strength and siderophile elements in this zone (Fig. 8B), as these elements and their carrier phases were concentrated during the dissolution of kaolinite and mixed-layer illite–smectite which are scarcer in the transitional zone (Fig. 4A; Table 1). This enrichment is also accompanied with an enrichment in large ion lithophile elements (Fig. 8B), which were most likely enriched during the ingression of marine porewaters in the palaeosol through the fractures.

Glauconite is also present as two types, a light green, more oxidised type, and dark green, more reduced type. These two glauconites have different paragenetic relationships but appear to form interchangeably (Fig. 4F) and are usually accompanied with the formation of pyrite (Fig. 4C, F). This interplay between the oxidised and reduced form of glauconite coupled with their paragenetic relationship with pyrite suggests redox fluctuations during glauconite formation. This can be linked to the oscillating transgression recorded in the cover sequence of the nearby Rovinj bauxite (Durn et al., 2003), where clays and freshwater/brackish limestones cyclically alternate. Such variations in the sea level could have affected the input of organic matter in the area where the Zlatni Rt palaeosol was forming, as the accumulation and mineralisation of organic matter is increased during flooding episodes in wetland soils (Sahrawat, 2003). The short-lived flooding periods can also lead to the mobilisation of solubilised organic matter, where large amounts of dissolved organic matter can be delivered into seawater (Majidzadeh et al., 2017). Thus, oscillations in sea level during the initial stages of the transgression could have caused variations in the supply of organic matter during glauconite formation, which in turn affected the intensity of microbial reduction in its local environment. This could have led to fluctuations in redox potential, which in turn caused variations in iron mobility. Glauconitisation also scavenges mobilised iron more poorly than pyritisation (Eder et al., 2007; Baldermann et al., 2013; Giresse, 2022), and as such during the periods of the increased input of organic matter euxinic conditions could have been achieved, leading to pyrite formation at the expense of glauconite. The glauconitisation phase was followed with the diagenetic formation of large, euhedral pyrite crystals (Fig. 4A–D, F). These crystals are ubiquitous in the glauconite-rich zone, which led to the enrichment of chalcophile elements in the glauconite-rich zone compared to the palaeosol pocket and the transitional zone (Fig. 8B). Thus, the formation of diagenetic pyrite is most likely related to the final flooding of the Zlatni Rt palaeosol and its burial. All the main processes which preceded and led to the formation of glauconite are schematically represented and summarised on Fig. 10.

5.4. Palaeoenvironmental evolution of the studied area

On all three studied outcrops, the formation of the Zlatni Rt palaeosol was preceded with the deposition of Muča limestones in a high to moderate energy environment, comprising the lower portions of the studied sections. As previously discussed, their formation was followed by the terrestrial phase, initiated by the uplift generated in response to the obduction of the Vardar Ocean (Schmidt et al., 2008, 2020; Picotti and Cobianchi, 2019; van Hinsbergen et al., 2020). This phase was characterised by the formation of ferralitic soils and wetland soils such as the Zlatni Rt palaeosol, which formed from a combination of volcanic material, aeolian dust and insoluble residue (Fig. 11A). The Zlatni Rt palaeosol formed in a marshy environment, as inferred from its features indicating the influence of both waterlogging and seasonally vadose conditions. Such material was then washed and redeposited into the previously karstified channels and depressions, such as the palaeosol pocket observed on the Zlatni Rt-1 section, while some material remained on the palaeosurface, visible as the Zlatni Rt palaeosol observable on all three studied sections. As previously discussed, the

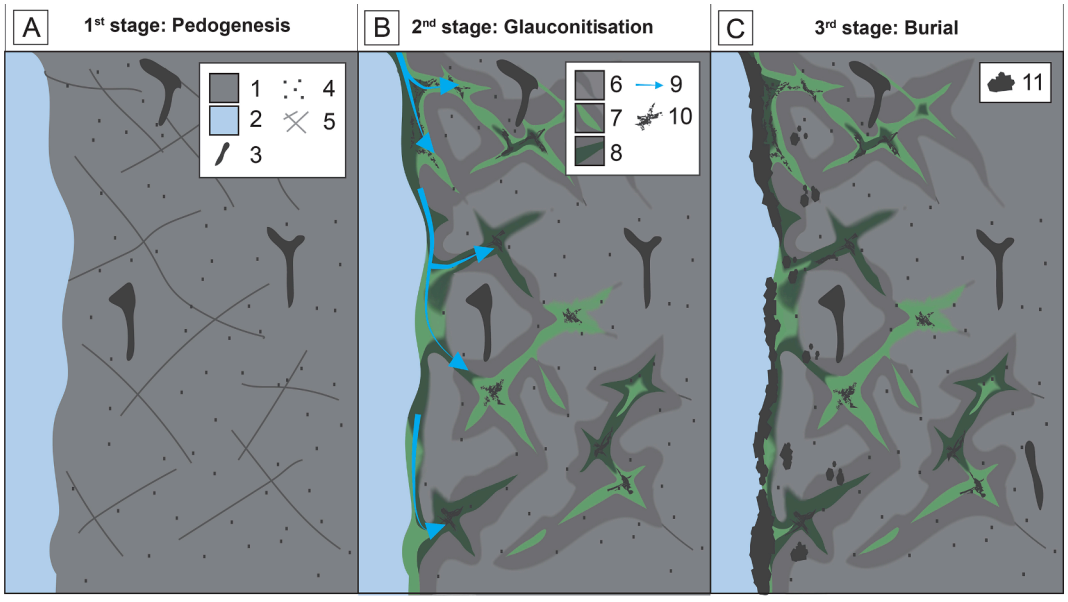

Fig. 10. Schematic representation of the different stages in the evolution of the Zlatni Rt palaeosol with the description of the most important processes during each stage. **(A)** Pedogenic stage: formation of pyritised roots (3), formation of pedogenic pyrite (4), pedogenic illite ($1M_d$) and mixed-layer illite–smectite. **(B)** Glauconitization stage: microbially facilitated dissolution of clayey groundmass (6), formation of oxidized (7) and reduced (8) glauconite, ingression of marine porewater (9) and precipitation of pyrite veins (10). **(C)** Burial stage: precipitation of coarse euhedral pyrite (11). Legend: 1 – clayey groundmass; 2 – carbonate bedrock; 3 – pyritized roots; 4 – pedogenic pyrite; 5 – fractures; 6 – dissolution halo; 7 – oxidized glauconite; 8 – reduced glauconite; 9 – circulation of marine porewater; 10 – pyrite veinlets; 11 – diagenetic pyrite.

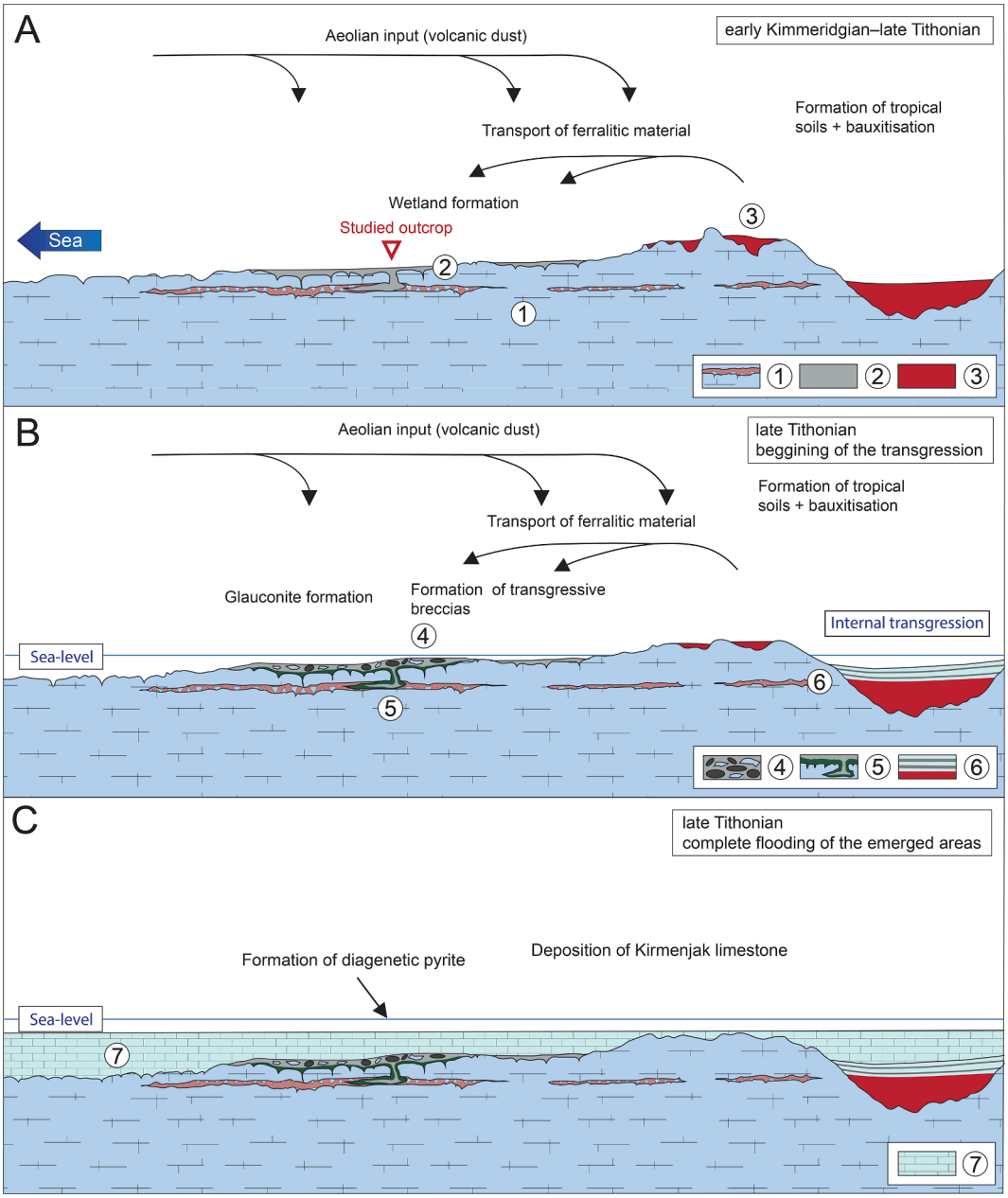

Fig. 11. Schematic representation of the palaeoenvironmental evolution of the Zlatni Rt palaeosol and its surrounding area. (A) Early Kimmeridgian to late Tithonian subaerial exposure phase marked with the formation of bauxites together with tropical and wetland soils. (B) Late Tithonian – beginning of the transgression marked with the formation and deposition of black pebbles and transgressive breccias, coupled with glauconite formation, together with deposition of the cyclical cover sequence in the Rovinj bauxite deposit (Šinkovec, 1974). (C) Flooding of the previously subaerially exposed carbonate terrain marked with the deposition of Kirmenjak unit limestones (Šinkovec, 1974). Legend: 1 – karstified upper Oxfordian to lower Kimmeridgian limestones with subaerial exposure horizons; 2 – wetland soils; 3 – tropical soils and bauxites; 4 – transgressive breccias; 5 – glauconite formation; 6 – alternation of clays and freshwater/brackish limestones in the Rovinj deposit; 7 – upper Tithonian shallow-marine Kirmenjak unit.

formation of glauconite in the Zlatni Rt palaeosol marks the beginning of the transgression which is also recorded through the formation of transgressive breccias, visible as a mixture of bedrock fragments and black pebbles which were embedded within the palaeosol during the flooding episodes in the initial stages of the transgression (Fig. 11B). Tišljar (1986) described the formation of such deposits, where he concluded that such materials formed in supratidal brackish to freshwater marshes. The presence of these fragments indicates the contemporaneous presence of such materials during the formation of the palaeosol, which were then redeposited and embedded within the clayey material of the palaeosol during the transgression. The final drowning of the Zlatni Rt palaeosol and its burial are marked by the formation of diagenetic pyrite and deposition of lagoonal limestones of the Kirmenjak unit (Fig. 11C).

6. Conclusions

This study was focused on the evolution of the Zlatni Rt palaeosol in Western Istria and its surrounding landscape and the detailed characterisation of the glauconite occurrence which developed within it. Based on the collected data and its interpretation, several major conclusions can be emphasised as follows:

1. The studied Zlatni Rt palaeosol formed in the wetland environment, which was developed over the karstified Muča limestones and Rovinj breccias during the subaerial exposure phase which lasted between the early Kimmeridgian and the late Tithonian in the NW part of the Adriatic Carbonate Platform
2. The palaeosol is primarily composed of mixed-layer illite–smectite, $2M_1$ and $1M_d$ illite, together with kaolinite, iron sulphides and titanium oxides. $1M_d$ illite and mixed-layer illite–smectite formed during the repeated cycles of wetting and drying, while the presence of kaolinite indicates the input of ferralitic material during the palaeosol formation.
3. In the late Tithonian, the transgression enveloped the palaeosol and the surrounding area, which led to the formation of transgressive breccia and glauconite formation. Further sea level rise led to the complete flooding of the former subaerially exposed areas, the deposition of Kirmenjak limestone and the formation of diagenetic pyrite crusts in the palaeosol.
4. The green clay mineral from the Zlatni Rt palaeosol was identified as glauconite, which was confirmed by FTIR, XRPD and SEM-EDS. As such, this occurrence presents itself as one of the rare examples of glauconite formation through the alteration of a palaeosol in shallow-marine environments.
5. Two processes played the major role during glauconite formation, the uptake of potassium and iron of present clay phases, and their microbial dissolution and reprecipitation in the presence of iron and potassium ions.
6. The glauconite is present in both reduced and oxidised forms, which alternate together with pyrite, suggesting redox fluctuations during its formation. This was linked to the variations in sea level which influenced the organic matter supply during the initial stages of the transgression following the formation of the palaeosol.

Overall, this is the first detailed study of the Zlatni Rt palaeosol, providing a detailed view into one of the environments which existed in the NW part of the AdCP during the early Kimmeridgian and late Tithonian subaerial exposure phase. The detailed study of the glauconite occurrence provided an additional invaluable insight into the conditions which were present during the initial stages of the transgression, which could not have been obtained otherwise. Based on the data of this research it can be stated that the glauconite occurrences similar to the one from this study can be used as an indicator and stratigraphic marker for transgressive events, while their detailed study can be used as a tool for the environmental reconstruction during the initial phases of the transgression.

CRediT authorship contribution statement

Ivor Perković: Conceptualization, Data curation, Formal analysis, Investigation, Methodology, Visualization, Writing – original draft, Writing – review & editing. **Blanka Cvetko Tešović:** Data curation, Investigation, Methodology, Visualization, Writing – original draft, Writing – review & editing. **Maja Martinuš:** Conceptualization, Data curation, Investigation, Methodology, Visualization, Writing – original draft, Writing – review & editing. **Srečo D. Škapin:** Methodology. **Igor Vlahović:** Investigation, Writing – original draft, Writing – review & editing. **Darko Matešić:** Investigation. **Goran Durn:** Investigation, Resources, Supervision, Project administration, Funding aquisition, Writing - review & editing.

Declaration of competing interest

The authors declare that they have no known competing financial interests or personal relationships that could have appeared to influence the work reported in this paper.

Data availability

Data will be made available on request.

Acknowledgements

This work has been fully supported by the Croatian Science Foundation under the project IP-2019-04-8054 – WIANLab (Western Istrian Anticline as an Ideal Natural Laboratory for the Study of the Regional Unconformities in Carbonate Rocks, PI Goran Durn). We would also like to thank Milan Mihovilović (Geo-5 d.o.o. company, Rovinj) for his invaluable support during our work on the deposits from this regional unconformity.

Appendix A. Supplementary data

Supplementary data to this article can be found online at https://doi.org/10.1016/j.catena.2024.107841.

References

Alibo, D.S., Nozaki, Y., 1999. Rare earth elements in seawater: Particle association, shale-normalization, and Ce oxidation. Geochim. Cosmochim. Acta 63 (3–4). https://doi.org/10.1016/S0016-7037(98)00279-8.

Alonso-Zarza, A.M., 2003. Palaeoenvironmental significance of palustrine carbonates and calcretes in the geological record. Earth Sci. Rev. 60, 261–298. https://doi.org/10.1016/S0012-8252(02)00106-X.

Amram, K., Ganor, J., 2005. The combined effect of pH and temperature on smectite dissolution rate under acidic conditions. Geochim. Cosmochim. Acta 69 (10), 2535–2546. https://doi.org/10.1016/j.gca.2004.10.001.

Andersen, F.A., Brečević, L., 1991. Infrared spectra of amorphous and crystalline calcium carbonate. Acta Chem. Scand. 45, 1018–1024.

Andreoli, C.Y., Robert, M., Pons, C.H., 1989. First steps of smectite-illite transformation with humectation and desiccation cycles. Appl. Clay Sci. 4 (5–6), 423–435.

Baioumy, H., Boulis, S., 2012. Non-pelletal glauconite from the Campanian Qusseir formation, Egypt: implication for glauconitization. Sediment. Geol. 249, 1–9. https://doi.org/10.1016/j.sedgeo.2012.01.003.

Baldermann, A., Warr, L.N., Grathoff, G.H., Dietzel, M., 2013. The rate and mechanism of deep-sea glauconite formation at the Ivory Coast-Ghana marginal ridge. Clays Clay Miner. 61 (3), 258–276. https://doi.org/10.1346/CCMN.2013.0610307.

Baldermann, A., Warr, L.N., Letofsky-Papst, I., Mavromatis, V., 2015. Substantial iron sequestration during green-clay authigenesis in modern deep-sea sediments. Nat. Geosci. 8 (11), 885–889. https://doi.org/10.1038/ngeo2542.

Baldermann, A., Dietzel, M., Mavromatis, V., Mittermayr, F., Warr, L.N., Wemmer, K., 2017. The role of Fe on the formation and diagenesis of interstratified glauconite-smectite and illite-smectite: a case study of Lower Cretaceous shallow-water carbonates. Chem. Geol. 453, 21–34. https://doi.org/10.1016/j.chemgeo.2017.02.008.

Baldermann, A., Banerjee, S., Czuppon, G., Dietzel, M., Farkaš, J., Löhr, S., Moser, U., Scheiblhofer, E., Wright, N.M., Zack, T., 2022. Impact of green clay authigenesis on element sequestration in marine settings. Nat. Commun. 13 (1) https://doi.org/10.1038/s41467-022-29223-6.

Banerjee, S., Chattoraj, S.L., Saraswati, P.K., Dasgupta, S., Sarkar, U., Bumby, A., 2012. The origin and maturation of lagoonal glauconites: a case study from the Oligocene Maniyara Fort Formation, western Kutch. India. Geol. J. 47 (4), 357–371. https://doi.org/10.1002/gj.1345.

Banerjee, S., Bansal, U., Thorat, A., 2016. A review on palaeogeographic implications and temporal variation in glaucony composition. J. Palaeogeogr. 5, 43–71.

Banerjee, S., Choudhury, T.R., Saraswati, P.K., Khanolkar, S., 2020. The formation of authigenic deposits during Palaeogene warm climatic intervals: a review. J. Palaeogeogr. 9, 1–27. https://doi.org/10.1186/s42501-020-00076-8.

Bansal, U., Banerjee, S., Ruidas, D.K., Pande, K., 2018. Origin and geochemical characterization of the glauconites in the Upper Cretaceous Lameta Formation, Narmada Basin, central India. J. Palaeogeogr. 7 (2), 99–116. https://doi.org/10.1016/j.jop.2017.12.001.

Bauer, A., Schäfer, T., Dohrmann, R., Hoffmann, H., Kim, J.I., 2001. Smectite stability in acid salt solutions and the fate of Eu, Th and U in solution. Clay Miner. 36 (1), 93–103. https://doi.org/10.1180/000985501547376.

Burst, J.F., 1958. Mineral heterogeneity in "Glauconite" pellets. Am. Mineral. 43 (5), 481–497.

Censi, P., Sprovieri, M., Saiano, F., Di Geronimo, S.I., Larocca, D., Placenti, F., 2007. The behaviour of REEs in Thailand's Mae Klong estuary: suggestions from the Y/Ho ratios and lanthanide tetrad effects. Estuarine Coastal Shelf Sci. 71 (3), 569–579. https://doi.org/10.1016/j.ecss.2006.09.003.

Coppin, F., Berger, G., Bauer, A., Castet, S., Loubet, M., 2002. Sorption of lanthanides on smectite and kaolinite. Chem. Geol. 182 (1), 57–68. https://doi.org/10.1016/S0009-2541(01)00283-2.

Davranche, M., Grybos, M., Gruau, G., Pédrot, M., Dia, A., Marsac, R., 2011. Rare earth element patterns: a tool for identifying trace metal sources during wetland soil

reduction. Chem. Geol. 284 (1–9), 127–137. https://doi.org/10.1016/j.chemgeo.2011.02.014.
Deng, Y., Ren, J., Guo, Q., Cao, J., Wang, H., Liu, C., 2017. Rare earth element geochemistry characteristics of seawater and porewater from deep sea in western Pacific. Sci. Rep. 7 (1), 1–13. https://doi.org/10.1038/s41598-017-16379-1.
Doebelin, N., Kleeberg, R., 2015. Profex: A graphical user interface for the Rietveld refinement program BGMN. J. Appl. Crystallogr. 48 (5), 1573–1580. https://doi.org/10.1107/S1600576715014685.
Dupraz, C., Strasser, A., 1999. Microbialites and micro-encrusters in shallow coral bioherms (Middle to Late Oxfordian, Swiss Jura Mountains). Facies 40, 101–130. https://doi.org/10.1007/BF02537471.
Durn, G., 2003. Terra rossa in the Mediterranean region: Parent materials, composition and origin. Geol. Croat. 56 (1), 83–100. https://doi.org/10.4154/GC.2003.06.
Durn, G., Ottner, F., Tišljar, J., Mindszenty, A., Barudžija, U., 2003. Regional subaerial unconformities in shallow-marine carbonate sequences of Istria: sedimentology, mineralogy, geochemistry and micromorphology of associated bauxites, palaeosols and pedo-sedimentary complexes. In Vlahović, I., Tišljar, J. (Eds.), Evolution of depositional environments from the palaeozoic to the quaternary in the Karst Dinarides and the Pannonian Basin, 22nd IAS Meeting of Sedimentology, Opatija 2003, Field trip guidebook pp. 209–255, Zagreb.
Durn, G., Perković, I., Stummeyer, J., Ottner, F., Mileusnić, M., 2021. Differences in the behaviour of trace and rare-earth elements in oxidizing and reducing soil environments: case study of terra rossa soils and Cretaceous palaeosols from the Istrian peninsula. Croatia. Chemosphere 283. https://doi.org/10.1016/j.chemosphere.2021.131286.
D.D. Eberl J. Środoń H.R. Northrop Potassium fixation in smectite by wetting and drying. In: Davis A.J., Hayes, K.F. (Eds), Geochemical Processes at Mineral Surfaces (&editors), Am. Chem. Soc. Symposium Series 323 1986 296 326.
Eder, V.G., Martín-Algarra, A., Sánchez-Navas, A., Zanin, Y.N., Zamirailova, A.G., Lebedev, Y.N., 2007. Depositional controls on glaucony texture and composition, Upper Jurassic. West Siberian Basin. Sedimentology 54 (6), 1365–1387. https://doi.org/10.1111/j.1365-3091.2007.00885.x.
El Albani, A., Meunier, A., Fürsich, F., 2005. Unusual occurrence of glauconite in a shallow lagoonal environment (Lower Cretaceous, northern Aquitaine Basin, SW France). Terra Nova 17 (6), 537–544. https://doi.org/10.1111/j.1365-3121.2005.00646.x.
M. Esteban C.F. Klappa Subaerial exposure environment. In: Scholle, P.A., Bebout D.G., Moore, C.H. (Eds.), Carbonate depositional environments. American Association of Petroleum Geologists Memoir 33, Tulsa, Oklahoma 2 95 1983.
Flügel, E., 2004. Microfacies od Carbonate Rocks. Analysis, Interpretation and Application. Springer, Heidelberg, p. 984.
Ford, D., Williams, P., 2007. Karst Hydrogeology and Geomorphology. John Wiley & Sons, Chichester, p. 562.
Giresse, P., 2022. Quaternary glauconitization on Gulf of Guinea, glauconite factory: overview of and new data on tropical Atlantic continental shelves and deep slopes. Minerals 12 (7). https://doi.org/10.3390/min12070908.
Giresse, P., Wiewióra, A., 2001. Stratigraphic condensed deposition and diagenetic evolution of green clay minerals in deep water sediments on the Ivory Coast-Ghana Ridge. Mar. Geol. 179 (1–2) https://doi.org/10.1016/S0025-3227(01)00193-1.
Graulis, S., Chateigner, D., Downs, R.T., Yokochi, A.F.T., Quirós, M., Lutterotti, L., Manakova, E., Butkus, J., Moeck, P., Le Bail, A., 2009. Crystallography open database - an open-access collection of crystal structures. J. App. Crystallogr. 42 (4) https://doi.org/10.1107/S0021889809016690.
Han, W., Hong, H.L., Yin, K., Churchman, G.J., Li, Z.H., Chen, T., 2014. Pedogenic alteration of illite in subtropical China. Clay Miner. 49 (3) https://doi.org/10.1180/claymin.2014.049.3.03.
Hao, W., Flynn, S.L., Kashiwabara, T., Alam, M.S., Bandara, S., Swaren, L., Robbins, L.J., Alessi, D.S., Konhauser, K.O., 2019. The impact of ionic strength on the proton reactivity of clay minerals. Chem. Geol. 529 https://doi.org/10.1016/j.chemgeo.2019.119294.
Hower Jr., J., 1961. Some factors concerning the nature and origin of glauconite. Am. Mineral. 46 (2).
Huggett, J.M., 2004. Sedimentary rocks: clays and their diagenesis. In Encyclopedia of Geology. https://doi.org/10.1016/B0-12-369396-9/00311-7.
Huggett, J., Adetunji, J., Longstaffe, F., Wray, D., 2017. Mineralogical and geochemical characterisation of warm-water, shallow-marine glaucony from the Tertiary of the London Basin. Clay Miner. 52 (1), 25–50.
Huggett, J.M., Cuadros, J., 2005. Low-temperature illitization of smectite in the Late Eocene and Early Oligocene of the Isle of Wight (Hampshire basin), U.K. Am. Mineral. 90 (7), 1192–1202. https://doi.org/10.2138/am.2005.1674.
Huggett, J.M., Cuadros, J., 2010. Glauconite formation in lacustrine/palaeosol sediments, Isle of Wight (Hampshire Basin). UK. Clay Miner. 45 (1), 35–49. https://doi.org/10.1180/claymin.2010.045.1.35.
K. Jelić M. Kovačić S. Koščak-Kolin State of the Art of the Geothermal Resources in Croatia in the Year 2004. In: Horne, R., Stacey, R., Juliusson, E., Villaluz, A., Chen, C-Y., Dastan, A., LI, K., Garner, L., Bolds, J., Polyakova, J. (Eds.), Proceedings of the World Geothermal Congress Antalya Turkey 2005 588 596.
Leinfelder, R.R., Nose, M., Schmid, D.U., Werner, W., 1993. Microbial crusts of the Late Jurassic: composition, palaeoecological significance and importance in reef construction. Facies 29, 195–230. https://doi.org/10.1007/BF02536929.
López-Quirós, A., Escutia, C., Sánchez-Navas, A., Nieto, F., Garcia-Casco, A., Martín-Algarra, A., Evangelinos, D., Salabarnada, A., 2019. Glaucony authigenesis, maturity and alteration in the Weddell sea: an indicator of paleoenvironmental conditions before the onset of Antarctic glaciation. Sci. Rep. 9 (1) https://doi.org/10.1038/s41598-019-50107-1.
López-Quirós, A., Sánchez-Navas, A., Nieto, F., Escutia, C., 2020. New insights into the nature of glauconite. Am. Mineral. 105 (5), 674–686. https://doi.org/10.2138/am-2020-7341.
Madejova, J., Madejova, M., Komadel, P., 2001. Baseline studies of The Clay Minerals Society Source Clays: infrared methods. Clays Clay Miner. 49 (5), 410–432. http://pubs.geoscienceworld.org/ccm/article-pdf/49/5/410/3270398/clmn-49-05-0410.pdf.
Majidzadeh, H., Uzun, H., Ruecker, A., Miller, D., Vernon, J., Zhang, H., Bao, S., Tsui, M. T.K., Karanfil, T., Chow, A.T., 2017. Extreme flooding mobilized dissolved organic matter from coastal forested wetlands. Biogeochemistry 136 (3), 293–309. https://doi.org/10.1007/s10533-017-0394-x.
Mareschal, L., Nzila, J.D.D., Turpault, M.P., Thongo M'Bou, A., Mazoumbou, J.C., Bouillet, J.P., Ranger, J., Laclau, J.P., 2011. Mineralogical and physico-chemical properties of Ferralic Arenosols derived from unconsolidated Plio-Pleistocenic deposits in the coastal plains of Congo. Geoderma 162 (1–2), 159–170. https://doi.org/10.1016/j.geoderma.2011.01.017.
D. Matičec I. Velić J. Tišljar I. Vlahović S. Marinčić L. Fuček Osnovna geološka karta Republike Hrvatske mjerila 1:50 000 – list Rovinj 3. Hrvatski geološki institut. 2015.
Matičec, D., Vlahović, I., Velić, I., Tišljar, J., 1996. Eocene limestones overlying Lower Cretaceous deposits of western Istria (Croatia): Did some parts of present Istria form land during the Cretaceous? Geol. Croat. 49 (1), 117–127. https://doi.org/10.4154/GC.1994.46.
Meunier, A., El Albani, A., 2007. The glauconite-Fe-illite-Fe-smectite problem: a critical review. Terra Nova 19 (2), 95–104. https://doi.org/10.1111/j.1365-3121.2006.00719.x.
D.M. Moore R.C.jr. Reynolds X-Ray Diffraction and the Identification and Analysis of Clay Minerals (second edition). Oxford University Press. Oxford UK 1997 378 pp.
Odin, G.S., Matter, A., 1981. De glauconiarum origine. Sedimentology 28 (5), 611–641. https://doi.org/10.1111/j.1365-3091.1981.tb01925.x.
Peacor, D.R., Coveney, R.M., Zhao, G., 2000. Authigenic illite and organic matter: the principal hosts of vanadium in the Mecca Quarry Shale at Velpen. Indiana. Clays Clay Miner. 48 (3), 311–316. https://doi.org/10.1346/CCMN.2000.0480301.
Pellenard, P., Nomade, S., Martire, L., De Oliveira Ramalho, F., Monna, F., Guillou, H., 2013. The first ^{40}Ar-^{39}Ar date from Oxfordian ammonite-calibrated volcanic layers (bentonites) as a tie-point for the Late Jurassic. Geol. Mag. 150 (6), 1–7. https://doi.org/10.1017/S0016756813000605.
V. Picotti M. Cobianchi Jurassic stratigraphy of the Belluno Basin and Friuli Platform: a perspective on far-field compression in the Adria passive margin. Swiss J. Geosci., 110 3 2017 10.1007/s00015- 017-0280-5.
Pugliese Andrade, G.R., de Azevedo, A.C., Cuadros, J., Souza, V.S., Correia Furquim, S. A., Kiyohara, P.K., Vidal-Torrado, P., 2014. Transformation of kaolinite into smectite and iron-illite in Brazilian mangrove soils. Soil Sci Soc. Am. J. 78 (2), 655–672. https://doi.org/10.2136/sssaj2013.09.0381.
Pytte, A.M., Reynolds, R.C., 1989. The Thermal Transformation of Smectite to Illite. In: Thermal History of Sedimentary Basins. Springer, New York, pp. 133–140. https://doi.org/10.1007/978-1-4612-3492-0_8.
Sahrawat, K.L., 2003. Organic matter accumulation in submerged soils. Adv. Agron. 81, 169–201. https://doi.org/10.1016/S0065-2113(03)81004-0.
Sánchez-Navas, A., Martín-Algarra, A., Eder, V., Reddy, B.J., Nieto, F., Zanin, Y.N., 2008. Color, mineralogy and composition of Upper Jurassic West Siberian glauconite: useful indicators of paleoenvironment. Can. Mineral. 46 (5), 1249–1268. https://doi.org/10.3749/canmin.46.5.00.
Šćavničar, B., Nikler, L., 1976. Vitric tuff in Upper Jurassic Lemeš-deposits of Mt. Velika Kapela (Croatia). Geol. Vjesn. 29, 269–275.
Schmid, S.M., Bernoulli, D., Fügenschuh, B., Matenco, L., Schefer, S., Schuster, R., Tischler, M., Ustaszewski, K., 2008. The Alpine–Carpathian–Dinaridic orogenic system: correlation and evolution of tectonic units. Swiss J. Geosci. 101, 139–183. https://doi.org/10.1007/s00015-008-1247-3.
Schmid, S.M., Fügenschuh, B., Kounov, A., Matenco, L., Nievergelt, P., Oberhänsli, R., Pleuger, J., Schefer, S., Schuster, R., Tomljenović, B., Ustaszewski, K., van Hinsbergen, D.J.J., 2020. Tectonic units of the Alpine collision zone between Eastern Alps and western Turkey. Gondwana Res. 78, 308–374.
Schmid, D.U., Leinfelder, R.R., 1996. The Jurassic *Lithocodium aggregatum–Troglotella incrustans* foraminiferal consortium. Palaeontology 39, 21–52.
Shaheen, S.M., Alessi, D.S., Tack, F.M.G., Ok, Y.S., Kim, K.H., Gustafsson, J.P., Sparks, D. L., Rinklebe, J., 2019. Redox chemistry of vanadium in soils and sediments: interactions with colloidal materials, mobilization, speciation, and relevant environmental implications - a review. Adv. Colloid Interface Sci. 265, 1–13. https://doi.org/10.1016/j.cis.2019.01.002.
Šinkovec, B., 1974. Jurski boksiti zapadne Istre. Geol. Vjesn. 27, 217–226.
Slonimskaya, M.V., Besson, G., Dainyak, L.G., Tchoubar, C., Drits, V.A., 1986. Interpretation of the IR spectra of celadonites and glauconites in the region of OH-stretching frequencies. Clay Miner. 21, 377–388.
Środoń, J., 1980. Precise identification of illite/smectite interstratifications by X-ray powder diffraction. Clays Clay Miner. 28 (6), 401–411.
Środoń, J., 2006. Identification and quantitative analysis of clay minerals. Dev. Clay Sci. 1765–1787. https://doi.org/10.1016/S1572-4352(05)01028-7.
G. Stoops Guidelines for Analysis and Description of Soil and Regolith Thin Sections Vol. 184 2021 John Wiley & Sons.
Taylor, S.R., McLennan, S.M., 1985. The continental crust: its composition and evolution. An examination of the geochemical record preserved in sedimentary rocks, Blackwell, Oxford, p. 312.
Tišljar, J., 1986. Postanak crnih oblutaka i ulomaka ("black pebbles") u periplimskim vapnencima titona zapadne Istre i barema otoka Mljeta. Geol. Vjesn. 39, 75–94.
Van Hinsbergen, D.J.J., Torsvik, T.H., Schmid, S.M., Maţenco, L.C., Maffione, M., Vissers, R.L.M., Gürer, D., Spakman, W., 2020. Orogenic architecture of the

Mediterranean region and kinematic reconstruction of its tectonic evolution since the Triassic. Gondwana Res. 81, 79–229.
Védrine, S., Strasser, A., Hug, W., 2007. Oncoid growth and distribution controlled by sea-level fluctuations and climate (Late Oxfordian), Swiss Jura Mountains. Facies 53, 535–552. https://doi.org/10.1007/s10347-007-0114-4.
Velić, I., 2007. Stratigraphy and palaeobiography of Mesozoic benthic foraminifera of the Karst Dinarides (SE Europe). Geol. Croat. 60, 1–113.
I. Velić D. Matičec J. Tišljar I. Vlahović Opći prikaz geološke građe Istre (A review of the geology of Istria). In: Vlahović, I., Velić, I. (Eds.), Excursion Guide-Book, 1st Croatian Geological Congress Zagreb1995a 5 30 (includes English summary).
Velić, I., Tišljar, J., 1988. Litostratigrafske jedinice u dogeru i malmu zapadne Istre (zapadna Hrvatska, Jugoslavija). Geol. Vjesn. 41, 25–49.
Velić, I., Tišljar, J., Vlahović, I., Velić, J., Koch, G., Matičec, D., 2002. Palaeogeographic variability and depositional environments of the Upper Jurassic carbonate rocks of Velika Kapela Mt. (Gorski Kotar Area, Adriatic Carbonate Platform, Croatia). Geol. Croat. 55 (2), 121–138.
Vitzthum, M.A., Gawlick, H.J., Sachsenhofer, R.F., Neumeister, S., 2022. Changing depositional environments in the semi-restricted Late Jurassic Lemeš Basin (Outer Dinarides; Croatia). Facies 68 (1), 2.
Vlahović, I., Tišljar, J., Velić, I., 1994. Influence of synsedimentary tectonics and eustatic changes on deposition of the Cenomanian platform carbonates in Istria (Western Croatia). Geol. Mediterr. 21 (3–4), 177–180. https://doi.org/10.3406/geolm.1994.1561.
Vlahović, I., Tišljar, J., Velić, I., Matičec, D., 2005. Evolution of the Adriatic Carbonate Platform: palaeogeography, main events and depositional dynamics. Palaeogeogr. Palaeoclimatol. Palaeoecol. 220 (3–4), 333–360. https://doi.org/10.1016/j.palaeo.2005.01.011.
I. Vlahović J. Tišljar I. Velić D. Matičec P. Skelton T. Korbar L. Fuček Main events recorded in the sedimentary succession of the Adriatic Carbonate Platform from Oxfordian to the upper Santonian in Istria (Croatia). In: Vlahović, I., Tišljar, J. (Eds.), Evolution of Depositional Environments from the Palaeozoic to the Quaternary in the Karst Dinarides and the Pannonian Basin, Opatija, Field Trip Guidebook, Zagreb,22nd IAS Meeting of Sedimentology 2003 19 58.
Vlahović, I., Velić, I., Matičec, D. 2023. A brief introduction to the geology of Istria. In: Fio Firi, K. Čobić, A. (Eds.), Excursion Guide-book, 7th Croatian Geological Congress, Zagreb. 1-13.
Vlahović, I., Velić, I., Tišljar, J., Matičec, D., Dragičević, I., 2001. Malmian palaeogeography of the Adriatic Carbonate Platform as a consequence of the synsedimentary tectonics. In: Velić, I. (Ed.), Dragičević, I. The first Scientific Meeting, Carbonate Platform or Carbonate Platforms of Dinarides, Abstract Book, pp. 51–54.
Wanty, R.B., Goldhaber, M.B., 1992. Thermodynamics and kinetics of reactions involving vanadium in natural systems: accumulation of vanadium in sedimentary rocks. Geochim. Cosmochim. Acta 56 (4), 1471–1483. https://doi.org/10.1016/0016-7037(92)90217-7.
Wei, W., Algeo, T.J., 2020. Elemental proxies for paleosalinity analysis of ancient shales and mudrocks. Geochim. Cosmochim. Acta 287, 341–366. https://doi.org/10.1016/j.gca.2019.06.034.
M.J. Wilson The origin and formation of clay minerals in soils: past, present and future perspectives. Clay Miner., 34 1 1999 7 10.1180/000985599545957.
Zanin, Y., Eder, V., Zamirailova, A., 2004. Bacterial forms in glauconites from Upper Cretaceous deposits of the West Siberian Plate. Russ. Geol. Geophys. 45 (6), 774–777. http://pubs.geoscienceworld.org/rgg/article-pdf/45/6/774/5157059/s11jun04.pdf.
Zviagina, B.B., Drits, V.A., Dorzhieva, O.V., 2020. Distinguishing features and identification criteria for K-dioctahedral 1M micas (Illite-aluminoceladonite and illite-glauconite-celadonite series) from middle-infrared spectroscopy data. Minerals 10 (2), 153. https://doi.org/10.3390/min10020153.

Paper 3

***Perković, I.**, Martinuš, M., Cvetko Tešović, B., Vlahović, I., Matešić, D., Newton, R.J., He, T., Šoufek, M., Razum, I. & Durn, G. (2024): Tracing the evolution of the world's first mined bauxite from palaeotopography to pyritization: Insights from Minjera deposits, Istria, Croatia. Geologia Croatica, 77/2, 159–178,*

Geologia Croatica
Journal of the Croatian Geological Survey and the Croatian Geological Society
2024 | 77/2 | 159–178 | 18 Figs. | www.geologia-croatica.hr

Tracing the evolution of the world's first mined bauxite from palaeotopography to pyritization: Insights from Minjera deposits, Istria, Croatia

Ivor Perković[1,*], Maja Martinuš[2], Blanka Cvetko Tešović[2], Igor Vlahović[1], Darko Matešić[1], Robert J. Newton[3], Tianchen He[3,4], Marin Šoufek[5], Ivan Razum[5] and Goran Durn[1]

[1] University of Zagreb, Faculty of Mining, Geology and Petroleum Engineering, HR-10000 Zagreb, Croatia;
[2] University of Zagreb, Faculty of Sciences, Department of Geology, HR-10000 Zagreb, Croatia
[3] University of Leeds, School of Earth and Environment, LS2 9JT Leeds, United Kingdom
[4] Hohai University, College of Oceanography, 210024 Nanjing, China
[5] Croatian Natural History Museum, HR-10000, Zagreb, Croatia
(*corresponding author: ivor.perkovic@rgn.unizg.hr)

doi: 10.4154/gc.2024.12

Article history:
Manuscript received: April 16, 2024
Revised manuscript accepted: May 29, 2024
Available online: June 21, 2024

Abstract

The Minjera bauxites are the first analysed and mined bauxites in the world. They are a group of pyritised bauxites situated in northern Istria, developed during the subaerial exposure phase which marked a major part of the Late Cretaceous and Palaeocene in northern Istria. In this study, the morphology, petrography, mineralogy, geochemistry as well as stable sulphur isotopes of the D-1 and D-15 deposits from Minjera were studied, as well as the evolution of their bedrock and cover. This study found that those two deposits differ in morphology, mineralogy and geochemistry as a consequence of their different palaeotopographical positions, with the D-1 deposit located at a higher position at the time of its formation compared to D-15, which led to the higher degree of leaching and desilicification in the D-1 deposit. The pyritisation in the studied deposits was a multi-phase process, which began with the deposition of framboidal pyrite and micrometre-sized anhedral pyrite, over which colloform pyrite was precipitated. This indicates that the solutions were initially supersaturated with iron sulphide, saturation of which subsequently changed, as finally euhedral, dendritic and acicular pyrite were deposited, indicating undersaturated conditions. The final stage was marked by deposition of pyrite veins. This formational sequence of pyrites is also supported by stable sulphur isotopes, as the $\delta^{34}S$ values exhibit a wide range from -40.86 to 2.32 ‰, where lower values indicate an open system with an unrestricted sulphate supply in which supersaturated conditions could have been achieved, while the higher values indicate a change towards a closed system with limited sulphate supply. The organic matter necessary for microbial sulphate reduction was derived from the marshy environment established atop of the bauxite. The initial flooding started in the Palaeocene, with the first part of the sequence being deposited under lacustrine conditions, which changed towards fully marine with the deposition of Foraminiferal limestones.

Keywords: Minjera, Istrian Palaeogene bauxites, Pyritisation in karst bauxites, Iron sulphide morphology in karst bauxites, Stable sulphur isotopes in karst bauxites

1. INTRODUCTION

The Minjera bauxites are a unique and historically important group of karst bauxite deposits from Istria, Croatia, as they represent the first locality where bauxite was mined in the world, even though, at that time, it was not known that this material would be named bauxite in the future. The mining activity dates back as far as the 16th century, but was historically recorded only from 1784 until 1824, when the majority of mining activity occurred (D'AMBROSI, 1926). The bauxite ore was used in the production of alum and vitriol, which were obtained after the ore was processed in the production plant. The ore was particularly suitable for the production of these materials as it has a high pyrite content, a very specific feature of these deposits compared to other Palaeogene bauxites in Istria. All this has made these deposits appealing for geological investigations and field excursions, with the first and most complete study being that by ŠINKOVEC et al. (1994), which was followed by brief investigations for field excursions led by DURN et al. (2003, 2006, 2023).

Pyritised bauxites have been documented all over the Mediterranean bauxite belt (BARDOSSY, 1982; DRAGOVIĆ, 1989; ÖZTÜRK et al., 2002; LASKOU & ECONOMOU-ELIOPOULOS, 2007, 2013; RADUSINOVIĆ & PAPADOPOULOS, 2021, ECONOMOU-ELIOPOULOS et al., 2022), and elsewhere (ZARASVANDI et al., 2012; ELLAHI et al., 2015, 2017; CHEN et al., 2022; ZHAO et al., 2023). The pyritisation phase is a consequence of diagenetic changes and is related to the transgression that followed the bauxitisation phase, during which a marshy environment was established on top of the bauxites, promoting the mobilisation of iron and pyrite formation. Pyrite morphology is a useful tool in the palaeoenvironmental and redox reconstructions in sedimentary settings and in the formation of ore deposits (CHEN, 1978;

RAISWELL, 1982; WIGNALL & NEWTON, 1998; BARRIE et al., 2009; HUANG et al., 2020; HE et al., 2022; MEDERSKI et al., 2022; WANG et al., 2022). This is also used as one of the foundations for the reconstruction of the genetic evolution of pyritised bauxites (ÖZTÜRK et al., 2002; LASKOU & ECONOMOU-ELIOPOULOS, 2007, 2013; ZARASVANDI et al., 2012; ELLAHI et al., 2017; CHEN et al., 2022; ZHAO et al., 2023), which is commonly coupled with the use of stable sulphur isotopes allowing the identification of the sulphur source and its evolutionary pathway which led to pyrite formation (ÖZTÜRK et al., 2002; LASKOU & ECONOMOU-ELIOPOULOS, 2007; CHEN et al., 2022; ZHAO et al., 2023). Such an approach was also used here through careful analysis of iron sulphide morphologies and sulphur isotopes, in an attempt to produce improved reconstruction of diagenetic changes that led to the pyritisation of the Minjera bauxites. Since the flooding of the bauxite and its alteration in a marshy environment is one of the key aspects of those deposits, the Kozina beds from the immediate cover of the bauxites were also studied, in order to better understand the palaeoenvironmental changes that followed the subaerial exposure phase. To additionally enhance the reconstruction of the diagenetic changes that the Minjera bauxite experienced, as well as the original conditions in which they formed, the trace and rare earth elements (REE) were carefully studied. Namely, their behaviour has been extensively used to reconstruct the genesis of different bauxite deposits, since they respond to physico-chemical changes, intensity of chemical weathering as well as changes in pH and redox potential (MAKSIMOVIĆ et al., 1991; MAKSIMOVIĆ & PANTÓ, 1991; MONGELLI, 1997; ABEDINI & CALAGARI, 2014; MONGELLI et al., 2014, 2017; ELLAHI et al., 2017; ABEDINI et al., 2018, 2019; YANG et al., 2019; TOMAŠIĆ et al., 2021).

Overall, this study aims to enhance the current knowledge regarding the historically important Minjera bauxites and Istrian Palaeogene bauxites in general, through the construction of an updated genetic model based on different analytical methods, which should also prove useful in the future studies of pyritised bauxites elsewhere.

2. REGIONAL GEOTECTONIC SETTING

Palaeogene bauxites are common throughout northern, eastern and southern Istria, and their stratigraphic position fits within the widespread Perimediterranean bauxitization event resulting in formation of a vast bauxite belt stretching from Hungary through Slovenia, Croatia, Bosnia and Herzegovina, Montenegro, and Albania to Greece.

This widespread bauxitization event coincided with the Late Cretaceous closure of the Vardar Ocean (SCHMID et al., 2008, 2020; van HINSBERGEN et al., 2020), which led to the formation of a large foreland basin in the area of today's Internal Dinarides, causing the tectonic uplift of the Adriatic Carbonate Platform area due to the development of the flexural forebulge in response to the overburden pressure generated by the advancing nappes (OTONIČAR 2006, JEŽ & OTONIČAR, 2018). The emerged areas in the flexural forebulge served as the environment in which the Palaeogene bauxites of Istria and Dalmatia formed. Consequently, these bauxites belong to those formed in collisional settings, known as type-1 bauxites according to D'ARGENIO & MINDSZENTY (1995).

The duration of subaerial exposure between the Cretaceous and Palaeogene in Istria lasted mostly between 28 My (in southern Istria and Mt. Učka klippe) and 40 My (in northern Istria). However, in the Western Istrian Anticline subaerial exposure locally persisted for more than 75 My, as indicated by erosional remnants of Eocene Foraminiferal limestones which locally transgressively cover different levels of karstified Lower Cretaceous limestones (the oldest being Valanginian in age; MATIČEC et al., 1996). More than 10,000 bauxite occurrences and small bauxite deposits are known in Istria (Milan Mihovilović, pers. comm.), serving as evidence of widespread and intense bauxitization during this period. As deformation continued, rapid subsidence of the foreland area along the partially exposed former Adriatic Carbonate Platform commenced, leading to restoration of marine carbonate production in the form of Foraminiferal limestones, followed by deepening, recorded by transitional marls and turbidites (VLAHOVIĆ et al., 2005).

3. GEOLOGICAL SETTING

The Minjera bauxites are located in the easternmost part of the northern Istrian Buzet–Savudrija Anticline (Fig. 1), also known as the Buje Anticline (BERGANT et al., 2020). Bauxites are situated on karstified Upper Cenomanian limestones belonging to the Milna Fm. (BERGANT et al., 2020), with their hanging wall comprising the freshwater to brackish Palaeogene Kozina beds (ŠINKOVEC et al., 1994).

During the Albian, relatively uniform shallow-marine environments predominated over the entire area of the Adriatic Carbonate Platform. However, in northern Istria, significant changes in depositional environments occurred during the early Cenomanian (VLAHOVIĆ et al., 1994). In the western part of northern Istria, shallow marine sedimentary environments persisted, while in the central part, prograding sand bars composed of finely crushed rudist and chondrodont bioclasts formed. In contrast, the eastern part of northern Istria, including the study area, experienced a deepening of sedimentary environments. There, in addition to typical lagoonal limestones, hummocky cross-stratified deposits occasionally occurred in the offshore-transition zone, along with limestones reflecting pelagic influences containing calcisphaeres, silicisponge spicules, algae, and rare planktonic foraminifera (VLAHOVIĆ et al., 1994). Towards the end of the Cenomanian, a gradual regression occurred throughout northern Istria, leading to a regional unconformity in the area, although pelagic influences persisted occasionally in the eastern part.

Throughout the entire area of the Savudrija–Buzet Anticline, the topmost parts of the Upper Cenomanian limestones are heavily karstified due to subaerial exposure. In the studied area of the Mirna River valley, an irregularly karstified surface is covered with numerous small bauxite bodies and transgressive Palaeogene beds. Intense karstification occurred especially along fractured zones, resulting in numerous smaller and larger sinkholes and decametre-sized karstic canyons that served as sediment traps for the accumulation of the source material for bauxite formation. The red colour and common oolitic structure of the Palaeogene

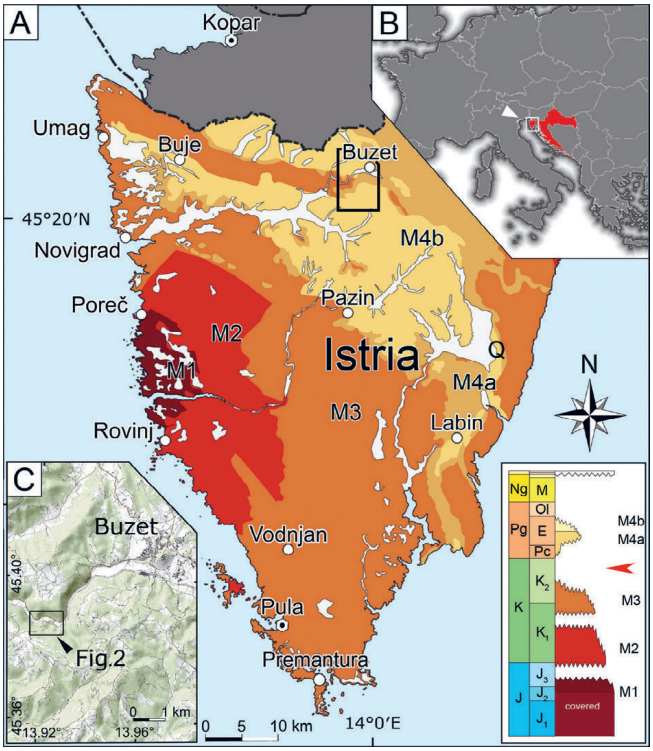

Figure 1. Geological map of the Istrian peninsula and its position in Europe. A – Geological map of Istria, modified after VELIĆ et al. (1995) with the schematic geological column. Legend: M1 – 1st Megasequence (lower Bathonian–lower Kimmeridgian); M2 – 2nd Megasequence (upper Tithonian–lower/upper Aptian); M3 – 3rd Megasequence (lower/upper Albian–upper Santonian); M4a – Carbonate deposits of the 4th Megasequence (mostly lower–middle Eocene); M4b – Clastic deposits of the 4th Megasequence (middle–upper Eocene); Q – Quaternary deposits. Position of the Palaeogene bauxites on the schematic geological column is indicated by a red arrow. (B) Map of central, western and southern Europe with the indicated location of Istrian peninsula. (C) Map of Buzet area and geographic position of the Minjera bauxites.

bauxites in northern Istria indicate highly elevated and intensely karstified carbonate bedrock, typical of vadose lithofacies in carbonate terrains uplifted at least several dozen metres above sea level (D'ARGENIO & MINDSZENTY, 1995). Some bauxite occurrences in northern Istria were exposed to reduced pore waters during the subsequent transgression, resulting in the reduction of iron oxides and the precipitation of iron sulphides. In some cases entire bauxite bodies were exposed to this process, resulting in their complete transformation into grey and pyritised bauxite, as observed in the Minjera bauxites. The transgression was marked by deposition of the Palaeogene Kozina beds directly overlying the bauxites, deposited in freshwater and brackish ponds developed in a network of bauxite-filled sinkholes, empty palaeodepressions, and vadose canyons. The Kozina beds in this area consist of a sequence of bituminous, gastropod-rich limestones with some coal seams. The presence of charophyte oogonia in most layers confirms a freshwater to brackish-water depositional environment, although their alternation with layers abundant in milliolids indicates periodic marine incursions during their deposition (ŠINKOVEC et al., 1994). The Kozina beds are overlain by Foraminiferal limestones, indicating a gradual transition to open marine environments on the slopes of the newly formed Pazin foreland basin to the south.

4. MATERIALS AND METHODS

After detailed investigation of all deposits from the Minjera locality, only two deposits (D-1 and D-15; Fig. 2) were deemed suitable for further investigation, since they still contained enough unweathered bauxite. These two deposits were selected for sampling, with the addition of the red bauxite sample from the tailing heaps left by the historic mining activity, which was found next to the D-14 deposit (Fig. 2). In the D-15 deposit most bauxite samples were collected from the sides of the deposit, as most of the bauxite was completely mined out. Two smaller profiles (Profile 1 – Fig. 2A: D15-1, D15-2, D15-3 and D15-10, Profile 2 – Fig. 2B: D15-5, D15-6, D15-7 and D15-8) encompassing the upper metre of the bauxite were sampled, as well as a portion close to the bedrock (D15-4), and the top section of the bauxite in the adit (D15-9). In the D-15 deposit, the footwall and the hanging wall of the bauxite were sampled over a total thickness of 6.1 m (Figs. 4, 6C). In the D-1 deposit, samples were collected in the lower section of the deposit, as the upper section was not accessible. Most of the samples were collected on the eastern side of the deposit (D1-1 to D1-9, Fig. 6), while additional samples were collected from the central part of the deposit (D1-10 to D1-12; Fig 6D). In this deposit, only the bedrock of the deposit was sampled. Red bauxite was collected from tailing heaps near one of the historic processing plants (Fig. 2), as it was previously located in the centre of the pyritised deposits but it was mined out from all deposits (ŠINKOVEC et al., 1994).

Thin-sections were prepared from all the limestone and bauxite samples. Additionally, thin-sections were made from separated heavy and light mineral fractions using sodium polytungstate (SPT) solution (3.0 g/cm^3) after obtaining granulometric fractions ranging from 250 to 63 μm from both the grey and the red bauxite. Prior to sieving, iron oxides from the red bauxite underwent dissolution using the Dithionite-Citrate-Bicarbonate method (MEHRA & JACKSON, 1960) to release individual mineral grains. All thin sections were

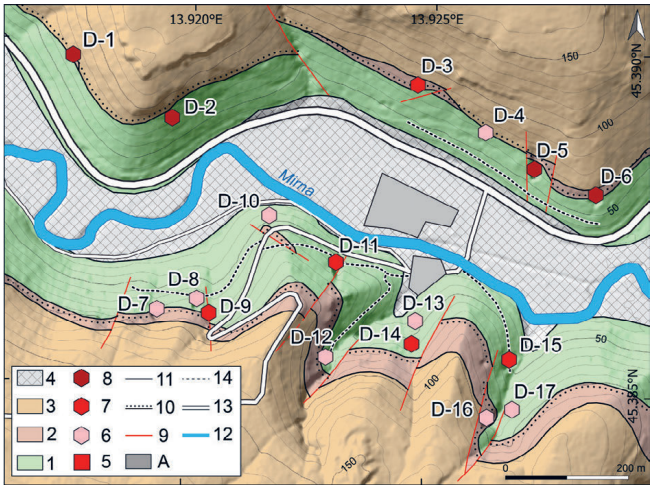

Figure 2. Geological map of the Minjera area with different types of bauxite deposits indicated, modified after ŠINKOVEC et al (1994). Legend: 1 – Upper Cenomanian limestones; 2 – Palaeocene Kozina beds; 3 – Eocene Foraminiferal limestones; 4 – Quaternary; 5 – Red bauxite tailing heaps; 6 – Sinkhole bauxite deposits; 7 – Small canyon bauxite deposits; 8 – Large canyon bauxite deposits; A – Remnants of the processing plants and infrastructure from the past mining activities.

analysed using the OPTIKA B-1000 series polarizing microscope, equipped with the OPTIKA C-P6 FL camera and OPTIKA PROVIEW software. Bauxites were analysed following the micromorphological and petrographic methodologies outlined by BARDOSSY (1982), while sedimentological and micropalaeontological analyses of limestone sections were performed according to FLÜGEL (2004). For the additional study of iron sulphide morphology and general mineralogy SEM-EDS was employed on three samples, using the TESCAN VEGA GMU SEM. EDS analysis was also used, and was available using live SEM scanning window of Essence™ software using a fully integrated energy dispersive X-ray spectroscopy (EDS) detector.

X-ray powder diffraction (XRPD) analysis was conducted on most bauxite samples. A portion of each sample was gently crushed and sieved through a 0.5 mm sieve. Subsequently, samples were milled in a McCrone micronizing mill for 15 minutes with a mixture of 2 ml of the sieved material and 7 ml of isopropyl alcohol. The resulting slurry was air-dried and disaggregated in an agate pestle and mortar. Dried samples were side-loaded to ensure random orientation and uniform grain size, essential for accurate Rietveld refinement. Rietveld refinement was performed using Profex version 5.2.4 software (DOEBELIN & KLEEBERG, 2015), utilizing structural data from built-in files and the crystallography open database (GRAULIS et al., 2009).

To determine concentrations of major, minor, trace, and rare earth elements, five bauxite samples from both deposits and one red bauxite sample were selected. These samples were analysed using inductively-coupled-plasma mass-spectrometry (ICP-MS) at the Bureau Veritas, Canada commercial laboratory. Analysis was performed using the lithium metaborate/tetraborate fusion and nitric acid digestion. Total sulphur and carbon values were measured separately from other major oxides. Trace element and rare earth element (REE) values were normalized to the upper continental crust values according to TAYLOR & MCLENNAN (1985).

Samples from both deposits were selected for stable sulphur isotope analysis. The procedure started with silver sulphide extraction from pyrite in the samples using the chromous chloride distillation method (CANFIELD et al., 1986). Sulphur-isotope analysis was undertaken on the resulting silver sulphide precipitates, which was performed on an Elementar vario PYRO cube linked to a GV Isoprime mass spectrometer in continuous flow mode, in the Cohen Geochemistry Laboratories of the School of Earth and Environment, University of Leeds. About 0.150 mg of silver sulphide was weighed and packed into tin cups, which was afterwards flash-combusted at 1150 °C in the presence of pure research grade O_2 and helium carrier gas to produce SO_2. Excess O_2 was consumed by reaction with copper wires at 850 °C and water was removed by a Sicapent trap. Subsequently, SO_2 was separated from other gases using a temperature-controlled trap and purge column. Results were calibrated to the Vienna-Canyon Diablo Troilite (V-CDT) using a seawater laboratory standard (SWS-3) and a chalcopyrite inter-lab standard (CP1), with their respective values of +20.3 and -4.56 ‰, respectively. The calibration of this material was in turn performed using the IAEA S-3 (-32.06 ‰) international standard.

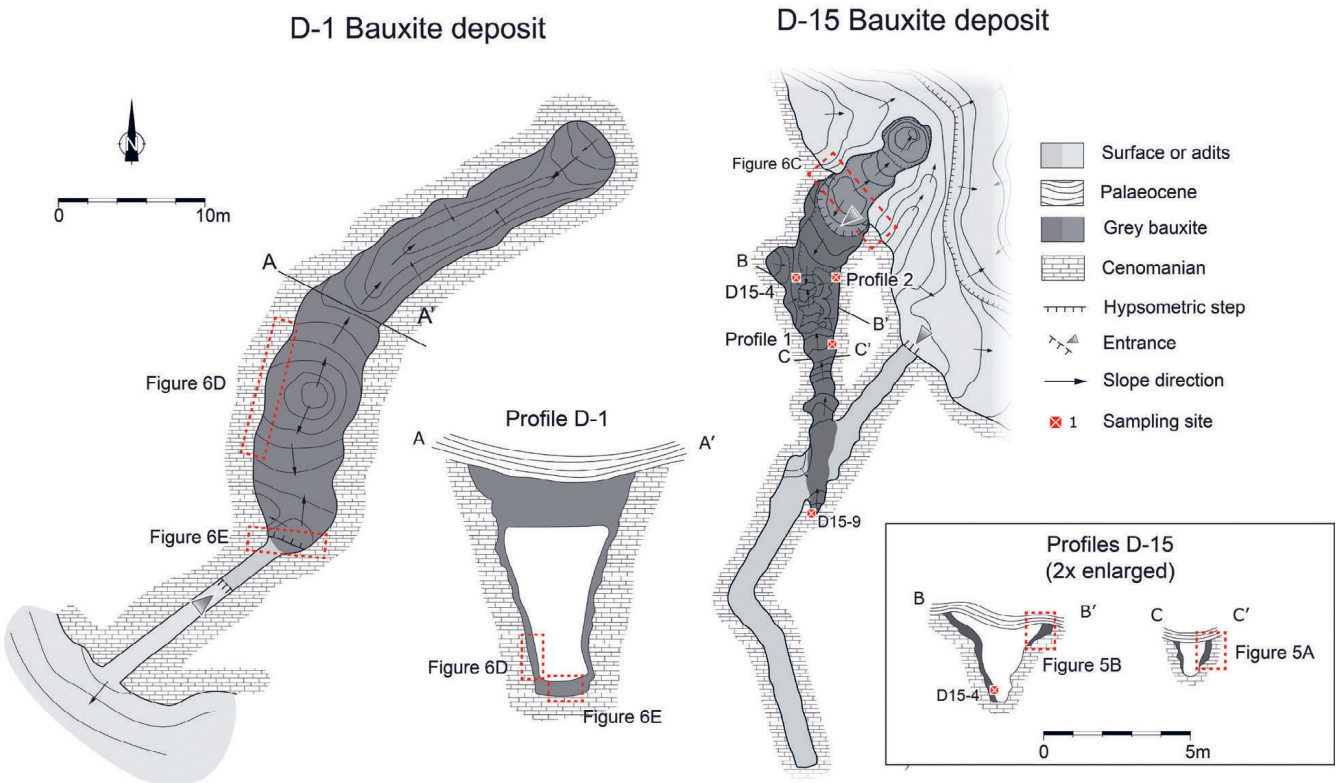

Figure 3. Plans of the D-1 and D-15 deposits with their respective cross-sections and sampling sites. Note that the B–B' and C–C' cross-sections are enlarged with respect to both plans and A–A' cross-section, in order to demonstrate the sampled profiles and sample positions more clearly.

5. RESULTS

5.1. Outcrop and field descriptions

5.1.1. Bauxite bedrock and cover – lithostratigraphy and biostratigraphy

The Minjera section comprises the 3.6 m thick succession of Upper Cenomanian beds underlying the regional unconformity and the D-15 Bauxite deposit, and the 3.4 m thick Palaeogene beds overlying the bauxite (Fig. 4). Based on the macro- and microscopic lithological and microfossil features, four lithofacies types (LF1–LF4) were differentiated (Fig. 4). Peloidal-bio-intraclastic wackestone–packstone to packstone–grainstone with small benthic foraminifera, fragmented and micritized bivalve shells and in places small pelagic bioclasts

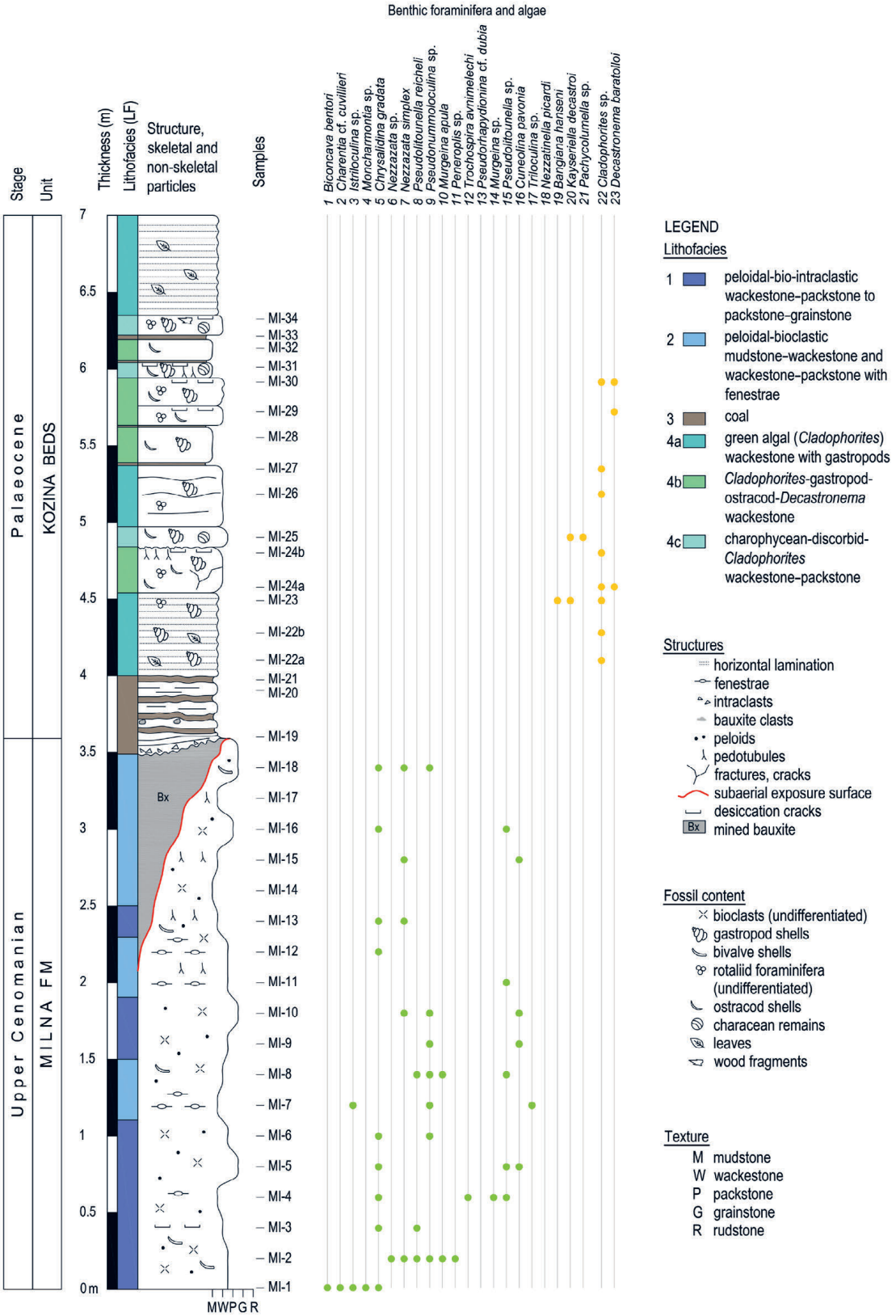

Figure 4. A stratigraphic column of the Minjera section (D-15 Bauxite bedrock and cover) with structures, fossil content, lithofacies and biostratigraphy.

(LF1), in the lower part of the Cenomanian strata indicate formation in subtidal environments of an inner carbonate platform, with occasional input of material from the open sea (Fig. 5A, B). The upper part of the Cenomanian strata comprises peloidal-bioclastic mudstone–wackestone and wackestone–packstone with similar fossil content (LF2), but the presence of fenestrae, circumgranular cracks and pedotubules indicates shallowing of the depositional environment (very shallow subtidal and intertidal) and occasional subaerial exposures preceding the prolonged terrestrial phase marked by the regional unconformity (Fig. 5C–E). A microfossil assemblage composed of various benthic foraminifera, among which the most important taxa are *Chrysalidina gradata*, *Nezzazata simplex*, *Pseudolituolunella reicheli*, *Trochospira avnimelechi*, *Pseudonummuloculina* sp., and *Cuneolina pavonia*, indicates the upper Cenomanian age of the strata underlying the regional unconformity at the studied Minjera locality (Fig. 4).

The irregular unconformity and the D-15 Bauxite deposit is overlain by decimetre-thick beds of brownish to dark grey lacustrine limestones (LF4; Figs. 4, 6C), which include centimetre- to decimetre-thick coal interbeds in their base, formed in freshwater marsh (LF3; Fig. 5F). The contact between the bauxite and the cover sequence is marked by dark brown, organic matter- and coal-rich bauxite mixed with large carbonate pebbles and in places boulders likely eroded from the surrounding carbonate rocks and embedded within the top sections of the bauxites during the initial flooding of the area. In their lower part, the lacustrine limestones are composed of green algal (*Cladophorites*) wackestone with gastropod shells and rare small rotalids indicating lacustrine near-shore and shore depositional settings (LF4a; Fig. 5G, H). The middle part is composed of wackestone with *Cladophorites*, gastropod shells, *Decastronema*, ostracods, and discorbids commonly with pedotubules and in places desiccation cracks, indicating a lake shore environment with plants (LF4b; Fig. 5I). In the

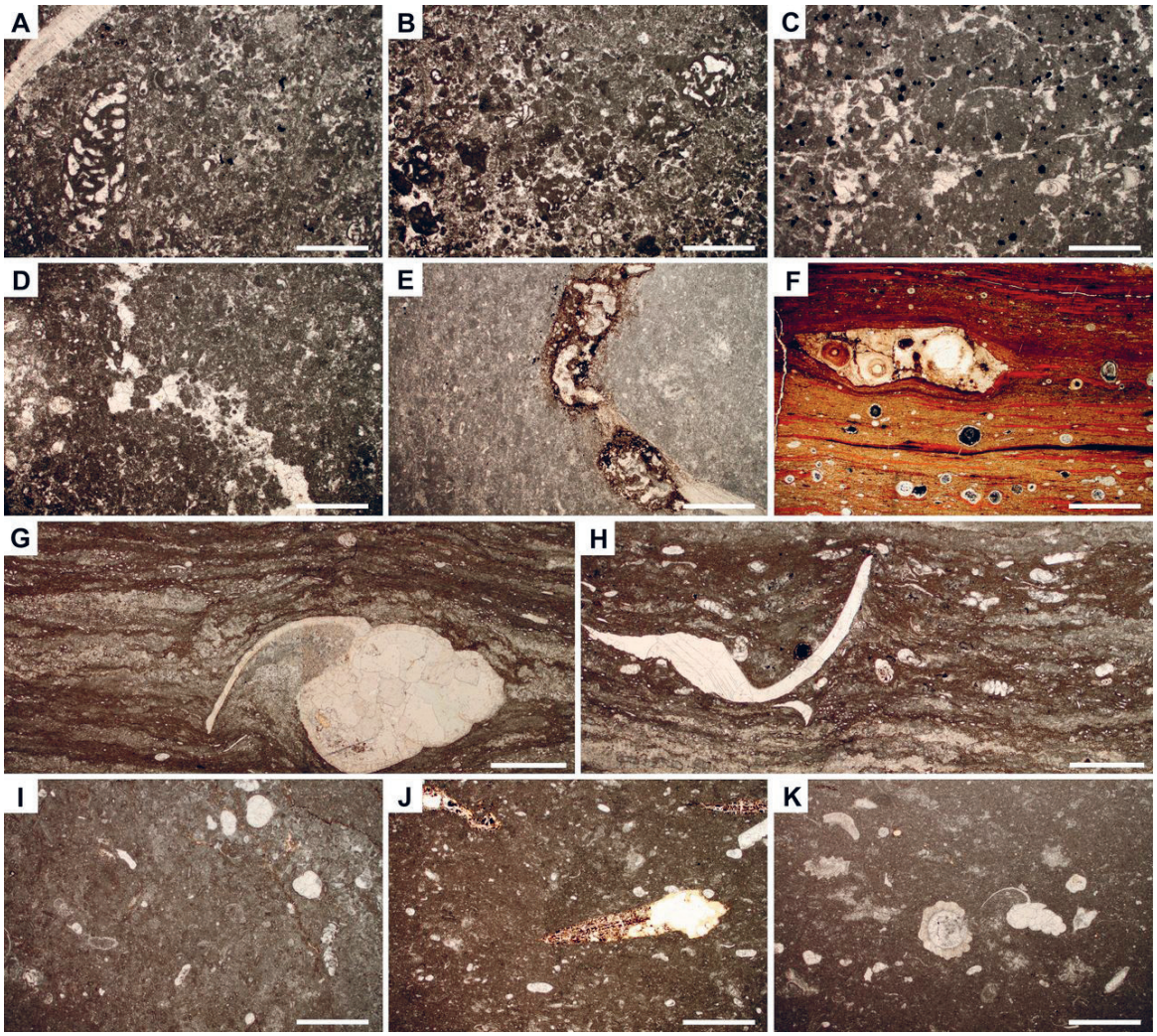

Figure 5. Photomicrographs of the lithofacies (LF) in the Minjera bauxite bedrock and cover. A – LF1: Peloidal packstone-grainstone with benthic foraminifera (sample MI-6). B – LF1: Peloidal-bio-intraclastic packstone-grainstone (sample MI-10). C – LF2: Bioclastic mudstone with circumgranular cracks and rare benthic foraminifera (sample MI-8). D – LF2: Fenestral peloidal mudstone-wackestone with rare benthic foraminifera (sample MI-16). E – LF2: Indistinctly laminated peloidal-bioclastic wackestone with pedotubules (sample MI-17). F – LF3: Laminated coal with iron ooids (pisoids) (sample MI-20). G – LF4a: Laminated green algal (*Cladophorites*) mudstone-wackestone (bafflestone) with gastropod shells (sample MI-22a). H – LF4a: Laminated green algal (*Cladophorites*) mudstone-wackestone with gastropod shells and rotalid foraminifera (sample MI-23). I – LF4b: *Decastronema*-ostracod-discorbid wackestone (sample MI-24a). J – LF4c: Discorbid-charophycean wackestone (sample MI-34). K – LF4c: Discorbid-charophycean wackestone with wood fragments (sample MI-34). Size of the scale bar is 1 mm on all photomicrographs.

upper part of the lacustrine limestones, charophycean-discorbid wackestone prevails with discorbids, charophycean oogonia and thalli parts, *Cladophorites*, gastropod and ostracod shells, and in places wood fragments (LF4c; Fig. 5J, K). Such fossil remains indicate similar lacustrine near-shore settings including brackish environments of a coastal lake. Small rotalid foraminifera often present in thin laminae in all lithofacies were probably transported by storm events from neighbouring marine environments. The microfossil assemblage including *Bangiana hanseni, Kayseriella decastroi* and fragments of *Pachycolumella* indicates a Palaeocene age of the strata directly overlying the D-15 Bauxite deposit at the studied Minjera locality (Fig. 4).

5.1.2. Description of bauxite deposits

Three main deposit types were distinguished based on field observations (Fig. 2): the large canyon (elongated, deeper than 10 metres and between 20 and 40 metres in its longer axis), small canyon (elongated, less than 10 metres deep with the longer axis shorter than 20 metres) and sinkhole deposits (spherical, less than 10 metres deep and smaller than 10 metres in diameter). Most of the smaller canyon and sinkhole deposits are located south of the Mirna River, while most of the large canyon deposits are located north of the Mirna River. The D-1 deposit is of the large canyon type, being very steep, almost 40 metres long and thicker than 15 metres (Figs. 2 and 3), while the D-15 deposit represents the smaller canyon type, as it is less steep, up to 20 metres long and up to five metres thick (Figs. 2 and 3). The bauxite from these two deposits also differs macroscopically, with those from the D-15 being mostly grey (Fig. 6A and B) and those from the D-1 deposit being darker due to the higher pyrite content (Fig. 6D and F). Coal-rich bauxite can be found on top of the bauxite in both D-1 (Fig. 6A and B) and D-15 deposits, but it has only been sampled in the D-15 deposit. In the D-15 and other deposits, it can be seen that a number of carbonate clasts are embedded within the bauxite in its uppermost part (Fig. 6A and B). Several pyritised bauxite types can be discerned visually: the "striped" or "spotted" bauxite composed of a grey matrix within which large veins or spots of iron sulphides are visible (Fig. 6G), grey bauxite containing visibly very little pyrite (Fig. 6A, B, D, F), and black bauxite completely impregnated with iron sulphides (Fig. 6D and F). Pyritised root relics have also been observed but only in the grey bauxite from the D-15 deposit.

5.2. Petrography and micromorphology

All bauxite samples from D-1 and D-15 deposits as well as sampled red bauxite have oolitic texture (Fig. 7A–F), with varying proportions of ooids (sensu BARDOSSY, 1982) and the pelitomorphic matrix. The ooids in the red bauxite are between 50 and 200 μm in size, composed of iron oxide-rich and oxide-poor laminae, with the majority having an iron oxide-poor outer cortex (Fig. 7A). Large bauxite clasts can also be found in the red bauxite (Fig. 7A), which are usually richer in iron oxides than the surrounding matrix, but occasionally have a deferrified outer rim. The aforementioned iron oxide enrichment and depletion in clasts and ooids was preserved through pyritisation in samples from both the D-1 and D-15 deposits, as the pyritised ooids display an alternation of pyrite-rich and pyrite-poor laminae (Fig. 7B), while bauxite clasts commonly contain more iron sulphides than the surrounding matrix (Fig. 7C). In places, in the D-15 deposit, the ooids are

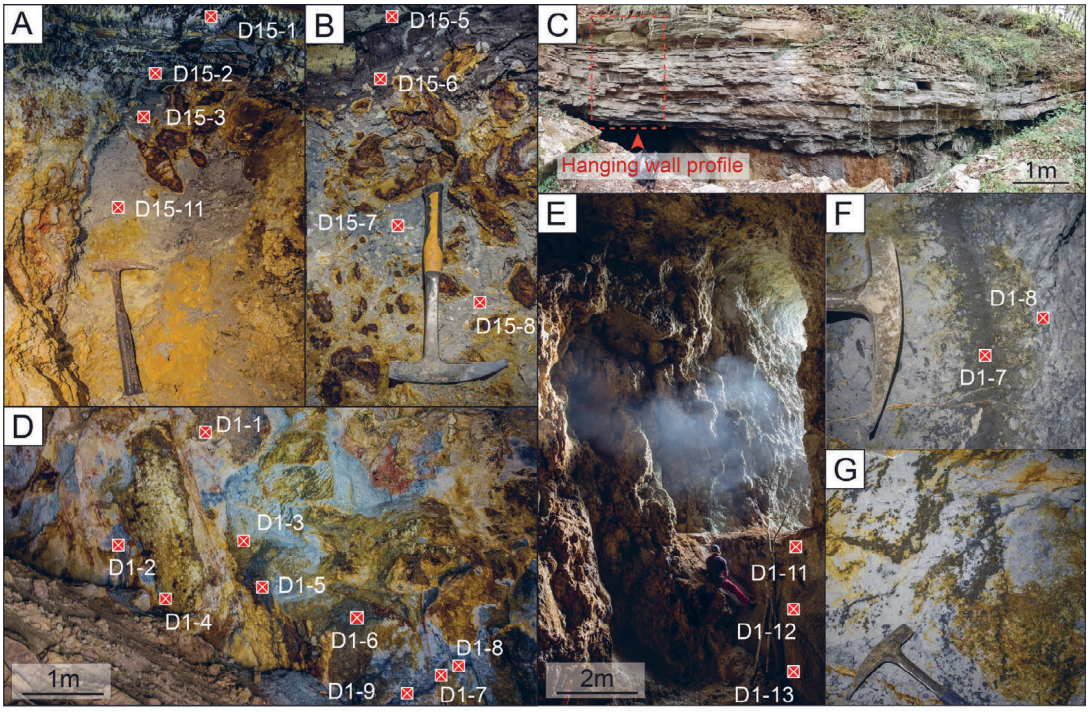

Figure 6. Photographs of the sampled profiles and sample positions. A – Profile 1 in the D-15 deposit with sample locations, composed of grey and coal-rich bauxite; B – Profile 2 in D-15 deposit with sample locations, composed of grey and coal-rich bauxite; C – Bauxite hanging wall composed of Kozina limestones in the D-15 deposit, with indicated position of the sampled hanging wall; D – Profile 1 in the D-1 deposit with indicated sample positions; E – entrance into the adit exposing D-1 deposit with indicated sample positions on the second profile; F – zonation of pyrite-poor and pyrite-rich bauxite with indicated sample positions; G – "striped" and "spotty" bauxite, composed of pyrite-poor bauxite and veins or spots of pyrite-rich bauxite.

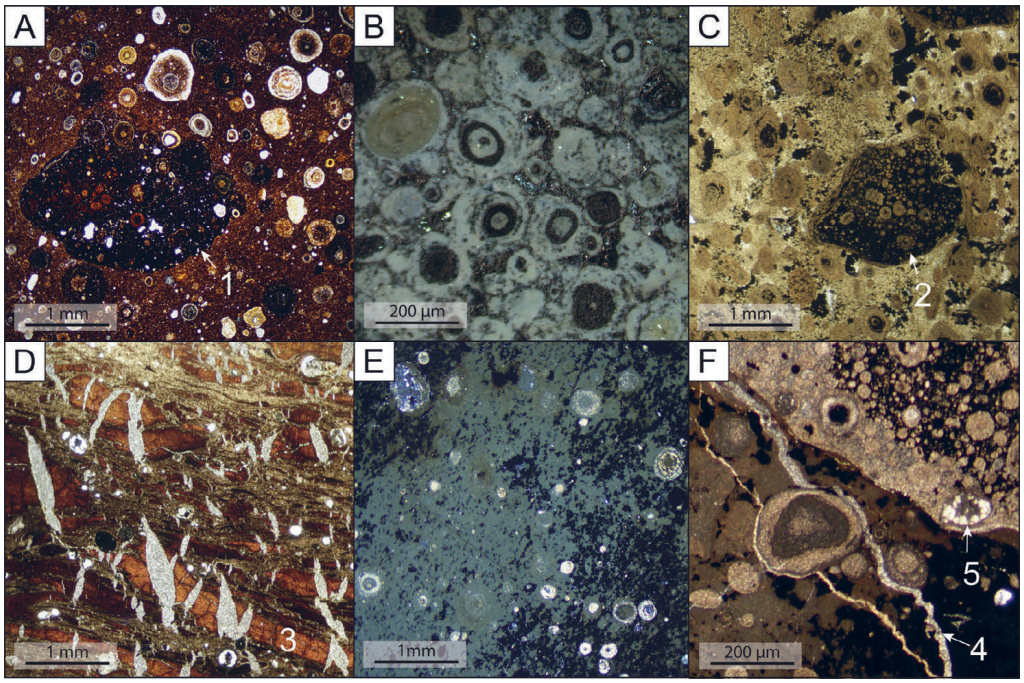

Figure 7. Photomicrographs of red, pyritised and coal-rich bauxite in plane-polarised (PPL)B or cross-polarised light (XPL). A – red bauxite with numerous ooids with visible deferrification in their cortices or lamellae, and a clast of iron-oxide rich oolitic bauxite (1), sample RB (PPL); B – kaolinitised and pyritised ooids, sample D1-3 (XPL); C – pyritised oolitic bauxite with a completely pyritised bauxite clast (2), sample D15-9 (PPL); D – coal-rich bauxite, composed of fan-like alternation of coal intercalations (3), reworked bauxite material and ooids, with the coal lenses cross-cut by gypsum veins, sample D1-6 (PPL); E – Pyritised bauxite with visible ooids composed of boehmite, sample D1-3 (XPL); , F – Pyritised bauxite clast and diaspore veins (4) and nests (5), sample D15-9 (PPL).

completely replaced by kaolinite (Fig. 7B). Organic matter and coal were also detected, but only in the coal-rich bauxite, alternating with reworked bauxite clasts and ooids (Fig. 7D). The samples from the D-15 deposit contain less aluminium oxide minerals than those from the D-15 deposit. The aluminium oxide minerals are diaspore and boehmite in both deposits. These two minerals make up the iron-poor laminae in ooids (Fig. 7E) and they are also likely present in the cryptocrystalline matrix. Besides the ooids, diaspore is also present in veins or nests (Fig. 7F). The two deposits also differ in their iron sulphide content, the D-1 deposit contains much more iron sulphide, while the D-15 deposit contains less iron sulphide. The iron sulphides are mainly present as pyrite in both deposits with the sporadic occurrence of marcasite. Pyrite displays an array of different morphologies, most of which are present in both deposits. It is present as framboids with a diverse size range between 5 and 40 µm, which are either present individually in the matrix (Fig. 8A), or are aggregated (Fig. 8C) and concentrated within the pores between ooids or in the matrix. Framboids are commonly associated with micrometre-sized anhedral pyrite (MSAP, Fig. 8B), which also impregnates large portions of the bauxite matrix in some samples (Figs. 4C and D), as well as ooid lamellae and bauxite clasts (Fig. 8D). Both the framboids and MSAP are frequently overgrown with colloform pyrite, which is present as: 1 – impregnations of MSAP (Fig. 8D), 2 – thin overgrowths of individual framboids (Fig. 8A), and 3 – large-scale impregnations, overgrowths and replacements of MSAP and framboids in the matrix (Fig. 8C), ooid laminae (Fig. 8D) or bauxite clasts. Colloform pyrite also forms banded textures in places and is commonly overgrown with euhedral pyrite (Fig. 8F). Euhedral pyrite can be also found as a replacement of individual framboids within the matrix (Fig. 8E), preserving their original size and shape, dominated by octahedrons and hexahedrons (Fig. 8E). Dendritic pyrite was also observed, mainly present as overgrowths over euhedral pyrite (Fig. 8G). Acicular pyrite also formed in some samples and is exclusively present in the bauxite matrix (Fig.8H). The pyrite veins were found in most samples, cross-cutting other pyrite features and structural elements (Fig. 8I and J). Pyritised root remains were found in the samples from the D-15 deposit, composed of hollow tubes of colloform or euhedral pyrite, filled with matrix material or some authigenic phase such as diaspore or kaolinite (Fig. 8L). Besides pyrite, marcasite was also found, but mostly in rosettes composed of elongated crystals smaller than 100 µm (Fig. 8K).

Extracted light and heavy mineral fractions were also studied: in the heavy mineral fraction staurolite, grunerite-cummingtonite, tourmaline and barite were detected (Figs. 9A–D), while chert and opal were detected in the light mineral fraction (Figs. 9E and F). Most of the minerals from the heavy mineral fraction and chert are rounded to subrounded, while only barite displays some euhedral grains. Opal is found as irregular masses and shards, indicating its authigenic origin.

5.3. XRPD

The mineralogical composition was primarily analysed using XRPD, as most phases in bauxites are hard to identify microscopically due to their cryptocrystalline occurrence. Clear differences in mineralogy were found between the D-1 and D-15 deposits, with the samples from the D-1 deposit containing much higher amounts of pyrite and boehmite

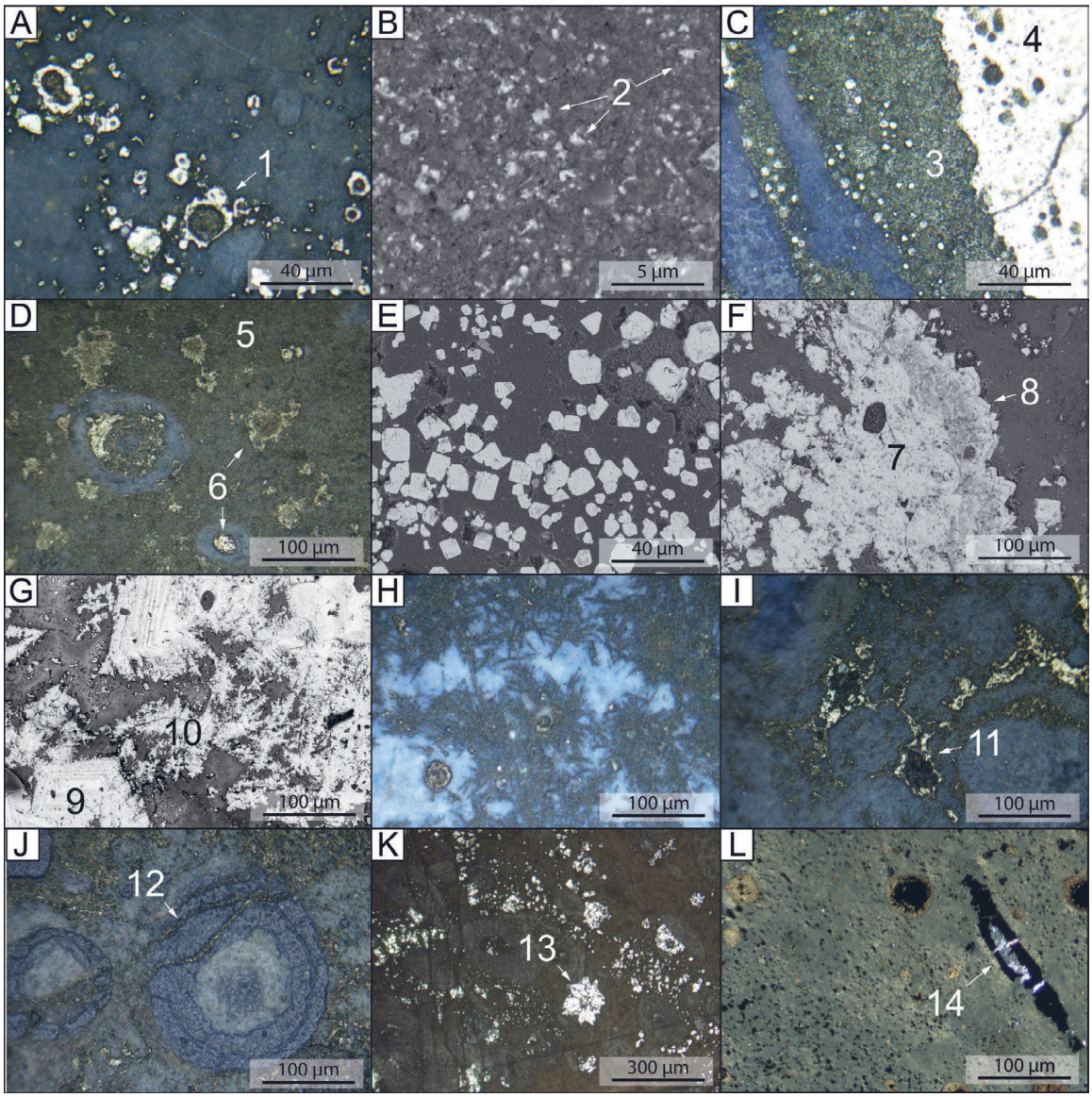

Figure 8. Photomicrographs taken using XPL or reflected light (RL) and BSE images of different iron sulphide morphologies. A – Pyrite framboids (1) overgrown with colloform pyrite, sample D15-10 (RL); B – dispersed grains of MSAP (2) in the bauxite matrix, sample D15-10 (BSE); C – Mixture of pyrite framboids and MSAP (3) overgrown with colloform pyrite (4), sample D1-12 (RL); D – photomicrograph of pyritised ooids and bauxite matrix impregnated with MSAP (5), with visible impregnations of colloform pyrite (5) and replacement of MSAP with colloform pyrite in ooid lamellae (6), sample D1-3 (RL); E – individual euhedral pyrite crystals in the bauxite matrix, sample D1-3 (BSE); F – colloform pyrite (7) overgrown with euhedral pyrite crystals with visible growth bands (8), sample D15-10 (BSE); G – euhedral pyrite crystals (9) overgrown with dendritic pyrite (10), sample D15-10 (BSE); H – acicular pyrite crystals in the bauxite matrix, sample D1-6 (RL); I – veins composed from pyrite and kaolinite (11), sample D1-8 (RL); J – Ooid cross-cut by pyrite veins (12), sample D1-9 (RL); K – marcasite rossete (K) in bauxitic matrix with different pyrite morphologies, sample D15-10 (RL); L – pyritised root filled with diaspore crystals (14), sample D15-8 (XPL).

compared to samples from the D-15 deposit, which mostly have a lower boehmite content and higher kaolinite content (Fig 10). Based on this, samples from the D-1 deposit are genuinely bauxites while the ones from D-15 deposit are clayey bauxites. In both deposits, variable amounts of diaspore and marcasite are present, together with anatase, rutile and different secondary sulphate minerals such as pickeringite, jarosite and gypsum. Red bauxite differs from those samples since it is composed mainly of boehmite and haematite with smaller amounts of kaolinite, anatase and rutile.

5.4. Geochemistry and stable sulphur isotopes

The major oxide content of the studied samples is in accordance with their mineralogical composition, with the pyrite- and boehmite-rich samples from the D-1 deposit having a higher amount of Fe_2O_3, LOI, Na_2O and TOT/S, while the kaolinite-rich samples from the D-15 deposit have higher amounts of CaO, K_2O, MgO, MnO and SiO_2 (Fig. 11). The D15-6 sample is an exception in the D-15 deposit, as it has a lower content of the aforementioned elements and is enriched in TOT/C (Fig. 11), indicating its high organic matter content, which corresponds to the abundance of coal in that sample (Fig. 7D). Compared to samples from both the D-1 and D-15 deposits, red bauxite has a higher Cr_2O_3 and MnO and lower LOI, Na_2O, P_2O_5 and TOT/S values (Fig. 11). The ternary diagram SiO_2–Al_2O_3–Fe_2O_3 (after ALEVA, 1994) also highlights the differences between the two deposits (Fig. 12), as most of the samples from the D-15 deposit are kaolinitic bauxites or pure

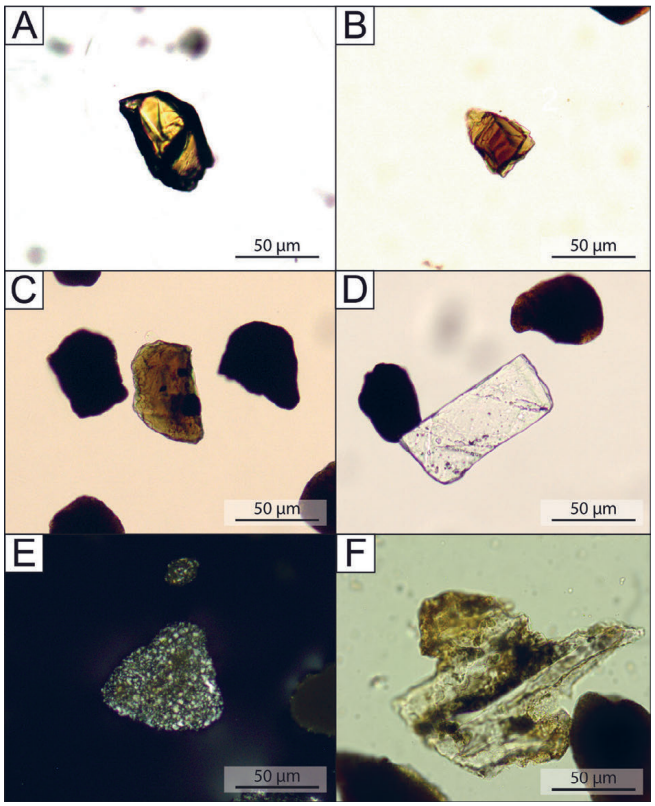

Figure 9. Photomicrographs of different mineral grains from the light and heavy mineral fractions in PPL. A – staurolite, B – cummingtonite-grunerite group amphibole, C – tourmaline, D – baryte, E – chert, F – opal.

bauxites, while those from the D-1 deposit are ferritic bauxites or pure bauxites. The red bauxite falls in the ferritic bauxite field.

The differences between the deposits and sample types are also visible in the trace element contents. The samples from the D-1 deposit are enriched in As, Cu, Co, Ni and Sb when compared to the D-15 deposit and red bauxite, while the samples from the D-15 deposit are enriched in Ba, Cs, Rb, Sr, U and Zn compared to D-1 deposit and red bauxite (Fig. 13). Samples from both deposits are enriched in Cd, Hg, Mo, Se and Tl, as well as depleted in Bi, Ga, Nb, Sn, Ta, Th, V and Zr compared to the red bauxite sample (Fig. 13). Red bauxite has a higher Ga, Nb, Pb, Sn, Ta, Th, V and Zr content than samples from D-1 and D-15 deposits (Fig. 13). While showing some similarities to other samples from the D-15 deposit, the coal-rich bauxite shows several differences – higher Hg, Mo and Sb values and lower values of Co, Cs, Cu, Ni, Pb, Th and Tl (Fig. 13). Compared to the upper continental crust, all samples are enriched in As, Ga, Hf, Hg, Nb, Ni, Sb, Sn, U, V, W, Y and Zr, while being depleted in Ba, Rb, Se and Sr (Fig. 14A).

Rare earth elements display similar trends in all sample types with few variations. Generally, all samples display a "saddle" pattern, with a visible depletion in middle rare earth elements (MREE) compared to Light (LREE) and heavy rare earth elements (HREE, Fig. 14B–D). Red bauxite has a higher HREE and MREE content than the samples from the D-1 and D-15 deposits, and a pronounced negative Ce anomaly (Fig. 15). Samples from the D-1 and D-15 have the same REE patterns (Fig. 14B, C), but the samples from D-15 deposit have higher LREE values, total REE values and La/Y ratios, as well as lower Y/Ho ratios (Figs. 14B, C and 15). The D15-6 differs from the rest of the samples from the D-15 deposit in REEs as well, having lower LREE values and La/Y as well as higher Y/Ho values (Figs. 14C and 15). Both deposits display either very low negative Ce anomalies or their absence (Fig. 15).

$\delta^{34}S$ values do not display any apparent differences between the deposits and their position within them (Fig. 16). Their values range between -40.86 to 2.32 ‰ (Fig. 16).

6. DISCUSSION

6.1. Genesis of the Minjera deposits

The Minjera bauxites were developed over the karstified upper Cenomanian limestones which announced the subaerial exposure phase, partly through the shallowing of the depositional environment and the repeated occurrence of brief subaerial exposure surfaces and partly by features such as fenestrae, circumgranular cracks and pedotubules. Finally, the start of the subaerial exposure phase is indicated by the formation of the Minjera bauxites in the studied area. The source and the type of material from which the Minjera

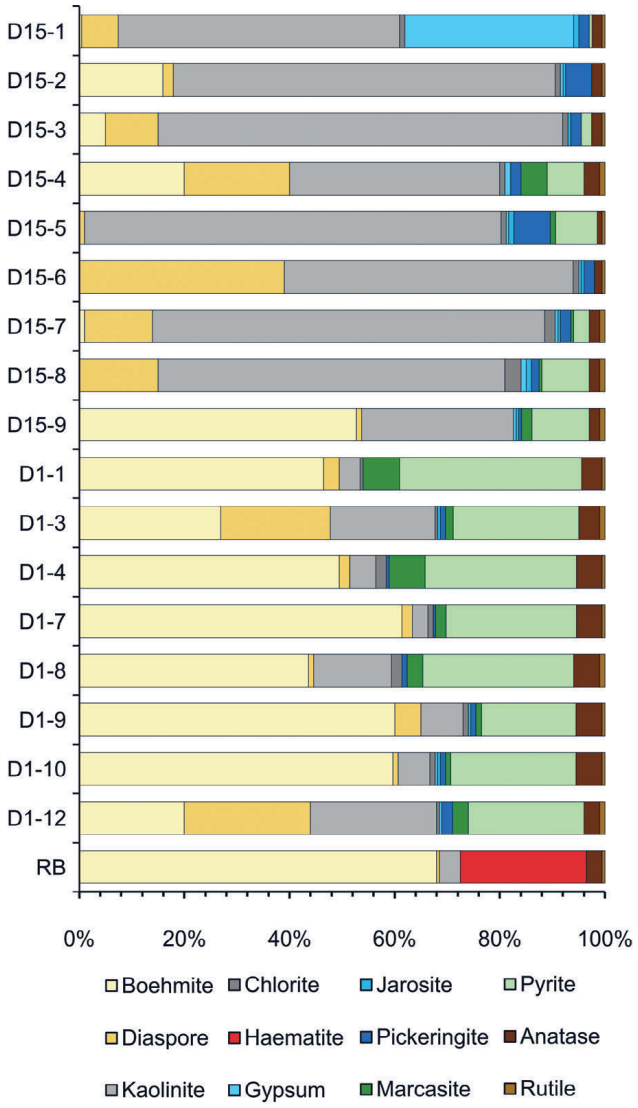

Figure 10. Mineralogical bulk composition of samples analysed using XRPD.

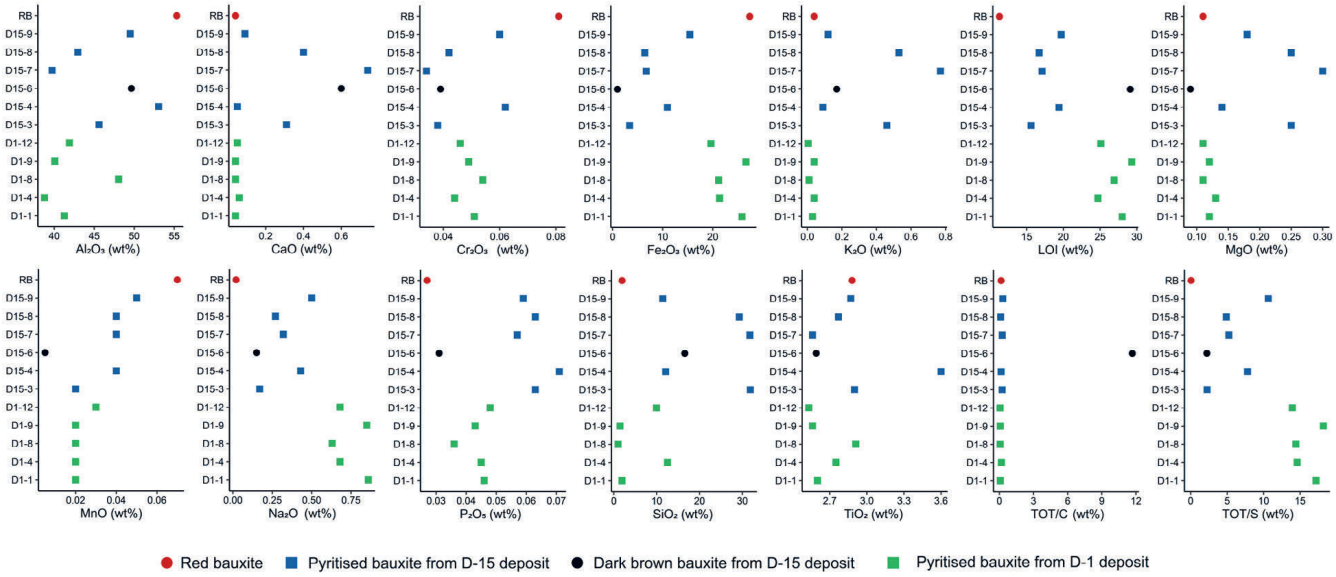

Figure 11. Values of different major oxides plotted against individual samples.

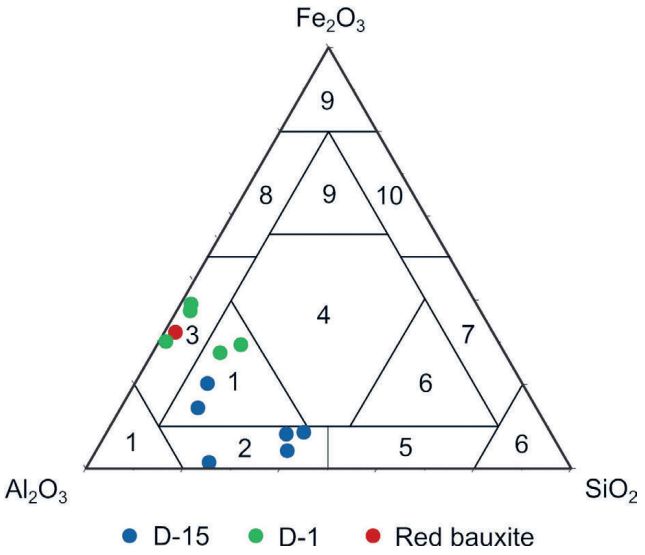

Figure 12. A bauxite classification diagram based on Al_2O_3 Fe_2O_3 and SiO_2 content according to ALEVA (1994). 1 – bauxite, 2 – kaolinitic bauxite, 3 – ferritic bauxite, 4 – laterite, 5 – bauxitic kaolinite, 6 – kaolinite, 7 – ferritic kaolinite, 8 – bauxitic ferrite, 9 – ferrite, 10 – kaolinitic ferrite, 11 – ferrite.

bauxites have formed is hard to determine, since bauxitisation leads to the loss of primary textures, structure and composition of the parent material. Nevertheless, the material from which these bauxites formed can be tentatively reconstructed based on the content of the light and heavy mineral fractions. The presence of metamorphic minerals such as staurolite, tourmaline and clinohumite-grunerite amphiboles (Fig. 5A–D) indicate the contribution of a mixture of aeolian material during its formation. The insoluble residue from the underlying carbonates can neither be confirmed nor disputed and should be regarded as a possible minor source of the parent material. Karst bauxites are also commonly formed from volcanic dust (BARDOSSY, 1982; D'ARGENIO & MINDSZENTY, 1995; KELEMEN et al., 2017, 2023; BRLEK et al., 2021), but there is no evidence for such an input in the case of the Minjera bauxites, as no zircons have been found which could have been dated and connected to contemporaneous volcanic activity. The deposition and accumulation of source materials for the bauxites was initiated by the tectonic deformation of the Adriatic Carbonate Platform in response to the load of the advancing nappes following the closure of the Vardar Ocean at the end of the Cretaceous (VAN HINSBERGEN et al., 2020; SCHMID et al., 2008, 2020). Following this, karstification also ensued, creating a diverse karst landscape, as seen by the different morphologies and sizes of the Minjera deposits (Fig. 2). The prevalence of large canyon deposits north of the Mirna River and their absence south of the river coupled with the abundance of sinkhole and smaller canyon deposits (Fig. 2) suggests the geomorphological differences between these two areas. The Kozina beds are also much thicker south of the Mirna River (Fig. 2), indicating altogether the lower palaeotopographical position of the deposits on the southern side compared to the northern side, which resulted in the formation of deeper karstic features on the northern side. This is reflected in the mineralogical and geochemical composition of the two studied bauxite deposits, as the differences in the morphology of the deposits affected the drainage and the intensity of fluid-flow of percolating porewaters. The larger and steeper D-1 deposit has a higher boehmite content compared to the D-15 deposit, and is composed of bauxite and ferritic bauxite (Fig. 12). The D-15 deposit contains more kaolinite (Fig. 10) and is composed of bauxite and kaolinitic bauxite (Fig. 12), which is probably a result of better drainage and higher distance from the water table in the D-1 deposit and vice-versa. The clear relationship between bauxites and their palaeotopographical position was described by D'ARGENIO & MINDSZENTY (1995) and has also been observed in other studies (YANG et al., 2017; MO et al., 2023), indicating that the bauxite lithofacies and grade depend on their position in the karst terrains. Based on this, the bauxites on the northern side of the Mirna River can be attributed to the vadose bauxite lithofacies, while those from the southern side represent the intermediate bauxite lithofacies sensu D'ARGENIO & MINDSZENTY (1995). Diagenetic resilicification is a

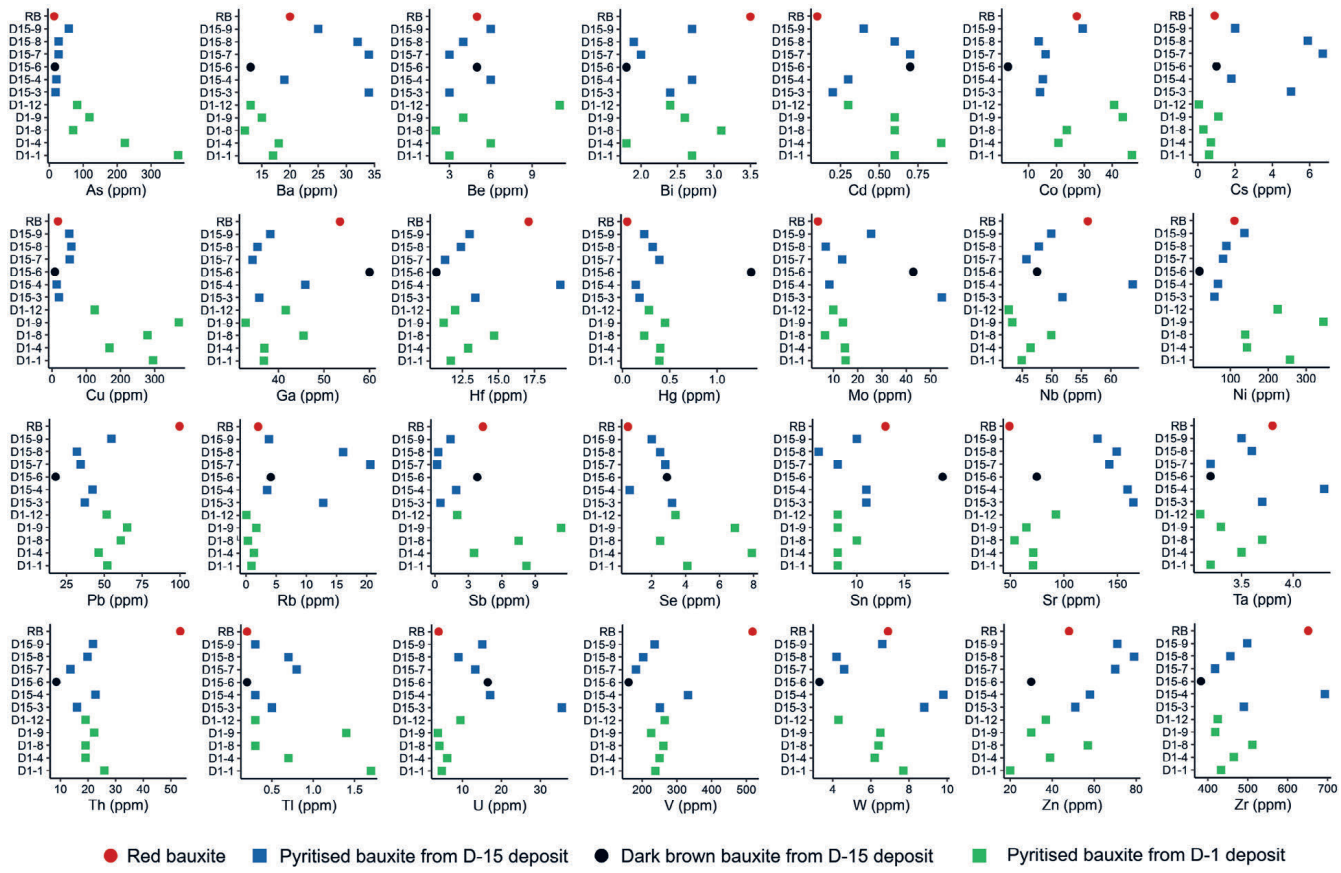

Figure 13. Values of different trace elements plotted against individual samples.

common phenomenon in bauxites after their formation (BARDOSSY, 1982; MAMELI et al., 2007; MONGELLI et al., 2021) and should not be excluded as a factor resulting in the higher kaolinite content of the D-15 deposit, as the replacement of boehmite with kaolinite in ooids can be seen in some samples (Fig. 7B). Veins filled by an association of pyrite and kaolinite crystals were also found (Fig. 8I) in both deposits, indicating that resilicification was also present in the D-1 deposit. Diaspore also formed during this phase, replacing boehmite in the bauxite matrix and within the ooids but also forming nests within the pyritised roots and the bauxite as well as in veins (Figs. 7F and 8L). Diaspore can form in several ways, either in response to increasing pressure during burial diagenesis (BARDOSSY, 1982; WILLIAMS, 2014; GAMALETSOS et al., 2017; MONDILLO et al., 2022), or it can form in the reducing environment (NIA, 1968; BARDOSSY, 1982; D'ARGENIO & MINDSZENTY, 1995; LIU et al., 2013; ZHANG et al., 2022). In the case of Minjera bauxites, it is clear that diaspore formation happened in reducing conditions, as it crystallised directly from percolating solutions, as indicated by its presence in nests and veins (Figs. 7F and 8L). A proportion of diaspore might also be inherited from the originally red bauxite, as a minor amount of diaspore has been detected in the red bauxite (Fig. 10).

6.2. Iron sulphide morphology and stable sulphur isotopes

A large number of iron sulphide morphologies were found in the Minjera bauxites, the formation of which was initiated as the microbial sulphate reduction and dissolution of iron oxides

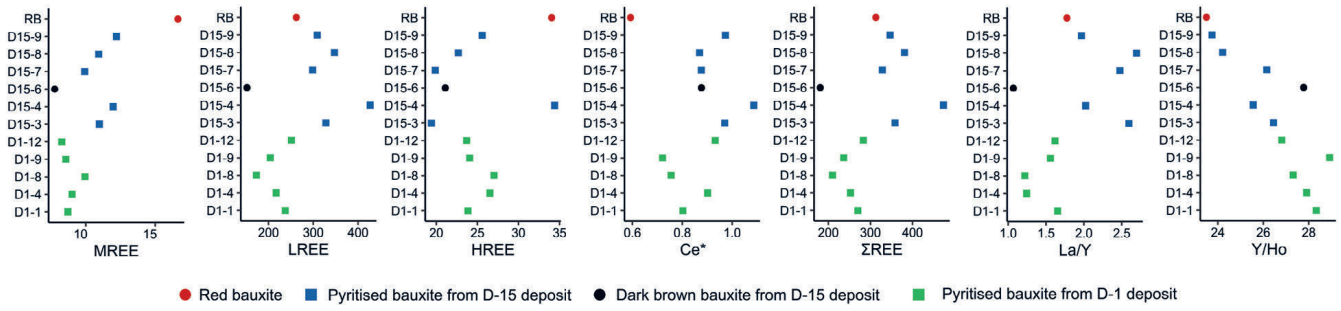

Figure 14. Values of trace elements and rare elements in different samples after normalisation against the upper continental crust. A – values of trace elements, B – values of rare earth elements in the D-1 deposit, C – values of rare earth elements in the D-15 deposit, D – values of rare earth elements in the red bauxite.

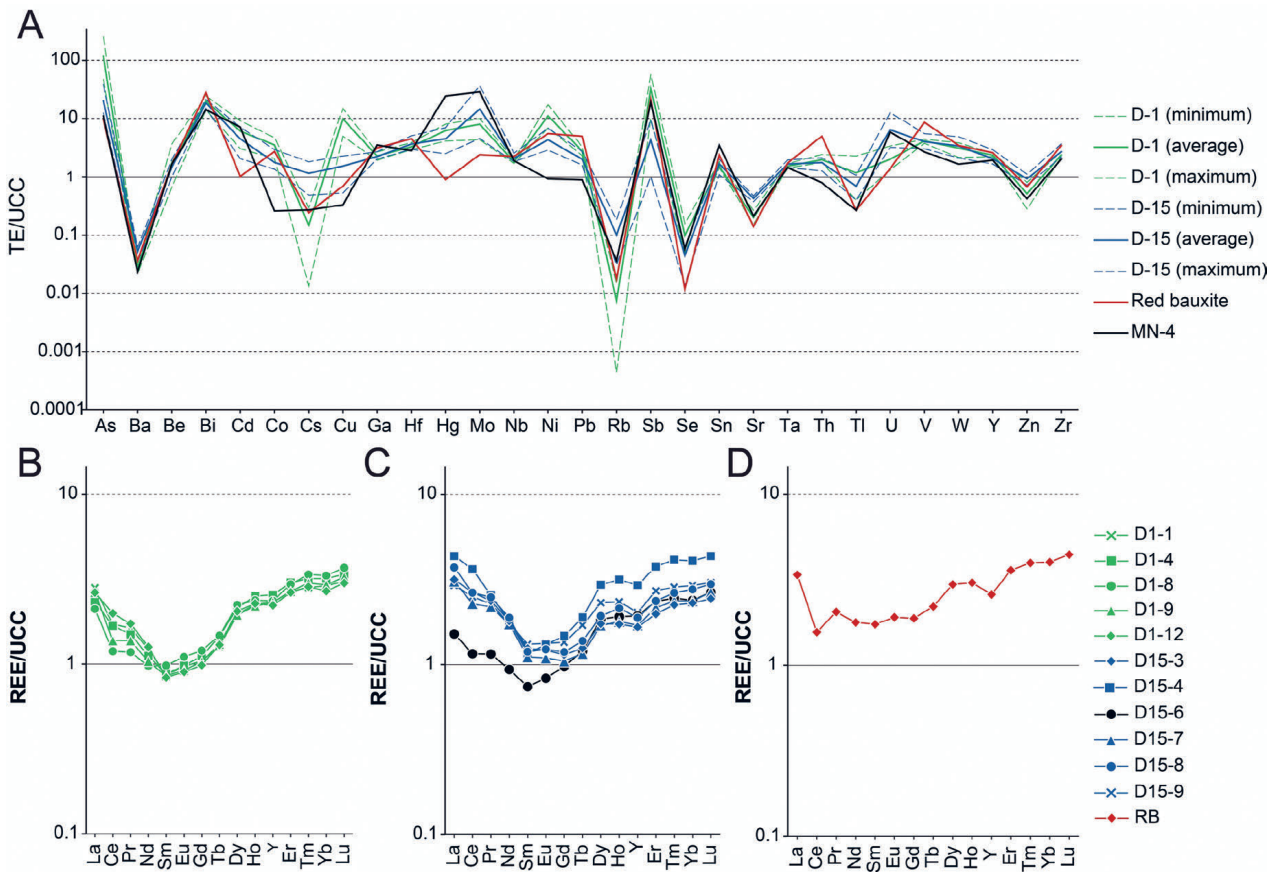

Figure 15. Values of different REE groups, total REE content, Ce anomaly and different REE ratios plotted against individual samples.

began in a newly established marshy environment. Macroscopically, they exhibit several different types across the two studied deposits, where they form bands and nodules within the iron-poor bauxite matrix in the cases of "striped" and "spotted" pyritised bauxites (Fig. 6G). This can be linked to the differences in the redox potential and the degree of pyrite saturation in the porewaters, allowing its crystallisation in spots or bands, with the bands of the "striped" bauxite being controlled by the direction of fluid-flow. In the case of the D-1 deposit, a zonal arrangement of pyrite-rich and pyrite-poor bauxite was observed, with the increase of pyrite content towards the interior of the deposit, with the completely pyritised region separating the zone with less and more pyrite (Fig. 6F). This zonation is parallel to the karstified bedrock and is probably a result of changes in the redox potential, with the completely pyritised zone likely indicating the redox boundary, where conditions for iron sulphide precipitation were apparently optimal. This could also reflect the pH differences within the sediment, as the inflow of saline and karstic porewaters during the flooding of the bauxite was the highest in this zone, where the pyrite-rich zone could reflect the zone with near-neutral to slightly alkaline conditions which are generally required for its formation (WILKIN & BARNES, 1996). On the micro-scale, there is a clear order in the formation of different iron sulphide morphologies (Figs. 17 and 18). The first pyrite morphologies that formed (Figs. 17 and 18) were the framboidal pyrite and the impregnations of MSAP (Figs. 8A–D), which formed in the pore spaces, in the matrix (Figs. 8B, 8D and 18A), as a replacement of roots (Figs. 8L and 18A), or as an in-situ replacement of originally iron oxide-rich bauxite clasts and ooid lamellae (Figs. 7B, 7C and 18A). It should be noted that pyrite framboids were also found in other pyritised bauxites (LASKOU & ECONOMOU-ELIOPOULOS, 2007; ZARASVANDI et al., 2012; ECONOMOU-ELIOPOULOS et al., 2022), appearing to be a common feature in pyritised bauxites. Framboidal pyrite usually forms first from the initially precipitated iron monosulphides (BERNER, 1970; HÁMOR 1994), which can then serve as crystallisation sites for later stages of pyrite growth (YUE et al., 2020). As such, both the framboids and MSAP were overgrown by colloform pyrite (Figs. 8A, C and D). The presence of both framboidal and colloform pyrite in the first two stages (Figs. 17, 18A and 18B) indicates that the solutions were supersaturated with respect to pyrite (ROEDDER, 1968; CHEN, 1978; BARRIE et al., 2009). It should be noted that the colloform pyrite also frequently displays a banded character, indicating the fluctuations in pyrite saturation during its precipitation (BARRIE et al., 2009). The formation of colloform pyrite was followed by the formation of euhedral pyrite which overgrows framboids as well as colloform pyrite (Figs. 8F and 18C), and which replaces framboids with individual euhedral crystals (Figs. 8E and 18C). The formation of euhedral pyrite indicates that the porewaters became undersaturated with respect to pyrite in this stage (RAISWELL, 1982; BARRIE et al., 2009; CAVALAZZI et al., 2012; HE et al., 2022). They also commonly display distinct growth bands, where some of them contain matrix impurities (Fig. 8F), indicating the fluctuations in growth rates. The further drop in pyrite saturation is

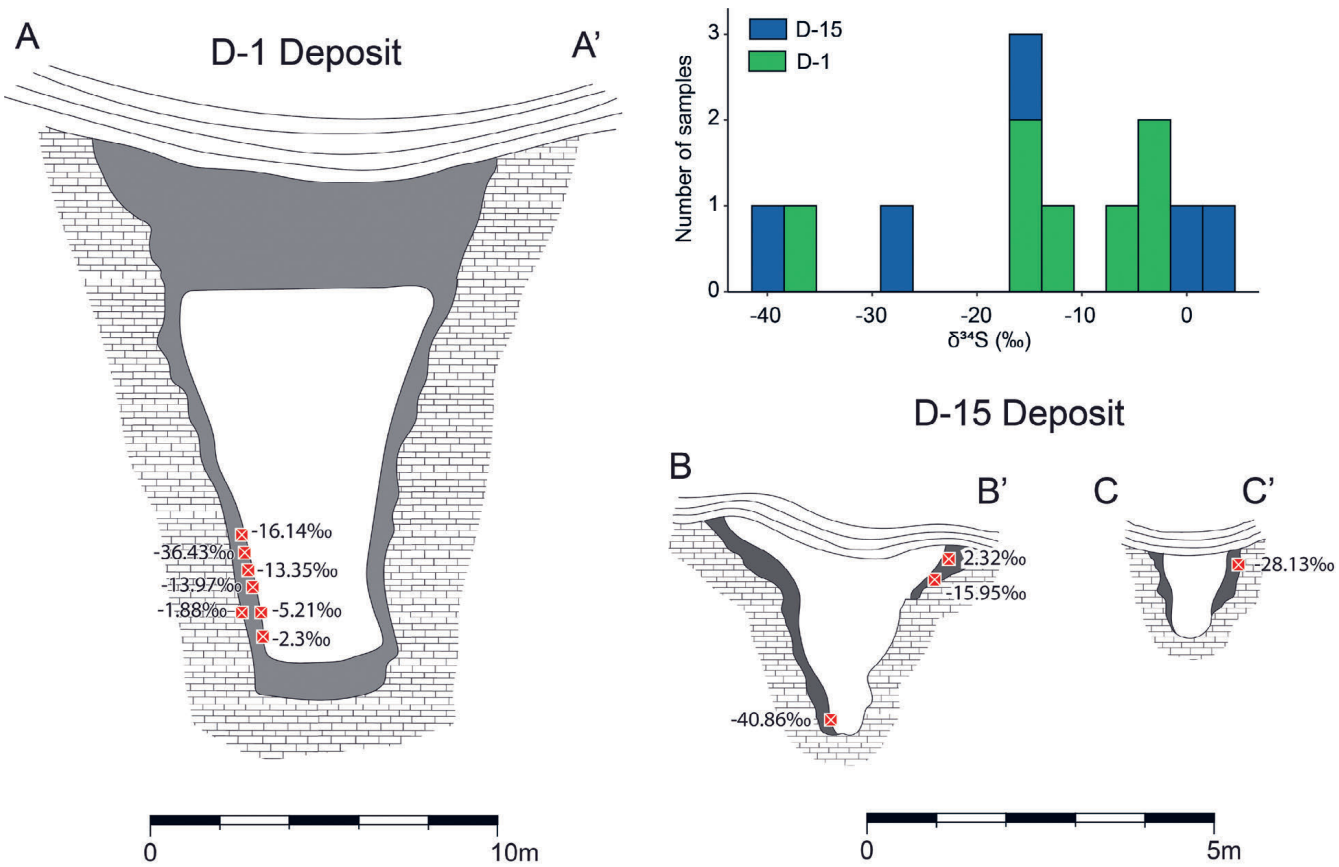

Figure 16. The position of different $\delta^{34}S$ values in the D-1 and D-15 deposits, together with the histogram of obtained $\delta^{34}S$ values.

recorded via the precipitation of dendritic pyrite (BARRIE et al., 2009), which represents the final overgrowth on the previously deposited pyrite morphologies where present (Figs. 8G and 18C). Its formation is also coupled with the crystallisation of acicular pyrite (Figs. 8H, 17 and 18C). The final pyrite deposition and late diagenesis is marked by the consolidation and brittle fracturing of the bauxite within which the final stage of iron sulphides precipitated as pyrite and kaolinite veins (Figs. 8K, 8L, 17 and 18D). Marcasite is found only as rosettes or radial crystal clusters which cannot be precisely related to any of the stages of pyrite formation (Figs. 8K and 17). Its presence indicates the local presence of acidic conditions within the deposit, as La/Y ratios >1 indicate that the bauxites generally formed under alkaline to near-alkaline conditions (Fig. 11; MAKSIMOVIĆ & PANTÓ, 1991). Stable sulphur isotope values indicate the role of microbial sulphate reduction in pyrite formation, as most of the $\delta^{34}S$ values are negative (Fig. 16). Similar $\delta^{34}S$ values were

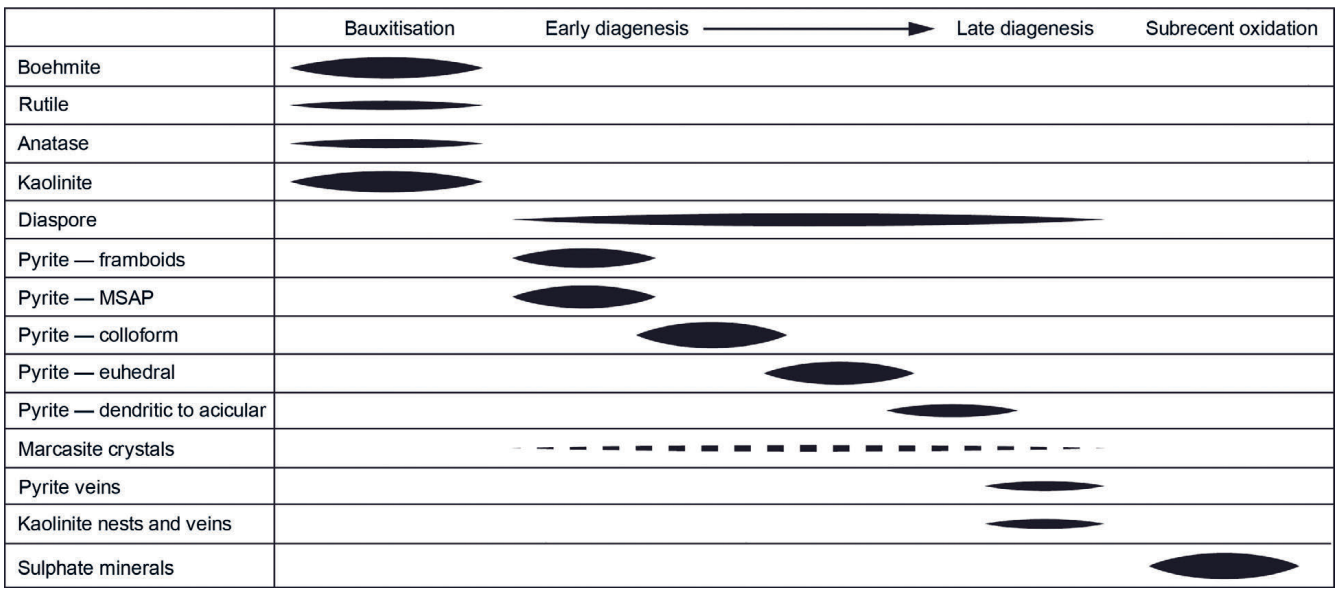

Figure 17. A paragenetic sequence of the Minjera deposits and the succession of the formation of different iron sulphide morphologies.

found in most pyritised bauxites where stable sulphur isotopes were studied (ÖZTÜRK et al., 2002; LASKOU & ECONOMOU-ELIOPOULOS, 2007; ZARASVANDI et al., 2012; ELLAHI et al., 2015; ZHAO et al., 2023). The $\delta^{34}S$ values from the Minjera bauxite also display a wide range of values, from -40.86 to 2.32 ‰ (Fig. 16), which compared to the global seawater ^{34}S values between 17 ‰ and 19 ‰ during the Late Cretaceous and Palaeocene (ALGEO et al., 2015) yield enrichment factors between -60 ‰ and -15 ‰. The high negative values indicate that the system was open, since the sulphate content was not limited, allowing the continuous enrichment of ^{32}S via microbial reduction (CHAMBERS & TRUDINGER, 1979; ALGEO et al., 2015; PASQUIER et al., 2017; HOUGH et al., 2019). The sulphate-rich marine to brackish solutions were likely pumped through the underground karstic conduits and channels through tidal pumping, a common phenomenon which induces salinity changes in blue holes in the Bahamas (MARTIN et al., 2012; SMITH et al., 2021). On the other hand, the intermediate and lower values (Fig. 16) indicate the shift towards a closed or partially open system in which the sulphate content was limited, which leads to utilisation of heavier ^{34}S in microbial sulphate reduction, as the sulphate with ^{32}S was depleted and not replenished (CHAMBERS & TRUDINGER, 1979; ALGEO et al., 2015; HOUGH et al., 2019; PASQUIER et al., 2021). This was also observed in other studies (ZARASVANDI et al., 2012; ELLAHI et al., 2015; ZHAO et al., 2023), and in the case of the Minjera bauxites it can be related to their progressive and final burial, which led to the hydrological closure of this system. The progressive closure could also be related to the progressive undersaturation of pore solutions with respect to pyrite, as indicated by the presence of euhedral, dendritic and acicular pyrite in the later stages (Figs. 8E–H, 17 and 17C), as the sulphur content became a limiting factor during its precipitation.

6.3. Geochemistry of the Minjera bauxites

When comparing the trace element composition of the Minjera bauxites with the Upper Continental Crust values (TAYLOR & MCLENNAN, 1985), they are enriched in most trace elements such as lithophile and high field strength elements (HFSE), while being depleted in large ion lithophile elements (LILE, Fig. 13). This is commonly observed in most bauxite deposits as elements such as HFSE are retained during bauxitisation (MONGELLI, 1997; CALAGARI & ABEDINI, 2007; ABEDINI & CALAGARI, 2014; MONGELLI et al., 2014, ELLAHI et al., 2017; ABEDINI et al., 2020) while the more mobile elements including bases and LILE are leached away (MONGELLI, 1997; CALAGARI & ABEDINI, 2007; XIAO et al., 2021). Fractionation of trace elements changed

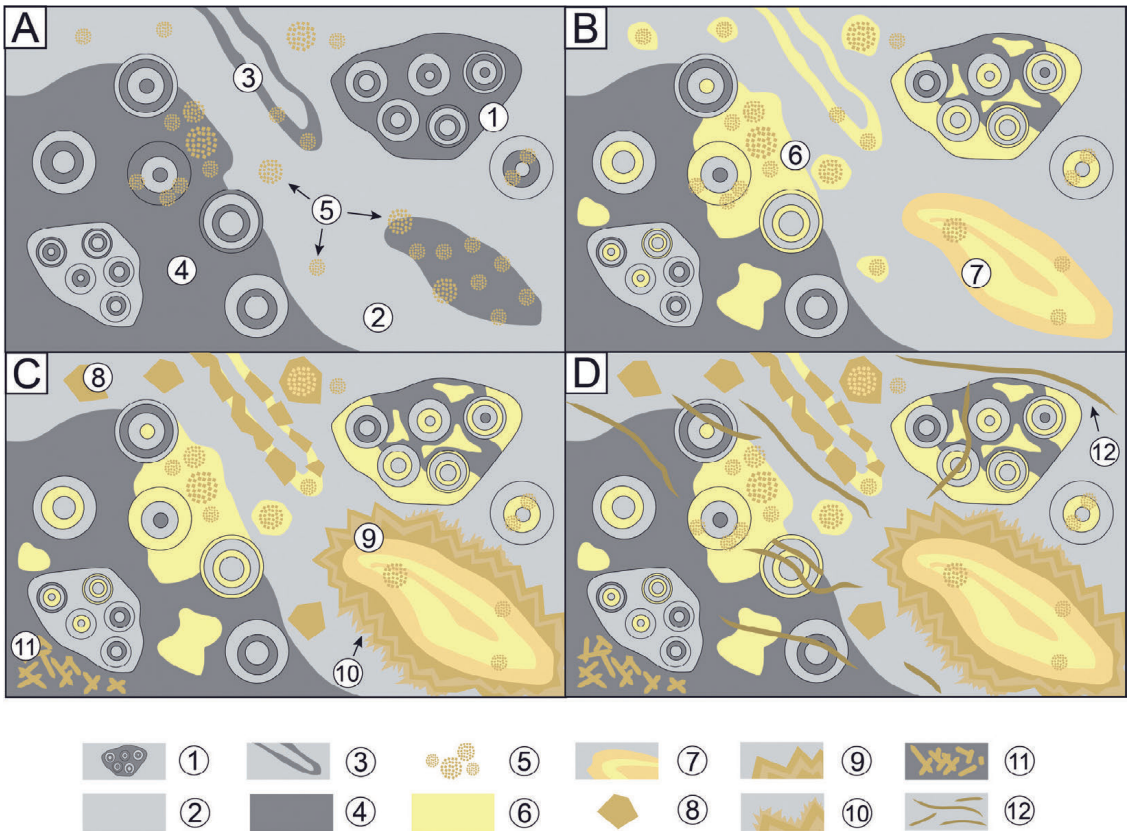

Figure 18. A schematic reconstruction of the succession of different iron sulphide morphologies. A – Formation of MSAP in the bauxite matrix (1), bauxite clasts (2), root remains (3) and ooid lamellae, coupled with the formation of pyrite framboids (4) together with MSAP or individually in the bauxite matrix; B – Overgrowth of colloform pyrite (6) over MSAP and framboids in the matrix, bauxite clasts, pyritised roots or ooid lamellae, which locally display banded textures (7); C – overgrowth and recrystallisation of framboids (8), MSAP and colloform pyrite into euhedral pyrite (9), followed by its overgrowth with dendritic pyrite (10) and formation of acicular pyrite in the matrix (11); D – formation of pyrite and kaolinite veins (12), over the previously formed iron sulphide morphologies and bauxite. Legend: 1 – MSAP; 2 – bauxite clasts; 3 – pyritised root remains; 4 – pyrite framboids; 5 – bauxite matrix; 6 – colloform pyrite; 7 – banded colloform pyrite; 8 – replacement of individual framboids with euhedral pyrite crystals; 9 – euhedral pyrite overgrowths; 10 – dendritic pyrite overgrowths; 11 – acicular pyrite; 12 – kaolinite and pyrite veins.

during the reduction and pyritisation of the red bauxite, as the newly established reducing and hydrogen sulphide-rich environment led to the accumulation and enrichment of chalcophile and redox-sensitive elements such as Cd, Hg, Mo, Se, and Tl (Fig. 13). This also affected the content of trace elements such as Pb and V which are preferentially enriched by iron oxides (WANTY & GOLDHABER, 1992; TABELIN et al., 2018; SHAHEEN et al., 2019), released during their reduction and dissolution, leading to their depletion in the pyritised bauxites compared to the red bauxite (Fig. 13). REEs were also affected by this process, since there is a significant depletion in MREEs within the pyritised bauxites (Fig. 14B, C), which is linked to the dissolution of iron oxides during their reduction which usually enriched the MREEs (TANG & JOHANNESSON, 2003; GRYBOS et al., 2007; LAVEUF et al., 2008; DAVRANCHE et al., 2011; ZHOU et al., 2020). This is further supported by the higher MREE content of the red bauxite sample compared to the pyritised bauxites (Fig. 15), confirming that they were indeed leached during the dissolution of iron oxides. Organic acids also preferentially adsorb MREEs compared to other REEs (GRYBOS et al., 2007; POURRET et al., 2007; DAVRANCHE et al., 2011), which could have been the mechanism through which they were removed from the bauxite as the organic-rich marshy environment was established on top of the bauxite. This is more pronounced in the organic-matter rich D15-6 sample, where LREEs and MREEs are even more depleted (Figs. 14C and 15). They also exhibit an enrichment in Hg, Mo, and Sb, which can be linked to the higher organic matter content of this sample (Figs. 13 and 14A). The pyritised bauxites also differ from red bauxite with respect to the Ce anomaly, as the red bauxite displays a negative Ce anomaly which is either weaker or absent in the pyritised bauxites (Figs. 14B–C and 14). The Ce anomaly in the red bauxite is likely a result of preferential retention of Ce in the upper parts of the bauxite (MONGELLI, 1997; WANG et al., 2013; VIND et al., 2018), since this leads to the development of a negative Ce anomaly in the lower sections of bauxites (MONGELLI, 1997). This negative anomaly could have been masked by the remobilisation of Ce in the presence of organic matter and acids during the flooding of the bauxite. This process preferentially concentrated Ce (POURRET et al., 2008; DAVRANCHE et al., 2011), because this could have caused its redistribution in the pyritised bauxite, masking the previously developed Ce anomalies.

The trace elemental content also supports the differences between the D-1 and D-15 deposits discussed in section 6.1, as besides the aforementioned differences in major elements between the deposits, the D-15 deposit also displays higher values of leachable elements such as Ca, K, Mg, Mn and LILE compared to D-1 (Figs. 12 and 13), which is in turn enriched in chalcophile elements such as As, Cu, Co, Ni and Sb (Fig. 13), indicating their association with iron sulphides which are much more abundant in the D-1 deposit. The higher Y/Ho ratio in the D-1 deposit compared to the D-15 deposit (Fig. 15) also indicates its higher degree of leaching, as this ratio can be used as a proxy for the intensity of water–rock interactions in soils (JI et al., 2004; FENG, 2010), since Ho is more mobile than Y in the aqueous environment (BAU et al., 1997; DIAKONOV et al., 1998) and complexes more easily with organic matter and HCO_3^- (KAWABE et al., 1991). The higher content of leachable elements in the D-15 deposit is also related to the greater alkalinity in this deposit, indicated by the higher La/Y values compared to the D-1 deposit (Fig. 15), which are commonly used as pH proxies in bauxites, with values >1 indicating formation under alkaline conditions (MAKSIMOVIĆ & PANTÓ, 1991). The increased alkalinity is also evident from the higher total REE content in the D-15 deposit (Fig. 15), as REEs are more stable in alkaline solutions (CAO et al., 2001; FERREIRA DA SILVA et al., 2009; OLÍAS et al., 2018).

6.4. Bauxite cover sequence

The Palaeocene lacustrine limestone cover sequence began with coal intercalations overlying the dark brown bauxite rich in organic matter, altogether indicating the flooding of a previously exposed karst terrain. The topmost section of the bauxite is commonly intermixed with carbonate clasts and boulders (Fig. 6A, B), which were likely eroded from the surrounding carbonate rocks and embedded within the bauxites during the initial flooding. The first part of the cover sequence was deposited in a lacustrine environment with typical flora and fauna composed of fresh water green algae *Cladophorites*, ostracods, gastropods and Charophyta. The strengthening of a marine influence is visible upwards in the cover sequence through the common presence of benthic foraminifera. This phase is linked to the internal transgression of the exposed carbonate terrain, which was later followed by overland transgression, during which the fully marine Foraminiferal limestones were deposited. The evolution of the bauxite cover from restricted lacustrine, brackish and freshwater environments towards fully marine carbonate deposition can be described as a typical "blue hole" sequence (RASMUSSEN & NEUMANN, 1988, CARANNANTE et al., 1994a, b). The presence of coal-seams, organic matter and plant remains in the top sections of the bauxite and the rest of the cover sequence confirms the establishment of a marshy environment on top of the bauxites, which served as a source of organic matter for microbial sulphate reduction.

7. CONCLUSIONS

This study focused on the genesis of the historically important Minjera bauxites, situated in the western part of the Savudrija–Buzet anticline, which developed during the subaerial exposure phase that marked the end of the Cretaceous and Palaeocene periods in Istria. This was done using the trace and rare earth elements as proxies for the physicochemical changes during the formation of the studied bauxites, as well as stable sulphur isotopes and iron sulphide morphology. This study also focused on the evolution of the cover in the studied bauxite deposits, in order to reconstruct the immediate palaeoenvironmental changes that followed the subaerial exposure phase. Several conclusions can be drawn from the collected data and their interpretation:

1 – The parent material from which the Minjera bauxites developed was polygenetic in origin, and was accumulated and bauxitised in karstic canyons and sinkholes developed over upper Cenomanian limestones the shallowing trend

of which and subaerial exposure features anticipated the long-lasting subaerial exposure phase during which the Istrian Palaeogene bauxites developed.

2 – The pyritisation of the Minjera bauxites produced geochemical differences between the originally red bauxite and the pyritised bauxite, as chalcophile elements were enriched during pyritisation under euxinic conditions, while the MREEs, V, and Pb were dissolved and depleted as a consequence of the solubilisation of iron oxides.

3 – Petrographic, mineralogical and geochemical differences were observed between the D-1 and D-15 deposits, as the D-1 deposit contains more pyrite, boehmite, chalcophile elements and a higher Y/Ho ratio, while the D-15 deposit formed in more alkaline conditions, and contains more kaolinite as well as more leachable elements such as LILE, Mn, Ca, Mg and K. Based on this, the D-1 deposit is of the true vadose type, which formed in a higher palaeotopographical position and higher above the water table compared to the D-15 deposit, which exhibits some features of phreatic bauxites and was formed in a lower palaeotopographic position, closer to the water table.

4 – Pyritisation in the Minjera bauxites was a multi-stage process. In the first phase, micrometre-sized anhedral pyrite and pyrite framboids were formed, which were later overgrown and replaced by colloform pyrite in the second phase, where all of these morphologies indicate that the solutions were supersaturated with respect to pyrite. In the following stages, euhedral, dendritic, and acicular pyrite formed, indicating that the solutions became undersaturated with respect to pyrite. The final stage of pyritisation is marked by the formation of pyrite veins.

5 – Stable sulphur isotopes support the diagenetic evolution of the system outlined by pyrite morphologies, as the $\delta^{34}S$ values exhibit a large range between -40.86 and 2.32 ‰. This indicates the evolution from an open system, during which the sulphate source was not restricted and the solutions were supersaturated with respect to pyrite, towards a closed system as the bauxite deposit was being progressively buried and more isolated, in which the sulphate supply was limited, leading to the drop in saturation of the solutions with respect to pyrite.

6 – The cover sequence of the bauxite is of Palaeocene age and can be described as a "blue hole" sequence, typical for the internal transgression of karst terrains, as it exhibits the transition from lacustrine conditions, characterised by fresh water green algae, charophyta and ostracods, towards a more marine environment indicated by the appearance of benthic foraminifera, before transitioning into the fully marine Foraminiferal limestones.

Based on the above, this study significantly added to the previous knowledge of the historically important Minjera bauxites, as it provides novel insight into their genesis and subsequent pyritisation. The detailed reconstruction of the different stages of their subsequent pyritisation is also a valuable addition to the current knowledge on pyritisation in bauxites, as few studies distinguished and described the pyritisation of a bauxite deposit in such detail. This study also revealed that the local differences in palaeorelief on subaerially exposed karst terrains can produce bauxites of different morphology and mineralogy, as well as different geochemical signatures. The important contribution is also the determination of the cover of Minjera deposits as Palaeocene, which is a new finding in the studied area.

ACKNOWLEDGEMENT

This work has been fully supported by the Croatian Science Foundation under the project IP-2019-04-8054 – WIANLab (Western Istrian Anticline as an Ideal Natural Laboratory for the Study of the Regional Unconformities in Carbonate Rocks; PI Professor Goran DURN).

REFERENCES

ABEDINI, A., AZIZI, M.R. & CALAGARI, A.A. (2019): Ree mobility and tetrad effects in bauxites: An example from the Kanisheeteh deposit, NW Iran.– Acta Geodynamica et Geomaterialia, 16/1, 11–26. doi: 10.13168/AGG.2019.0002

ABEDINI, A. & CALAGARI, A.A. (2014): REE geochemical characteristics of titanium-rich bauxites: The Permian Kanigorgeh horizon, NW Iran.– Turkish Journal of Earth Sciences, 23, 513–532. doi: 10.3906/yer-1404-11

ABEDINI, A., CALAGARI, A.A. & AZIZI, M.R. (2018). The tetrad-effect in rare earth elements distribution patterns of titanium-rich bauxites: Evidence from the Kanigorgeh deposit, NW Iran.– Journal of Geochemical Exploration, 186, 129–142. doi: 0.1016/j.gexplo.2017.12.007

ABEDINI, A., MONGELLI, G., KHOSRAVI, M. & SINISI, R. (2020): Geochemistry and secular trends in the middle–late Permian karst bauxite deposits, northwestern Iran.– Ore Geology Reviews, 124, 1–20. doi: 10.1016/j.oregeorev.2020.103660

ALEVA, G.J.J. (1994): Laterites: Concepts, Geology, Morphology and Chemistry.– In: International Soil Reference and Information Center (ISRIC) The Corlat Handbook, Corlat Technical, ISRIC, Wageningen, 169 p.

ALGEO, T.J., LUO, G.M., SONG, H.Y., LYONS, T.W. & CANFIELD, D.E. (2015): Reconstruction of secular variation in seawater sulfate concentrations.– Biogeosciences, 12/7, 2131–2151. doi: 10.5194/bg-12-2131-2015

BÁRDOSSY, G. (1982): Karst Bauxites: Bauxite Deposits on Carbonate Rocks.– Elsevier Scientific Publishing Company, Amsterdam–Oxford–New York, 441 p.

BARRIE, C.D., BOYCE, A.J., BOYLE, A.P., WILLIAMS, P.J., BLAKE, K., OGAWARA, T., AKAI, J. & PRIOR, D.J. (2009): Growth controls in colloform pyrite.– American Mineralogist, 94/4, 415–429. doi: 10.2138/am.2009.3053

BAU, M., MÖLLER, P. & DULSKI, P. (1997): Yttrium and lanthanides in eastern Mediterranean seawater and their fractionation during redox-cycling.– Marine Chemistry, 56/1–2, 123–131. doi: 10.1016/S0304-4203(96)00091-6

BERGANT, S., MATIČEC, D., FUČEK, L., PALENIK, D., KORBAR, T., ŠPARICA, M., KOCH, G., GALOVIĆ, I. & PRTOLJAN, B. (2020): Basic Geological Map of the Republic of Croatia scale 1:50.000, sheet: Rovinj 2.– Department of Geology, Croatian Geological Survey, Zagreb.

BERNER, R.A. (1970): Sedimentary pyrite formation.– American Journal of Science, 28, 1–23. doi: 10.2475/ajs.268.1.1

BRLEK, M., GAYNOR, S.P., MONGELLI, G., BAULUZ, B., SINISI, R., BRČIĆ, V., PEYTCHEVA, I., et al. (2021): Karst bauxite formation during Miocene Climatic Optimum (central Dalmatia, Croatia): mineralogical, compositional and geochronological perspectives.– International Journal of Earth Sciences, 110/531. doi: 10.1007/s00531-021-02091-z

CALAGARI, A.A. & ABEDINI, A. (2007): Geochemical investigations on Permo-Triassic bauxite horizon at Kanisheeteh, east of Bukan, West-Azarbaidjan, Iran.– Journal of Geochemical Exploration, 94/1, 1–18. doi: 10.1016/j.gexplo.2007.04.003

CANFIELD, D.E., RAISWELL, R., WESTRICH, J.T., REAVES, C.M. & BERNER, R.A. (1986): The use of chromium reduction in the analysis of reduced inorganic sulfur in sediments and shales.– Chemical Geology, 54/1, 149–155. doi: 10.1016/0009-2541(86)90078-1

CAO, X., CHEN, Y., WANG, X., & DENG, X. (2001): Effects of redox potential and pH value on the release of rare earth elements from soil.– Chemosphere, 44/4, 655–661. doi: 10.1016/S0045-6535(00)00492-6

CARANNANTE, G., MINDSZENTY, A., NEUMANN, A.C., RASMUSSEN, K.A., SIMONE, L. & TÓTH, K. (1994): Inland blue-hole-type ponds in the Mesozoic–Tertiary karst filling sequences.– In: IAS 15th Regional Meeting, Abstracts. Ischia, 102–103.

CARANNANTE, G., D'ARGENIO, B., MINDSZENTY, A., RUBERTI, D., & SIMONE, L. (1994). Cretaceous–Miocene shallow water carbonate sequences. Regional unconformities and facies patterns.– In: CARANNANTE, G & TONIELLI, R. (eds.): Field Trip Guide Book: 15th Regional IAS Meeting. De Frede, Napoli, 25–60.

CAVALAZZI, B., BARBIERI, R., CADY, S.L., GEORGE, A.D., GENNARO, S., WESTALL, F., LUI, A., et al. (2012): Iron-framboids in the hydrocarbon-related Middle Devonian Hollard Mound of the Anti-Atlas mountain range in Morocco: Evidence of potential microbial biosignatures.– Sedimentary Geology, 263/264,183–264. doi: 10.1016/j.sedgeo.2011.09.007

CHAMBERS, L.A. & TRUDINGER, P.A. (1979): Microbiological fractionation of stable sulfur isotopes: a review and critique.– Geomicrobiology Journal, 1/3, 249–293. doi: 10.1080/01490457909377735

CHEN, J., WANG, Q., ZHANG, Q., CARRANZA, E.J.M. & WANG, J. (2018): Mineralogical and geochemical investigations on the iron-rich gibbsitic bauxite in Yongjiang basin, SW China.– Journal of Geochemical Exploration, 188. doi: 10.1016/j.gexplo.2018.02.007

CHEN, P., LIU, B., WANG, T., ZHOU, L., WANG, Y., SUN, G., HOU, K., et al. (2022): Genesis of the Danping bauxite deposit in northern Guizhou, Southwest China: Constraints from in-situ elemental and sulfur isotope analyses in pyrite.– Ore Geology Reviews, 148. doi: 10.1016/j.oregeorev.2022.105056

CHEN, T. (1978): Colloform and framboidal pyrite from the Caribou deposit, New Brunswick.– Canadian Mineral., 16/1, 9–15.

D'AMBROSI, C. (1926): Rapporti fra morfologia e trasgresioni nel Cretaceo e nel terziario dell'Istria.– Atti Della Accademia Scientifica Veneto–Trentino–Istriana, 16/13, 90–98.

D'ARGENIO, B. & MINDSZENTY, A. (1995): Bauxites and related paleokarst: tectonic and climatic event markers at regional unconformities.– Eclogae Geologicae Helvetiae, 88/3, 453–499.

DAVRANCHE, M., GRYBOS, M., GRUAU, G., PÉDROT, M., DIA, A. & MARSAC, R. (2011): Rare earth element patterns: A tool for identifying trace metal sources during wetland soil reduction.– Chemical Geology, 284/1–2, 127–137. doi: 10.1016/j.chemgeo.2011.02.014

DIAKONOV, I.I., RAGNARSDOTTIR, K.V. & TAGIROV, B.R. (1998): Standard thermodynamic properties and heat capacity equations of rare earth hydroxides: II. Ce(III)-, Pr-, Sm-, Eu(III)-, Gd-, Tb-, Dy-, Ho-, Er-, Tm-, Yb-, and Y-hydroxides. Comparison of thermochemical and solubility data.– Chemical Geology, 151/1–4, 327–347. doi: 10.1016/s0009-2541(98)00088-6

DOEBELIN, N. & KLEEBERG, R. (2015): Profex: A graphical user interface for the Rietveld refinement program BGMN.– Journal of Applied Crystallography, 48, 1573–1580. doi: 10.1107/S1600576715014685

DRAGOVIĆ, D. (1989): The red and white karstic bauxites of Montenegro (Yugoslavia.).– Travaux, 19/22, 249–257.

DURN, G., MINDSZENTY, A., TIŠLJAR, J. & MILEUSNIĆ, M. (2006): Clay mineralogy of bauxites and palaeosols in Istria formed during regional subaerial exposures of the Adriatic Carbonate Platform.– In: VLAHOVIĆ, I., TIBLJAŠ, D. & DURN, G. (eds.): 3rd Mid-European Clay Conference: Field Trip Guidebook, University of Zagreb, Faculty of Science and Faculty of Mining, Geology and Petroleum Engineering, Zagreb, Croatia, 3–30.

DURN, G., OTTNER, F., TIŠLJAR, J., MINDSZENTY, A. & BARUDŽIJA, U. (2003): Regional subaerial unconformities in shallow-marine carbonate sequences of Istria: Sedimentology, mineralogy, geochemistry and micromorphology of associated bauxites, palaeosols and pedo-sedimentary complexes.– In VLAHOVIĆ, I. & TIŠLJAR, J. (eds.): Field Trip Guidebook: Evolution of Depositional Environments from the Palaeozoic to the Quaternary in the Karst Dinarides and the Pannonian Basin. 22nd IAS Meeting of Sedimentology, Institute of Geology Zagreb, Zagreb, 209–255.

DURN, G., PERKOVIĆ, I., MILEUSNIĆ, M., VLAHOVIĆ, I., RUŽIČIĆ, S., MATEŠIĆ, D., CVETKO TEŠOVIĆ, B., et al. (2023): Red Istria: Western Istrian Anticline as an ideal natural laboratory for the study of the regional unconformities in carbonate rocks.– In: FIO FIRI, K. & ČOBIĆ, A. (eds.): Field trip A2, Excursion Guide-Book, 7th Croatian Geological Congress with International Participation, Hrvatski geološki institut, Zagreb, 33–58.

ECONOMOU-ELIOPOULOS, M., KONTOU, M. & MEGREMI, I. (2022): Biogeochemical redox processes controlling the element cycling: Insights from karst-type bauxite, Greece.– Minerals, 12/4:446. doi: 10.3390/min12040446

ELLAHI, S.S., TAGHIPOUR, B. & NEJADHADAD, M. (2017): The role of organic matter in the formation of high-grade Al deposits of the Dopolan karst type bauxite, Iran: Mineralogy, geochemistry, and sulfur isotope data.– Minerals, 7/6. doi: 10.3390/min7060097

ELLAHI, S.S., TAGHIPOUR, B., ZARASVANDI, A., BIRD, M.I. & D SOMARIN, A.K. (2015): Mineralogy, geochemistry and stable isotope studies of the Dopolan bauxite deposit, Zagros mountain, Iran.– Minerals, 6/1. doi: 10.3390/min6010011

FENG, J. L. (2010): Behaviour of rare earth elements and yttrium in ferromanganese concretions, gibbsite spots, and the surrounding terra rossa over dolomite during chemical weathering.– Chemical Geology, 271/3–4, 112–132. doi: 10.1016/j.chemgeo.2010.01.003

FERREIRA DA SILVA, E., BOBOS, I., XAVIER MATOS, J., PATINHA, C., REIS, A.P. & CARDOSO FONSECA, E. (2009): Mineralogy and geochemistry of trace metals and REE in volcanic massive sulfide host rocks, stream sediments, stream waters and acid mine drainage from the Lousal mine area (Iberian Pyrite Belt, Portugal).– Applied Geochemistry, 24/3, 383–401. doi: 10.1016/j.apgeochem.2008.12.001

FLÜGEL, E. (2004): Microfacies of Carbonate Rocks, Microfacies of Carbonate Rocks.– Springer Verlag, Berlin, 976 p. doi: 10.1007/978-3-662-08726-8

GAMALETSOS, P.N., GODELITSAS, A., KASAMA, T., CHURCH, N.S., DOUVALIS, A.P., GÖTTLICHER, J., STEININGER, R., et al. (2017): Nano-mineralogy and geochemistry of high-grade diasporic karst-type bauxite from Parnassos–Ghiona mines, Greece.– Ore Geology Reviews, 84. doi: 10.1016/j.oregeorev.2016.11.009

GRAULIS, S., CHATEIGNER, D., DOWNS, R.T., YOKOCHI, A.F.T., QUIRÓS, M., LUTTEROTTI, L., MANAKOVA, E., et al. (2009): Crystallography Open Database – An open-access collection of crystal structures.– Journal of Applied Crystallography, 42/4. doi: 10.1107/S0021889809016690

GRYBOS, M., DAVRANCHE, M., GRUAU, G. & PETITJEAN, P. (2007): Is trace metal release in wetland soils controlled by organic matter mobility or Fe-oxyhydroxides reduction?– Journal of Colloid and Interface Science, 314/2, 490–501. doi: 10.1016/j.jcis.2007.04.062

HÁMOR, T. (1994): The occurrence and morphology of sedimentary pyrite.– Bulletin of the Hungarian Geological Society, 37/1–2, 153–181.

HE, J., YANG, L., SHI, X., ZHAO, S., CAO, L., PAN, S., WU, F., et al. (2022): Genetic Mechanism of Pyrite in the Shale of the Longmaxi Formation and Its Influence on the Pore Structure: A Case Study of the Changning Area, South Sichuan Basin of SW China.– Frontiers in Earth Science, 10. doi: 10.3389/feart.2022.919923

VAN HINSBERGEN, D.J.J., TORSVIK, T.H., SCHMID, S.M., MAŢENCO, L.C., MAFFIONE, M., VISSERS, R.L.M., GÜRER, D., et al. (2020): Orogenic architecture of the Mediterranean region and kinematic reconstruction of its tectonic evolution since the Triassic.– Gondwana Research, 81, 79–229. doi. 10.1016/j.gr.2019.07.009

HOUGH, G., SWAPP, S., FROST, C. & FAYEK, M. (2019): Sulfur isotopes in biogenically and abiogenically derived uranium roll-front deposits.– Economic Geology, 114/2, doi: 10.5382/econgeo.2019.4634

HUANG, F., GAO, S., CHEN, L., SU, L., LI, Y., MENG, L., LIU, K., et al. (2020): Micro-texture and in situ sulfur isotope of pyrite from the Baiyunpu Pb–Zn deposit in central Hunan, South China: Implications for the growth mechanism of colloform pyrite aggregates.– Journal of Asian Earth Sciences, 193. doi: 10.1016/j.jseaes.2020.104302

JEŽ, J., OTONIČAR, B. (2018): Late Cretaceous geodynamics of the northern sector of the Adriatic Carbonate Platform (Western Slovenia).– Newsletters on Stratigraphy, 51/4, 381–410.

JI, H., WANG, S., OUYANG, Z., ZHANG, S., SUN, C., LIU, X. & ZHOU, D. (2004): Geochemistry of red residua underlying dolomites in karst terrains of Yunnan–Guizhou Plateau II. The mobility of rare earth elements during weathering.– Chemical Geology, 203/1–2, 1–27. doi: 10.1016/j.chemgeo.2003.08.012

KAWABE, I., KITAHARA, Y. & NAITO, K. (1991): Non-chondritic yttrium/holmium ratio and lanthanide tetrad effect observed in pre-Cenozoic limestones.– Geochemical Journal, 25/1, 31–44. doi:10.2343/geochemj.25.31

KELEMEN, P., DUNKL, I., CSILLAG, G., MINDSZENTY, A., VON EYNATTEN, H. & JÓZSA, S. (2017): Tracing multiple resedimentation on an isolated karstified plateau: The bauxite-bearing Miocene red clay of the Southern Bakony Mountains, Hungary.– Sedimentary Geology, 358/1, 84–96. doi: 10.1016/j.sedgeo.2017.07.005

KELEMEN, P., DUNKL, I., CSILLAG, G., MINDSZENTY, A., JÓZSA, S., FODOR, L. & VON EYNATTEN, H. (2023): Origin, timing and paleogeographic implications of Paleogene karst bauxites in the northern Transdanubian range, Hungary.– International Journal of Earth Sciences, 112/1. doi: 10.1007/s00531-022-02249-3

LASKOU, M. & ECONOMOU-ELIOPOULOS, M. (2007): The role of microorganisms on the mineralogical and geochemical characteristics of the Parnassos–Ghiona bauxite deposits, Greece.– Journal of Geochemical Exploration, 93/2, 67–77. doi: 10.1016/j.gexplo.2006.08.014

LASKOU, M. & ECONOMOU-ELIOPOULOS, M. (2013): Bio-mineralization and potential biogeochemical processes in bauxite deposits: Genetic and ore quality significance.– Mineralogy and Petrology, 107/4, 471–486. doi: 10.1007/s00710-012-0257-z

LAVEUF, C., CORNU, S. & JUILLOT, F. (2008): Rare earth elements as tracers of pedogenetic processes.– Comptes Rendus – Geoscience, 340/8, 523–532. doi: 10.1016/j.crte.2008.07.001

LIU, X., WANG, Q., FENG, Y., LI, Z. & CAI, S. (2013). Genesis of the Guangou karstic bauxite deposit in western Henan, China.– Ore Geology Reviews, 55/C, 162–175. doi: 10.1016/j.oregeorev.2013.06.002

MAKSIMOVIĆ, Z., MINDSZENTY, A. & PANTO, G. (1991): Contribution to the geochemistry of Hungarian karst bauxites and the allochthony/autochthony problem.– Acta Geologica Hungarica, 34/4, 317–334.

MAKSIMOVIĆ, Z. & PANTÓ, G. (1991): Contribution to the geochemistry of the rare earth elements in the karst-bauxite deposits of Yugoslavia and Greece.– Geoderma, 51/1–4, 93–109. doi: 10.1016/0016-7061(91)90067-4

MAMELI, P., MONGELLI, G., OGGIANO, G. & DINELLI, E. (2007): Geological, geochemical and mineralogical features of some bauxite deposits from Nurra (Western Sardinia, Italy) Insights on conditions of formation and parental affinity.– International Journal of Earth Sciences, 96/5, 887–902. doi:10.1007/s00531-006-0142-2

MATIČEC, D., VLAHOVIĆ, I., VELIĆ, I. & TIŠLJAR, J. (1996): Eocene limestones overlying Lower Cretaceous deposits of western Istria (Croatia): did some parts of present Istria form land during the Cretaceous.– Geologia Croatica, 49/1, 117–127. doi: 10.4154/GC.1994.46

MEDERSKI, S., PRŠEK, J., MAJZLAN, J., KIEFER, S., DIMITROVA, D., MILOVSKÝ, R., KOCH, C.B., et al. (2022): Geochemistry and textural evolution of As–Tl-Sb-Hg-rich pyrite from a sediment-hosted As-Sb-Tl-Pb ± Hg ± Au mineralization in Janjevo, Kosovo.– Ore Geology Reviews, 151, doi: 10.1016/j.oregeorev.2022.105221

MEHRA, O.P. & JACKSON, M.L. (1960), Iron Oxide Removal From Soils and Clays By a Dithionite–Citrate System Buffered With Sodium Bicarbonate.– In: Clays and clay minerals: Proceedings of the Seventh National Conference, Clays and Clay Minerals.

MO, H., YANG, R., LUO, C., LI, X., JI, Y., YANG, G., ZHOU, X., et al. (2023): Effect of Karst Geomorphology on the Sedimentary Mineralization and Geochemical Distribution of Bauxite: An Example from the Xiaoyuan Area in Qingzhen, Guizhou Province.– Minerals, 13/8. doi: 10.3390/min13081013

MONDILLO, N., DI NUZZO, M., KALAITZIDIS, S., BONI, M., SANTORO, L. & BALASSONE, G. (2022): Petrographic and geochemical features of the B3 bauxite horizon (Cenomanian–Turonian) in the Parnassos–Ghiona area: A contribution towards the genesis of the Greek karst bauxites.– Ore Geology Reviews, 143. doi: 10.1016/j.oregeorev.2022.104759

MONGELLI, G. (1997): Ce-anomalies in the textural components of Upper Cretaceous karst bauxites from the Apulian carbonate platform (southern Italy).– Chemical Geology, 140/1–2, 69–79. doi: 10.1016/S0009-2541(97)00042-9

MONGELLI, G., BONI, M., BUCCIONE, R. & SINISI, R. (2014): Geochemistry of the Apulian karst bauxites (southern Italy): Chemical fractionation and parental affinities.– Ore Geology Reviews, 63, 9–21. doi: 10.1016/j.oregeorev.2014.04.012

MONGELLI, G., BONI, M., OGGIANO, G., MAMELI, P., SINISI, R., BUCCIONE, R. & MONDILLO, N. (2017): Critical metals distribution in Tethyan karst bauxite: The cretaceous Italian ores.– Ore Geology Reviews, 86, 526–536. doi: 10.1016/j.oregeorev.2017.03.017

MONGELLI, G., MAMELI, P., SINISI, R., BUCCIONE, R. & OGGIANO, G. (2021): Rees and other critical raw materials in Cretaceous Mediterranean-type bauxite: The case of the Sardinian ore (Italy).– Ore Geology Reviews, 139/B. doi: 10.1016/j.oregeorev.2021.104559

NIA, R. (1968): Geologische, petrographische, geochemische Untersuchungen zum Problem der Boehmit-Diaspor-Genese in griechischen Oberkreide-Bauxiten der Parnass-Kiona-Zone.– PhD thesis, University of Hamburg, 1–133.

OTONIČAR, B. (2006): Upper Cretaceous to Palaeogene forebulge unconformity associated with foreland basin evolution (Kras, Matarsko polje and Istria, southwestern Slovenia and northwestern Croatia).– Acta Carsologica, 36/1, 101–120. doi.org/10.3986/ac.v36i.213

OLÍAS, M., CÁNOVAS, C.R., BASALLOTE, M.D. & LOZANO, A. (2018): Geochemical behaviour of rare earth elements (REE) along a river reach receiving inputs of acid mine drainage–. Chemical Geology, 493, 468–477. doi: 10.1016/j.chemgeo.2018.06.029

ÖZTÜRK, H., HEIN, J.R. & HANILÇI, N. (2002): Genesis of the Doğankuzu and Mortaş bauxite deposits, Taurides, Turkey: Separation of Al, Fe, and Mn and implications for passive margin metallogeny.– Economic Geology, 97/5, 1063–1077. doi: 10.2113/gsecongeo.97.5.1063

PASQUIER, V., FIKE, D.A. & HALEVY, I. (2021): Sedimentary pyrite sulfur isotopes track the local dynamics of the Peruvian oxygen minimum zone.– Nature Communications, 12/1:440312/1. doi: 10.1038/s41467-021-24753-x

POURRET, O., DAVRANCHE, M., GRUAU, G. & DIA, A. (2007): Rare earth elements complexation with humic acid.– Chemical Geology, 243/1–2, 128–141. doi: 10.1016/j.chemgeo.2007.05.018

POURRET, O., DAVRANCHE, M., GRUAU, G. & DIA, A. (2008): New insights into cerium anomalies in organic-rich alkaline waters.– Chemical Geology, 251/1–4, 120–127. doi: 10.1016/j.chemgeo.2008.03.002

RADUSINOVIĆ, S. & PAPADOPOULOS, A. (2021): The potential for REE and associated critical metals in karstic bauxites and bauxite residue of Montenegro.– Minerals, MDPI, 11/9, 975. doi: 10.3390/min11090975

RAISWELL, R. (1982): Pyrite texture, isotopic composition and the availability of iron.– American Journal of Science, 282/8, 1244–1263. doi: 10.2475/ajs.282.8.1244

RASMUSSEN, K., NEUMANN, A.C.N. (1988): Holocene overprint of Pleistocene paleokarst: Bight of Abaco, Bahamas.– In: JAMES, N.P., CHOQUETTE P.W. (eds.): Paleokarst. Springer-Verlag, 132–148.

ROEDDER, E. (1968): The non-colloidal origin of 'colloform' textures in sphalerite ores.– Economic Geology, 63/5, 451–471. doi: 10.2113/gsecongeo.63.5.451

SCHMID, S.M., BERNOULLI, D., FÜGENSCHUH, B., MATENCO, L., SCHEFER, S., SCHUSTER, R., TISCHLER, M., et al. (2008): The Alpine–Carpathian–Dinaridic orogenic system: Correlation and evolution of tectonic units.– Swiss Journal of Geosciences, 101/1, 139–183. doi: 10.1007/s00015-008-1247-3

SCHMID, S.M., FÜGENSCHUH, B., KOUNOV, A., MAŢENCO, L., NIEVERGELT, P., OBERHÄNSLI, R., PLEUGER, J., et al. (2020): Tectonic units of the Alpine collision zone between Eastern Alps and western Turkey.– Gondwana Research, 308–374. doi: 10.1016/j.gr.2019.07.005

SHAHEEN, S.M., ALESSI, D.S., TACK, F.M.G., OK, Y.S., KIM, K.H., GUSTAFSSON, J.P., SPARKS, D.L., et al. (2019). Redox chemistry of vanadium in soils and sediments: Interactions with colloidal materials, mobilization, speciation, and relevant environmental implications – A review.– Advances in Colloid and Interface Science, 265, 1–13. doi: 10.1016/j.cis.2019.01.002

ŠINKOVEC, B., SAKAČ, K. & DURN, G. (1994): Pyritized bauxites from Minjera, Istria, Croatia.– Natura Croatica, 3/1, 41–65.

TABELIN, C.B., IGARASHI, T., VILLACORTE-TABELIN, M., PARK, I., OPISO, E.M., ITO, M. & HIROYOSHI, N. (2018): Arsenic, selenium, boron, lead, cadmium, copper, and zinc in naturally contaminated rocks: A review of their sources, modes of enrichment, mechanisms of release, and mitigation strategies.– Science of the Total Environment, 645/7, 1522–1553. doi: 10.1016/J.SCITOTENV.2018.07.103

TANG, J. & JOHANNESSON, K.H. (2003): Speciation of rare earth elements in natural terrestrial waters: Assessing the role of dissolved organic matter from the modeling approach.– Geochimica et Cosmochimica Acta, 67/13, 2321–2339. doi: 10.1016/S0016-7037(02)01413-8

TAYLOR, S.R. & MCLENNAN, S.M. (1985): The Continental Crust: Its Composition and Evolution, The Continental Crust: Its Composition and Evolution. An Examination of the Geochemical Record Preserved in Sedimentary Rocks.– Blackwell Science, Oxford, 312 p.

TOMAŠIĆ, N., ČOBIĆ, A., BEDEKOVIĆ, M., MIKO, S., ILIJANIĆ, N., GIZDAVEC, N. & MATOŠEVIĆ, M. (2021): Rare earth elements enrichment in the Upper Eocene Tošići-Dujići bauxite deposit, Croatia, and relation to ree mineralogy, parent material and weathering pattern.– Minerals, 11/1:1260. doi: 10.3390/min11111260

VELIĆ, I., MATIČEC, D., TIŠLJAR, J. & VLAHOVIĆ, I. (1995): Opći prikaz geološke građe Istre (A review of the geology of Istria).– In: VLAHOVIĆ, I. & VELIĆ, I. (eds.): 1st Croatian Geological Congress, Excursion Guidebook. Croatian Geological survey, Zagreb, 5–30.

VIND, J., MALFLIET, A., BLANPAIN, B., TSAKIRIDIS, P.E., TKACZYK, A.H., VASSILIADOU, V. & PANIAS, D. (2018): Rare earth element phases in bauxite residue.– Minerals, 8/2:77. doi: 10.3390/min8020077

VLAHOVIĆ, I., TIŠLJAR, J. & VELIĆ, I. (1994): Influence of synsedimentary tectonics and eustatic changes on deposition of the Cenomanian platform carbonates in Istria (Western Croatia).– Géologie Méditerranéenne, 21/3–4, 189–193. doi: 10.3406/geolm.1994.1561

VLAHOVIĆ, I., TIŠLJAR, J., VELIĆ, I. & MATIČEC, D. (2005): Evolution of the Adriatic Carbonate Platform: Palaeogeography, main events and depositional dynamics.– Palaeogeography, Palaeoclimatology, Palaeoecology, 220/3–4, 333–360. doi: 10.1016/j.palaeo.2005.01.011

WANG, X., JIAO, Y., DU, Y., LING, W., WU, L., CUI, T., ZHOU, Q., et al. (2013): REE mobility and Ce anomaly in bauxite deposit of WZD area, Northern Guizhou, China.– Journal of Geochemical Exploration, 133, 103–117. doi: 10.1016/j.gexplo.2013.08.009

WANG, B., LEI, H. & HUANG, F. (2022): Impacts of sulfate-driven anaerobic oxidation of methane on the morphology, sulfur isotope, and trace element content of authigenic pyrite in marine sediments of the northern South China Sea.– Marine and Petroleum Geology, 139. doi: 10.1016/j.marpetgeo.2022.105578

WANTY, R.B. & GOLDHABER, M.B. (1992): Thermodynamics and kinetics of reactions involving vanadium in natural systems: Accumulation of vanadium in sedimentary rocks.– Geochimica et Cosmochimica Acta, 56/4, 1471–1483. doi: 10.1016/0016-7037(92)90217-7

WIGNALL, P.B. & NEWTON, R. (1998): Pyrite framboid diameter as a measure of oxygen deficiency in ancient mudrocks.– American Journal of Science, 298/7, 537–552. doi: 10.2475/ajs.29

WILKIN, R.T., BARNES, H.L. (1996): Pyrite formation by reactions of iron monosulfides with dissolved inorganic and organic sulfur species.– Geochimica et Cosmochimicha.Acta, 60/21, 4167–4179. doi: 10.1016/S0016-7037(97)81466-4

WILLIAMS, J.R. (2014): Karst-Associated Bauxite Deposits of Parnassos–Ghiona, Central Greece: Ore Genesis and Structural Evolution.– Ph.D. Thesis, University of Brighton, 311 p.

XIAO, J., LI, Y., YANG, H., XU, J. & HUANG, M. (2021): Geochemistry of the Yudong bauxite deposit, south-eastern Guizhou, China: Implications for conditions of formation and parental affinity.– Journal of Geochemical Exploration, 220. doi: 10.1016/j.gexplo.2020.106676

YANG, L., WANG, Q., ZHANG, Q., CARRANZA, E.J.M., LIU, H., LIU, X. & DENG, J. (2017): Interaction between karst terrain and bauxites: Evidence from Quaternary orebody distribution in Guangxi, SW China.– Scientific Reports, 7/1. doi: 10.1038/s41598-017-12181-1

YANG, S., WANG, Q., DENG, J., WANG, Y., KANG, W., LIU, X. & LI, Z. (2019): Genesis of karst bauxite-bearing sequences in Baofeng, Henan (China), and the distribution of critical metals.– Ore Geology Reviews, 115. doi: 10.1016/j.oregeorev.2019.103161

YUE, L., JIAO, Y., WU, L., RONG, H., FAYEK, M. & XIE, H. (2020): Evolution and origins of pyrite in sandstone-type uranium deposits, northern Ordos Basin, north-central China, based on micromorphological and compositional analysis.– Ore Geology Reviews, 118. doi: 10.1016/j.oregeorev.2020.103334

YUSTE, A., BAULUZ, B. & MAYAYO, M.J. (2017): Origin and geochemical evolution from ferrallitized clays to karst bauxite: An example from the Lower Cretaceous of NE Spain.– Ore Geology Reviews, 84/3, 67–79. doi: 10.1016/j.oregeorev.2016.12.025

ZARASVANDI, A., CARRANZA, E.J.M. & ELLAHI, S.S. (2012): Geological, geochemical, and mineralogical characteristics of the Mandan and Deh-now bauxite deposits, Zagros Fold Belt, Iran.– Ore Geology Reviews, 48, 125–138. doi: 10.1016/j.oregeorev.2012.02.010

ZHANG, J.-Y., WANG, Q., LIU, X.-F., ZHOU, G.-F., XU, H.-P. & ZHU, Y.-G. (2022): Provenance and ore-forming process of Permian lithium-rich bauxite in central Yunnan, SW China.– Ore Geology Reviews, 145. doi: 10.1016/j.oregeorev.2022.104862

ZHAO, L., LIU, X., WANG, Q., MA, X., LIU, L., SUN, X. & DENG, J. (2023): Genetic mechanism of super-large karst bauxite in the northern North China Craton: Constrained by diaspore in-situ compositional analysis and pyrite sulfur isotopic compositions.– Chemical Geology, 622. doi: 10.1016/j.chemgeo.2023.121388

ZHOU, W., HAN, G., LIU, M., SONG, C. & LI, X. (2020): Geochemical distribution characteristics of rare earth elements in different soil profiles in Mun River Basin, Northeast Thailand.– Sustainability, 12/2, 457. doi: 10.3390/su12020457

3. DISCUSSION

3.1. 1st Unconformity

3.1.1. Provenance of the parent material and geotectonic setting

The formation of the 1st Unconformity started with the emergence of the Istrian part of the AdCP during the late Oxfordian to early Kimmeridgian. This event marked the beginning of the karstification of exposed carbonate rocks and the deposition of the parent material from which the bauxite was formed. The uplift was essentially caused by the obduction of the Vardar Ocean ophiolites over the NE margin of the Adria Microplate (Schmid et al., 2008, 2020; Picotti & Cobianchi, 2017; van Hinsbergen et al., 2020), where the load of the advancing (ophiolitic) nappes created a foreland basin and beyond that a foreland-bulge. The start of this long-lasting subaerial exposure phase is marked locally by the formation of Rovinj breccia, followed by the formation of bauxites, with Rovinj-1 deposit as the best example (Šinkovec, 1974; Velić and Tišljar, 1988) or palaeosols, such as the Zlatni Rt palaeosol (Velić and Tišljar, 1988; Vlahović et al., 2003). In some places the unconformity is present only as an erosional contact between the units of the 1st and 2nd Megasequences. The exact source and type of the material from which the soil-derived-sediments of the 1st Unconformity developed are hard to pinpoint, as their original geochemical signatures and structures were destroyed by pedogenesis or bauxitisation. Nevertheless, some general facts about the type of the parent material were obtained through the examination of the heavy and light mineral fraction and petrographical observations from the Rovinj-1 bauxite coupled with the mineralogical composition from both the Rovinj-1 bauxites and Zlatni rt palaeosol. The data from the Rovinj-1 deposit included here are from the unpublished paper by Perković et al. (submitted). The occurrence of metamorphic minerals such as clinozoisite, garnet, kyanite and epidote coupled with the presence of finely dispersed equidimensional mica, quartz and feldspar grains in the bauxite matrix indicate the contribution of aeolian material during its deposition. The exact source of the aeolian material could have been precisely pinpointed by the dating of detrital zircons (Kelemen et al., 2017, 2023; Brlek et al., 2021), but since this was not performed in this study, exact source of the aeolian material could not have been established. The presence of euhedral zircons likely indicates the contribution of volcanic material, which is also plausibly supported by the presence of amphiboles. There is evidence of contemporaneous volcanic activity as occurrences of several levels of bentonites/tuffs of Kimmeridgian–Tithonian age are documented in the nearby Gorski Kotar, Croatia (Šćavničar & Nikler, 1976; Velić et al., 1994, 2002) and in the Trento Plateau, NE Italy (Pellenard et al., 2013; Picotti & Cobianchi, 2017). These materials were likely derived from the volcanic centres formed during the obduction of the Vardar Ocean ophiolites, as suggested by Picotti & Cobianchi (2017). The contribution of the insoluble carbonate residue cannot be overlooked, as Muča limestones, which compose the bedrock of both the Rovinj-1 bauxite deposit and Zlatni rt palaeosol, contain a relatively high content of insoluble residue (2.19 %; Durn et al., 1999), which was liberated and accumulated during the karstification of these limestones. Zlatni rt

palaeosol is mainly composed of pedogenic $1M_d$ illite, but it also contains a certain portion of detrital $2M_1$ illite, which could have been derived from the insoluble residue of Muča limestones, which is mainly illitic. Therefore, it can be proposed that the parent material from which the deposits of the 1st Unconformity were formed was polygenetic in origin and derived from aeolian dust, volcanic dust and insoluble carbonate residue.

3.1.2. Palaeoenvironmental and palaeoclimatic evolution of the 1st Unconformity

The influence of the upcoming emergence started before the karstification, erosion and pedogenesis which marked the 1st Unconformity, through the appearance of cyclical occurrences of subaerial exposure surfaces in the Muča unit in the bedrock of the Zlatni rt palaeosol. Nevertheless, the main event which characterises the 1st Unconformity was the formation of ferrallitic materials, such as the Rovinj-1 bauxite, and palaeosols, such as the Zlatni rt palaeosol. As such, the palaeoenvironmental evolution of such deposits is important for its understanding, where for this purpose both the Zlatni rt palaeosol and the Rovinj-1 deposit were studied, and the data from an unpublished paper by Perković et al. (submitted) are included in this thesis regarding the Rovinj-1 deposit, as this was one of the cornerstones for the proper reconstruction of the evolution of the 1st Unconformity.

The Rovinj bauxite was formed in situ, as indicated by its uniform chemical and mineralogical composition (cf. Bardossy, 1982; D'Argenio & Mindszenty, 1992), and is composed of boehmite, kaolinite, haematite, hydroxyl-interlayered vermiculite, illite and titanium oxides. However, the uppermost section of the deposit is largely composed of clastic bauxite, implying the reworking and potential contribution from other surrounding ferralitic soils and/or bauxite, suggesting partially parallochtonous origin. High kaolinite and silica content, as well as a generally planar morphology of the deposit suggest proximity to the water table during its formation, which limited the degree of karstification and reduced the drainage efficiency (cf. Bardossy, 1982; Combes & Bardossy, 1995). The clastic bauxite lithologies display a coarsening-upward trend, which is likely a consequence of diminishing vegetation cover. Vegetation is an important factor in bauxite formation as it is a source of organic acids and CO_2 dissolving to form carbonic acid, which both amplify the chemical weathering and removal of bases, but they are also important as a protection against erosion by torrential floods in bauxitic terrains (see Bardossy 1982 and references therein). The upper clastic lithologies are also iron oxide-enriched, featuring reworked iron oxide impregnations and iron-rich pseudooids. This is altogether indicative of climatic aridification as aridification promotes iron oxide precipitation in bauxites (Bardossy, 1982; Yang et al., 2019) while also negatively impacting the plant cover. This observed aridification in the Rovinj-1 deposit temporally aligns with climate trends in NW Europe during the Tithonian, which also display the shift towards drier climate (Wignall & Ruffell, 1990; Brigaud et al., 2008; Hesselbo et al., 2009; Alberti et al., 2017; Błażejowski et al., 2023). This aridification trend continues in the cover of the Rovinj-1 bauxite, composed of an alternation of limestones, *black-pebble* breccias and clays/marls. The clay mineralogy of the clay/marl layers was analysed, demonstrating a clear trend which shows the decrease in kaolinite content and an increase in illite as well as mixed-layered illite-smectite

content, indicating the shift towards drier climate. The illite and mixed-layered smectite were developing in the still emerged surrounding areas, on which pedogenesis was likely still an ongoing process, where these soils were able to respond to the climate change through the switch from siallitisation to bisiallitisiation. Nevertheless, some of the illite and mixed-layered illite-smectite could have also developed through wetting and drying of the soil in a brackish to saline environment, which was proposed as a mechanism for the formation of these minerals in the Zlatni rt palaeosol (cf. Huggett & Cuadros, 2005).

The cyclical cover sequence in the deposit represents a part of a so called *blue hole sequence*, which starts with karstification and palaeosol formation, followed by the deposition of limestones in a schizohaline environment and finally fully marine limestones. Such blue hole sequences are typical for the internal transgression in karst terrains (Rasmussen & Neumann, 1988; Carannante et al., 1994a, b), characterised by the water table rise through karstic conduits in the palaeotopographic depressions during the initial stages of the transgression by tidal pumping (Martin et al., 2012; Smith et al., 2021). Similar blue hole sequence was also described in the cover of the Hungarian Gánt bauxite deposit (Bignot et al., 1985; Trabelsi et al., 2021). The presence of Ostracods and charophycean oogonia, with sporadic occurrences of miliolid foraminifera and *Favreina* faecal pellets in the limestones of this sequence indicates its formation in a restricted schizohaline karstic lake.

During the initial flooding, the red bauxite was transfomed into grey bauxite through pyritisation in the marshy environment, as well as into the white bauxite through dissolution of iron oxides as the reducing and acid porewaters were percolating along the cracks and faults into the red bauxite. The white bauxite also formed through decomposition of roots, since a few metres thick, dense network of white bauxite veins can be seen below the grey bauxite.

The redox conditions in the lake shifted during its deposition, with euxinic conditions marking the start of the cover sequence while oxic to equivocal conditions mark its later phases. This is recorded through the changes in Fe_{hr}/Fe_{tot} and Fe_{py}/Fe_{hr} ratios, the decrease in pyrite content and variations in trace elemental contents. The progressive sea-level rise led to the increasing connection of the originally restricted lake/ponds with surrounding marine environments, which probably led to the reduced redox stratification in the lake as this connection likely increased the water circulation in the lake. It is hard to exactly pinpoint these redox changes, but the progressive sea-level rise can be suggested as the possible driver of these changes. The sea-level rise could have also impacted the supply of organic matter, whose decomposition drives anoxia in sediments (Berner, 1970), as flooding has shown to impact the production and accumulation of organic matter (Sahrawat, 2003; Majidzadeh et al., 2017). The decreased organic matter production might also be a result of climate aridification, since aridification can cause the decrease in plant productivity (Hu et al., 2021), but this is not entirely straightforward and is hard to properly address without additional research. The shift from restricted towards open conditions is also indicated by the occurrence of glauconite in the upper part of the cover sequence, which suggests an increasing marine influence in the lake, as its formation requires the source of potassium (Odin & Matter, 1981; Giresse & Wiewióra, 2001;

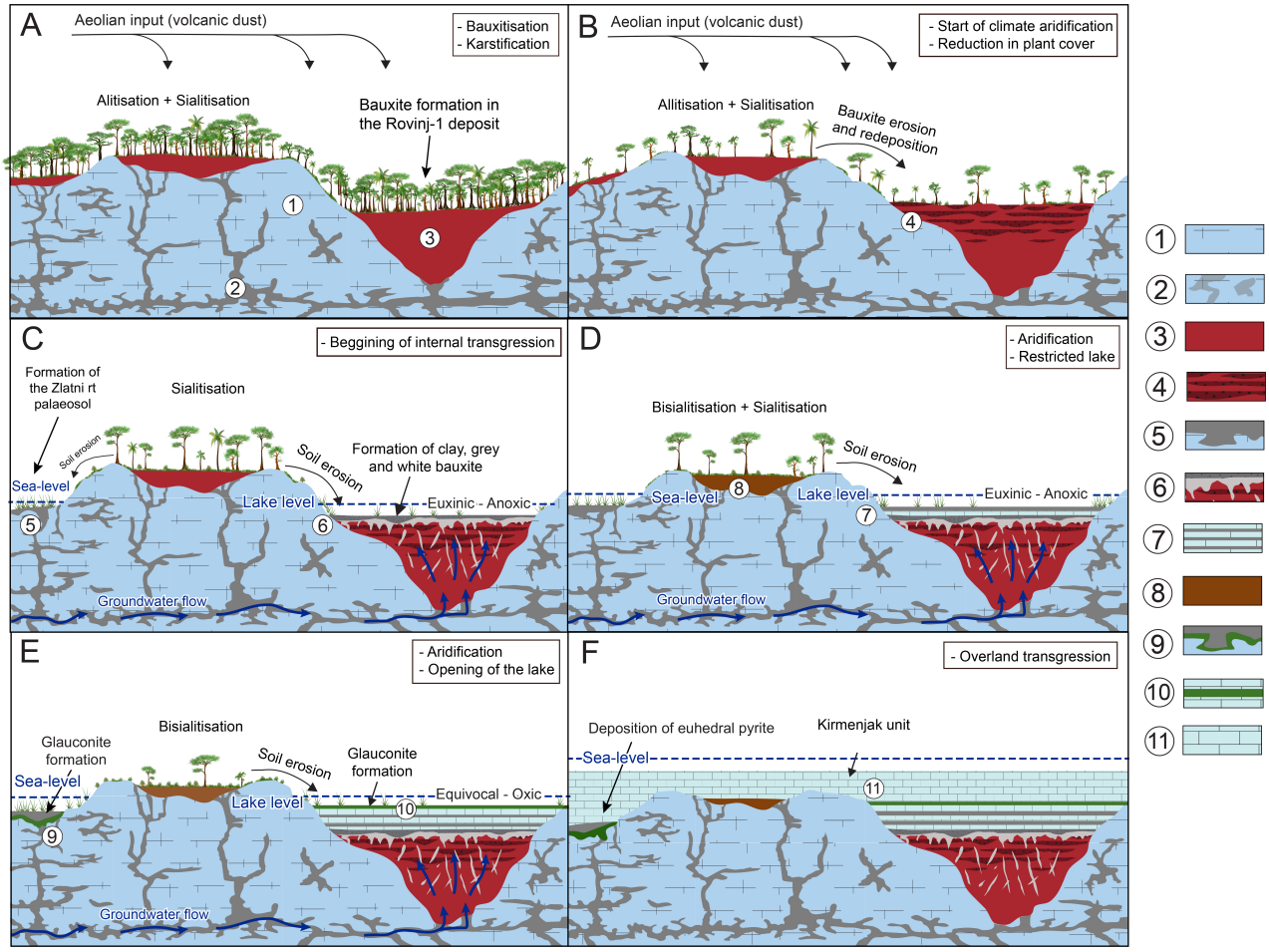

Figure 2. Summarised genesis of the Rovinj-1 bauxite deposit, Zlatni rt palaeosol and their surrounding area, modified after Perković et al. (submitted). (A) Karstification of emerged carbonates and bauxitisation of aeolian and volcanic dust together with insoluble carbonate residue. (B) Start of climate aridification which led to the reduction of plant cover, allowing the increased erosion and redeposition of Rovinj-1 bauxite and surrounding soils and bauxites. (C) Beginning of the transgression which led to the formation of karstic lake above the Rovinj-1 bauxite in which grey and white bauxite as well as clays formed in euxinic to anoxic conditions, together with the formation of the Zlatni rt palaeosol in the wetland environment. (D) Continued climate aridification recorded through the increasing illite and mixed-layered illite-smectite (MLIS) content and the reduction in kaolinite content in the Rovinj-1 deposit. (E) Continued climate aridification simultaneously with the opening of the lake in the Rovinj-1 deposit, visible through the redox change to oxic to equivocal conditions as well as the glauconitisation event in both the Rovinj-1 deposit and the Zlatni rt palaeosol (Perković et al., 2024). (F) End of subaerial exposure phase – overland transgression of the emerged carbonate terrain and deposition of shallow-marine Kirmenjak unit, which also caused the precipitation of euhedral pyrite crusts in the Zlatni rt palaeosol. Legend: 1 – limestones of Oxfordian to lower Kimmeridgian Muča unit; 2 – karstification, 3 – bauxite and ferralsols; 4 – clastic bauxite; 5 – wetland soils; 6 – grey and white bauxite; 7 – alternation of clays/marls and limestones; 8 – soils hosting sialitisation and bisialitisation; 9 – glauconite in clays/marls; 10 – glauconite in palaeosols; 11 – limestones of upper Tithonian Kirmenjak unit.

Meunier & El Albani, 2007; Baldermann et al., 2015, 2017), which is readily found in the seawater. Its presence also supports the shift towards equivocal conditions, as its formation requires both oxic and reducing conditions, since it contains both ferric and ferrous iron. A similar material as the clays/marls from the upper part of cover sequence of the Rovinj-1 bauxite is found in the Zlatni rt area, which also host such peculiar glauconite occurrence. Glauconite occurrence is there found within the contact zone between the palaeosol and its karstified bedrock together with euhedral

pyrite crusts. This glauconite occurrence, together with the palaeosol in which it was formed, was studied in detail, as this is one of the rare instances of glauconite formation within a palaeosol, which is a valuable and important finding for the understanding of glauconite formation in such settings. The palaeosol was a wetland soil during its formation, likely a vertisol, as indicated by its grey colour, cross-striated and parallel striated b-fabric, as well as a large number of reworked clay coatings. It was derived from aforementioned parent materials, but with the addition of locally derived ferralitic material, as indicated by the presence of pedogenic kaolinite and supported by the vicinity of the Rovinj-1 deposit, located just a few kilometers away. This was likely the source of iron required for glauconite formation. It is primarily illitic, composed of illite, together with minor amounts of kaolinite, dioctahedral vermiculite, iron sulphides and titanium oxides. The glauconite was found to be formed through two processes: (1) the gradual uptake of potassium, magnesium and iron by the host clays such as illite as well as mixed-layered illite-smectite, and (2) through direct precipitation as the host clays were being dissolved and potassium and iron ions were introduced to the dissolved aluminium and silica compounds, altogether mediated by microbes as indicated by the caterpillar morphology in most glauconites. The glauconite is also present as a light green, likely more ferric glauconite, and a darker bluish green glauconite which likely contains more ferrous iron. These two types are either present individually in the palaeosol or alternate together with pyrite in veinlets within it. This interplay between the pyrite and glauconite with different proportions of ferric and ferrous iron indicates fluctuations within its formational environment, which was probably linked to the the sea-level oscillations as the transgression progressed. The oscillating character of the transgression is also visible by the cyclical character of the cover sequence in the Rovinj-1 deposit. The instances of this same glauconite occurrence in a wider area suggest that this was a glauconitisation event, which characterised one of the stages of the internal transgression following the 1st Unconformity in the Rovinj area. The glauconitisation was followed by the deposition of transgressive black pebble breccias in the area of Zlatni rt, which are also present in several levels above the Rovinj-1 bauxite deposit. This is likely a result of the different setting of these two localities, where the Rovinj-1 deposit, due to its formation in a large sinkhole surrounded by elevated areas, was protected from high-energy events during the first stages of flooding, which likely led to the erosion and reworking in the Zlatni rt area which was not situated in a such protected karstic feature. The deposition of the Kirmenjak limestone at both localities marks the final end of the 1st Unconformity and the shift from an internal to an overland transgression. In the Zlatni rt palaeosol, this final burial of the palaeosol was connected to the formation of euhedral pyrite crusts in its contact with the carbonate bedrock.

3.2. 3rd Unconformity – Minjera bauxites

3.2.1. Geotectonic setting and provenance of the Minjera deposits

Minjera bauxites are a part of a widespreaded occurrence of Palaeogene bauxites, which are common throughout northern, eastern and southern Istria. Their stratigraphic position fits them

within the well-known Perimediterranean bauxitisation event, which resulted in a formation of a vast bauxite belt stretching from Hungary through Slovenia, Croatia, Bosnia and Herzegovina, Montenegro, and Albania to Greece. The Dinaric part of this bauxite belt is a result of the Late Cretaceous closure of the Vardar Ocean (Schmid et al., 2008, 2020; Van Hinsbergen et al., 2020), as it led to the formation of a large foreland basin in the area, located in present area of Internal Dinarides. This caused the tectonic uplift of the former Adriatic Carbonate Platform as a flexural forebulge developed in response to the overburden pressure generated by the advancing nappes (Otoničar, 2006; Jež & Otoničar, 2018). This event also initiated the subaerial exposure phase which causing the karstification and accumulation of parent material, resulting in the development of bauxites, including the Minjera deposit. The exact source material from which these deposits formed is hard to determine due to the destructive nature of bauxitisation, but certain possible types of parent material are implied based on the data from the heavy mineral fraction. The presence of metamorphic minerals such as staurolite and amphiboles suggests an aeolian contribution, while the absence of minerals related to volcanism, such as zircons, suggests that volcanic material was not one of the main sources of parent material. This however does not completely exclude it, as volcanic material is commonly one of the primary parent materials from which karst bauxites form (Bardossy, 1982; D'Argenio & Mindszenty, 1995; Kelemen et al., 2017, 2023; Brlek et al., 2021). Insoluble carbonate residue could have also played the role in the formation of these deposits, but its contribution cannot be either confirmed or disputed.

3.2.2. Palaeoenvironmental evolution of Minjera bauxites

The palaeoenvironmental reconstruction of the Minjera bauxites was mostly focused on the palaeoenvironmental changes after their deposition, as it produced a significant amount of pyritised bauxite, which can be used as a very good example of pyritisation in karst bauxites in general. However, the obtained data did not allow any additional palaeoclimatic reconstruction, beyond the fact that humid and tropical climate characterised the 3rd Unconformity, which is clearly apparent from the presence of numerous karst bauxites. Despite this part of the research being focused on the changes after the deposition of Minjera bauxites, some interesting differences signifying the variability in the palaeoenvironment of individual deposits prior to their pyritisation were identified. These differences can be primarily seen through the variations in the morphology of individual bauxites from the Minjera deposits, as three different types were identified: the large canyon deposits (elongated, deeper than 10 m and between 20 and 40 m along its longer axis), small canyon deposits (elongated, less than 10 m deep with the longer axis shorter than 20 m) and sinkhole deposits (circular shape, less than 10 m deep and smaller than 10 m in diameter). Both the smaller canyon deposits and sinkhole deposits were found mostly on the southern bank of the Mirna River, while the larger canyon deposits were found on the northern side. The Kozina beds are also much thicker on the southern side, supporting this palaeotopographic disposition.

Described morphological differences are also reflected in the geochemical and mineralogical composition of the two studied deposits, the D-15 deposit which is of the smaller canyon type from the southern side and the D-1 deposit which is a larger canyon deposit from the northern side. The

D-1 deposit contains much more boehmite and smaller amounts of leachable elements such as large-ion litophile elements, Ca, K, Mg and Mn, compared to the D-15 deposit which is predominantly composed of kaolinite and contains larger quantities of these elements. This altogether reflects the differences in palaeotopography of the area where Minjera bauxites formed, since the northern part was apparently located in the higher palaeotopographic position which promoted the formation of deeper karstic features in which fluid-flow was more intense and led to the higher leaching of silica and other leachable elements resulting in formation of boehmitic and deeper bauxite bodies, compared to the southern part where shallower bauxite bodies with higher kaolinite content were formed. This is one of the significant new findings in the Minjera bauxites, as this work was primarily focused on the pyritisation of these deposits which were already studied to a certain degree in the work by Šinkovec et al. (1994). The addition of SEM-EDS and stable sulphur isotopes in the present study allowed a much more detailed reconstruction of the pyritisation that marked the current occurrence of these bauxite deposits.

Based on the gathered data, the pyritisation was a multi-phase process, where four stages of pyritisation were determined. In the first phase, framboidal and micrometre-sized anhedral pyrite formed, replacing the iron oxide-rich features in the red bauxite such as the iron oxides in the matrix, ooid cortices and in the reworked bauxite clasts. This was followed by the deposition of colloform pyrite in the second phase, which formed as overgrowths on these previously formed pyrite morphologies. During the deposition of pyrite during these two phases, the aqueous environment was supersaturated towards pyrite, as colloform pyrite and framboidal pyrite form in such conditions (Roedder, 1968; Chen, 1978; Barrie et al., 2009). In the third phase, euhedral pyrite formed, also overgrowing the pyrite deposited during the first two phases, with its formation indicating a shift towards undersaturated solutions with respect to pyrite (Roedder, 1968; Chen, 1978; Barrie et al., 2009). The formation of pyrite veins which cross-cut previously deposited pyrite morphologies and textural elements indicates the final stage of pyritisation. These pyritisation phases are supported by the stable sulphur isotopes, as the $\delta^{34}S$ values display a wide range of values, from -40.86 to 2.32 ‰, and when compared to the global seawater ^{34}S values of 17 ‰ and 19 ‰ recorded during the Late Cretaceous and Palaeocene (Algeo et al., 2015) yield the enrichment factors between -60 ‰ and -15 ‰. The highly negative values indicate the significant enrichment of the lighter ^{32}S isotope, which indicate microbial sulphate reduction as the main driver behind the pyritisation of these bauxites. Such highly negative values also indicate that the system was open during this time, as in the open system the supply of sulphate is virtually unlimited for the microbes, which will then utilise the lighter ^{32}S isotope instead of the heavier ^{34}S, leading to the high enrichment of the lighter isotope, reflected through the high negative values of $\delta^{34}S$ (Chambers & Trudinger, 1979; Algeo et al., 2015; Hough et al., 2019; Pasquier et al., 2021). During the phase when the system was open, the first two phases of pyritisation likely took place, as the sulphur supply was not limited. This changed however, as we see the drop in saturation of the porewaters with respect to pyrite, which is also reflected by the higher values of $\delta^{34}S$, as higher values indicate that the system was completely or partially closed, forcing the microbes to utilize the heavier sulphur isotope as the sulphate supply was not being renewed (Chambers & Trudinger, 1979; Algeo

et al., 2015; Hough et al., 2019; Pasquier et al., 2021). This likely caused the drop in the saturation of porewaters, which caused the formation of euhedral pyrite and pyrite veins, probably as a result of the progressive burial of the bauxites.

The microbial sulphur reduction requires a source of organic matter, and in the Minjera deposits it was supplied by the marshy environment that was established atop of the bauxites during the initial stages of the Palaeocene transgression. This is visible in the beginning of the bauxite cover-sequence, where limestones are intercalated with coal seams. These limestones were deposited in a lacustrine environment, as indicated by the presence of the typical flora and fauna together with fresh water green algae *Cladophorites*, ostracods, gastropods and Charophyta. These changes are recorded in the upper part of the cover sequence, as the increased marine influence is visible through the more common occurrences of benthic foraminifera. This sequence was deposited during the internal transgression of the exposed carbonate terrain and was later followed with the deposition of fully marine Foraminiferal limestones. This sequence represents another example of the "blue hole" sequence deposited after the phase of bauxitisation, similar to the Rovinj-1 bauxite deposit (Perković et al., submitted).

3.3. Differences in behaviour of trace elements in reducing and oxidising conditions in bauxites and palaeosols

The study of trace and rare earth elements across a range of different materials deposited in all four studied unconformities in the depositional sequence of the Western Istrian Anticline showed an array of differences in the behaviour of these elements between the materials formed in oxidising and reducing conditions. One of the primary drivers for the observed differences is the change in mobility of some trace and rare earth elements. One of the examples are Mo, V and U shifting to lower oxidation states in which they are immobile or in which they form immobile complexes (Wanty & Goldhaber, 1992; Hua et al., 2006; Helz et al., 2011; Vodyanitskii, 2011; Smedley & Kinniburgh, 2017; Shaheen et al., 2019; Bone et al., 2020) and Ce which shifts from Ce^{3+} to Ce^{4+} under oxidising conditions where ferromanganese oxides commonly promote the oxidation of Ce (Bau, 1999; Kawabe et al., 1999; Ohta & Kawabe, 2001). The other mechanism which facilitates the differences in the behaviour of trace and rare earth elements in different redox conditions is the formation of different phases which are usually redox-specific. Different phases display an affinity for different elements, with iron and manganese oxides as the main phase which promotes the enrichment of elements such as As, Co, Pb, Zn, V and Mo in the oxidising pedoenvironment (Bowell, 1994; Lienemann et al., 1997; Bennett & Dudas, 2003; Shaheen et al., 2016; Tabelin et al., 2018). Iron sulphides are the common phases which facilitate the immobilisation and enrichment of different elements, as pyrite commonly binds chalcophile elements such as As, Co, Cu, Se, Sb, Mo, Tl and Zn within its structure during its precipitation (Diehl et al., 2012; He et al., 2022; Mederski et al., 2022).

3.3.1. Oxidising pedoenvironment

Three main materials were used as representative for oxidising conditions: the terra rossa soils and red bauxites from the Rovinj-1 and Minjera bauxite deposits, as well as from the Cretaceous palaeosols due to their subrecent oxidation and formation of iron oxides. In terra rossa soils the behaviour of trace elements is mainly related to the presence of ferromanganese oxides and organic matter. This is apparent when viewing the proportions of each element in Tessier extraction data, where the organic matter (oxidisable fraction) is one of the sinks for most analysed elements, especially Pb, Sb and V, while ferromanganese oxides (reducible fraction) are one of the sinks for almost all analysed elements, especially Co, Mn and Pb. Besides the organic matter and ferromanganese oxides, some elements such as Ba, Cd, Mn and especially Sb are also adsorbed (exchangeable fraction), indicating their increased mobility in the pedoenvironment of the studied terra rossas. Despite the Cretaceous palaeosols being used as a representative material for reducing conditions, a minor amount of subrecent oxidation occurred on their outcrops, where iron oxides and jarosite precipitated. These phases comprise the reducible fraction in those materials, representing a sink for Co, Sb, V and especially Cu, Mo, Ni, Pb together with Zn.

Although no sequential extraction data was obtained for red bauxites from Minjera deposits and Rovinj-1 deposit, some trace elements clearly showed an association with iron oxides, which was inferred either from statistical analysis or through comparison with their reduced counterparts. In the Rovinj-1 deposit, elements like Sr, U, Mo, P, S, W, Cd and V are associated with iron oxides and are enriched in the upper part of the deposit due to an increase in iron oxide content. Minjera bauxites differ from the Rovinj-1 bauxite, as the red bauxite there is enriched in Pb, Sb and V compared to their pyritised counterparts.

Rare earth elements are also affected by the presence of iron oxides, as light and especially middle rare earth elements are preferentially enriched by iron oxides (Tang & Johannesson, 2003; Grybos et al., 2007; Laveuf et al., 2008; Davranche et al., 2011; Zhou et al., 2020). This relationship between REE and iron oxides was observed both in terra rossa soils and red bauxite from the Rovinj-1 deposit as well as the Minjera deposits. A clear enrichment in middle rare earth elements (MREEs) and some light rare earth elements (LREEs) is clearly seen in the reducible (ferromanganese oxides) fraction in all terra rossa soils, which is also accompanied by the presence of positive Ce anomalies, related to its immobilisation in oxidising conditions. The same exact REE distribution is also visible in the oxidising fraction (organic matter). In the Rovinj-1 deposit, the upper section of the bauxite which shows an enrichment in iron oxides and iron-oxide impregnations displays several horizons of LREE and MREE enrichment, but it displays a negative Ce anomaly. The immobilisation of Ce in bauxites commonly leads to the depletion in the section below the uppermost part of the bauxite (Mongelli, 1997; Wang et al., 2013; Vind et al., 2018), which was likely eroded in the Rovinj-1 deposit or reworked into the clays that overlie it. Ce was also preferentially enriched in the lowermost part of the deposit, which is either caused by the formation of Ce-rich fluorocarbonate minerals closer to the carbonate bedrock (Maksimović & Pantó, 1991; Mongelli, 1997; Mongelli et al., 2021), or through the preferential retention of Ce

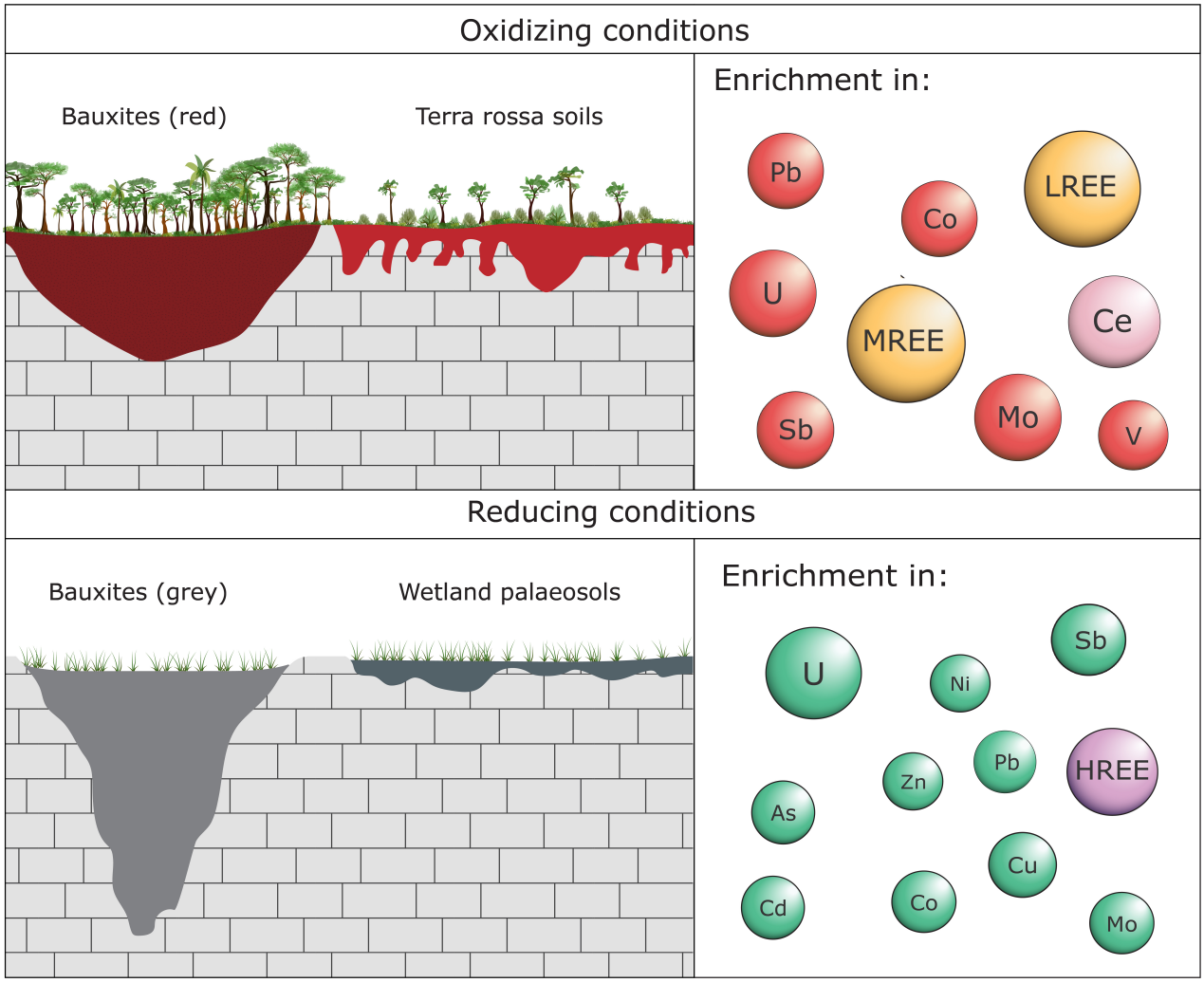

Figure 3. Graphical summary of the differences in the behaviour of different trace and rare earth elements between the reducing and oxidising conditions found in the different materials of the studied four unconformities of the Western Istrian Anticline.

through its oxidation if the lower part once represented the uppermost part of the deposit. The Minjera bauxites do not show such clear relationship between the REEs and iron oxides, but when comparing the red bauxite with pyritised bauxite, the red bauxite is enriched in MREEs and some LREE. The red bauxite also has a slight negative Ce anomaly, which is likely a result of the same process as in the upper part of the Rovinj-1 deposit. Cretaceous palaeosols should also be included in this section, as they displayed positive Ce anomalies in the silicate fraction (residual fraction), which is likely a consequence of seasonally oxidising conditions, common for wetland soils.

Despite all of these results being collected from different materials analysed with different methods across the four studied unconformities, it can be clearly seen that some elements such as Co, Pb, Sb and V are almost always enriched or related to the presence of iron and/or manganese oxides, which are in turn a product of oxidising conditions during pedogenesis. This is also true for REEs, as a clear association and control of MREEs by iron oxides can be seen in all four unconformities, coupled with the anomalous behaviour of Ce under oxidising conditions.

3.3.2. Reducing conditions

Three materials were used as representatives for reducing conditions: the Cretaceous palaeosols and pyritised bauxites from the Rovinj-1 and Minjera deposits. The Cretaceous palaeosols display an enrichment in Cd, Sb, V, and especially U and Mo compared to the terra rossa soils. This is clearly a result of reducing conditions, but some elements such as Mo and Zn are related to iron oxides (reducible fraction) while some elements such as Cd and Zn are present in the exchangeable fraction. This is likely a consequence of subrecent oxidation of pyrite and the soil in general where Mo, Zn and Cd were remobilised or released from the pyrite lattice and were either incorporated into the newly formed jarosite and iron oxides or retained in the soil through adsorption onto clay particles. Nevertheless, the pyrite (oxidisable fraction) in the Cretaceous palaeosols scavenges Cu, Mo, Ni, Pb, Sb and Zn, although the obtained proportions are likely diminished due to its oxidation and release of most of these elements. In the Rovinj-1 deposit the flooding of the bauxite during the initial stages of the transgression produced a marshy, oxygen-poor environment which caused changes in trace elemental content. The grey bauxite and clay formed during this initial flooding show an enrichment in As, Co, Cu, Mo, Ni, Sb, V, Tl and Zn linked to their release from the red bauxite upon its reduction, and subsequent accumulation in an oxygen-poor environment during pyrite formation. It should be noted that a significant enrichment in Zn was observed in the clay formed atop of the grey bauxite, over 0.3 wt%. After the initial flooding, a cyclic alternation of clays/marls and limestones was deposited in a restricted lake environment, under probably eutrophic conditions which shifted towards equivocal to oxic as the transgression progressed. Here, the accumulation of chalcophiles diminished, but the redox sensitive elements such as U, V and Mo continued to accumulate. In the Minjera bauxites flooding also followed their deposition, bringing the red bauxite into the newly established marshy environment, characterised by euxinic conditions. Here, the originally red bauxite was pyritised and iron oxides were solubilised, which led to the mobilisation of Pb, Sb and V while chalcophile and redox-sensitive elements such as As, Cd, Cu, Co, Hg, Ni, Mo, Sb, Se, U and Tl were enriched.

Rare earth elements are not directly affected by the reducing conditions, except for Ce which does not display any anomalous behaviour under such conditions and Eu which can be reduced into Eu^{2+} under these conditions. The main mechanism that facilitates redox-based difference between the oxidising and reducing conditions during pedogenesis appears to be the reduction of ferromanganese oxides, which preferentially scavenge MREEs. This leads to the development of a saddle-like REE distribution pattern, as upon the dissolution of ferromanganese oxides MREEs are solubilised as well and removed from the soil, with only some LREE and HREE remaining. This also leads to the decreased REE content upon the reduction of the material which was previously formed under oxidising conditions. This process was observed in almost all samples formed under reducing conditions from the Rovinj-1 bauxites, Zlatni rt palaeosol, Cretaceous palaeosols and Minjera bauxites. The MREE depletion is also accompanied by the enrichment in HREEs, but although this effect is not redox-sensitive in nature it is an interesting finding as it is present in almost all of the aforementioned materials. This HREE enrichment is likely the result of the interaction of brackish to saline solutions with those materials upon their flooding and reduction,

as HREEs are increasingly more adsorbed onto clays compared to LREE in high-ionic strength solution (Coppin et al., 2002; Hao et al., 2019). HREEs also form more mobile aqueous and carbonate complexes than the rest of the REE (Coppin et al., 2002; Duncan and Shaw, 2003; Liankai et al., 2020), which could make them more available for adsorption, especially in a karstic environment.

Based on the observed behaviour of trace and rare earth elements in the Rovinj-1 bauxite, Cretaceous palaeosols and Minjera bauxite, some persistent similarities related to their formation under reducing conditions were observed. Most notable is the enrichment of redox sensitive and chalcophile elements, where As, Cd, Co, Cu, Mo, Ni, Pb, Sb, U and Zn appear to be consistently enriched in a reducing environment (Fig. 3). When comparing the trace elements between the reducing and oxidising conditions, it can also be seen that some elements such as Co, Pb, Sb, U and Mo are enriched in both the reducing and oxidising conditions (Fig. 3.). The studied materials representative of reducing conditions REEs also display similarities in their behaviour, where a depletion in MREEs is almost always present, coupled with the additional enrichment of HREEs which is not related to redox conditions but to the interaction of those materials with marine porewaters.

3.4. Geotectonic evolution of the Western Istrian Anticline

The Western Istrian Anticline is one of the most prominent tectonic structures in the Istrian peninsula, and its formation is a major cause of the today's geographic outlook of Istria. One of the objectives of this thesis was contribution to the geotectonic reconstruction of its evolution based on the changes of the parent material provenance between studied unconformities. However, the bauxites from the 1st and 3rd Unconformities yielded very few heavy and light mineral grains upon separation with SPT, which were only used for the tentative reconstruction of the type of their parent material but not its source, as this is already a difficult task even when having a statistically sufficient number of heavy and light mineral grains. The geochemical data were also not used for the discrimination of the type of the source material for the 1st and 3rd Unconformities as it was planned, due to the fact that the heavy and light mineral analysis was intended to form the basis for the determination of the type and source of the parent material, which would then be complemented with geochemical data. This stems from the fact that bauxites are a product of long and persistent chemical weathering which can mask the original geochemical signature of the parent material, which is unreliable on its own. Nevertheless, the collection of new and larger quantities of samples as well as new analyses such as U-Pb zircon dating, are planned for future research, which should allow the acquisition of a better dataset from which the geotectonic evolution of the Western Istrian Anticline will be revisited. Additional reason why the geotectonic reconstruction of the Western Istrian Anticline was not performed, was that some other aspects of the studied materials proved to be more scientifically interesting including some unexpected findings, and they were pursued since the results regarding the provenance of the studied materials proved to be subpar compared to the rest of the obtained data, such as the finding of glauconite in an unusual environment in the

materials of the 1st Unconformity, the palaeoclimatic changes recorded in the Rovinj-1 deposit, the differences in the behaviour of trace and rare earth elements in oxidising and reducing environments as well as the epigenetic changes in Minjera deposits and their multi-stage pyritisation.

4. CONCLUSIONS

This PhD Thesis was focused on the detailed analysis and description of the terrestrial materials which developed during the 1st and 3rd Unconformities in the succession of the Western Istria Anticline, with the emphasis on the reconstruction of palaeoclimatic and palaeoenvironmental evolution as well as their provenance. The data employed in this study were obtained using a wide array of analytical methods such as thin section petrography, XRPD, XRF, ICP-MS, FTIR, SEM-EDS as well as the analysis of iron speciation and stable sulphur isotopes. Several conclusions can be drawn from the collected data and their interpretation:

1 The formation of the Rovinj-1 bauxite deposit and the Zlatni rt palaeosol started with the uplift of the Istrian part of the Adriatic Carbonate Platform in response to the obduction of the Vardar Ocean in the Late Jurassic, after which karstification and the accumulation of volcanic ash, aeolian dust and insoluble residue of the carbonate bedrock were initiated.

2 The chemical and mineralogical uniformity of the Rovinj-1 bauxite suggests that it primarily formed in situ, although the clastic bauxite lithologies indicate a degree of reworking and possible local input, which is especially apparent towards the end of its formation. These changes were found to be related to the progressive regional aridification in the late Tithonian, which also caused the changes during the deposition of the bauxite cover sequence, as the progressive aridification of the wider surroundings is reflected in the changes of the clay mineral composition due to the increased formation of illite and MLIS over kaolinite.

3 The sea-level rise during Tithonian begun as an oscillating internal transgression progressing into the overland transgression, which is visible through the deposition of a blue-hole sequence over the Rovinj-1 bauxite. It started by the deposition of schizohaline limestones, black pebble breccias and clays/marls within a karstic lake, which gradually experienced increasing marine influence, culminating by the deposition of the Kirmenjak limestone marking the overland transgression of the previously exposed carbonate terrain. In the Zlatni rt palaeosol, the transgression is only recorded through the presence of black pebble breccias, which are covered with Kirmenjak limestone, whose deposition is also recorded through the precipitation of pyrite crusts in the palaeosol.

4 The transgression was also marked by an important glauconitisation event, which led to the formation of glauconite in the cover of the Rovinj-1 deposit and the Zlatni rt palaeosol. The glauconite was studied in detail in the Zlatni rt palaeosol, where two processes played a major role during glauconite formation: (1) the uptake of potassium and iron into present clay phases, and (2) their dissolution and reprecipitation in the presence of iron and potassium ions in the presence of microbes. The glauconite is present in both reduced and oxidised form, alternating with pyrite, which indicates redox fluctuations during its formation, probably due to the variations in sea level that affected the supply of organic matter.

5 The formation of Minjera bauxites coincides with the late Cretaceous obduction of the Vardar ocean, causing the uplift in the Istrian part of the AdCP and beginning of karstification and accumulation of parent materials, primarily composed of aeolian dust.

6 Differences in palaeotopography were determined in the Minjera area during the formation of bauxite, since the bauxites on the northern bank of the Mirna river were formed in a higher palaeotopographical position compared to the ones on the southern side. This is also supported by the presence of bauxites filling deeper karstforms on the northern side and mineralogical and geochemical differences between the D-1 an D-15 deposit. The D-1 deposit is present on the northern side and has a higher boehmite content, while the southern D-15 deposit has the higher content of kaolinite and leachable elements, indicating its formation closer to the water table.

7 Pyritisation is the defining feature of the Minjera bauxites and was found to be a multi-stage process. During the first phase micrometre-sized anhedral pyrite and pyrite framboids were formed, which was followed by their overgrowth and replacement with colloform pyrite during the second phase, where the formation of these morphologies indicates the presence of supersaturated solutions with respect to pyrite. During the third stage euhedral, dendritic and acicular pyrites were formed, suggesting that the solutions became undersaturated with respect to pyrite. The final, fourth stage of pyritisation is marked by the formation of pyrite veins. The recognized stages of pyritisation are supported by the obtained values of stable sulphur isotopes, which indicate that the system had an unlimited sulphate supply during the first phases, allowing the development of supersaturated solutions, which changed when the sulphate supply became limited, leading to the drop in the saturation of porewaters.

8 The cover sequence of the bauxite is of Palaeocene age and represents another example of the *blue hole* sequence in the bauxites of the Western Istrian Anticline. During the transgression a marshy environment was developed which served as a source of organic matter used for microbial sulphate reduction, which facilitated the pyritisation of Minjera bauxites.

9 Combining the data from all four unconformities, this work proved that in the formation of bauxites and palaeosols (including their diagenesis) there are clear differences in the behaviour of trace elements and REEs between the oxidising and reducing environments. Reducing conditions immobilize elements like Mo, V, and U, while oxidising conditions lead to the enrichment in Co, Pb, Sb, and V through their scavenging by iron ferromanganese oxides formed in oxidising conditions. Iron oxides also facilitate the enrichment of MREEs and some LREEs in oxidising conditions, which are released upon their dissolution in reducing environments, leading to their depletion and relative enrichment in HREEs. HREEs were also enriched in reducing conditions, which was not related to the low redox potential, but to the presence of saline fluids. Reducing conditions

also enrich certain elements, mainly through their uptake during pyrite formation and their immobilisation in the reducing conditions, where chalcophile and redox-sensitive elements such as As, Cd, Co, Cu, Mo, Ni, Pb, Sb, U, and Zn, are also enriched. Elements such as Co, Pb, Sb, U, and Mo were found to be enriched in both the reducing and oxidising conditions.

Altogether, the findings from this study provide an important contribution to the understanding of the processes and changes that characterised the formation of the terrestrial materials which formed during the 1st and 3rd Unconformity. The most important contributions in this regard are the finding of a unique glauconite occurrence in the Zlatni rt palaeosol and the Rovinj-1 deposit which is important for the understanding of glauconite formation in such environments, the previously undocumented late Tithonian climate aridification during the end of the 3rd Unconformity and finally the palaeotopographic differences in Minjera bauxites and the reconstruction of their multi-phase pyritisation which should prove useful in future studies of pyritised bauxites in general. Besides this, an important contribution was made to the understanding of the behaviour of trace and REEs between reducing and oxidising environments during the formation of bauxites and palaeosols.

5. LITERATURE

Abedini, A. & Calagari, A.A. (2014) REE geochemical characteristics of titanium-rich bauxites: The Permian Kanigorgeh horizon, NW Iran. *Turkish Journal of Earth Sciences*, *23*(5). https://doi.org/10.3906/yer-1404-11

Abedini, A., Calagari, A.A. & Azizi, M.R. (2018) The tetrad-effect in rare earth elements distribution patterns of titanium-rich bauxites: Evidence from the Kanigorgeh deposit, NW Iran. *Journal of Geochemical Exploration*, *186*(February), 129–142. https://doi.org/10.1016/j.gexplo.2017.12.007

Abedini, A., Azizi, M.R., & Calagari, A.A. (2019a) REE mobility and tetrad effects in bauxites: An example from the Kanisheeteh deposit, NW Iran. *Acta Geodynamica et Geomaterialia*, *16*(1), 11–26. https://doi.org/10.13168/AGG.2019.0002

Abedini, A., Rezaei Azizi, M. & Calagari, A.A. (2019b) REE tetrad effect as a powerful indicator of formation conditions of karst bauxites: A case study of the Shahindezh Deposit, NW Iran. *Acta Geologica Sinica*, *93*(4), 912–927. https://doi.org/10.1111/1755-6724.13763

Alberti, M., Fürsich, F.T., Abdelhady, A A. & Andersen, N. (2017) Middle to Late Jurassic equatorial seawater temperatures and latitudinal temperature gradients based on stable isotopes of brachiopods and oysters from Gebel Maghara, Egypt. *Palaeogeography, Palaeoclimatology, Palaeoecology*, *468*, 301–313. https://doi.org/10.1016/j.palaeo.2016.11.052

Algeo, T.J., Luo, G.M., Song, H.Y., Lyons, T.W. & Canfield, D.E. (2015). Reconstruction of secular variation in seawater sulfate concentrations. *Biogeosciences*, *12*(7), 2131–2151. https://doi.org/10.5194/bg-12-2131-2015

Baldermann, A., Dietzel, M., Mavromatis, V., Mittermayr, F., Warr, L.N. & Wemmer, K. (2017) The role of Fe on the formation and diagenesis of interstratified glauconite-smectite and illite-smectite: A case study of Lower Cretaceous shallow-water carbonates. *Chemical Geology*, *453*, 21–34. https://doi.org/10.1016/j.chemgeo.2017.02.008

Baldermann, A., Warr, L.N., Letofsky-Papst, I. & Mavromatis, V. (2015) Substantial iron sequestration during green-clay authigenesis in modern deep-sea sediments. *Nature Geoscience*, *8*(11), 885–889. https://doi.org/10.1038/ngeo2542

Bardossy, G. (1982) Karst bauxites. *Elsevier*, 441, Amsterdam, Netherlands.

Barrie, C.D., Boyce, A.J., Boyle, A.P., Williams, P.J., Blake, K., Ogawara, T., Akai, J. & Prior, D.J. (2009) Growth controls in colloform pyrite. *American Mineralogist*, *94*(4), 415–429. https://doi.org/10.2138/am.2009.3053

Bau, M. (1999) Scavenging of dissolved yttrium and rare earths by precipitating iron oxyhydroxide: Experimental evidence for Ce oxidation, Y-Ho fractionation, and lanthanide

tetrad effect. *Geochimica et Cosmochimica Acta*, *63*(1), 67–77. https://doi.org/10.1016/S0016-7037(99)00014-9

Bennett, B. & Dudas, M.J. (2003) Release of arsenic and molybdenum by reductive dissolution of iron oxides in a soil with enriched levels of native arsenic. *Journal of Environmental Engineering and Science*, *2*(4), 265–272. https://doi.org/10.1139/s03-028

Berner, R.A. (1970) Sedimentary pyrite formation. *American Journal of Science*, *268*(1), 1–23. https://doi.org/10.2475/ajs.268.1.1

Bignot, G., Blondeau, A., Guernet, C., Perrau, M., Poignant, A., Renard, M. & Riveline, J. (1985) Age and characteristics of the Eocene transgression at Gánt (Vértes mts, Transdanubia, Hungary). *Acta Geologica Hungarica, 28*(1–2), 29–48.

Birkeland, P.W. (1985) Soils and Geomorphology. *Oxford University Press*. 372, New York, USA. https://doi.org/10.1017/S0016756800031617

Błazėjowski, B., Pszczółkowski, A., Grabowski, J., Wierzbowski, H., Deconinck, J.F., Olempska, E., Teodorski, A. & Nawrocki, J. (2023) Integrated stratigraphy and clay mineralogy of the Owadów–Brzezinki section (Lower–Upper Tithonian transition, central Poland): Implications for correlations between the Boreal and the Tethyan domains and palaeoclimate. *Journal of the Geological Society*, *180*(2), jgs2022-073 . https://doi.org/10.1144/jgs2022-073

Bone, S.E., Cliff, J., Weaver, K., Takacs, C.J., Roycroft, S., Fendorf, S. & Bargar, J.R. (2020) Complexation by organic matter controls uranium mobility in anoxic sediments. *Environmental Science and Technology*, *54*(3), 1493–1502. https://doi.org/10.1021/acs.est.9b04741

Bowell, R.J. (1994) Sorption of arsenic by iron oxides and oxyhydroxides in soils. *Applied Geochemistry*, *9*(3), 279–286. https://doi.org/10.1016/0883-2927(94)90038-8

Brigaud, B., Pucéat, E., Pellenard, P., Vincent, B. & Joachimski, M.M. (2008) Climatic fluctuations and seasonality during the Late Jurassic (Oxfordian–Early Kimmeridgian) inferred from $\delta^{18}O$ of Paris Basin oyster shells. *Earth and Planetary Science Letters*, *273*(1–2), 58–67. https://doi.org/10.1016/j.epsl.2008.06.015

Brindley, G.W. & Brown, G. (1980) Crystal Structures of Clay Minerals and their X-Ray Identification. *Mineralogical Society of Great Britain and Ireland*. 495, London. https://doi.org/10.1180/mono-5

Brlek, M., Gaynor, S. P., Mongelli, G., Bauluz, B., Sinisi, R., Brčić, V., Peytcheva, I., Mišur, I., Tapster, S., Trinajstić, N., Laita, E., Yuste, A., Šuica, S., Grizelj, A., Kukoč, D. & Schaltegger, U. (2021) Karst bauxite formation during Miocene Climatic Optimum (central Dalmatia, Croatia): mineralogical, compositional and geochronological perspectives.

International Journal of Earth Sciences, *110*(8), 2899–2922. https://doi.org/10.1007/s00531-021-02091-z

Brlek, M. & Glumac, B. (2014) Stable isotopic ($\delta^{13}C$ and $\delta^{18}O$) signatures of biogenic calcretes marking discontinuity surfaces: A case study from Upper Cretaceous carbonates of central Dalmatia and eastern Istria, Croatia. *Facies*, *60*(3), 773–788. https://doi.org/10.1007/s10347-014-0403-7

Carannante, G., Mindszenty, A., Neumann, A.C., Rasmussen, K.A., Simone, L. & Tóth, K. (1994) Inland blue-hole-type ponds in the Mesozoic–Tertiary karst filling sequences, *Abstracts, IAS 15th Regional Meeting*, *Ischia, Italy,* 102–103.

Carannante, G., D'Argenio, B., Mindszenty, A., Ruberti, D. & Simone, L. (1994) Cretaceous–Miocene shallow water carbonate sequences. Regional unconformities and facies patterns. In: Carannante, G. & Tonielli, R. (Eds.), *Field Trip Guide Book: 15th Regional IAS Meeting*. *De Frede*, 25–60.

Canfield, D.E., Raiswell, R., Westrich, J.T., Reaves, C.M. & Berner, R.A. (1986) The use of chromium reduction in the analysis of reduced inorganic sulfur in sediments and shales. *Chemical Geology*, *54*(1–2), 149–155. https://doi.org/10.1016/0009-2541(86)90078-1

Cao, Jy., Wu, Qh., Li, H., Ouyang, C.X., Kong, H. & Xi, X.S.. (2017) Metallogenic mechanism of Pingguo bauxite deposit, western Guangxi, China: Constraints from REE geochemistry and multi-fractal characteristics of major elements in bauxite ore. *Journal of Central South University*, *24*(7), 1627–1636. https://doi.org/10.1007/s11771-017-3568-8

Chambers, L.A. & Trudinger, P.A. (1979) Microbiological fractionation of stable sulfur isotopes: a review and critique. *Geomicrobiology Journal*, *1*(3), 249–293.

Chanvry, E., Marchand, E., Lopez, M., Séranne, M., Le Saout, G. & Vinches, M. (2020) Tectonic and climate control on allochthonous bauxite deposition. Example from the mid-Cretaceous Villeveyrac basin, southern France. *Sedimentary Geology*, *407*, *105727*. https://doi.org/10.1016/j.sedgeo.2020.105727

Chen, J., Wang, Q., Zhang, Q., Carranza, E.J.M. & Wang, J. (2018) Mineralogical and geochemical investigations on the iron-rich gibbsitic bauxite in Yongjiang basin, SW China. *Journal of Geochemical Exploration*, *188*, 413–426. https://doi.org/10.1016/j.gexplo.2018.02.007

Chen, T. (1978). Colloform and framboidal pyrite from the Caribou deposit, New Brunswick. *Canadian Mineralogist*, *16*(31), 9–15.

Combes, P.-J. & Bardossy, G. (1995) Geodynamics of Bauxites in the Tethyan Realm. In: Nairn, A.E.M., Ricou, L.-E., Vrielynck, B. & Dercourt, J. (Eds.) *The Tethys Ocean*. Springer, 347–365. https://doi.org/10.1007/978-1-4899-1558-0_11

D'Argenio, B. & Mindszenty, A. (1992) Tectonic and climatic control on paleokarst and bauxites. *Giornale Di Geologia*, *54*(1), 207–218.

D'Argenio, B. & Mindszenty, A. (1995) Bauxites and related paleokarst: tectonic and climatic event markers at regional unconformities. *Eclogae Geologicae Helvetiae*, *88*(3), 453–499.

Davranche, M., Grybos, M., Gruau, G., Pédrot, M., Dia, A. & Marsac, R. (2011) Rare earth element patterns: A tool for identifying trace metal sources during wetland soil reduction. *Chemical Geology*, *284*(1–2), 127–137. https://doi.org/10.1016/j.chemgeo.2011.02.014

Diehl, S.F., Goldhaber, M.B., Koenig, A.E., Lowers, H.A. & Ruppert, L.F. (2012) Distribution of arsenic, selenium, and other trace elements in high pyrite Appalachian coals: Evidence for multiple episodes of pyrite formation. *International Journal of Coal Geology*, *94*, 238–249. https://doi.org/10.1016/j.coal.2012.01.015

Durn, G. (2003) Terra Rossa in the Mediterranean region: Parent materials, composition and origin. *Geologia Croatica*, *56*(1), 83–100. https://doi.org/10.4154/GC.2003.06

Durn, G., Aljinović, D., Crnjaković, M. & Lugović, B. (2007) Heavy and light mineral fractions indicate polygenesis of extensive terra rossa soils in Istria, Croatia. In: Mange, M. & Wright, D. (Eds.), *Heavy minerals in use. Developments in Sedimentology*. Elsevier, 701–737. https://doi.org/10.1016/S0070-4571(07)58028-3

Durn, G., Ottner, F. & Slovenec, D. (1999) Mineralogical and geochemical indicators of the polygenetic nature of terra rossa in Istria, Croatia. *Geoderma*, *91*(1–2), 125–150. https://doi.org/10.1016/S0016-7061(98)00130-X

Ellahi, S.S., Taghipour, B. & Nejadhadad, M. (2017) The role of organic matter in the formation of high-grade al deposits of the Dopolan karst type bauxite, Iran: Mineralogy, geochemistry, and sulfur isotope data. *Minerals*, *7*(6), 2075-163X. https://doi.org/10.3390/min7060097

Galović, E.K., Ilijanić, N., Peh, Z., Miko, S. & Hasan, O. (2012) Geochemical discrimination of early Palaeogene bauxites in Croatia. *Geologia Croatica*, *65*(1), 53–65. https://doi.org/10.4154/gc.2012.04

Giresse, P. & Wiewióra, A. (2001) Stratigraphic condensed deposition and diagenetic evolution of green clay minerals in deep water sediments on the Ivory Coast–Ghana Ridge. *Marine Geology*, *179*(1–2), 51–70. https://doi.org/10.1016/S0025-3227(01)00193-1

Golroudbary, S. R., Makarava, I., Kraslawski, A. & Repo, E. (2022) Global environmental cost of using rare earth elements in green energy technologies. *Science of the Total Environment*, *832*, 155022.

Grybos, M., Davranche, M., Gruau, G. & Petitjean, P. (2007) Is trace metal release in wetland soils controlled by organic matter mobility or Fe-oxyhydroxides reduction? *Journal of Colloid and Interface Science*, *314*(2), 490–501. https://doi.org/10.1016/j.jcis.2007.04.062

He, J., Yang, L., Shi, X., Zhao, S., Cao, L., Pan, S., Wu, F. & Wang, M. (2022) Genetic mechanism of pyrite in the shale of the Longmaxi Formation and its influence on the pore structure: A case study of the Changning Area, South Sichuan Basin of SW China. *Frontiers in Earth Science*, *10*, 919923. https://doi.org/10.3389/feart.2022.919923

Helz, G.R., Bura-Nakić, E., Mikac, N. & Ciglenečki, I. (2011) New model for molybdenum behavior in euxinic waters. *Chemical Geology*, *284*(3–4), 323–332. https://doi.org/10.1016/j.chemgeo.2011.03.012

Hesselbo, S.P., Jean-François, D., Huggett, J.M. & Morgans-Bell, H.S. (2009) Late Jurassic palaeoclimatic change from clay mineralogy and gamma-ray spectrometry of the Kimmeridge Clay, Dorset, UK. *Journal of the Geological Society*, *166*(6), 1123–1133. https://doi.org/10.1144/0016-76492009-070

Hough, G., Swapp, S., Frost, C. & Fayek, M. (2019) Sulfur isotopes in biogenically and abiogenically derived uranium roll-front deposits. *Economic Geology*, *114*(2), 353–373. https://doi.org/10.5382/econgeo.2019.4634

Hrenović, J., Durn, G., Goić-Barišoć, I. & Kovačić, A. (2014) Occurrence of an environmental *Acinetobacter baumannii* strain similar to a clinical isolate in paleosol from Croatia. *Applied and Environmental Microbiology*, *80*(9), 2860–2866. https://doi.org/10.1128/AEM.00312-14

Hu, W., Ran, J., Dong, L., Du, Q., Ji, M., Yao, S., Sun, Y., Gong, C., Hou, Q., Gong, H., Chen, R., Lu, J., Xie, S., Wang, Z., Huang, H., Li, X., Xiong, J., Xia, R., Wei, M. & Deng, J. (2021) Aridity-driven shift in biodiversity–soil multifunctionality relationships. *Nature Communications*, *12*(1), 5350. https://doi.org/10.1038/s41467-021-25641-0

Hua, B., Xu, H., Terry, J. & Deng, B. (2006) Kinetics of uranium(VI) reduction by hydrogen sulfide in anoxic aqueous systems. *Environmental Science and Technology*, *40*(15), 4666–4671. https://doi.org/10.1021/es051804n

Huggett, J.M. & Cuadros, J. (2005) Low-temperature illitization of smectite in the late Eocene and early Oligocene of the Isle of Wight (Hampshire basin), U.K. *American Mineralogist*, *90*(7), 1192–1202. https://doi.org/10.2138/am.2005.1674

Jež, j. & Otoničar, B. (2018) Late Cretaceous geodynamics of the northern sector of the Adriatic Carbonate Platform (Western Slovenia). *Newsletters on Stratigraphy*, 51(*4*), 381–410.

Kawabe, I., Ohta, A., Ishii, S., Tokumura, M. & Miyauchi, K. (1999) REE partitioning between Fe-Mn oxyhydroxide precipitates and weakly acid NaCl solutions: Convex tetrad effect and fractionation of Y and Sc from heavy lanthanides. *Geochemical Journal*, *33*(3), 167–179. https://doi.org/10.2343/geochemj.33.167

Kelemen, P., Dunkl, I., Csillag, G., Mindszenty, A., Józsa, S., Fodor, L. & von Eynatten, H. (2023) Origin, timing and paleogeographic implications of Paleogene karst bauxites in the northern Transdanubian range, Hungary. *International Journal of Earth Sciences*, *112*(1), 243–264. https://doi.org/10.1007/s00531-022-02249-3

Kelemen, P., Dunkl, I., Csillag, G., Mindszenty, A., von Eynatten, H. & Józsa, S. (2017) Tracing multiple resedimentation on an isolated karstified plateau: The bauxite-bearing Miocene red clay of the Southern Bakony Mountains, Hungary. *Sedimentary Geology*, *358*, 84–96. https://doi.org/10.1016/j.sedgeo.2017.07.005

Khosravi, M., Vérard, C. & Abedini, A. (2021) Palaeogeographic and geodynamic control on the Iranian karst-type bauxite deposits. *Ore Geology Reviews*, *139*, 104589. https://doi.org/10.1016/j.oregeorev.2021.104589

Kleeberg, R., Monecke, T. & Hillier, S. (2008) Preferred orientation of mineral grains in sample mounts for quantitative XRD measurements: How random are powder samples? *Clays and Clay Minerals*, *56*(4), 404–415. https://doi.org/10.1346/CCMN.2008.0560402

Laveuf, C., Cornu, S. & Juillot, F. (2008) Rare earth elements as tracers of pedogenetic processes. *Comptes Rendus – Geoscience*, *340*(8), 523–532. https://doi.org/10.1016/j.crte.2008.07.001

Lienemann, C.P., Taillefert, M., Perret, D. & Gaillard, J.F. (1997) Association of cobalt and manganese in aquatic systems: Chemical and microscopic evidence. *Geochimica et Cosmochimica Acta*, *61*(7), 1437–1446. https://doi.org/10.1016/S0016-7037(97)00015-X

Majidzadeh, H., Uzun, H., Ruecker, A., Miller, D., Vernon, J., Zhang, H., Bao, S., Tsui, M.T.K., Karanfil, T. & Chow, A.T. (2017) Extreme flooding mobilized dissolved organic matter from coastal forested wetlands. *Biogeochemistry*, *136*(3), 293–309. https://doi.org/10.1007/s10533-017-0394-x

Maksimović, Z., Mindszenty, A. & Panto, G. (1991) Contribution to the geochemistry of Hungarian karst bauxites and the allochthony/autochthony problem. *Acta Geologica Hungarica*, *34*(4), 317–334.

Maksimović, Z. & Pantó, G. (1991) Contribution to the geochemistry of the rare earth elements in the karst-bauxite deposits of Yugoslavia and Greece. *Geoderma*, *51*(1–4), 93–109. https://doi.org/10.1016/0016-7061(91)90067-4

Mameli, P., Mongelli, G., Oggiano, G. & Dinelli, E. (2007) Geological, geochemical and mineralogical features of some bauxite deposits from Nurra (Western Sardinia, Italy): Insights on conditions of formation and parental affinity. *International Journal of Earth Sciences*, *96*(5), 887–902. https://doi.org/10.1007/s00531-006-0142-2

Martin, J.B., Gulley, J. & Spellman, P. (2012) Tidal pumping of water between Bahamian blue holes, aquifers, and the ocean. *Journal of Hydrology*, 416, 28–38. https://doi.org/10.1016/j.jhydrol.2011.11.033

Matičec, D. (1994) Neotectonic deformations in western Istria, Croatia. *Geologia Croatica*, *47*(2), 199–204.

Matičec, D., Vlahović, I., Velić, I. & Tišljar, J. (1996) Eocene limestones overlying Lower Cretaceous deposits of western Istria (Croatia): Did some parts of present Istria form land during the Cretaceous? *Geologia Croatica*, *49*(1), 117–127. https://doi.org/10.4154/GC.1994.46

Mederski, S., Pršek, J., Majzlan, J., Kiefer, S., Dimitrova, D., Milovský, R., Koch, C.B. & Kozień, D. (2022) Geochemistry and textural evolution of As-Tl-Sb-Hg-rich pyrite from a sediment-hosted As-Sb-Tl-Pb ± Hg ± Au mineralization in Janjevo, Kosovo. *Ore Geology Reviews*, *151*, 105221. https://doi.org/10.1016/j.oregeorev.2022.105221

Meunier, A. & El Albani, A. (2007) The glauconite-Fe-illite-Fe-smectite problem: A critical review. *Terra* Nova, *19*(2), 95–104. https://doi.org/10.1111/j.1365-3121.2006.00719.x

Mindszenty, A. (2016) Bauxites: Feedbacks of System Earth at greenhouse times. *Geologia Croatica*, *69*(1), 79–87. https://doi.org/10.4154/gc.2016.07

Mindszenty, A., D'Argenio, B. & Aiello, G. (1995) Lithospheric bulges recorded by regional unconformities. The case of Mesozoic-Tertiary Apulia. *Tectonophysics*, *252*(1–4), 137–161. https://doi.org/10.1016/0040-1951(95)00091-7

Mongelli, G. (1997) Ce-anomalies in the textural components of Upper Cretaceous karst bauxites from the Apulian carbonate platform (southern Italy). *Chemical Geology*, *140*(1–2), 69–79. https://doi.org/10.1016/S0009-2541(97)00042-9

Mongelli, G., Boni, M., Buccione, R. & Sinisi, R. (2014) Geochemistry of the Apulian karst bauxites (southern Italy): Chemical fractionation and parental affinities. *Ore Geology Reviews*, *63*, 9–21. https://doi.org/10.1016/j.oregeorev.2014.04.012

Mongelli, G., Boni, M., Oggiano, G., Mameli, P., Sinisi, R., Buccione, R. & Mondillo, N. (2017) Critical metals distribution in Tethyan karst bauxite: The Cretaceous Italian ores. *Ore Geology Reviews*, *86*, 526–536. https://doi.org/10.1016/j.oregeorev.2017.03.017

Mongelli, G., Buccione, R. & Sinisi, R. (2015) Genesis of autochthonous and allochthonous Apulian karst bauxites (Southern Italy): Climate constraints. *Sedimentary Geology*, *325*, 168–176. https://doi.org/10.1016/j.sedgeo.2015.06.005

Mongelli, G., Mameli, P., Sinisi, R., Buccione, R. & Oggiano, G. (2021) REEs and other critical raw materials in Cretaceous Mediterranean-type bauxite: The case of the Sardinian ore (Italy). *Ore Geology Reviews*, *139*, 104559. https://doi.org/10.1016/j.oregeorev.2021.104559

Moore, D.M. & Reynolds, R.C. jr. (1997) X-Ray Diffraction and the Identification and Analysis of Clay Minerals, Second edition. *Oxford University Press*. BROJ STR

O'Connor, B.H. & Chang, W.-J. (1986) The amorphous character and particle size distributions of powders produced with the Micronizing Mill for quantitative x-ray powder diffractometry. *X-Ray Spectrometry*, *15*(4), 267–270. https://doi.org/10.1002/xrs.1300150409

Odin, G.S. & Matter, A. (1981) De glauconiarum origine. *Sedimentology*, *28*(5), 121–151. https://doi.org/10.1111/j.1365-3091.1981.tb01925.x

Ohta, A. & Kawabe, I. (2001) REE(III) adsorption onto Mn dioxide (δ-MnO_2) and Fe oxyhydroxide: Ce(III) oxidation by δ-MnO_2. *Geochimica et Cosmochimica Acta*, *65*(5), 695–703. https://doi.org/10.1016/S0016-7037(00)00578-0

Otoničar, B. (2007) Upper Cretaceous to Paleogene forebulge unconformity associated with foreland basin evolution (Kras, Matarsko Podolje and Istria; SW Slovenia and NW Croatia). *Acta Carsologica*, *36*(1), 101–120. https://doi.org/10.3986/ac.v36i1.213

Ottner, F., Durn, G., Schwaighopfer, B. & Tišljar, J. (1999) Clay minerals in paleosols of Cretaceous age in Istria, Croatia. *Chinese Science Bulletin*, *44*, 145–151. https://doi.org/10.1360/sb1999-44-S1-145

Pasquier, V., Fike, D.A. & Halevy, I. (2021) Sedimentary pyrite sulfur isotopes track the local dynamics of the Peruvian oxygen minimum zone. *Nature Communications*, *12*(1), 4403. https://doi.org/10.1038/s41467-021-24753-x

Peh, Z. & Galović, E. (2016) Geochemistry of Lower Palaeogene bauxites – A unique signature for the tectonostratigraphic evolution of part of the Croatian Karst. *Geologia Croatica*, *69*(2), 269–279. https://doi.org/10.4154/gc.2016.24

Peh, Z. & Kovačević Galović, E. (2014) Geochemistry of Istrian Lower Palaeogene bauxites - Is it relevant to the extent of subaerial exposure during Cretaceous times? *Ore Geology Reviews*, *63*, 296–306. https://doi.org/10.1016/j.oregeorev.2014.05.020

Pellenard, P., Nomade, S., Martire, L., De Oliveira Ramalho, F., Monna, F. & Guillou, H. (2013) The first ^{40}Ar-^{39}Ar date from Oxfordian ammonite-calibrated volcanic layers (bentonites) as a tie-point for the Late Jurassic. *Geological Magazine*, *150*(6), 1136–142. https://doi.org/10.1017/S0016756813000605-1

Perković, I., Cvetko Tešović, B., Martinuš, M., Škapin, S.D., Vlahović, I., Matešić, D. & Durn, G. (2024) Glauconitisation of an Upper Jurassic palaeosol: Case study of the Zlatni Rt, Istria, Croatia. *Catena*, *238*, 107841. https://doi.org/10.1016/j.catena.2024.107841

Perković, I., Cvetko Tešović, B., Martinuš, M., Vlahović, I., Razum, I., Škapin, S.D., Matešić, D., Mihovilović, M., He, T., Newton, R. & Durn, G. (submitted) Genesis of the Rovinj-1

bauxite deposit (Istria, Croatia): Record of palaeoclimatic trends and palaeoenvironmental changes during the Latest Jurassic of the Adriatic Carbonate Platform. Submitted to *Ore Geology Reviews*.

Picotti, V. & Cobianchi, M. (2017) Jurassic stratigraphy of the Belluno Basin and Friuli Platform: A perspective on far-field compression in the Adria passive margin. *Swiss Journal of Geosciences*, *110*(3), 833–850. https://doi.org/10.1007/s00015-017-0280-5

Poulton, S.W. (2021) The Iron Speciation Paleoredox Proxy. *Cambridge University Press*. 34, Cambridge, UK.. https://doi.org/10.1017/9781108847148

Poulton, S.W. & Canfield, D.E. (2005) Development of a sequential extraction procedure for iron: Implications for iron partitioning in continentally derived particulates. *Chemical Geology*, *214*(3–4), 209–221. https://doi.org/10.1016/j.chemgeo.2004.09.003

Poulton, S.W. & Canfeld, D.E. (2011) Ferruginous conditions: A dominant feature of the ocean through Earth's history. *Elements*, *7*(2), 107–112. https://doi.org/10.2113/gselements.7.2.107

Rasmussen, K., Neumann, A.C.N. (1988) Holocene overprint of Pleistocene paleokarst: Bight of Abaco, Bahamas. In: James, N.P. & Choquette P.W. (Eds.), *Paleokarst*. *Springer-Verlag*, 132–148.

Reinhardt, N., Proenza, J.A., Villanova-De-Benavent, C., Aiglsperger, T., Bover-Arnal, T., Torró, L., Salas, R. & Dziggel, A. (2018) Geochemistry and mineralogy of rare earth elements (REE) in bauxitic ores of the Catalan coastal range, NE Spain. *Minerals*, *8*(12), 562. https://doi.org/10.3390/min8120562

Roedder, E. (1968) The non-colloidal origin of "colloform" textures in sphalerite ores. *Economic Geology*, *63*(5), 451–471. https://doi.org/10.2113/gsecongeo.63.5.451

Sahrawat, K.L. (2003) Organic matter accumulation in submerged soils. *Advances in Agronomy*, *81*, 169–201. https://doi.org/10.1016/S0065-2113(03)81004-0

Šćavničar, B. & Nikler, L. (1976) Vitric tuff in Upper Jurassic Lemeš-deposits of Mt. Velika Kapela (Croatia). *Geološki vjesnik*, *29*, 269–275.

Schmid, S.M., Bernoulli, D., Fügenschuh, B., Matenco, L., Schefer, S., Schuster, R., Tischler, M. & Ustaszewski, K. (2008) The Alpine–Carpathian–Dinaridic orogenic system: Correlation and evolution of tectonic units. *Swiss Journal of Geosciences*, *101*(1), 139–183. https://doi.org/10.1007/s00015-008-1247-3

Schmid, S.M., Fügenschuh, B., Kounov, A., Maţenco, L., Nievergelt, P., Oberhänsli, R., Pleuger, J., Schefer, S., Schuster, R., Tomljenović, B., Ustaszewski, K. & Van Hinsbergen, D.J.J. (2020) Tectonic units of the Alpine collision zone between Eastern Alps and western Turkey. *Gondwana Research*, *78*, 308–374. https://doi.org/10.1016/j.gr.2019.07.005

Shaheen, S.M., Alessi, D.S., Tack, F.M.G., Ok, Y.S., Kim, K.H., Gustafsson, J.P., Sparks, D.L. & Rinklebe, J. (2019) Redox chemistry of vanadium in soils and sediments: Interactions with colloidal materials, mobilization, speciation, and relevant environmental implications – A review. *Advances in Colloid and Interface Science*, *265*, 1–13. https://doi.org/10.1016/j.cis.2019.01.002

Shaheen, S.M., Rinklebe, J., Frohne, T., White, J.R. & DeLaune, R.D. (2016) Redox effects on release kinetics of arsenic, cadmium, cobalt, and vanadium in Wax Lake Deltaic freshwater marsh soils. *Chemosphere*, *150*, 740–748. https://doi.org/10.1016/j.chemosphere.2015.12.043

Šinkovec, B. (1974). Jurski glinoviti boksiti zapadne Istre. *Geološki vjesnik*, *27*, 217–226.

Šinkovec, B., Sakač, K. & Durn, G. (1994) Pyritized bauxites from Minjera, Istria, Croatia. *Natura Croatica*, *3*(1), 41–65.

Smedley, P.L. & Kinniburgh, D.G. (2017) Molybdenum in natural waters: A review of occurrence, distributions and controls. *Applied Geochemistry*, *84*, 387–432. https://doi.org/10.1016/j.apgeochem.2017.05.008

Smith, M.E., Wynn, J.G., Scharping, R.J., Moore, E.W., Garey, J.R. & Onac, B.P. (2021) Source of saline groundwater on tidally influenced blue holes on San Salvador Island, Bahamas. *Hydrogeology Journal*, *29*(1), 429–441. https://doi.org/10.1007/s10040-020-02266-z

Środoń, J. (2006) Identification and quantitative analysis of clay minerals. In: Bergaya, F. & Gerhard, L. (Eds.), *Handbook of Clay Science*. Elsevier, 25–49. https://doi.org/10.1016/S1572-4352(05)01028-7https://doi.org/10.1016/S1572-4352(05)01028-7

Stoops, G. (2021) Guidelines for analysis and description of soil and regolith thin sections. *John Wiley & Sons*. 256, Hoboken, USA.

Tabelin, C.B., Igarashi, T., Villacorte-Tabelin, M., Park, I., Opiso, E.M., Ito, M. & Hiroyoshi, N. (2018) Arsenic, selenium, boron, lead, cadmium, copper, and zinc in naturally contaminated rocks: A review of their sources, modes of enrichment, mechanisms of release, and mitigation strategies. In *Science of the Total Environment*, 1522–1553. https://doi.org/10.1016/j.scitotenv.2018.07.103

Tang, J. & Johannesson, K.H. (2003) Speciation of rare earth elements in natural terrestrial waters: Assessing the role of dissolved organic matter from the modeling approach. *Geochimica et Cosmochimica Acta*, *67*(13), 2321–2339. https://doi.org/10.1016/S0016-7037(02)01413-8

Tišljar, J. (1986) Postanak crnih oblutaka i ulomaka (“black pebbles”) u periplimskim vapnencima titona zapadne Istre i barema otoka Mljeta. *Geološki vjesnik*, *39*, 75–94.

Tišljar, J. & Velić, I. (1987) The Kimmeridgian tidal-bar calcarenite facies of western Istria (Western Croatia, Jugoslavia). *Facies*, *17*(1), 277–284. https://doi.org/10.1007/BF02536792

Tišljar, J. & Velić, I. (1991) Carbonate facies and depositional environments of the Jurassic and Lower Cretaceous of the coastal Dinarides (Croatia). *Geološki vjesnik*, *44*, 215–234.

Tišljar, J., Vlahović, I., Matičec, D. & Velić, I. (1995) Platformni facijesi od gornjeg titona do gornjega alba u zapadnoj Istri i prijelaz u tempestitne, klinoformne i rudistne biolititne facijese donjega cenomana u južnoj Istri. In: Vlahović, I. & Velić, I. (Eds.), *1st Croatian Geological Congress, Excursion Guide-Book,* Hrvatski geološki institut, 67–110, .

Tišljar, J., Vlahović, I., Velić, I., Matičec, D. & Robson, J. (1998) Carbonate facies evolution from the late Albian to middle Cenomanian in southern Istria (Croatia): Influence of synsedimentary tectonics and extensive organic carbonate production. *Facies*, *38*, 137–152. https://doi.org/10.1007/bf02537361

Tomašić, N., Čobić, A., Bedeković, M., Miko, S., Ilijanić, N., Gizdavec, N. & Matošević, M. (2021) Rare earth elements enrichment in the upper Eocene Tošići–Dujići bauxite deposit, Croatia, and relation to REE mineralogy, parent material and weathering pattern. *Minerals*, *11*(11), 1260. https://doi.org/10.3390/min11111260

Trabelsi, K., Sames, B., Wagreich, M., Kázmér, M., Mindszenty, A. & Martín-Closas, C. (2021) A new diverse charophyte flora and biozonation of the Eocene bauxite cover-sequence at Gánt (Vértes Hills, Hungary). *Journal of Systematic Palaeontology*, *19*(7), 541–563. https://doi.org/10.1080/14772019.2021.1938264

van Hinsbergen, D.J.J., Torsvik, T.H., Schmid, S.M., Maţenco, L.C., Maffione, M., Vissers, R. L.M., Gürer, D. & Spakman, W. (2020) Orogenic architecture of the Mediterranean region and kinematic reconstruction of its tectonic evolution since the Triassic. *Gondwana Research*, *81*, 79–229. https://doi.org/10.1016/j.gr.2019.07.009

Velić, I., Matičec, D., Tišljar, J. & Vlahović, I. (1995) Opći prikaz geološke građe Istre (A review of the geology of Istria). In: Vlahović, I. & Velić, I. (Eds.), 1st Croatian Geological Congress, Excursion Guide-Book, Hrvatski geološki institut, 5–30.

Velić, I. & Tišljar, J. (1988) Litostratigrafske jedinice u dogeru i malmu zapadne Istre (zapadna Hrvatska, Jugoslavija). *Geološki vjesnik*, *41*, 25–49.

Velić, I., Tišljar, J. & Sokač, B. (1989) The variability of thicknesses of the Barremian, Aptian and Albian carbonates as a consequence of changing depositional environments and emersion in Western Istria (Croatia, Yugoslavia).– *Memorie della Società geologica italiana*, *40 (1987)*, 209–218.

Velić, I., Tišljar, J., Vlahović, I., Velić, J., Koch, G. & Matičec, D. (2002) Palaeogeographic variability and depositional environments of the Upper Jurassic carbonate rocks of Velika

Kapela Mt. (Gorski Kotar area, Adriatic Carbonate Platform, Croatia). *Geologia Croatica*, *55*(2), 121–138.

Velić, I., Vlahović, I. & Tišljar, J. (1994) Late Jurassic lateral and vertical facies distribution: From peritidal and inner carbonate ramps to perireefal and peritidal deposits in SE Gorski Kotar (Croatia). *Géologie Méditerranéenne*, *21*(3), 177–180. https://doi.org/10.3406/geolm.1994.1558

Villanova-de-Benavent, C., Proenza, J.A., Torró, L., Aiglsperger, T., Domènech, C., Domínguez-Carretero, D., Llovet, X., Suñer, P., Ramírez, A. & Rodríguez, J. (2023) REE ultra-rich karst bauxite deposits in the Pedernales Peninsula, Dominican Republic: Mineralogy of REE phosphates and carbonates. *Ore Geology Reviews*, *157*, 105422. https://doi.org/10.1016/j.oregeorev.2023.105422

Vind, J., Malfliet, A., Blanpain, B., Tsakiridis, P.E., Tkaczyk, A.H., Vassiliadou, V. & Panias, D. (2018) Rare earth element phases in bauxite residue. *Minerals*, *8*(2), 77. https://doi.org/10.3390/min8020077

Vlahović, I., Tišljar, J., Velić, I. & Matičec, D. (2005). Evolution of the Adriatic Carbonate Platform: Palaeogeography, main events and depositional dynamics. *Palaeogeography, Palaeoclimatology, Palaeoecology*, *220*(3–4), 333–360. https://doi.org/10.1016/j.palaeo.2005.01.011

Vlahović, I., Tišljar, J., Velić, I., Matičec, D., Skelton, P., Korbar, T. & Fuček, L. (2003) Main events recorded in the sedimentary succession of the Adriatic Carbonate Platform from Oxfordian to the upper Santonian in Istria (Croatia). In: Vlahović, I. & Tišljar, J. (Eds.), *Field Trip Guidebook: Evolution of Depositional Environments from the Palaeozoic to the Quaternary in the Karst Dinarides and the Pannonian Basin / 22nd IAS Meeting of Sedimentology*, Hrvatsko geološko društvo, 19–58.

Vlahović, I., Velić, I. & Matičec, D. (2023) A brief introduction to the geology of Istria. In: FioFiri, K. & Čobić, A. (Eds.), *Excursion Guide-book, 7th Croatian Geological Congress*, 1–13. Hrvatski geološki institut.

Vodyanitskii, Y.N. (2011) Chemical aspects of uranium behavior in soils: A review. *Eurasian Soil Science*, *44*(8), 862–873. https://doi.org/10.1134/S1064229311080163

Wang, X., Jiao, Y., Du, Y., Ling, W., Wu, L., Cui, T., Zhou, Q., Jin, Z., Lei, Z. & Weng, S. (2013) REE mobility and Ce anomaly in bauxite deposit of WZD area, Northern Guizhou, China. *Journal of Geochemical Exploration*, *133*, 103–117. https://doi.org/10.1016/j.gexplo.2013.08.009

Wanty, R.B. & Goldhaber, M.B. (1992) Thermodynamics and kinetics of reactions involving vanadium in natural systems: Accumulation of vanadium in sedimentary rocks. *Geochimica et Cosmochimica Acta*, *56*(4), 1471–1483. https://doi.org/10.1016/0016-7037(92)90217-7

Wei, T. & Simko, V. (2017) R package “corrplot”: Visualization of a Correlation Matrix (0.84). https://github.com/taiyun/corrplot

Wignall, P.B. & Ruffell, A.H. (1990) The influence of a sudden climatic change on marine deposition in the Kimmeridgian of northwest Europe. *Journal of the Geological Society (London)*, *147*(2), 365–371. https://doi.org/10.1144/gsjgs.147.2.0365

Yang, S., Wang, Q., Deng, J., Wang, Y., Kang, W., Liu, X. & Li, Z. (2019) Genesis of karst bauxite-bearing sequences in Baofeng, Henan (China), and the distribution of critical metals. *Ore Geology Reviews*, *115*, 103161. https://doi.org/10.1016/j.oregeorev.2019.103161

Yang, S., Wang, Q., Liu, X., Kan, Z., Santosh, M. & Deng, J. (2022) Global spatio-temporal variations and metallogenic diversity of karst bauxites and their tectonic, paleogeographic and paleoclimatic relationship with the Tethyan realm evolution. *Earth-Science Reviews*, *233*, 104184. https://doi.org/10.1016/j.earscirev.2022.104184

Yuste, A., Bauluz, B. & Mayayo, M.J. (2017) Origin and geochemical evolution from ferrallitized clays to karst bauxite: An example from the Lower Cretaceous of NE Spain. *Ore Geology Reviews*, *84*, 67–79. https://doi.org/10.1016/j.oregeorev.2016.12.025

Zarasvandi, A., Carranza, E.J.M. & Ellahi, S.S. (2012) Geological, geochemical, and mineralogical characteristics of the Mandan and Deh-now bauxite deposits, Zagros Fold Belt, Iran. *Ore Geology Reviews*, *48*, 125–138. https://doi.org/10.1016/j.oregeorev.2012.02.010

Zhou, J., Yu, W., Wei, W., Yang, M. & Du, Y. (2023) Provenance and tectonic evolution of bauxite deposits in the Tethys: Perspective from random forest and logistic regression analyses. *Geochemistry, Geophysics, Geosystems*, *24*(6), e2022GC010745. https://doi.org/10.1029/2022GC010745

Zhou, W., Han, G., Liu, M., Song, C. & Li, X. (2020). Geochemical distribution characteristics of rare earth elements in different soil profiles in Mun River Basin, Northeast Thailand. *Sustainability*, *12*(2), 457. https://doi.org/10.3390/su12020457

6. BIOGRAPHY OF THE AUTHOR

Ivor Perković was born on April 13th, 1997 in Pula, Croatia. After he finished elementary school, he attended the Gymnasium in Pula. In 2015 he started the undergraduate study of geology on the Faculty of Sciences (University of Zagreb), which he graduated in 2018. Afterwards he continued his education on the graduate study of mineralogy and petrology on the same Faculty, which he graduated in 2020. After graduating, he received the Hrvoje Posilović Award for the Best Master Thesis, given by the Croatian Geological Society. In the same year he started working on the Faculty of Mining, Geology and Petroleum Engineering as a teaching assistant, where he holds exercises in Clay Mineralogy. Since 2020 he is a member of the WIANLab project (Western Istrian Anticline as an Ideal Natural Laboratory for the Study of the Regional Unconformities in Carbonate Rocks), funded by the Croatian Science Foundation.

List of published papers and chapters:

Durn, G., Perković, I., Stummeyer, J., Ottner, F. & Mileusnić, M. (2021). Differences in the behaviour of trace and rare-earth elements in oxidizing and reducing soil environments: Case study of terra rossa soils and Cretaceous palaeosols from the Istrian peninsula, Croatia. Chemosphere, 283, 131286.

Durn, G., Perković, I., Razum, I., Ottner, F., Škapin, S.D., Faivre, S., Beloša, L., Vlahović, I. & Rubinić, V. (2023). A tropical soil (Lixisol) identified in the northernmost part of the Mediterranean (Istria, Croatia). Catena, 228, 107144.

Durn, G., Perković, I., Mileusnić, M., Vlahović, I., Ružičić, S., Matešić, D., Tešović Cvetko, B., Martinuš, M., Rubinić, V., Razum, I., Šegvić, B., Mihovilović, M. & Zvocak, S. (2023) Field trip A2 – Red Istria: Western Istrian Anticline as an ideal natural laboratory for the study of the regional unconformities in carbonate rocks. In: Fio Firi, K. & Čobić, A. (Eds.) Excursion guide-book, 7th Croatian Geological Congress with International Participation, 02.–04. 10. 2023., Poreč, Croatia. Croatian Geological Survey, 33–58.

Palinkaš, S.S., Perković, I., Čobić, A., Jurković, I., Tasev, G., Serafimovski, T. & Spangenberg, J. E. (2022). Evolution of ore-forming fluids in a post-collisional porphyry Cu-Au system: A case study from the Bučim deposit, Republic of North Macedonia. Ore Geology Reviews, 146, 104913.

Perković, I., Tešović, B.C., Martinuš, M., Škapin, S.D., Vlahović, I., Matešić, D. & Durn, G. (2024). Glauconitisation of an Upper Jurassic palaeosol: Case study of the Zlatni Rt, Istria, Croatia. Catena, 238, 107841.

Perković, I., Martinuš, M., Cvetko Tešović, B., Vlahović, I., Matešić, D., Newton, R. J., He, T., Šoufek, M., Razum, I. & Durn, G., (2024). Tracing the evolution of the world's first mined bauxite from palaeotopography to pyritization: Insights from Minjera deposits, Istria, Croatia. Geologia Croatica, 77(2), 159-178.